IN-SITU MAGNETORESISTANCE MEASUREMENTS DURING PATTERNING OF SPIN VALVE DEVICES

DEBORAH MORECROFT

DOWNING COLLEGE

CAMBRIDGE

AUGUST 2003

A DISSERTATION SUBMITTED FOR THE DEGREE OF DOCTOR OF PHILOSOPHY AT THE UNIVERSITY OF CAMBRIDGE.

Abstract

This dissertation describes an experimental study on the patterning of thin films and spin valve devices. Initially the change in the magnetisation reversal of ferromagnetic $Ni_{80}Fe_{15}Mo_5$ thin films was investigated as the shape anisotropy was increased using optical lithography to pattern wire arrays. These structures show a progressive increase in coercivity and a transition between single and two-stage reversal with increasing milling depth. A similar patterning technique was applied to unpinned ($Ni_{80}Fe_{20}$/Cu/$Ni_{80}Fe_{20}$) pseudo spin valve (PSV) structures in order to enhance the coercivity of one of the ferromagnetic layers. The increased coercivity induced by micropatterning changed the natural similarity of the magnetic layers and the structure exhibited a small spin valve response. These initial measurements were carried out with separate milling and electrical characterisation steps. However, it was decided that it would be ideal to design a technique to do *in-situ* magnetoresistance measurements during milling. This meant that the samples could be milled and characterised in the same step, leading to a much cleaner and more efficient process.

In-situ magnetoresistance measurements were carried out during micropatterning of PSV devices, and the measurements showed the evolution in the electrical response as wire structures were gradually milled through the thickness. Contrary to what was expected, the structures showed a maximum spin valve response when fully milled through. The effect of further increasing the shape anisotropy by reducing the wire width, and changing the material properties in the PSV structure has also been investigated. MR measurements were taken as the temperature was increased from 291K to 493K, and the results show that the patterned PSV structures have a better thermal stability than exchange biased spin valves with an IrMn pinning layer.

The experiment was extended to the nanoscale, and the results show that a significant increase in MR is not observed despite the fact that the magnetic configuration tends more towards single domain. This is thought to be due to an increase in the initial resistance of the structures. A small increase in MR was observed as the wire width was decreased from 730 to 470nm, although the spin valve response is heavily dependent on the gallium dosage density during patterning in the Focused Ion Beam (FIB). Micromagnetic simulations were carried out, which agree with the experimental results and showed the change in the magnetisation reversal from rotation to switching as the dimensions were reduced on the nanoscale.

Preface

This dissertation is submitted for the degree of Doctor of Philosophy in the University of Cambridge. Except where specific reference is made, this is entirely my own work and includes nothing that is the outcome of work done in collaboration. No part of this thesis has been or is being submitted for any other qualification at this or any other university. This dissertation does not exceed the limit of length.

Some of the work in this thesis has been published as listed below.

Publications

- **"***Control of the switching properties of magnetic thin films and spin valve devices by patterning",*

D.Morecroft, C.W. Leung, N.A. Stelmashenko, J.L. Prieto, D.B. Jardine and M.G. Blamire. IEEE Trans. Mag. 37 Issue: 4 Part: 1 (2001) pp. 2079 –2081.

- **"***In-situ magnetoresistance measurements during patterning of thin films and spin valve devices",*

D.Morecroft, C.W. Leung, J.L. Prieto, G.Burnell and M.G. Blamire
J. Appl. Phys. 91, pp. 8575-8578 (May-2002).

- **"***In-situ magnetoresistance measurements of nanopatterned pseudo spin valve devices",*

D. Morecroft, D.J. Kang, B. Van Aken, J.L. Prieto and M.G. Blamire.
J. Appl. Phys., (To be submitted).

- **"***A study of exchange bias in spin valve devices by in-situ magnetoresistance measurements."*

D. Morecroft, J.L. Prieto and M.G. Blamire.
J. Magn. Magn. Mater., (To be submitted).

- **"***Integrated magnetic field sensor based on magnetoresistive Spin Valve structure",* J.L.Prieto, N.Rouse, N.K. Todd, **D. Morecroft**, J. Wolfman, J.E.Evetts, M.G. Blamire. Sensors & Actuators A 94 (2001) pp. 64-68.

Deborah Morecroft
Device Materials Group, Department of Materials Science, Cambridge University.
August 2003.

Acknowledgements

So many people have contributed in different ways towards the publication of this thesis and I feel truly indebted. I am grateful to my supervisor Dr. Mark Blamire for guiding me through the Ph.D. project and for proof reading this thesis. Special thanks go to Dr. Jose Prieto for his constant support and encouragement, for his valuable comments on this thesis, for convincing me that I could run a marathon and for being a great friend. Thanks to Dr. Bas Van Aken 'the long legged runner' for his enlightening simulations and for checking through this thesis. Thanks to Dae-Joon Kang for the FIB work, and for never shying away from 'just one more chip'. Thanks to Dennis Leung for providing the initial test samples, for interesting discussions and helpful advice throughout the project. Thanks to the Head of the Device Materials Group, Prof. Jan Evetts for always having his office door open, and for inspiring me with his deep insight in materials physics. Thanks to Dr. Gavin Burnell, Dr. John Durrell and Dr. Karen Yates for contributing towards the smooth running of the lab.

I would like to thank my friends in the lab for making it a fun place to work, Brian "Spaghettino" Pang, Laura "Laurina" Singh, Edgar "the flying Equadorian", Dr. Luis "Spaniardo" Hueso, the G- gang Dr. Ashish Garg and Dr. Yee-Siau Cheng, Dr. Ruman "daddy" Tomov, Dr. Vassilka "mummy" Tsaneva, Chris Bell, Sibe Mennema, Rachel Speaks, Dr. Chiranjib Mitra, Dr. Veni Madhav Adyam, James Loudon, Dr. Noel Rutter, James Ransley, Ugi Balasumbramaniam, James Chapman, Dr. Karl Sandeman, as well as former group members Dr. Jerome Wolfman, Dr. Robert "Salsa" Hadfield, Dr. Phil McBrien, you don't realise what a difference you made.

I have been financially supported by a grant from the Engineering and Physical Sciences Research Council (EPSRC). I am grateful to Nordiko for supplying the spin valve wafers for testing.

A big thank you to my Dad, the true science enthusiast of the family, for reminding me what research is all about and for patiently reading through this thesis. Thanks to my sister Jane for the cartoon in the dedication, and to her husband Andrea for recently giving me a nephew 'Thomas'. Thanks to my Mum, sister Simona and brother Anthony for their wise counsel and for putting up with me. Last but not least, thanks to Fenners gym and Cornucopia coffee….I couldn't have made it through without you!

Glossary of Acronyms

MR	Magnetoresistance
AMR	Anisotropic magnetoresistance
GMR	Giant magnetoresistance
TMR	Tunneling magnetoresistance
VSM	Vibrating sample magnetometer
AFM	Atomic force microscopy
PSV	Pseudo spin valve
SV	Spin valve
AFM	Antiferromagnetic
FM	Ferromagnetic
NM	Non-magnetic
MRAM	Magnetic random access memory
SDT	Spin dependent tunnelling
RF	Radio frequency
LMIS	Liquid metal ion source
SPM	Scanning probe microscopy
STM	Scanning tunnelling microscopy
PSD	Position sensitive detector
EPD	End-point detection

For my parents

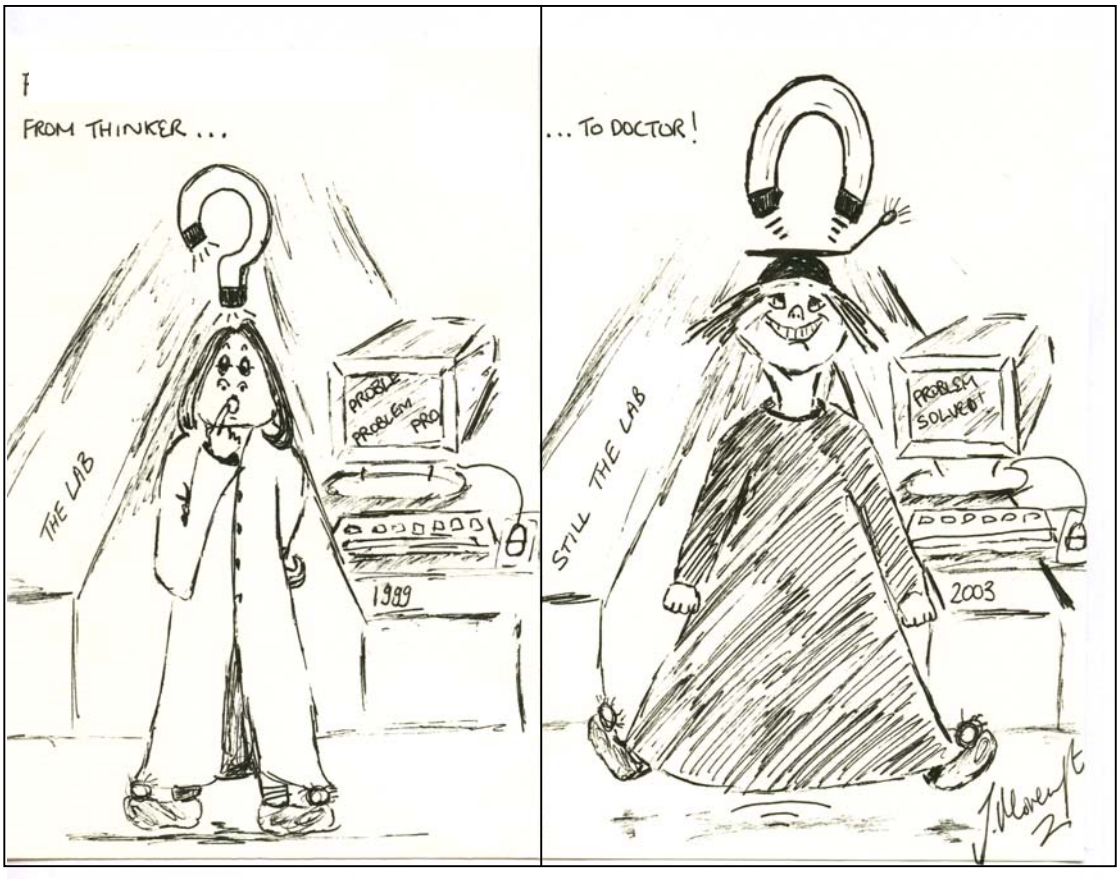

Contents.

Chapter 6

Chapter 7

Chapter 8

Imagination is more important than knowledge.
Albert Einstein

Chapter 1

Introduction

1.1 Spintronics.

Recent years have seen rapid developments in the new field of spintronics, (also called magnetoelectronics or spin electronics) [1]. This new research area combines two traditional branches of physics: magnetism and electronics. The aim is to find ways to manipulate the electron spin in transport processes. Until recently information processing technology has been based on purely charge-based devices, ranging from the vacuum tube to today's million-transistor microchips. These devices rely on the movement of electric charges, and ignore the extra degree of freedom which is inherent to every electron: the electron spin. Magnetism and electron spin are interlinked and according to quantum theory two electrons are allowed to have the same energy as long as they have different spin directions: spin-up (↑) electrons and spin down (↓) electrons. In an ordinary electric circuit the spins are randomly oriented and have no effect on current flow. In a magnetic field the spin-up and spin-down electrons have different energies depending on their orientation with respect to the applied field. Spintronic devices manipulate spin-polarised currents by using the electron spin to control current flow. Ferromagnetic materials are particularly appropriate for these devices because they exhibit spontaneous magnetisation in the absence of an applied field, which creates an imbalance of spin populations near the Fermi level in the electronic structure. The imbalance of available energy states for spin-up and spin-down electrons leads to a difference in the resistance of the two types of electron, i.e. ferromagnetic materials can provide charge carriers that are spin polarised. In fact, the modulation of spin-polarised currents in ferromagnetic materials has received considerable attention partly due to the possible magnetoelectronic applications [2], but also due to the interesting fundamental physics.

Magnetism (and hence electron spin) has always been important for information storage, and magnetic recording is by far the largest economical application of magnetism [3]. Therefore, it is not surprising that the information storage industry has provided the initial successes in spintronics technology. Computers now come fitted with high-capacity hard drives that rely on a spintronic effect, giant magnetoresistance (GMR) to read the densely packed data. Magnetic Random Access Memory (MRAM) is a strong competitor for the next new type of computer memory. MRAM will have the capability to retain the magnetic information even when the power is switched off, but unlike present forms of non-volatile memory, it will have switching rates and re-writability challenging those of conventional RAM.

Another interesting area of spintronics research is looking at the possibility of achieving spin-polarised currents in semiconductors instead of metals. This would allow a wealth of existing microelectronics techniques to be co-opted and would open up the possibility of other types of devices controlled by polarized light or electric fields [4,5]. This avenue of research may lead to a new class of multifunctional electronics that combine logic, storage and communications

on a single chip. Among the major achievements of spintronics to date is the understanding of spin dependent transport properties in various physical systems. These include metallic multilayers showing giant magnetoresistance, ferromagnetic tunnel junctions exhibiting spin dependent tunnelling and certain ferromagnetic oxides showing colossal magnetoresistance near the metal-insulator transitions. The transport of spin polarised currents in semiconductors is barely understood to date, but interesting first results have been achieved [6]. In 1999, two groups succeeded in injecting spin across the interface between two semiconductors – one magnetic and one non-magnetic. Laurens Molenkamp and colleagues at the University of Würzburg in Germany used the magnetic semiconductor zinc selenide as the spin-aligning ferromagnetic layer [7]. Also Hideo Ohno of Tohoku University in Japan collaborated with David Awschalom's team at the University of California in Santa Barbara to produce manganese-doped GaAs as the ferromagnetic layer [8]. On both cases, the researchers passed their spin-polarised current into GaAs-based light-emitting diode with an efficiency of about 90 per cent. Their success was confirmed by the fact that the emitted light was circularly polarised- a direct consequence of the spin polarization of the current.

There are various types of magnetoresistance (MR) depending upon the different materials and construction designs. The recent research into new MR effects has lead to an extraordinary range of solid-state structures, e.g. magnetic multilayers and tunnel junctions. The next section will give a brief overview of the various types of MR effects.

1.2 Magnetoresistance.

Magnetoresistance (MR) is defined as a change in the electrical resistance of a substance in the presence of a magnetic field. The signal response of a device is often characterised by the percentage MR, as shown by Eqn. (1.1), where ΔR is the change in resistance in an applied field and R is the resistance in the absence of an applied field

$$MR(\%) = \frac{\Delta R}{R} \tag{1.1}$$

Many different forms of MR have been researched, using a variety of different materials and multilayer designs. This section will give an overview of the different types of magnetoresistance effect including ordinary MR, anisotropic MR, giant MR, tunnelling MR, colossal MR, and ballistic MR.

Ordinary magnetoresistance (OMR).

Consider a metal or semiconductor sample as shown in Fig. 1.1. The resistance R, measured by the voltage between A and B in the presence of a constant current I_x, is found to increase

by ΔR when a magnetic field is applied. This is the transverse magnetoresistance effect, and occurs because the conduction electrons are displaced from their trajectories by the Lorentz force. In general, $\Delta R/R=aH^2$, where a is a different constant for each metal [9]. An increase in resistance is also found when the applied field is parallel to the current, but ΔR is about half as large and is known as the longitudinal MR. Ordinary MR is very small for moderate magnetic fields <1%.

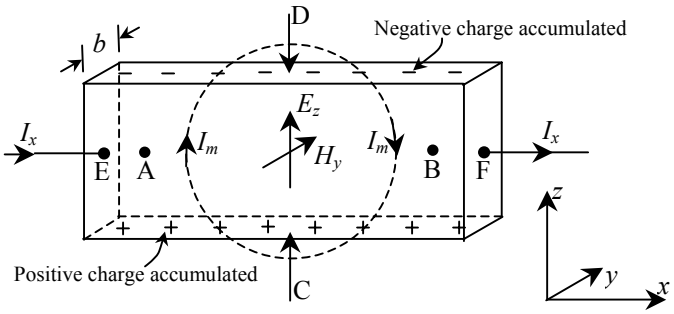

Fig. 1.1 *Schematic diagram to show the experimental arrangement for measuring transverse magnetoresistance effect. The sample shown has a negative Hall coefficient. H_y is into the page, and I_m is the current in the coils producing H_y. (After Ref[8]).*

Anisotropic magnetoresistance (AMR).

The variation in resistance of typical magnetic metals at room temperature depends upon the orientation of the field with respect to the measuring current. When the applied field is parallel to the current the resistance increases with increasing field, and when the applied field and current are orthogonal the resistance decreases with increasing field. The difference in resistance at high fields represents the anisotropic magnetoresistance effect (AMR) common to all ferromagnetic metals. The physical origin of the magnetoresistance effect lies in the spin-orbit coupling: as the magnetisation M_s rotates, the electron cloud about each nucleus deforms slightly, and this deformation changes the amount of scattering undergone by the conduction electrons in their passage through the lattice [10-12]. The amount of AMR varies for different materials, for Fe AMR $\Delta R/R \approx 0.4\%$, whilst for $Ni_{70}Co_{30}$ AMR $\Delta R/R \approx 5\%$. Fig. 1.2 shows examples of the anisotropic magnetoresistance effect in sputtered polycrystalline films of Fe, Co, Ni, $Ni_{81}Fe_{19}$, $Ni_{70}Co_{30}$, and $Ni_{50}Co_{50}$.

The change in resistance due to AMR can be described by Eqn. (1.2), where θ is the angle between the current and the magnetisation.

$$R_{tot} = R_{\min} + \Delta R_{AMR} \cos^2 \theta \qquad (1.2)$$

The AMR effect has commonly been used in computer hard-disk drives and other sensors, however they are now being replaced by spin valve and GMR multilayer sensors, which have larger sensing signals.

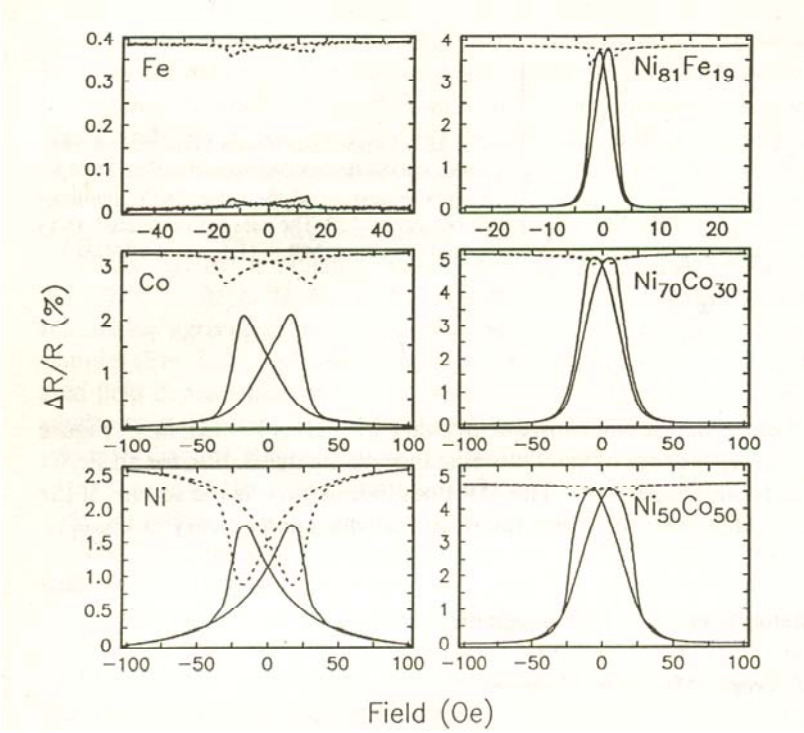

Fig. 1.2 *Examples of the anisotropic magnetoresistance effect in sputtered polycrystalline films of Fe, Co, Ni, $Ni_{81}Fe_{19}$, $Ni_{70}Co_{30}$ and $Ni_{50}Co_{50}$. The full and dotted lines correspond to magnetic field applied orthogonal and parallel to the current respectively in the plane of the films. The films in each case are ≅1000Å thick (After Ref [13]).*

Giant magnetoresistance (GMR).

In 1988 Baibich *et a*l. observed magnetoresistance changes as large as 50% at low temperatures in Fe/Cr multilayer structures [14]. The Fe layers were antiferromagnetically coupled across the Cr spacer layers, and the large change in resistance was found to be due to the change in the relative orientation of the ferromagnetic layers from antiparallel to parallel alignment as the field was increased. In order to achieve a large resistance change it was important for the Fe layers to be antiparallel in the absence of an applied field, and it was found that the interlayer coupling oscillated between ferromagnetic and antiferrromagnetic depending on the thickness of the Cr interlayer [15,16]. The effect has since been observed for a variety of different transition metal/non-magnetic metal multilayers, including Co/Cu which displayed GMR as large as 110% at room temperature for magnetic fields ~20kOe. Values of ~20% or more can be obtained for a field of a few tens of Oersteds. The resistance of the structure varies with the angle between the magnetisation of adjacent magnetic layers

as $\cos\theta$, and since the net moment of the structure M varies as $\cos(\theta/2)$, the change in resistance due to GMR can be described by Eqn. (1.3).

$$R(\theta) = R_{\min} + \Delta R_{GMR}\left(1 - \cos\theta\right)/2 \qquad (1.3)$$

The physical mechanism of GMR is extrinsic and it can be engineered, which is part of the reason why there was such intense interest in optimising the effect for sensor applications. It is best described using a two current model which assumes that the conduction electrons are sub-divided into two spin sub-bands: those with spins parallel to the magnetisation (majority) and those with spins antiparallel to the magnetisation (minority). There is a dissimilar scattering rate for the two electron channels due to a difference in the available energy states at the Fermi level. When the ferromagnetic layers are ferromagnetically coupled, the majority electrons see a low resistance channel through the entire structure, which leads to a lower resistance overall. When the ferromagnetic layers are antiferromagnetically coupled, both spin channels are equally scattered through the entire structure, leading to a higher resistance state. The GMR effect is shown schematically in Fig. 1.3.

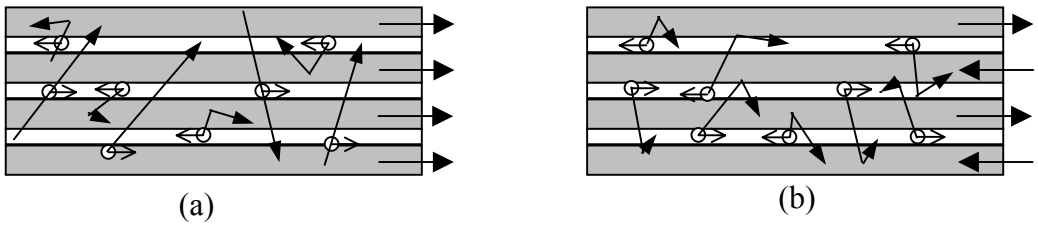

Fig. 1.3 *Schematic of conduction in multilayer magnetic film array, showing how differential spin scattering produces a different resistance for parallel (a) and antiparallel (b) film magnetisations.*

Since the initial discovery of GMR in magnetic/non-magnetic multilayers, many alternative designs have been investigated to control the relative orientations of the ferromagnetic layers and to optimise the signal response and sensitivity. These will be described in more detail in Chapter 3, where spin valve theory and devices will be reviewed. The GMR effect has been of great interest to the hard-disk drive industry and IBM introduced the first GMR read-head sensor in 1997, within 10 years of its initial discovery. The major advantages over AMR are the improved signal response which enabled miniaturisation and therefore increased data storage density, and also the ability to engineer the response. The figure of merit of a GMR sensor is given by the change in the MR divided by the field interval, and biasing magnets are normally used to move the operating point of the sensor to achieve the maximum figure of merit.

Tunnelling magnetoresistance (TMR).

In the spin dependent tunnelling (SDT) effect, electrons tunnel across a thin (1-3nm) insulating barrier between two ferromagnetic electrodes, and the tunnelling electric current between two metal layers depends on the relative angle between the magnetisation in the two metal layers. This phenomenon was first observed by Julliere [17] in a Fe-Ge-Co junction in 1975. Slonczewski showed theoretically that the tunnelling electric conductance varies as $\cos\theta$, where θ is the angle between magnetisations in the metal layers [18]. The TMR effect can be understood using the same two channel electron spin model as for GMR. However, TMR is due to a dissimilar tunnelling conductance between asymmetric spin sub-bands, whilst GMR occurs due to spin scattering asymmetry through the entire structure. The magnitude of TMR is strongly dependent on the spin polarisation of the conduction electrons, i.e. the spin asymmetry of the density of states at the Fermi level. Recently significant room temperature MR signals have been observed, ranging from 20-40% [19,20]. These recent advances have opened up a range of potential applications for TMR devices including non-volatile tunnel junction random access memories (TJRAM) and MR sensors for very high-density magnetic storage (HD drives). However, problems related to the insulating barrier still need to be overcome including reducing the junction resistance [21,22] and improving the thermal stability.

Colossal magnetoresistance (CMR).

The manganese oxides of general formula $RE_{1-x}M_xMnO_3$ (*RE*= rare earth, *M*= Ca, Sr, Ba, Pb) have remarkable interrelated structural, magnetic and transport properties induced by the mixed valence (3^+-4^+) of the Mn ions. In particular, they exhibit very large negative magnetoresistance, called colossal magnetoresistance (CMR), in the vicinity of the metal-insulator transition for certain compositions. Historically, the mixed-valence perovskites $La_{1-x}M_xMnO_3$ (*M*= Ca, Sr, Ba) were studied in the fifties, both experimentally [23,24] and theoretically [25-28]. The experiments performed on polycrystalline samples showed antiferromagnetic (AF) insulating behaviour at low and high *x* values and ferromagnetic (F) metallic behaviour in a certain range of concentrations centred around $x\approx1/3$. The research shows that the magnetic and electrical properties of the manganites are governed by exchange interactions between the Mn ion spins [25,26], although the fundamental physics is still not fully understood. The great interest in CMR materials has been partly due to their large MR, but also because they posses a high spin polarisation of the conduction electrons, which could have implications for spin injection devices. In 1993, 60% MR was reported at room temperature in $La_{0.67}Ba_{0.33}MnO_3$ thin film [29], and the following year an MR effect in excess of a million percent was reported as in $La_{0.67}Ba_{0.33}MnO_3$ at a temperature of 77K [30]. The

experiments were then extended to other CMR oxides such as the layered manganites, $La_{2-2x}Sr_{1+2x}Mn_2O_7$ [31] and Sr_2MoFeO_6 [32]. The main drawback of using CMR materials for technological applications is the need for large magnetic fields, typically in the range of several *T*. Also the MR tends to be very large around the Curie temperature T_c, whereas it becomes negligible at temperatures much lower or higher than T_c.

Ballistic magnetoresistance (BMR).

Ballistic magnetoresistance (BMR) is an effect that occurs in the conduction of spin-polarised electrons through highly constricted (≈10nm) junctions in which the spin-flip mean free path is long compared to the magnetic domain wall width. When a magnetic domain wall resides in the constriction, the electrical resistance is much larger than it is after an external magnetic field is applied to sweep out the domain wall. The resulting magnetoresistive effect is much larger than for GMR or TMR. Experimentally there is a large variation in the magnitude of the BMR, as well as a wide range in the conductance where the peak BMR occurs. García *et al.* observed BMR values up to ≈300% in mechanically formed nanocontacts of various ferromagnetic metals and up to 700% in electrodeposited Ni-Ni nanocontacts [33]. Verluijs et al. [34] observed 540% BMR in mechanically formed nanocontacts of the half-metallic ferromagnet Fe_3O_4. More recently Chopra and Hua [35] reported over 3000% BMR in Ni nanocontacts deposited on electropolished Ni tips, and even larger 100,000% BMR [36] using only mechanical pulled Ni wires to eliminate the possibility of any extraneous chemical layer being present. The results were shown to be stable over several cycles. According to Chung *et al.* [37], spin-ballistic transport through the nanocontact is responsible for BMR in different regimes of conductance from normal metal (Ni, Co, Fe), to semimetal (CrO_2) to insulators. The behaviour is determined by the spin-scattering at the domain wall and controlled by the domain wall thickness only. This implies a universal BMR mechanism, indicating that the effect should be observable in a very large class of ferromagnetic material systems.

1.3 Overview of the Dissertation.

There are currently two systems of units in widespread use in magnetism: the Gaussian or *cgs* system and the SI or *mks* unit system. The unit systems have advantages and disadvantages, and they are both used throughout this thesis. The *cgs* and *mks* systems of magnetic units have different philosophies. The *cgs* system took an approach based on magnetostatics and the concept of the 'magnetic dipole', while the *mks* system takes an electrodynamic approach to magnetism based on electric currents. The *mks* system is generally used where fundamental concepts and calculations are involved, and material properties are generally discussed in *cgs*

units. The table in Fig. 1.4 gives the equations for some of the magnetic quantities used in this thesis in *mks* and *cgs* units, as well as the conversion factors between them.

cgs units	*mks (SI)* units
$B=H+4\pi M$ B in gauss (G) H in oersteds (Oe) M in emu/cm^3	$B=\mu_0(H+M)$ B in tesla (T) H in amperes/metre (A/m) M in tesla
cgs to *SI*	*SI* to *cgs*
B: 1G=10^{-4}T H: 1Oe= 79.6A/m M: 1emu/cm^3=12.57×10^{-4}T	1T=10^{4}G 1A/m=12.57×10^{-3}Oe 1T=796emu/cm^3

Fig. 1.4 *A table to show the equations for some magnetic quantities in csg and mks units, the conversion factors are also shown.*

The theme of this dissertation is an experimental study of how the magnetic and electrical properties of ferromagnetic thin films and pseudo spin valve structures can be controlled by patterning. Chapter 2 gives a brief review of the general background including the theory of ferromagnetism, micromagnetics, and nanomagnetics. A review is also given of the experimental work already carried out within the field. Two different subjects are described, which are directly related to the following chapters: (1) the effect of patterning highly anisotropic structures in ferromagnetic thin films, and (2) the effect of miniaturisation to the sub-micron scale on the magnetisation reversal of ferromagnetic thin films.

Chapter 3 gives a review of the work carried out on GMR structures including antiferromagnetically coupled multilayers, exchange biased spin valves and pseudo spin valves. A brief overview of the current status of MRAM is also given, which is one of the applications for pseudo spin valve devices.

The experimental methods used in this work are described in Chapter 4, including microfabrication, nanofabrication, and a variety of analysis techniques.

Chapter 5 describes the initial experimental results including the micropatterning and magnetic analysis of soft magnetic thin films and the micropatterning of one of the layers in a $Ni_{80}Fe_{20}/Cu/Ni_{80}Fe_{20}$ pseudo spin valve structure and magnetoresistance analysis.

Chapter 6 describes the design, building and testing of the *in-situ* magnetoresistance measurement rig including the design of the sample holder and field coils, the voltage-offset amplifier, noise reduction measurements and system calibration.

Chapter 7 gives the first experimental measurements obtained from the *in-situ* rig showing the change in magnetoresistance with increasing milling depth as the pseudo spin valves are patterned with highly anisotropic wire array structures. Measurements were also carried out using a different pseudo spin valve construction with CoFe/Cu/CoFe. Magnetoresistance measurements were carried out at different temperatures to compare the thermal stability of the pseudo spin valve structures with exchange-biased spin valves.

Chapter 8 shows the *in-situ* magnetoresistance results from nanopatterning highly anisotropic structures in pseudo spin valves and compares the experimental results with micromagnetic modelling.

Finally this dissertation ends with a summary of the results in Chapter 9 including a section on ‘other work’.

References

[1] D.D. Awschalom, M.E. Flatté, N. Samarth, "Spintronics", Scientific American, June (2002); M. Ziese, M.J. Thornton (Eds.), *Spin Electronics*, Springer-Verlag Berlin Heidelberg, (2001).

[2] J.M. Daughton, A.V. Pohm, R.T. Fayfield, C.H. Smith, *J. Phys. D: Appl. Phys*., **32**, R169 (1999).

[3] R.M. White, J. Magn. Magn. Mater. **226-230**, 2042-2045 (2001)

[4] J.M. Kikkawa, D.D. Awschalom, *Nature*, **397**, 139 (1999).

[5] H. Ohno, D. Cgiba, F. Matsukura, T. Omiya, E. Abe, T. Dieti, Y. Ohno, K. Ohtani, *Nature*, **408**, 944 (2000).

[6] M. Ziese, *Spin Electronics*, **Chapter 17**, pg 396-415, Springer-Verlag Berlin Heidelberg, (2001).

[7] R. Fiederling *et al*. *Nature*, **402**, 787 (1999).

[8] Y. Ohno *et al*., *Nature*, **402**, 790 (1999).

[9] N. Cusack, *The Electrical and Magnetic Properties of Solids*, **Chapter 6**, pg 132, Longmans (1958).

[10] T. R. McGuire, R.I. Potter, *IEEE Trans. Mag.* **MAG-11**, 1018 (1975).

[11] J. Smit, *Physica* (Utrecht) **XVI**, 612 (1951).

[12] P. Ciureanu, "Magnetoresistive Sensors" in *Thin Film Resistive Sensors*, ed. by P. Ciureanu, S. Middelhoek, Institute of Physics Publishing, Bristol, pg. 253 (1992).

[13] S.S.P. Parkin, *Ultrathin Magnetic Structures II*, Springer-Verlag Berlin Heidelberg, **Chapter 2.4**, 156 (1994).

[14] M.N. Baibich, J.M. Broto, A. Fert, F. Nguyen-Van-Dau, F. Petroff, P. Etienne, G. Creuzet, A. Friedrich, J. Chazelas: *Phys. Rev. Lett.,***61**, 2472 (1988).

[15] S.S.P. Parkin, *Phys. Rev. Lett.*, **67**, 3598 (1991).

[16] S.S.P. Parkin, R. Bhadra, and K. P. Roche, *Phys. Rev. Lett.*, **66**, 2152 (1991).

[17] M. Jullière, *Phys. Lett.* **54A**, 225 (1975).

[18] J.C. Slonczewski, *Phys. Rev. B.,* **39**, 6995 (1989).

[19] J. Moodera, J. Nassar, G. Mathon, *Annu. Rev. Mater. Sci.,* **29**, 381 (1999).

[20] S.S.P. Parkin, K.P. Roche, M.G. Sammant, P.M. Rice, R.B. Beyers, R.E. Scheurlein, E.J. O'Sullivan, S.L. Brown, J. Bucchiganno, D.W. Abraham, Y. Lu, M. Rooks, P.L. Trouiloud, R.A. Wanner, W.J. Gallagher, *J. Appl. Phys.,* **85**, 5828 (1999); R.C. Sousa, J.J. Sun, V. Soares, P.P. Freitas, A. Kling, M.F. da Silva, J.C. Saores, *Appl. Phys. Lett.,* **73**, 3288 (1998); S. Cardoso, V. Gehanno, R. Ferreira, P.P Freitas, *IEEE Trans. Magn*., **35**, 2952 (1999).

[21] J.J. Ruigrok, R. Coehoorn, S.R. Cumpson, H. van Kesteren, *J. Appl. Phys.,* **87**, 5398 (2000).

[22] J.J. Sun, K. Shimazawa, N. Kasahara, K. Sato, S. Saruki, T. Kagami, O. Redon, S. Araki, H. Morita, N. Marsuzaki, *Appl. Phys. Lett.,* **76**, 2424 (2000).

[23] G.H. Jonker, J.H. Van Santen, *Physica,* **16,** 337 (1950); G.H. Jonker, J.H. Van Santen, *Physica,* **16,** 599 (1950); G.H. Jonker, *Physica,* **20,** 1118 (1954).

[24] E.O. Wollan, W.C. Koehler, *Phys. Rev.,* **100,** 545 (1955).

[25] C. Zener, *Phys. Rev.,* **81,** 440 (1951).

[26] P.W. Anderson, H. Hasegawa, *Phys. Rev.,* **100,** 675 (1955).

[27] P.G. de Gennes, *Phys. Rev.,* **118,** 141 (1960).

[28] J.B. Goodenough, *Phys. Rev.,* **100,** 564 (1955).

[29] R. von Helmholt, J. Singleton, D.A. Keen, R. McGreevy, K. Samwer, *Phys. Rev. Lett.*, **71**, 2331 (1993).

[30] S. Jin, T.H. Tiefel, M. McCormack, R.A. Fastnach, R. Ramesh, L.H. Chien, Science, 264, 413 (1994); M. McCormack, S. Jin, T.H. Tiefel, R.M. Fleming, J.M. Phillips, R. Ramesh, *Appl. Phys. Lett.,* **64**, 3035 (1994).

[31] Y. Morimoto, A. Asamitsu, H. Kuwahara, Y. Tokura, *Nature,* **380,** 141 (1996); Y. Morimoto, *Aust. J. Phys.,* **52,** 255 (1999).

[32] K.I. Kobayashi, T. Kimura, H. Sawada, K. Terakura, Y. Tokura, *Nature,* **395,** 677 (1998).

[33] N. García, M. Muñoz, Y.W. Zhao, *Phys. Rev. Lett.*, **82**, 2923 (1999); *Appl. Phys. Lett.,* **76**, 2586 (2000); N. García, M. Muñoz, G.C. Qian, H. Roher, I.G. Saveliev, Y.W. Zhao, *Appl. Phys. Lett.,* **79**, 4550 (2001).

[34] J.J. Verluijs, M.A. Bari, J.M.D. Coey, *Phys. Rev. Lett.*, **87**, 026601 (2001).

[35] H.D. Chopra, S.Z. Hua, Phys. Rev. B., 66, 020403-1 (2002).

[36] S.Z. Hua, H.D. Chopra, Phys. Rev. B., 66, 060401-1 (2003).

[37] S.H. Chung, M. Muñoz, N. García, W.F. Egelhoff, R.D. Gomez, *Phys. Rev. Lett.*, **89**, 287203-1 (2002).

Few subjects in science are more difficult to understand than magnetism.
Encyclopaedia Britannica.

Chapter 2

Background Reviews

2.1 Magnetic Materials

The various types of magnetic materials are traditionally classified according to their bulk susceptibility, χ, and are listed below.

(i) For diamagnetic materials the susceptibility is small and negative $\chi \approx -10^{-5}$, and the magnetic response opposes the applied magnetic field. Examples of diamagnets are copper, silver, gold, bismuth and beryllium. Superconductors form another special group of diamagnets for which $\chi \approx -1$.

(ii) For paramagnets the χ is small and positive and typically $\chi \approx 10^{-3}$-10^{-5}. The magnetisation of paramagnets is weak but aligned parallel with the direction of the magnetic field. Examples of paramagnets are aluminium, platinum and manganese.

(iii) For ferromagnets the susceptibility is positive, much greater than 1, and typically can have values $\chi \cong 50$ to 10,000. They exhibit spontaneous magnetisation in zero applied field, when the atomic magnetic moments tend to align parallel to each other. Examples of ferromagnetic materials are iron, cobalt, nickel, and several rare earth metals and their alloys.

(iv) Antiferromagnets are ionic compounds, i.e. oxides, sulphides, chlorides. They are similar to paramagnets in that they have a small positive susceptibility, but their susceptibility has a different dependence with temperature and they have an entirely different magnetic structure. They also exhibit spontaneous magnetisation in zero field, when the atomic magnetic moments tend to align antiparallel to each other.

This section will concentrate on the properties of ferromagnetic and antiferromagnetic materials, including the Weiss mean field model, the quantum theory of magnetism, a brief review of antiferromagnetism, the band theory of ferromagnetism and a review of the properties of $Ni_{80}Fe_{20}$ and CoFe, which are the magnetic materials used in this thesis.

2.1.1 The Weiss mean field model.

Around the beginning of the century Weiss developed a theory to explain the behaviour of ferromagnetic materials. He introduced the idea that elementary moments interact with one another, and the interaction can be expressed in terms of a fictitious internal field which he called 'the molecular field' H_m, which acts in addition to the applied field. He assumed that the molecular field was very large, its magnitude was independent of any externally applied field, and its direction was not fixed, but always parallel to the magnetisation. Weiss thought that the molecular field was caused by the magnetisation of the surrounding material and suggested that there was a proportional relationship between the molecular field and the bulk magnetisation M, $H_m = \gamma M$, where γ is a constant called the Weiss constant. As soon as a field is applied, M acquires a small non-zero value, so that a non-zero molecular field appears to aid the applied field in increasing the magnetisation. In order to explain the fact that

ferromagnetic materials do not remain saturated when the applied field is removed, Weiss introduced the concept of *magnetic domains*. He proposed that a ferromagnet is divided into regions (domains), within which the magnetisation is equal to the saturation value. The magnetisation in different domains is in different directions, so that the magnetisation of a ferromagnetic specimen could be small or even zero. Magnetic saturation (M_s) is achieved by aligning the magnetisation of each domain with the applied field. The value of M_s varies with temperature, T, decreasing from a maximum value at T=0K at first slowly, then more and more rapidly as T increases, becoming zero at the Curie temperature, T_c. Above T_c the behaviour is similar to a paramagnetic material, with the magnetisation being proportional to the field and the susceptibility decreasing with increasing temperature.

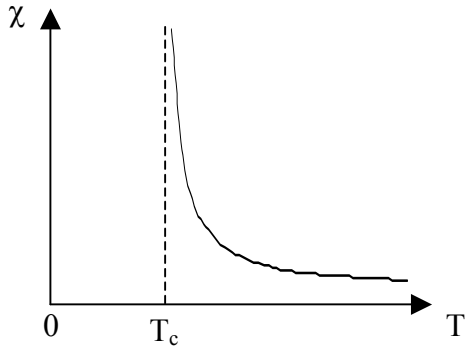

Fig. 2.1 *A schematic of the variation of susceptibility χ with temperature T for a ferromagnetic material according to the Curie-Weiss law.*

The change in the susceptibility χ with temperature is described by the Curie-Weiss law, given in Eqn. (2.1), where C is the Curie constant. The relationship is shown graphically in Fig. 2.1.

$$\chi = \frac{C}{T - T_c} \tag{2.1}$$

Above the Curie temperature, M is zero when there is no applied field, so that H_m is also zero. The molecular field is usually a very large value, for Fe, H_m=6.9×10^6 Oe, this value is much larger than any continuous field produced in the laboratory. Examples of the Curie temperatures of ferromagnetic elements are: iron, T_c=770°C, nickel, T_c=358°C, and cobalt, T_c=1130°C.

2.1.2 Quantum theory of magnetism.

The physical origin of the molecular field was not understood until 1928, when Heisenberg showed that it was caused by quantum-mechanical exchange forces. He showed that the

exchange force is a consequence of the Pauli exclusion principle, which states that two electrons can have the same energy only if they have opposite spins. Therefore, two hydrogen atoms can come so close together that their two electrons can have the same velocity and occupy very nearly the same small region of space, i.e. have the same energy, provided these electrons have opposite spin. If their spins are parallel, the two electrons will tend to stay far apart. The electrostatic energy is modified by the spin orientations, which means that the exchange force is fundamentally electrostatic in origin. (The term "exchange" came from the idea that the electrons on two hydrogen atoms are indistinguishable and can therefore exchange places. The interchange of electrons between the atoms introduces the additional term the exchange energy into the expression for the total energy of the two atoms). Heisenberg showed that the exchange energy plays a decisive role in ferromagnetics. If two atoms *i* and *j* have spin angular momentum $S_i h/2\pi$ and $S_j h/2\pi$, then the exchange energy between them is given by

$$E_{ex} = -2J_{ex}S_iS_jCos\phi \tag{2.2}$$

where J_{ex} is the exchange integral and ϕ is the angle between the spins. If J_{ex} is positive, E_{ex} is a minimum when the spins are parallel ($Cos\phi = 1$) and a maximum when the spins are anti-parallel ($Cos\phi = -1$). If J_{ex} is negative, the lowest energy state results from anti-parallel spins (antiferromagnetism). Ferromagnetism is due to the alignment of spin moments on adjacent atoms, so a positive value of exchange integral is necessary.

The idea that exchange forces are responsible for ferromagnetism and antiferromagnetism allowed scientists to rationalise the appearance of ferromagnetism in some metals and not in others. The curve in Fig. 2.2 is called the Bethe-Slater curve, and it shows the variation of the exchange integral with the ratio r_a/r_{3d}, where r_a is the radius of an atom and r_{3d} the radius of its *3d* shell of electrons. If two atoms of the same kind are brought closer and closer together without any change in the radius r_{3d} of their *3d* shells, the ratio r_a/r_{3d} will decrease from large to small values. When the ratio is large, J_{ex} is small and positive. As the ratio decreases and the *3d* electrons approach each other more closely, the positive exchange interaction, favouring parallel spins, becomes stronger and then decreases to zero. A further decrease in the interatomic distance brings the *3d* electrons so close together that their spins must become antiparallel (negative J_{ex}). This condition is called antiferromagnetism. The curve correctly separates the ferromagnetic *3d* elements iron, cobalt and nickel from the antiferromagnetic *3d* elements chromium and manganese.

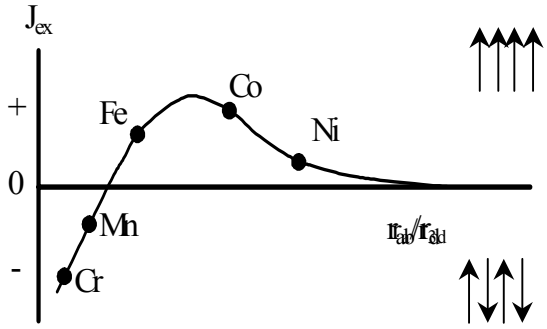

Fig. 2.2 *The Bethe-Slater curve representing the variation of the exchange integral J with interatomic spacing r_{ab} and radius of the unfilled d shell r_d. The positions of various magnetic elements on this curve are indicated. [1]*

2.1.3 Antiferromagnetism

The susceptibility of an antiferromagnetic material varies with temperature is shown in Fig. 2.3.

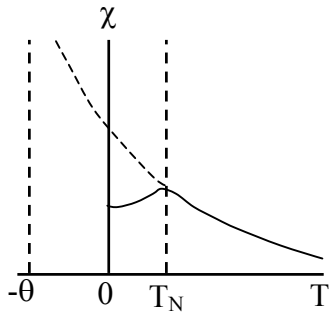

Fig. 2.3 *A schematic of the variation of χ with temperature in the paramagnetic regime of materials which undergo a transformation to antiferromagnetism. [2]*

As the temperature decreases, χ increases but finally goes through a maximum at a critical temperature T_N called the Néel temperature. The substance is paramagnetic above T_N and antiferromagnetic below it. The Curie-Weiss law also applies to antiferromagnets above their ordering temperatures. However the sign of the constant term T_N in the denominator is positive so the law becomes

$$\chi = \frac{C}{T + T_N} \tag{2.3}$$

In many ways the Néel temperature of an antiferromagnet is analogous to the Curie temperature of a ferromagnet. Both mark the borderline temperature above which the material is disordered and below which it is ordered. However, in an antiferromagnetic material the

molecular field tends to align the magnetic moments antiparallel to each other. In other words the exchange force is negative.

2.1.4 The band theory of ferromagnetism.

The Curie-Weiss and Heisenberg models of ferromagnetism are based on local moment theory, i.e. the electrons are localised around the atom. However, for most of the *3d* ferromagnetic materials the 'magnetic' electrons are outer electrons, which are free to move through the solid. Furthermore, the magnetic moments per atom are not integral multiples of the electron spin, the Bohr magneton as required by localised models. The band theory of ferromagnetism was first proposed by Stoner [3] and then independently by Slater [4]. It has been successful in explaining non-integral values of atomic magnetic moments and predicting some aspects of magnetic behaviour of the *3d* series metals and alloys.

In the case of 'free' atoms, i.e. atoms locates at large distances from one another, the electrons occupy sharply defined energy levels in accordance with the Pauli exclusion principle. However, when atoms are brought together to form a solid, their electron clouds overlap, which leads to a splitting of the energy levels. So when *N* atoms come together to form a solid, each level of the free atom must split into *N* levels, because the Pauli exclusion principle now applies to the whole group of *N* atoms. The extent of splitting is different for the different levels, as indicated in Fig. 2.4.

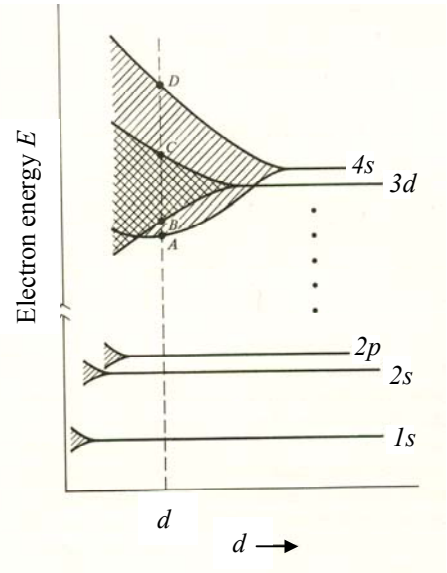

Fig. 2.4 *Splitting of the electron energy levels as the interatomic distance d decreases.(After Ref. [5])*

In the transition elements, the outermost electrons are the *3d* and *4s*; these electron clouds are the first to overlap as the atoms are brought together, and correspondingly the first to split. When the interatomic distance *d* has decreased to d_0, the equilibrium value for the atoms in the crystal, the *3d* levels are spread into a band extending from B to C, and the *4s* levels are spread into a much wider band, extending from A to D, because the *4s* electrons are further from the nucleus. Fig. 2.5 shows a schematic of the density of states of the *sp*- and *d*- bands of ferromagnetic Fe, Co and Ni. *N(E)* represents the density of states and *E* the electron energy. The density of *3d* levels is far greater than the *4s* levels, because there are five *3d* levels per atom with a capacity of 10 electrons, whereas there is only one *4s* level, with a capacity of 2 electrons. The area under the *N(E)* vs *E* curve is equal to the total number of levels in the band. Filled energy levels cannot contribute a magnetic moment, because the two electrons in each level have opposite spin and cancel each other out. In a partially filled energy band it is possible to have an imbalance of spins leading to a net magnetic moment per atom. This arises because the exchange energy removes the degeneracy of the spin-up and spin-down half bands.

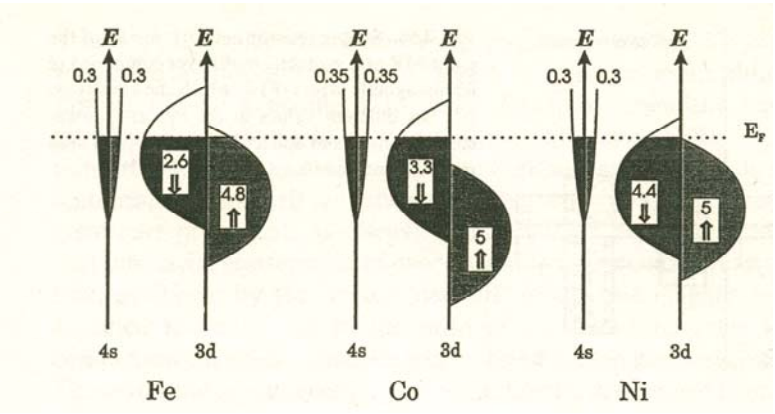

Fig. 2.5 *Schematic diagram of the density of states in the sp- and d- bands of ferromagnetic Fe, Co and Ni. The total numbers of electrons in the spin-down (left) and spin-up (right) bands are also shown. (After Ref [6]).*

The larger the exchange energy the greater the difference in energy between these two half bands. Electrons fill up the band *d* occupying the lowest energy levels first. If the half bands are split, the electrons can begin to occupy the spin down half band before the spin up half band is full. This usually leads to a non-integral number of magnetic moments per atom. The ferromagnetism of Fe, Co and Ni is due to spin imbalance in the *3d* band, and the force creating the imbalance is the exchange force. To create a spin imbalance, one or more electrons must be raised to higher energy levels, so these must not be too widely spaced or the exchange force will not be strong enough to have an effect. The *4s* electrons make no contribution to the spin imbalance, because the density of levels in the *4s* band is low, which

means that the levels are widely spaced. Usually it is assumed that in ferromagnetic metals the conductivity is primarily carried by electrons from the *sp*- bands which are broad and, as a consequence, have low effective masses. In contrast, the *d*- bands are narrow and have high effective masses. The *d*- bands play a very important role in providing final states into which the *sp* electrons can be scattered.

The criteria for the band theory of ferromagnetism can be summarised as follows:

1) The electrons must lie in partially filled bands so that there may be vacant energy levels available for electrons with unpaired spins to move into.

2) The density of levels in the band must be high, so that the increase in energy caused by spin alignment is small.

3) The atoms must be the right distance apart so that the exchange force can cause the electron spins in one atom to align the spins in the neighbouring atom.

2.1.5 $Ni_{80}Fe_{20}$ and CoFe magnetic materials.

The two ferromagnetic materials used in this thesis are NiFe alloys (Permalloy) and CoFe alloys (Permendur). The soft magnetic NiFe alloys have diverse properties and are used in many fields of electrical and electronic engineering. Their structure dependent magnetic properties, such as coercivity, permeability and hysteresis loop shape, depend on the basic magnetic constants and on the microstructure. Throughout the project NiFe alloys in the range 80% were used, which have the highest permeability and therefore a square hysteresis loop. The square hysteresis loop results because in thin sheet form the demagnetising field is insufficient to nucleate a reverse domain and the exchange coupling between the grains is sufficiently strong to maintain the material at saturation in the absence of the reversal field. They can be made with low or even zero magnetostriction, and they have low coercivity, low anisotropy, and the microstructure is isotropic.

Alloy	Relative permeability μ_{max}	Saturation induction B_s (T)	Coercivity Hc (Am^{-1})	Curie temperature (°C)
NiFe	5000-300,000	0.7	1-8	400
CoFe	5000	2.45	160	≈980

Fig. 2.6 *A table summarising the properties of NiFe and CoFe alloys used in this thesis work. (After Ref. [7, 8]).*

Cobalt is the only element which when alloyed with iron causes an increase in saturation magnetisation and Curie temperature. CoFe has a low anisotropy, a high permeability and is polycrystalline. Fig. 2.6 is a table summarising the magnetic properties of NiFe and CoFe.

2.2 Magnetisation Processes.

In order to understand the magnetisation state in zero field and the magnetisation reversal processes, it is important to consider that the magnetic structure is a consequence of energy minimisation. This section will start by describing the energy considerations and the resulting domain patterns, which can be calculated by micromagnetic equations. There will then be an overview of the different types of anisotropy and domain walls. The final section will be on small particle switching theory, which applies to small particles that are too small to contain regular domain walls.

2.2.1 Energy considerations and domain patterns.

In 1935 Landau and Lifshitz [9] showed that the existence of domains is a consequence of energy minimisation. The total energy of a ferromagnetic material in an applied field is given by the sum of the Zeeman energy, exchange energy, anisotropy energies and magnetostatic energy as shown in Eqn (2.4).

$$E_{tot} = \int \left(E_{Zee} + E_{ex} + E_{ani} + E_{stat} \right) dV . \tag{2.4}$$

The Zeeman energy is due to the interaction between the external field H and the magnetisation vector M, and is given by

$$E_{Zee} = -H \cdot M . \tag{2.5}$$

The exchange energy was described in the previous section, and is the energy between the atomic magnetic moments, which tends to align them parallel for a ferromagnetic material and antiparallel for an antiferromagnetic material. Eqn. (2.6) is Heisenberg's expression for the sum of the exchange energies across a material of finite size.

$$E_{ex} = -2 \sum_{ij} J_{ij} S_i \cdot S_j , \tag{2.6}$$

where J_{ij} is the exchange constant between the two adjacent classical spins with spin quantum numbers S_i and S_j at the i and j sites.

The magnetostatic energy per unit volume of a dipole of magnetisation M in a magnetic field H is given by

$$E_{stat} = -\mu_0 \int H . dM , \tag{2.7}$$

When subjected to its own demagnetising field H_d, which is generated by M, we can put H_d=-$N_d M$ in the integral where N_d is the demagnetising factor so that the energy becomes

$$E = \mu_0 N_d \int M.dM$$

$$E = \frac{\mu_0}{2} N_d M^2 \qquad (2.8)$$

A single domain specimen has a large magnetostatic energy associated with it, but the energy can be minimised by breaking up the magnetisation into localised regions (domains), providing for flux closure at the ends of the specimen. Providing that the decrease in magnetostatic energy is greater than the energy needed to form magnetic domain walls, a multidomain structure will occur. This is depicted in Fig. 2.7, which shows (a) the stray field from a uniformly magnetised sample, and a sample divided into (b) two, and (c) four domains. The sample has a high uniaxial anisotropy (e.g. Co), which is shown by the absence of closure domains.

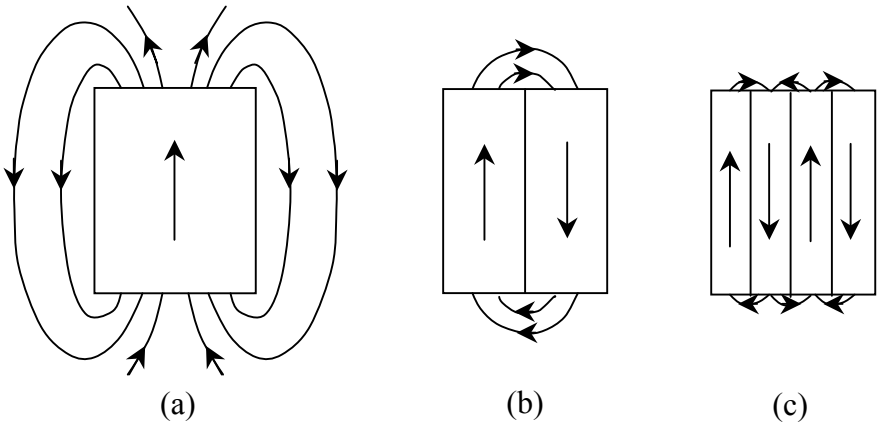

Fig. 2.7 *The stray field of (a) a uniformly magnetised sample, and a sample divided into (b) two, and (c) four domains.*

Magnetic anisotropy can significantly influence the shape of the hysteresis loop, and this term simply means that the magnetic properties depend on the direction in which they are measured. Anisotropy is exploited in the design of most magnetic materials of commercial importance and there are various different forms. It also plays a significant role in the experimental work in this thesis, and therefore the next section will explain the relevant types in more detail.

2.2.2 Magnetic anisotropy.

There are several forms of magnetic anisotropy:

1. Crystal anisotropy.
2. Anisotropy induced by magnetic annealing.
3. Shape anisotropy.
4. Exchange anisotropy.

Of all the different types, only crystal anisotropy is intrinsic to the material. The other forms are extrinsic or 'induced'.

Crystal anisotropy.

Crystal anisotropy is due to spin-orbit coupling, the coupling between the spin and orbital motion of the electrons. When an external field tries to reorient the spin of an electron, the orbit of that electron also tend to be re-orientated, but the orbit is strongly coupled to the lattice and tries to resist any rotation on the spin axis. The energy required to rotate the spin system of a domain away from the easy direction, which is the crystal anisotropy energy, is the energy required to overcome the spin-orbit coupling. The strength of the anisotropy in any particular crystal is measured by the magnitude of the anisotropy constants K_1, K_2, etc.

For cubic anisotropy the anisotropy energy E_K can be expressed in terms of a series expansion of the direction cosines of the magnetic saturation M_s relative to the crystal axes. If M_s makes angles a, b and c with the crystal axes, then α_1, α_2 and α_3 are the direction cosines of these angles,

$$E_K = K_0 + K_1\left(\alpha_1^2\alpha_2^2 + \alpha_2^2\alpha_3^2 + \alpha_3^2\alpha_1^2\right) + K_2\left(\alpha_1^2\alpha_2^2\alpha_3^2\right) + \ldots\ldots \tag{2.9}$$

where K_0, K_1, and K_2 are the anisotropy constants for a given material. K_2 is so small that it is normally ignored and K_0 is independent of angle. For Fe, $K_1>0$ and so the easy axis are the <100> directions. Ni has an FCC crystal structure, $K_1<0$ which represents that the easy axes are the <111> directions. Co is HCP and is a uniaxial crystal with only one easy direction and one hard direction; $[0001]$ and $[10\bar{1}0]$ respectively. For a HCP crystal, the anisotropy can be represented by the one constant approximation:

$$E_a = K_{ul}\sin^2\phi \tag{2.10}$$

where ϕ is the angle of magnetisation with respect to the unique axis, which for $K>0$ is the easy axis, while for $K<0$ it is the hard axis.

Crystal anisotropy can have a large effect on the hysteresis loop. Fig. 2.8 shows the magnetisation curve for iron in different crystallographic directions. The graph shows that saturation can be achieved with quite low fields in the <100> direction, which is the easy direction of magnetisation. If a field is applied along the easy axis direction saturation is completed by domain wall motion. If the field is applied along the <110> or medium direction, domain wall motion occurs at low field until the domains are aligned in the anisotropy axes closest to the field direction. Magnetisation can only increase further by rotation of the M_s vector of each domain until it is parallel with the applied field.

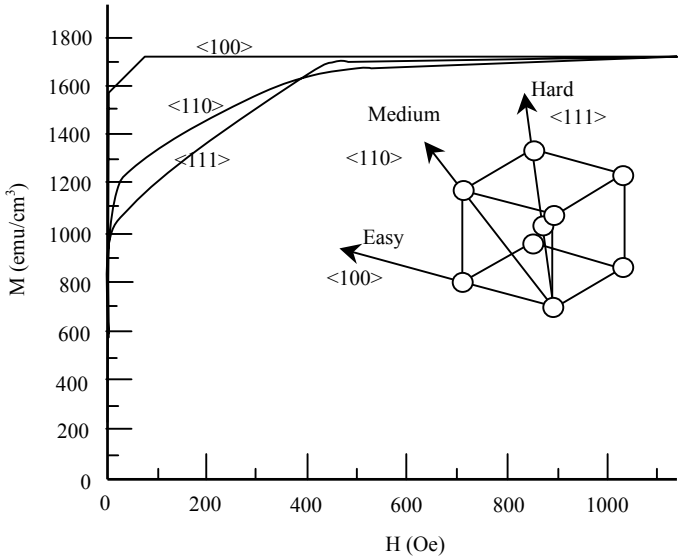

Fig. 2.8 *Magnetisation curve for single crystal iron. (After Ref. [10]).*

This is called domain rotation and it only occurs at high fields, because the field is acting against the strong anisotropy of the crystal. When the rotation is complete the domain wall disappears and the crystal is saturated. The crystal anisotropy is important when the sample is both single crystal and single domain; otherwise the magnetisation is dependent on other factors such as domain structures and induced anisotropy as discussed below. The crystal anisotropy of NiFe alloys ≈100J/m^{-3}, which is much smaller than for Fe ≈47,000J/m^{-3}.

Anisotropy induced by magnetic annealing.

When certain magnetic materials are deposited or heated (at $T<T_c$) in an applied field, they develop a permanent uniaxial anisotropy with the easy axis parallel to the direction of the applied field. They are then magnetically softer along this axis than they were before the treatment. The temperature must be below the Curie temperature but high enough to allow atomic diffusion to occur, and the applied field must be large enough to saturate the material to maximise the anisotropy. The theory is that if a saturating field is applied at a high temperature, the magnetisation will be everywhere in the same direction and diffusion will occur until there is a preferred orientation of like-atom pairs parallel to the magnetisation and the field. On cooling to room temperature, this directional order will be frozen in and the domains that form when the field is removed will be orientated to the axis of the directional order.

Shape anisotropy.

A polycrystalline material has no preferred orientation of it grains and therefore has no crystal anisotropy. If the sample is spherical, an applied field will magnetise it to the same extent in any direction. If it is non-spherical it will be easier to magnetise it along a long axis than along a short axis, due to demagnetising effects. When a bar is magnetised by a field applied from left to right and then removed, a north pole *N* is formed at the right end, and a south *S* pole at the left, as shown in Fig. 2.9 (a). The *H* lines radiate out from the *N* pole to the *S* and tend to demagnetise the material. The demagnetising field H_d acts in the opposite direction to the magnetisation *M* which creates it, and is present whenever magnetic poles are created in a material. Fig. 2.9 (b) shows that H_d is stronger near the poles, and this causes a non-uniformity of magnetisation across the bar: the lines diverge towards the ends, so that the flux density is less there than at the centre.

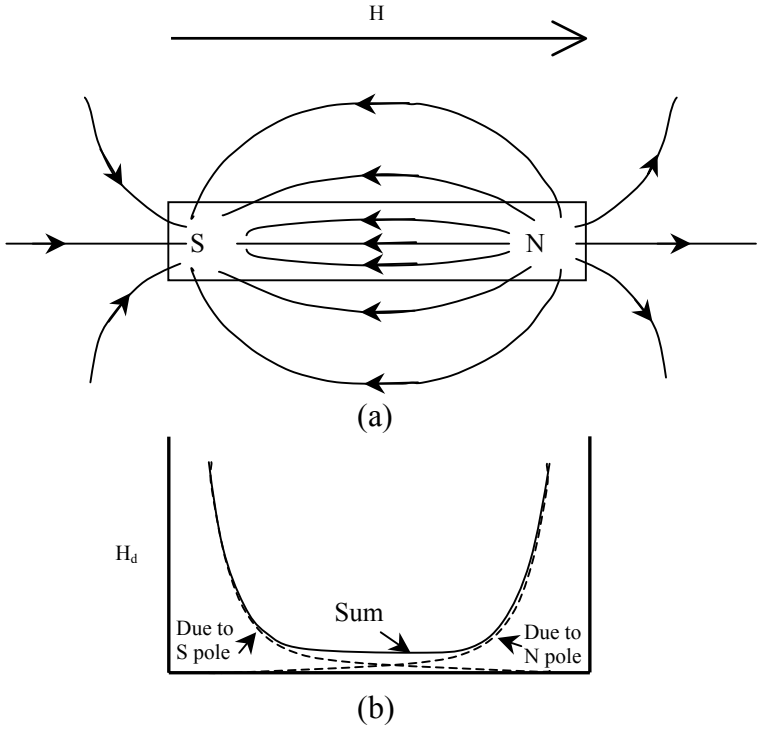

Fig. 2.9 *(a) The H field of a bar magnet after it has been magnetised by an applied field. (b) The variation in the demagnetising field on axis along the length of the bar magnet.*

If the magnet is tapered towards each end the H_d becomes more uniform along the length. If we consider a prolate spheroid (rod) as shown in Fig. 2.10, according to the above argument, a larger field will be required to magnetise the material along the width *a* than along the length *c* because of the larger demagnetising field.

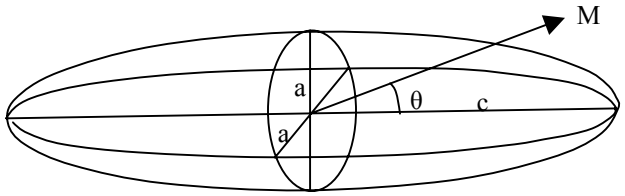

Fig. 2.10 *A prolate spheroid magnetic sample with long axis c and short axis a.*

The shape anisotropy constant K_s is given by

$$K_s = \frac{1}{2}(N_a - N_c)M^2 \tag{2.11}$$

where N_c and N_a represent the demagnetising coefficients along the hard axis and short axis respectfully. Eqn. (2.11) shows that the 'strength' of the shape anisotropy depends on both the length to width ratio *c/a*, which determines $(N_a - N_c)$, and on the magnetisation *M*. For comparison, a prolate spheroid of saturated Co with *c/a* = 3.5 and without any crystal anisotropy, would show the same uniaxial anisotropy as a spherical cobalt crystal with its usual crystal anisotropy, [11].

Exchange anisotropy.

Exchange bias anisotropy refers to the magnetic manifestations of an exchange coupling at the interface between two different magnetically ordered systems. This form of anisotropy was first discovered by Meiklejohn and Bean (M-B) in 1956 [12], when they observed that the hysteresis loop below room temperature of a sample of nominal Co nanoparticles was shifted along the field axis after cooling in an applied field. It was subsequently established that the particles had been partially oxidised to CoO, which is an AFM. Thus, the particles could be considered to consist of a core of single-domain Co with a shell of AFM CoO. In the more than 40 years since its discovery, the phenomenon of exchange anisotropy has become the basis for an important application in information storage technology, with a high current level of world-wide research and development activities. However, it has really only been in the last decade or so that a basic, quantitatively predictive, understanding of exchange anisotropy has begun to be developed significantly beyond the initial model presented by M-B. The relatively slow progression is primarily due to the exchange bias anisotropy being an interface effect between the FM and AFM materials, and the experimental and analytical tools for dealing with interfacial behaviour at the atomic scale have only recently become available. Research into obtaining a thorough and predictive understanding of exchange bias anisotropy is on-going, and there have been a number of conflicting theories [13, 14]. The role of many different parameters involved in exchange bias such as anisotropy, roughness and spin

configuration or magnetic domains, are far from being understood. Also a clear understanding of exchange bias at the microscopic level is still lacking. The next section will give a basic outline of the mechanism of exchange bias anisotropy.

Fig. 2.11 is a schematic diagram of the spin configuration of a FM-AFM bilayer at different stages (i)-(v) of an exchange bias hysteresis loop. This diagram is only meant to illustrate the effect of the coupling and is by no means an accurate portrait of the actual rotation of the FM or AFM magnetisation. When a field is applied in the temperature range $T_N<T< T_c$, the FM spins line up with the field, while the AFM spins remain random as shown in Fig. 2.11 (i). When cooling to $T<T_N$, the AFM spins next to the FM align ferromagnetically to those of the FM due to the interaction at the interface. Away from the interface, the AFM material maintains ordering producing zero net magnetisation, Fig. 2.11 (ii).

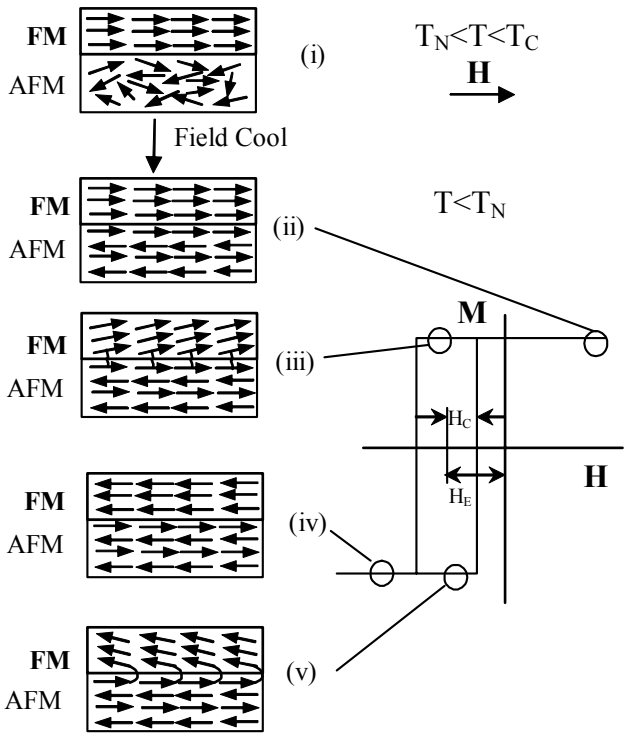

Fig. 2.11 *A schematic diagram of the spin configuration of an FM-AFM bilayer at different stages (i)-(v) of an exchange biased hysteresis loop. Please note that this is simply a schematic diagram and is not an accurate description of the actual rotation of the FM or AFM magnetisations. The strength of the exchange bias is given by H_E and the coercivity of the ferromagnetic layer is given by H_c. (After Ref. [15]).*

When the field is reversed the FM layer starts to rotate, but assuming the AFM layer has a sufficiently large anisotropy, the AFM spins remain unchanged, Fig. 2.11 (iii). The interfacial interaction between the AFM-FM spins tends to align them ferromagnetically, and the AFM spins exert a microscopic torque on the FM spins effectively pinning them in their original position. Therefore, the field required for magnetisation reversal of the FM layer is larger when it is contact with the AFM than when it is free; because a larger field is needed to overcome the microscopic torque, Fig. 2.11 (iv). This type of anisotropy is uniaxial because the FM spins have one stable configuration. When the field is rotated back to its original direction, the uniaxial anisotropy aids the magnetisation reversal and the FM spins rotate for a smaller field than in the free state, (the torque is in the same direction as the applied field), Fig. 2.11 (v). The ferromagnetic material behaves as if there were an extra (internal) biasing field, and the hysteresis loop is shifted in the field axis.

2.2.3 *Domain walls.*

As described previously, the magnetisation of a ferromagnetic material below the Curie temperature and away from M_s is broken up into domains, within which the magnetisation is homogeneous. The domains are separated by domain walls, which are transition regions in which the moments undergo a reorientation. The total displacement across a domain wall is often 180° or 90° and the change in direction takes place over many atomic planes. In thin films there are two types of domain wall: Bloch walls and Néel walls, as shown in Fig. 2.12**.**

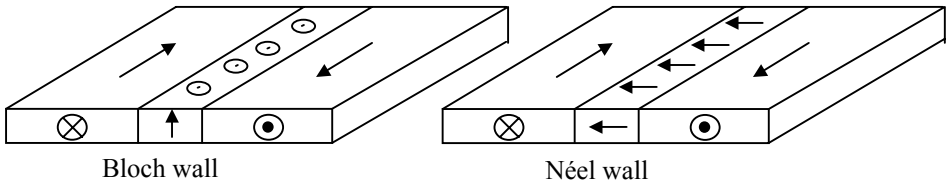

Fig. 2.12 *A conventional Bloch wall and Néel wall in a thin film ferromagnetic material.*

A Bloch wall requires that some of the magnetic moments be oriented normal to the plane of the film. This leads to a demagnetisation energy associated with the Bloch wall. The Néel wall has all the moments oriented in the plane. The Néel wall is energetically favoured once the film thickness decreases below a certain critical value. The width of the domain wall is found by considering the change in energy of the moments due to the exchange interaction and the anisotropy. The anisotropy tends to make the domain wall thinner because it is lowest when all the moments are aligned along crystallographic equivalent axes. The exchange energy tends to make the walls thicker since the exchange energy in a ferromagnet is

minimised when neighbouring moments are aligned parallel. The domain wall energy is the sum of the anisotropy and exchange energy per unit area as given below:

$$\gamma = \left(\frac{\pi^2 JS^2}{\ell a} \right) + K\ell \tag{2.12}$$

where J is the exchange constant, S is the spin quantum number, ℓ is the wall width, K is the anisotropy constant and a is the lattice spacing. The energy minimisation, $\partial\gamma/\partial\ell$ then determines the width of the wall to be

$$\ell = \left(\frac{\pi^2 JS^2}{Ka} \right)^{1/2} \tag{2.13}$$

If the anisotropy is the dominant term then the energy is minimised at small ℓ, whereas if the exchange is dominant the energy is minimised as large ℓ. On application of a field it is the moments within the domain walls, which can most easily be rotated. This is because the resulting directions of the moments within the walls are a fine balance between the exchange and anisotropy energy. Values of anisotropy energy, exchange energy and domain wall thickness for Fe, Co and Ni are summarised in the chart in Fig. 2.13.

Element	Exchange energy, J (J)	Anisotropy energy, K (Jm^{-3}) at 300K	Domain wall thickness (nm)
Fe	2.5×10^{-21}	4.8×10^{4}	40
Co	4.5×10^{-21}	45×10^{4}	15
Ni	2×10^{-21}	-0.5×10^{4}	100

Fig. 2.13 *Magnetic properties of iron, cobalt and nickel. (After Ref. [16]).*

Calculations which show the variation of wall energy with film thickness for various kinds of walls have been carried out for $Ni_{80}Fe_{20}$ [45]. The results show that the total energy of a Néel wall is less than a Bloch wall when the thickness is less than 50nm. The width of Bloch and Néel walls also vary in different ways with film thickness: the thinner the film, the narrower the Bloch wall and the wider the Néel wall. Work by Huber *et al*. [46] identified another type of domain wall in $Ni_{80}Fe_{20}$ films called a cross-tie wall. It consists of a special kind of Néel wall, crossed at regular intervals by Néel wall segments. Its energy is less than that of a Bloch wall or a Néel wall in a certain range of film thickness; the cross-tie wall therefore constitutes a transition form between the Bloch walls of very thick films and Néel walls of very thin films.

2.2.4 Magnetisation reversal of a single domain: coherent rotation.

When a sample is magnetised to saturation, or when it is sufficiently small that the magnetisation is uniform throughout, it may consist of a single magnetic domain. The magnetisation process of a single domain under the influence of an external field is unique in that the magnetisation reversal occurs by coherent rotation at a critical field without any domain wall motion. The Stoner-Wohlfarth model [17] describes the magnetisation curves of an aggregate of single-domain particles with uniaxial anisotropy either as a result of particle shape or from the magnetocrystalline anisotropy.

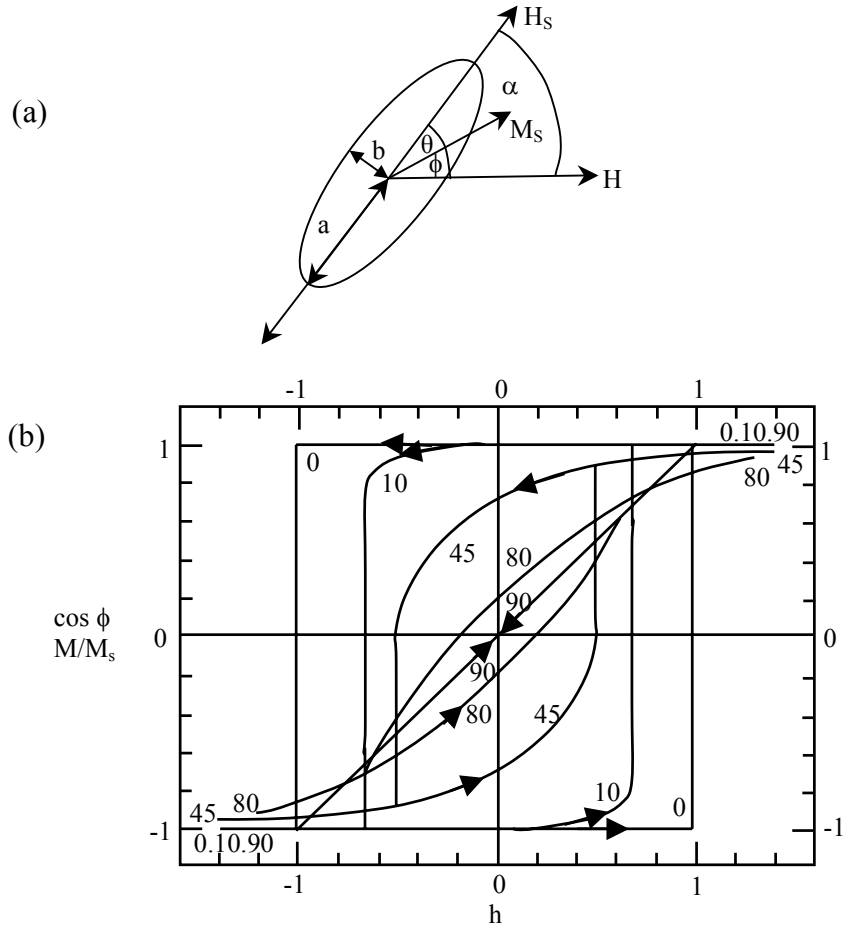

Fig. 2.14 (a) *Shape anisotropy of an ellipsoidal single-domain particle assumed to have neither crystal nor stress anisotropy. The shape anisotropy is due to the particle having a higher demagnetising factor N_d along the short axis than along the long axis. (b) Magnetisation curves obtained from the Stoner-Wohlfarth model for various angles between the direction of the magnetic field and the easy axis, from 0° (H along the easy axis) to 90° (H perpendicular to the easy axis).*

In their simplified model of an ellipsoid with uniaxial anisotropy, the anisotropy is given by

$$E_{an} = K \sin^2 \theta \tag{2.14}$$

When the magnetisation is oriented at an angle θ to the easy direction, as shown in Fig. 2.14 (a), this gives rise to a torque of

$$\tau_{an} = \frac{-dE_{an}}{d\theta} = -2K \sin\theta \cos\theta. \tag{2.15}$$

The torque produced by a field H will be dependent on the angle ϕ between the magnetisation and the field direction by

$$\tau_H = \mu_0 M_S \times H = \mu_0 H M_S \sin\phi \tag{2.16}$$

Equilibrium is reached when the torque produced by the field τ_H equals the torque due to the anisotropy τ_{an} as shown in Eqn. (2.17)

$$\begin{aligned} &\tau_H + \tau_{an} = 0 \\ &\mu_0 H M_S \sin\phi - 2K \sin\theta \cos\theta = 0. \end{aligned} \tag{2.17}$$

The field strength H_s needed to saturate a polycrystalline sample is the field required to rotate the magnetisation away from the easy axis into the field direction, which is assumed to be at 90° to the easy axis. According to the equations above, irreversible switching will occur when

$$H_s \geq \frac{2K}{\mu_0 M_S} \tag{2.18}$$

Stoner and Wohlfarth used this simple model to show that the critical values of the normalised field h required for magnetisation reversal, where the magnetisation reversal jumps discontinuously, depends on the angle between the field and the easy axis as shown in Fig. 2.14 (b). If H is perpendicular to the anisotropy axis the magnetisation is completely reversible. If H is antiparallel to the anisotropy axis there arises irreversible switching when H exceeds $2K/\mu_0 M_S$, and if H is at some arbitrary angle θ to the anisotropy axis the behaviour is partly reversible and partly irreversible.

2.3 Ferromagnetic Wire Structures.

The formation of magnetic domains in soft magnetic thin films has been well studied. If a thin film of $Ni_{80}Fe_{20}$ is saturated in the easy direction, it can remain single domain after the saturating field is removed. The reason is that the demagnetising field in the plane of the film is nearly zero, because the film is so thin; in addition the grain size is very small. The film can be demagnetised by saturating it in the hard direction. When the saturation field is removed, the film breaks up into narrow domains [47]. This is due to anisotropy dispersion, which causes the local magnetisation M_s to vary slightly from one point to another within a domain. In order to minimise the exchange and magnetostatic energy, the M_s direction varies in a

wavelike manner, called *magnetisation ripple*. However, when soft magnetic thin films are patterned into wire arrays, the domain formation is entirely different as described below.

Fluitman [18] carried out AMR measurements on NiFe films to investigate the effect of sample geometry on the magnetoresistance curves. The thickness of the films varied from 200Å to 1μm, and the width varied from 2 to 1000μm. The dependence of the coercivity, H_c on the width of the NiFe strips was derived from the longitudinal magnetoresistance data. The results showed that the geometry significantly influences the magnetoresistance behaviour. The easy axis coercive field H_c showed a clear shift to higher values for decreasing width w of the samples, as shown in Fig. 2.15.

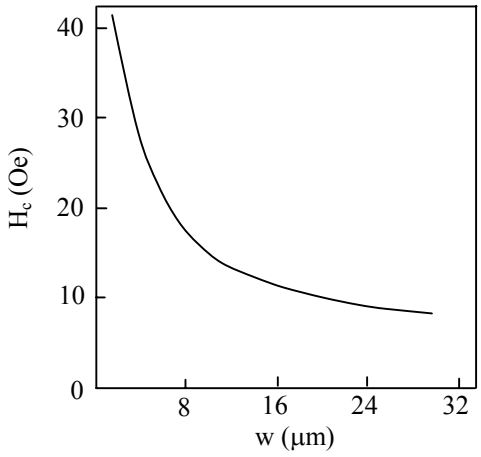

Fig. 2.15 *The change in the easy axis coercive field H_c, as the width w of the NiFe film is reduced. (After Ref. [18]).*

This was ascribed to the fact that small strips behave more and more like single domain systems. Further work was carried out by Kryder *et al* [19] on the magnetic properties and domain structures in narrow NiFe stripes. The 100μm long strips showed a factor of ten increase in coercivity as the width was decreased from 40μm to 1μm. The coercivity also increased with decreasing thickness as it does in sheet films, but the change in coercivity was much larger than in sheet films. For example, in 2μm by 100μm stripes the H_c increased from 10Oe to 35Oe as the thickness decreased from 180nm to 30nm. According to Kryder *et al* the coercivity increase with decreasing stripe width is caused by a buckling of the magnetisation perpendicular to the length of the chip. (Please note that the 'buckling process' described by Kryder *et al* is different to the 'magnetisation buckling' originally reported by Frei *et al* [24]. According to Frei *et al* magnetisation buckling is an incoherent reversal mode present in single domain particles, which give a lower coercivity than coherent rotation or curling).

The buckling process leads to the formation of walls perpendicular to the stripe, and the walls do not move, but block the reverse domains from propagating down the stripe. Fig. 2.16 shows an idealised diagram of the magnetisation buckling. At H=1Oe, a slight magnetisation ripple occurs, which leads to magnetic poles at the edges of the film. The surface poles produce stray field H_m, which acts in alternate half-wavelengths of the ripple to oppose and support the original magnetisation direction. At 8Oe the magnitude of the ripple is large and buckling starts to occur, the local stray field H_m is large enough to allow triangular shaped regions to remain pinned antiparallel to the applied field.

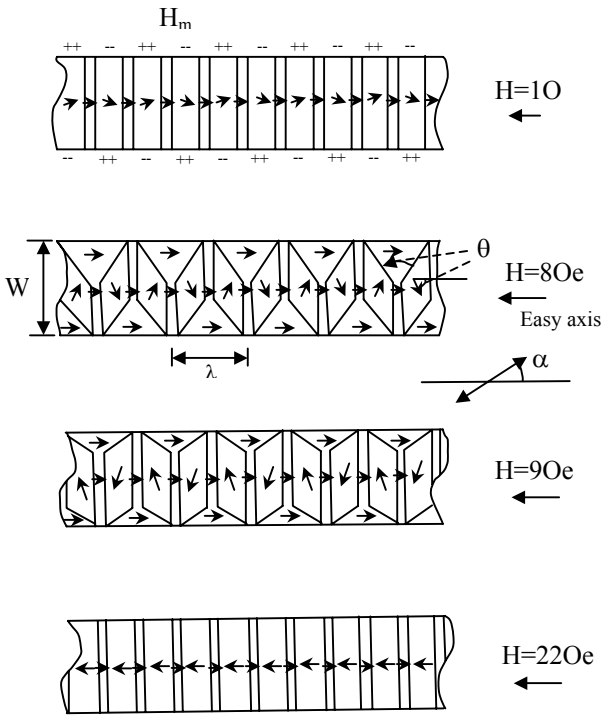

Fig. 2.16 *An idealised diagram of magnetisation buckling. (After Ref. [19]).*

In the alternate half-wavelengths where H_m is parallel to the applied field and anti-parallel to the magnetisation, only a narrow domain wall forms. As the external field is increased to 9Oe there is a reduction in the size of the triangular domains anti-parallel to the applied field, and there is a rotation of the magnetisation within the domain. Therefore at 9Oe, the domain walls separating the alternate half-wavelengths have an angle greater than 180°. At 22Oe the magnetisation has rotated so that the domain walls become 360° walls, which lie transverse to the stripe and the triangular domains have disappeared. This buckling process greatly increases the coercivity of the stripes, and occurs to reduce the magnetostatic energy. The periodicity is approximately equal to the strip width.

The technological requirements for high packing densities make the role played by magnetostatic interactions important as they may significantly modify the magnetic properties of an assembly. In principle, the strength of the magnetostatic interactions can be controlled in principle by varying the inter-element spacing. The effects of magnetostatic interactions upon the magnetisation reversal behaviour in NiFe wire arrays have been investigated, [20,21]. Planar wire arrays with width, w=2μm and variable separation s in the range of 0.5 to 15μm were measured. The wire length was 250μm and the array extended over 250μm. Fig. 2.17 shows the plot of coercive field as a function of s/w (wire spacing/ wire width), when the applied field is parallel to the direction of the sense current along the wire axis.

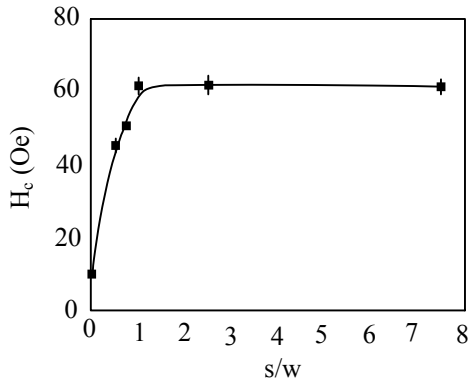

Fig. 2.17 *A plot of the coercive field as a function of wire s/w obtained from the MR measurements at room temperature for a 500-Å thick $Ni_{80}Fe_{20}$ wire array with w=2μm when the applied field is parallel to the easy axis of the wire array (After Ref. [20]).*

A clear reduction in the coercive field is observed for *s/w<1* due to inter-wire magnetostatic interactions, the strength of which increases as the spacing is decreased. When the field is parallel to the wire axis, the domains nucleate at the ends and then sweep through the wire. When a field is applied perpendicular to the easy axis (the hard axis), the demagnetising field is reduced due to magnetostatic interactions and the average hard axis saturation field is reduced. The question of how magnetostatic interactions may affect the MR behaviour of ferromagnetic wire arrays is important both in terms of a better fundamental understanding and improving device performance. The role of magnetostatic interactions on the transport properties of arrays of coupled micro-wires with wire width *w*=1μm and inter-wire spacing *s* in the range 50nm to 2μm has also been investigated by Adeyeye *et al*. [21]. Fig 2.18 shows the change in MR when the field is applied along the easy axis for a 25nm thick NiFe film patterned with wire arrays of width *w*=1μm, and various wire separation *s* for a reference film, *s*=2μm, *s*=200nm and *s*=50nm. The reference film (a) shows a hysteretic response, which is typical of the AMR behaviour in NiFe films.

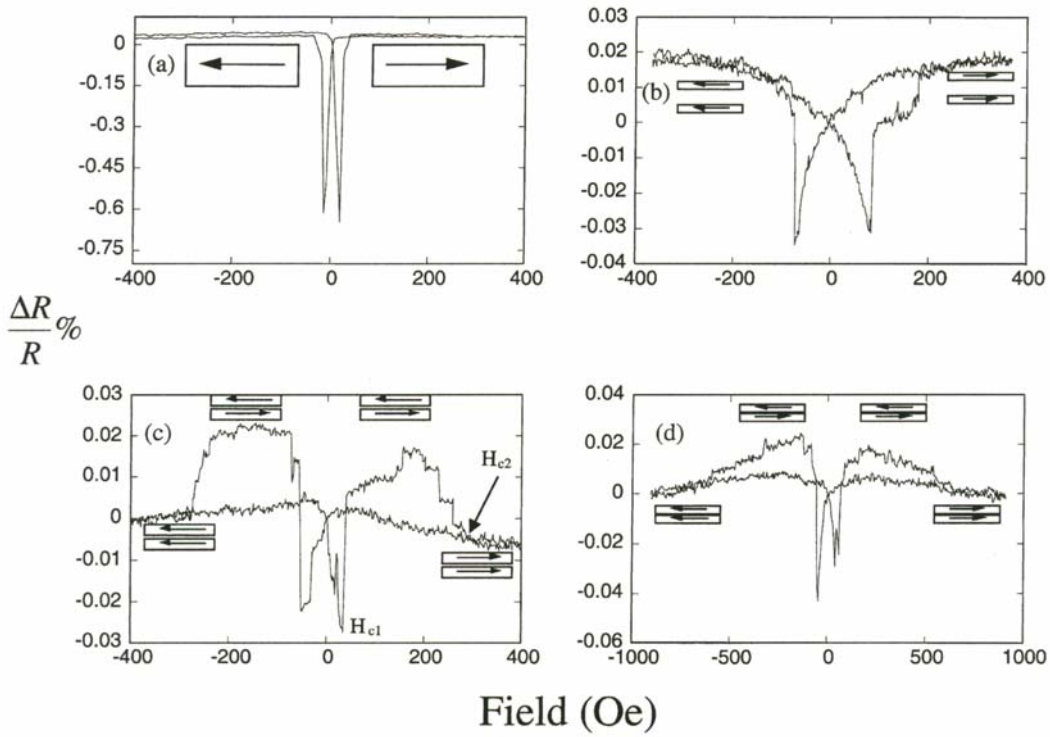

Fig. 2.18 *The MR response to fields applied along the easy axis for a 25nm thick NiFe film patterned with wire arrays of width w=1μm and various wire separation s measured at room temperature for (a) reference film (b) s=2μm (c) s=200nm and (d) s=50nm. (After Ref. [21]).*

A marked increase in coercivity is observed for s=2μm (b) compared to the reference film due to the finite size effect. As the spacing s is reduced further to s=200nm, the response is different due to magnetostatic interactions. As the magnetic field was decreased from negative field saturation, the MR response was reproducible and reversible until a critical field H_{c1}=60Oe. At this field some of the wires undergo magnetisation reversal resulting in an antiparallel alignment and a change in sign of the MR response. This state is stable until the applied field is large enough to overcome the interaction field H_{c2}≈275Oe. Further increase in applied field results in saturation of the magnetisation of the entire array. For s=50nm, similar features in the MR are found, except that the strength of the magnetostatic coupling is stronger. A field of about 670Oe was needed to overcome the interaction field H_{c2} for s=50nm. For fields applied along the hard axis of the wire, the shape of the MR response is strongly dependent on the inter-wire magnetostatic interactions. A marked reduction in the hard axis saturation field is observed in magnetostatically coupled wire arrays due to a reduction in the demagnetising field.

Detailed studies of the change in magnetoresistance as a function of the angular orientation ϕ of the applied field relative to the easy axis of permalloy wires has been carried out. Fig. 2.19 shows the MR curves for various field orientations relative to the wire axis for a 50nm thick NiFe wire array with (a) w=2μm and separation s=5μm, (b) a single wire with w=200μm. In this case, the separation between the wires is much larger than the wire width so that magnetostatic interactions are negligible. The graphs give a direct indication of how the magnetisation reversal changes as the applied field direction changes with respect to the easy axis (the wire axis).

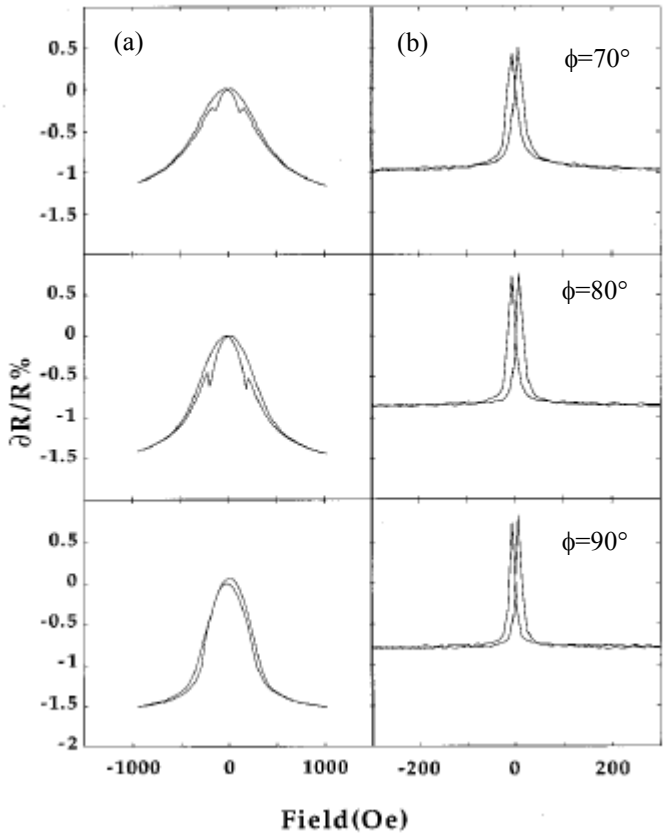

Fig. 2.19 *Representative MR curves for various field orientations relative to the wire axis for a 500 Å thick $Ni_{80}Fe_{20}$ wire array with (a) w=2μm and separation s=5μm (b) w=200μm measured at room temperature. (After Ref. [20]).*

For w=2μm, the MR response at 90° is almost reversible, this is because the component of the applied field along the easy axis is zero. Without a component of applied field along the easy axis, the central region within the wire will not undergo a domain wall displacement and there is no domain formation. For ϕ<90°, the MR is characterised by irreversible jumps in both the forward and reverse cycles giving rise to sharp displacements in the MR curve. The jumps are caused by the component of the applied field along the easy axis of the wire, which forces the

central region of the wire to undergo magnetisation reversal. There is a spatially varying demagnetising field and the central region of the wire has a smaller demagnetising field than the outer regions. The jumps in the MR are due to sudden switching of the magnetisation rather than domain wall motion and annihilation. For the single wire with w=200μm, the MR curve shows identical behaviour for all applied field directions. This is because the larger wire width has a smaller demagnetising field, and the magnetisation reversal process is dominated by domain wall motion as in a continuous film.

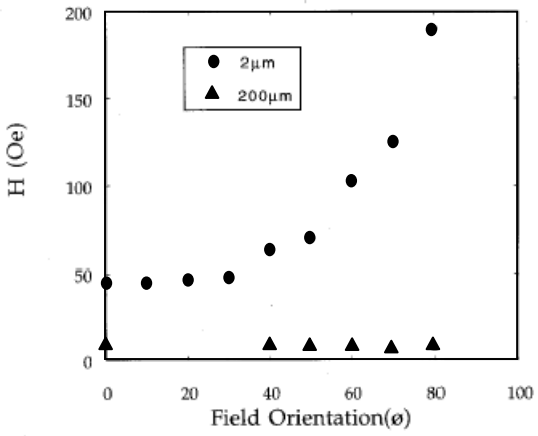

Fig. 2.20 *The angular variation of the 'jump' field for a 500 Å thick $Ni_{80}Fe_{20}$ wire array with w=2μm and s=5μm compared to that for which w=200μm for the same field orientation measured at room temperature. (After Ref. [20]).*

Fig. 2.20 shows a comparison for the coercivity versus field orientation for w=2μm and w=200μm. The graph shows that for the w=2μm wire array the 'jump' field increases with increasing field angle. This is because of the increase in the component of the applied field along the easy axis of the wire as ϕ increases. The orientation dependence of the jump field suggests that the reversal mechanism is incoherent. As expected the 'jump' field for w=200μm as a function of angle remains almost constant.

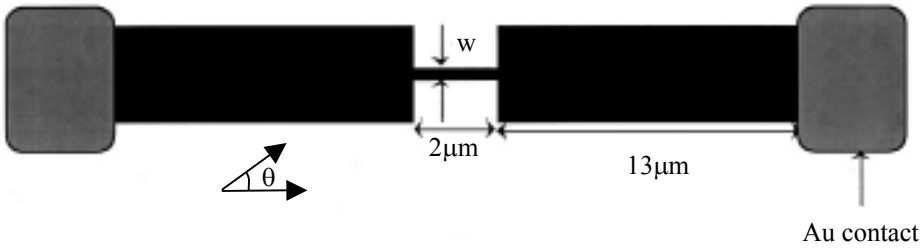

Fig. 2.21 *Schematic representation of the fabricated constricted $Ni_{80}Fe_{20}$ wire with Au external contacts. (After Ref. [22]).*

Magnetoresistance measurements of constricted wires have been carried out [22]. Fig. 2.21 shows the magnetic structure of a 25nm thick NiFe film, which was defined by electron beam lithography. The width and length of the wide parts are 5 and 13μm, and the width of the narrow section varied from 100-500nm. Fig. 2.22 shows the MR measurements for the field applied along the easy axis (a) and hard axis (b) respectfully. When the field is applied along the easy axis, during the initial sweep labelled *A*, the magnetisation is aligned along the negative direction. As the magnetic field is swept towards a positive value at a constant rate, the curve is completely reversible until $H \approx 30$Oe (position *B*). Beyond this point the behaviour was hysteretic corresponding to the magnetisation of the 5μm support switching to the positive field direction. At this point, the magnetisation in the narrow part of the wire still points in the negative direction. When the field is increased to point *C*, the magnetisation reversal of the narrow part occurs. As the width of the constriction is increased the coercivity is reduced.

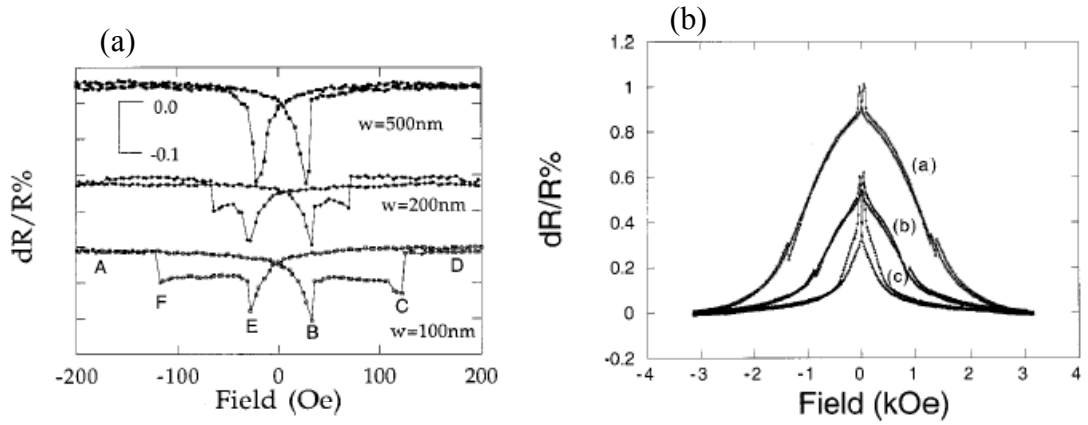

Fig. 2.22 *The MR response to fields applied along (a) the easy axis (b) the hard axis of a single 25nm thick $Ni_{80}Fe_{20}$ constricted wire for various w. In figure (b), (a) is for w=100nm, (b) for w=200nm and (c) w=500nm. (After Ref. [22]).*

These results show that altering the dimensions in different parts of the structure can alter the magnetisation reversal by locally changing the coercivity. This subsequently leads to a change in the MR characteristics as one part of the structure reverses magnetisation with respect to another.

Lee *et al.* studied the magnetisation reversal in two 200μm length regions with distinct widths w_1 and w_2 in the range 1-5μm [23]. They used Magnetic Force Microscopy (MFM) and micromagnetic calculations to show that several domain walls nucleate in the wider part and

are trapped in the junction area, as shown in Fig. 2.23. This implies that domain nucleation at the junction of the wire inititates magnetisation reversal in the narrow half. The switching fields are found to be identical in both halves, which suggests the possibility of designing structures which can be used to 'launch' reverse domains in narrow wires within a controlled field range.

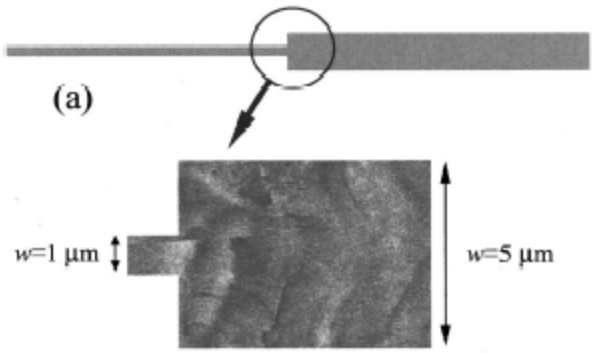

Fig. 2.23 *MFM image obtained at the junction area in the remanent state. (After Ref. [23]).*

2.4 Nanomagnetism.

The problem of predicting the magnetisation reversal field of a single domain particle is one of the oldest in micromagnetics, and is still much sought after due to the general trend towards miniaturisation. Part of the challenge is not only understanding how magnetic structures behave on the mesoscopic scale, but also engineering them for specific applications. For example, applications in magnetic sensors and data storage require different device characteristics. For sensing elements the magnetisation should ideally rotate coherently and reversibly in a small applied field. For magnetic storage the principal requirement is that patterned elements have two distinct magnetisation states and a reasonably high coercivity. Stoner and Wohlfarth's ground breaking paper in 1948 described magnetisation reversal and quantified the switching fields for ellipsoidal single domain particles by coherent rotation [17]. Kittel *et al* demonstrated the existence of single domain particles of Ni in 1950 [48]. Experimental work by Luborsky [49] showed that the coercivity of fine particles has a striking dependence on their size. As the particle size is reduced, it is typically found that the coercivity increases, goes through a maximum, and then tends toward zero. The conclusion was that the mechanism by which the magnetisation of a particle changes differs from one size range to another. Below a critical diameter the particles become single domain, and in this size range the coercivity reaches a maximum. As the particle size decreases further, the coercivity decreases because of thermal effects (the superparamagnetic effect). The measurements by Luborsky showed that the coercivity of single domain iron particles with

axial ratios from about 1 to more than 10 could not be explained by crystal anisotropy or shape anisotropy. This discrepancy forced theoreticians to consider possible modes of incoherent rotation in single domain particles, in which all spins do not remain parallel. The two most important of these incoherent modes are magnetisation *fanning* and *curling*. Jacobs and Bean [50] introduced magnetisation fanning as a possible reversal mechanism, in which the M_s vector of successive spheres in a chain fan out in a plane rotating in alternate directions in alternate spheres. The predictions of the fanning theory agreed well with the experimental results on highly elongated iron particles. In 1957, a second reversal mechanism called *curling* was introduced by Frei *et al* [24]. Since then, many authors have contributed to this field and analysed various configurations of particle shape and crystallinity [25-28]. In order to deal with particles more closely resembling the idealised models of micromagnetics, Luborsky and Morelock [51] examined the properties of iron and iron-cobalt alloy whiskers. These have straight, smooth sides and are structurally the most nearly perfect of all crystals. The coercivities were found to be very size dependent over the large range of whisker diameters investigated, from about 20nm to 100μm, and Luborsky and Morelock concluded from the nature of this size dependence that whiskers thinner than 100nm reversed by curling. The behaviour of thicker whiskers deviated from the predictions of curling theory.

Recent developments in nanofabrication and measurement technology have spurred renewed interest in this topic. It has become possible to fabricate single-crystal magnetic nanostructures, which consist of a single-domain and can widely vary in material, size and shape [29-33]. At the same time a variety of different analysis techniques are available to study the magnetic state of small particles including Magnetic Force Microscopy (MFM) [34] and Superconducting QUantum Interference Devices (SQUIDS) [35]. The various fabrication mechanisms for nanomagnets, such as interferometric lithography in conjunction with electroplating or evaporation [31], or chemical self-assembly [32,33], allow the fabrication of a range of shapes for which the reversal field due to shape anisotropy can be calculated analytically. By experimenting with particles of different sizes and shapes, it has been possible to observe the transition between different reversal mechanisms such as curling, fanning and coherent rotation. Curling and fanning are prevalent in larger samples to reduce the magnetostatic energy, and coherent reversal in smaller samples.

A powerful TEM technique has been developed by Kirk and Chapman [36,37], which allows in-situ magnetic measurements during imaging. The results have shown how the magnetic properties of acicular nanoelements are strongly affected by the shape of their ends. In the remanent state, an acicular element of rectangular shape tends to be almost single domain with the magnetisation directed predominantly along the long axis, except for small domains

at the ends, which achieve partial flux closure [36]. This configuration is shown in Fig. 2.24, and the domains are present in element widths down to 100nm and below.

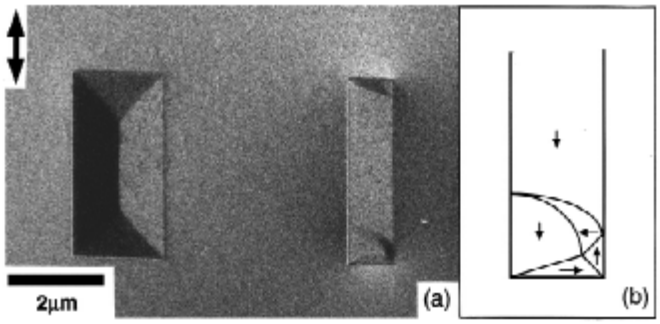

Fig. 2.24 *(a) The change from complete flux closure to partial closure in rectangular NiFe elements when the elements become more acicular, and (b) schematic diagram of end domains. (After Ref. [36]).*

The partial flux closure structure is not present in elements with pointed ends, which leads to the coercivity being more than doubled. Lorentz images have shown that in these structures the domains tend to form at the corners between the body of the element and the pointed ends. Studies on samples with elliptical ends have shown that the ends were sufficiently flat and wide that end domains were able to form and the switching field remained unchanged. However, as the width was reduced, at a threshold value the switching field started to increase steadily. According to micromagnetic modelling, this is thought to be due to domains being forced to form at the centre of the element instead of at the ends.

In nanomagnets the anisotropy depends not only on the band structure of the parent material, but also on the shape of the nanomagnet. A study into the influence of shape and size on the magnetic properties of nanostructures such as ellipses, triangles, squares, pentagons and circles in the size range 35-500nm has been carried out [38]. The parent material was Supermalloy because in bulk it is almost isotropic and so any anisotropy in the nanomagnets must come from their shape. Fig. 2.25 shows the hysteresis loops of nanomagnets of different geometries taken using the Magneto-optical Kerr Effect (MOKE) and averaged over an array. The array size was between $(5\mu m)^2$ and $(10\mu m)^2$; the spacing between each nanomagnet was usually at least equal to the diameter of the nanomagnet, and for the smallest structures was usually as large as three times the diameter. The loops are very different from one another and from that obtained from the conventional unstructured material.

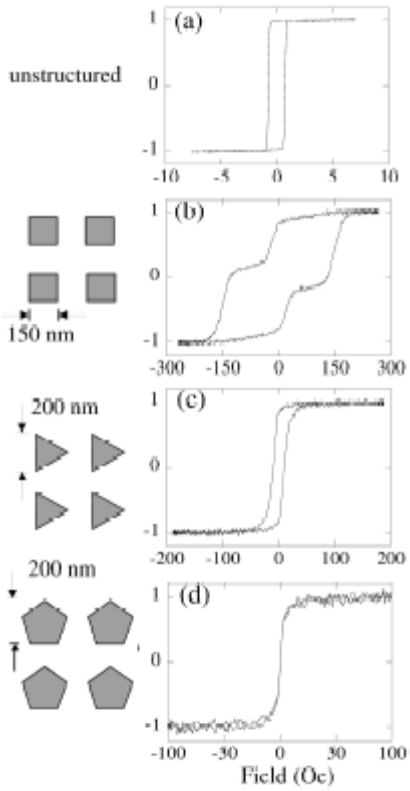

Fig. 2.25 *Hysteresis loops measured from different nanostructures using MOKE. For comparison (a) shows the loop from the unstructured Supermalloy. The y-axis of each graph is magnetisation, normalised to the saturation value. The applied field in the schematic pictures of the nanostructures is assumed to point up the page. The nanostructures have thickness of (a) 6nm, (b) 5nm, (c) 5nm and (d) 3nm. (After Ref. [38]).*

The properties range from those usually associated with hard magnetic materials with switching fields of hundreds of Oersteds down to those associated with very soft magnetic materials with relative permeability suitable for sensing. These changes in properties are a direct result of varying the thickness and symmetry of the nanomagnets in the arrays. Coercivity, hysteresis and susceptibility are all determined by anisotropy. The strong variations in these three parameters suggest that the nanomagnets posses a size-dependent anisotropy. MFM was used to measure the magnitude and symmetry of the anisotropy in nanomagnets of thickness 5nm. Fig. 2.26 shows the polar plots where the angle is the in-plane direction the nanomagnet, the radius gives the radius of the nanomagnet in that direction, and the colour gives the anisotropy field. The experimental data was taken from 22 different arrays of nanomagnets (eight sizes of triangles, eight sizes of squares and six sizes of pentagons), with the in-plane angle varying between 0-180° in 10° steps for triangles and squares and 5° steps for pentagons.

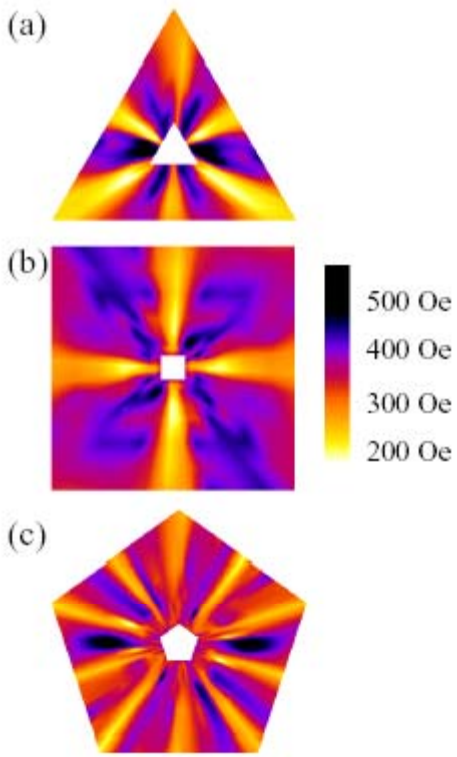

Fig. 2.26 *The experimentally measured anisotropy field inside 5nm thick nanomagnets of (a) triangular, (b) square and (c) pentagonal symmetry. These are colour plots where the direction gives the in-plane direction of the nanomagnet, the radius gives the nanomagnet radius in that direction and the colour gives the experimentally measured anisotropy field of a nanomagnet of that size. High field values correspond to easy anisotropy axes and low values to hard anisotropy axes. The lateral scale of the figure is such that the square data runs from edge length 50nm to 500nm. (After Ref. [38]).*

The triangular nanomagnet exhibits anisotropy with 6-fold symmetry, the square nanomagnet shows 4-fold symmetry anisotropy and the pentagon nanomagnets possess a remarkable 10-fold symmetry. The results for the anisotropy field were taken from the plot and the following equation was used to calculate the anisotropy energy

$$U = \frac{2M_s V H_a}{n^2} \tag{2.19}$$

where M_s is the saturation magnetisation, V the volume of the particle, H_a the anisotropy field and n the symmetry order of anisotropy. Fig. 2.27 shows a graph of anisotropy energy versus the square root of the area for the nanomagnets. As can be seen, the square has the highest anisotropy energy, which explains the high coercivity, remanence and hysteresis. The pentagons have the lowest configurational anisotropy energy and hence a low coercivity and hysteresis. In summary the configurational anisotropy of the nanomagnets appears to have a

symmetry related to the geometric shape, which comes from the difference in energy of different configurations as the magnetisation direction is varied.

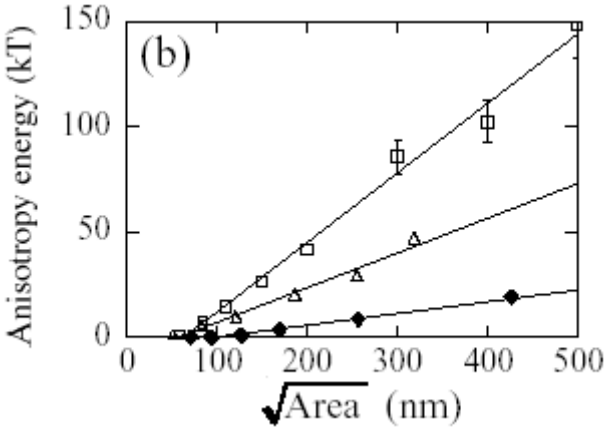

Fig. 2.27 *The anisotropy energy for nanomagnets of different size and symmetry. (After Ref. [38]).*

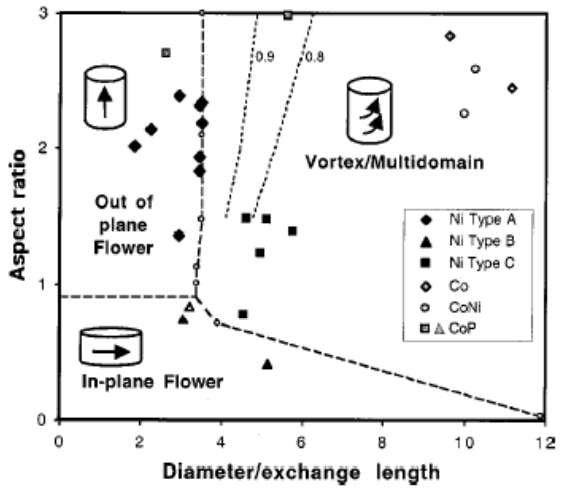

Fig. 2.28 *Solid lines represent the calculated boundaries of the remanent states of a cylinder as a function of aspect ratio and diameter. The magnetisation of the flower states is almost uniform, and the remanence is close to 1.0. In the vortex state, magnetisation twists around the axis of the cylinder and the remanence decreases with increasing diameter: dotted lines are contours of equal remanence, 0.9 or 0.8. Larger cylinders show multiple domains. The data points represent individual samples, coded according to the measured remanent state of each particle. The Ni type A samples behave like an out-of-plane dipole, Ni type B behave like an in-plane dipole, and Ni type C (plus the Co and CoNi samples) behave like a vortex or multidomain particle. These data points correspond very well to the calculated remanent states. (After Ref. [39]).*

Interference lithography has been used to make a variety of magnetic particle arrays over large areas, with periods of 100nm and higher [39]. These experiments were carried out to investigate how the properties of small magnetic structures change according to composition and shape. Magnetic particles with dimensions below 100nm show a rich behaviour depending on size, aspect ratio, microstructure, and composition. In agreement with micromagnetic models, small diameter cylinders or cones behave like single domains, while larger particles show vortex or multidomain behaviour, as show in Fig. 2.28.

It has been found that the switching field of patterned submicron film elements depends strongly on edge domain configurations [40,41]. Gadbois and Zhu [42] demonstrated numerically that edge roughness reduces the switching field of nanoscale Ni bars due to the formation of magnetisation vortices. Other work has shown that the complete magnetisation reversal of NiFeCo submicron structures occurs only after depinning and reversal of the edge magnetisation [43,44]. The edge pinning phemomenon is common in patterned submicron soft magnetic thin film structures.

References

[1] D. Jiles, *Introduction to Magnetism and Magnetic Materials*, 2nd edition, pg 300, Chapman & Hall, London (1998).

[2] D. Jiles, *Introduction to Magnetism and Magnetic Materials*, 2nd edition, pg 234, Chapman & Hall, London (1998).

[3] E. C. Stoner, *Phil. Mag.*, **15**, 1080 (1933).

[4] J. C. Slater, *Phys. Rev.*, **49**, 537 (1936).

[5] B. D. Cullity, *Introduction to Magnetic Materials*, pg 138, Addison-Wesley Publishing Company (1972).

[6] S.S.P. Parkin, *Ultrathin Magnetic Structures II*, Springer-Verlag Berlin Heidelberg, **Chapter 2.4**, 157 (1994).

[7] J. P. Jakubovics, *Magnetism and Magnetic Materials*, 2nd edition, **chapter 4**, The Institute of Materials (1994).

[8] J. Evetts, *Concise Encyclopedia of Magnetic and Superconducting Materials*, 349-356, and 477, Pergamon Press (1992).

[9] I. D. Landau and E. M. Lifshitz, *Physik Z. Sowjetunion*, **8**, 153 (1935).

[10] B. D. Cullity, *Introduction to Magnetic Materials*, pg 209, Addison-Wesley Publishing Company (1972).

[11] B. D. Cullity, *Introduction to Magnetic Materials*, pgs 49-61, Addison-Wesley Publishing Company (1972).

[12] W. H. Meikleohn and C. P. Bean, *Phys. Rev.*, **102**, 1412 (1956).

[13] D. Mauri, H. C. Siegmann, P. S. Bagus, and E. Kay, *J. Appl. Phys.*, **62**, 3047 (1987).

[14] A. P. Malozemoff, *Phys. Rev. B.*, **35**, 3679 (1987).

[15] J. Nogues and I. K. Schuller, *J. Magn. Magn. Mater*. **192**, 203 (1999).

[16] J. Evetts, *Concise Encyclopedia of Magnetic and Superconducting Materials*, 117-122, Pergamon Press (1992).

[17] E. C. Stoner and E. P. Wohlfarth, *Phil. Trans. Roy. Soc.*, **A240**, 599 (1948).

[18] J. H. Fluitman, *Thin Solid Films*, **16**, 269 (1973).

[19] M. H. Kryder, K. Y. Ahn, N. J. Mazzeo, S. Schwarzl, and S. M. Kane, *IEEE Trans. Magn.*, Vol. **Mag-16**, NO. 1, 99 (1980).

[20] A. O. Adeyeye, J. A. C. Bland, C. Daboo, and D. G. Hasko, *Phys. Rev. B*, **56**, 6 3265 (1997).

[21] A. O. Adeyeye, R. P. Cowburn, M. E. Welland, *J. Magn. Magn. Mater.*, **213**, L1-L6 (2000).

[22] A. O. Adeyeye, R. P. Cowburn, M. E. Welland, *J. Appl. Phys.*, **87**, 1, 299 (2000).

[23] W. Y. Lee, C. C. Yao, A. Hirohata, Y. B. Xu, H. T. Leung, S. M. Gardiner, S. McPhail, B. C. Choi, D. G. Hasko, and J. A. C. Bland, *J. Appl. Phys.,* **87**, 6, 3032 (2000).

[24] E. H. Frei, S. Shtrikman, and D. Treves, *Phys. Rev.*, **106**, 446 (1957).

[25] W. F. Brown, Jr., *Phys. Rev.*, **105**, 1479 (1957).

[26] A. Aharoni, *J. Appl. Phys*, 30, 70s (1959).

[27] E. W. Lee and J. E. L. Bishop, Proc. Phys. Soc. London, **89**, 661 (1966).

[28] R. W. DeBlois and C. P. Bean, *J. Appl. Phys,* **30**, 225S (1959).

[29] S. Y. Chou, M. Wei, P. R. Krauss, and P. B. Fischer, *J. Vac. Sci. Technol*. B **12**, 3695 (1994).

[30] R. M. H. New, R. F. W. Pease, and R. L. White, *J. Magn. Magn. Mater*. **155**, 140 (1996).

[31] C. A. Ross, H. I. Smith, T. Savas, M. Farhoud, M. Hwang, M. Walsh, M. C. Abraham, and R. J. Ram, *J. Vac. Sci. Technol*. B **17**, 3168 (1999).

[32] S. Sun and C. B. Murray, *J. Appl. Phys*. **85**, 4325 (1999).

[33] S. Sun, C. B. Murray, D. Weller, L. Folks, and A. Moser, *Science,* **287**, 1989 (2000).

[34] M. Lederman, S. Schultz, and M. Ozaki, *Phys. Rev. Lett*. **73**, 1986 (1994).

[35] W. Wernsdorfer, D. Mailly, and A. Benoit, *J. Appl. Phys,* **87**, 5094 (2000).

[36] K. J. Kirk, J. N. Chapman, C. D. W. Wilkinson, *Appl. Phys. Lett*. **71**, 4, 539 (1997).

[37] K. J. Kirk, J. N. Chapman, C. D. W. Wilkinson, *J. Appl. Phys,* **85**, 5237 (1999).

[38] R. P. Cowburn, *J. Phys. D: Appl. Phys*. **33** R1-R16 (2000).

[39] C. A. Ross, S. Haratani, F. J. Castaño, Y. Hao, M. Hwang, M. Shima, J. Y. Cheng, B. Vögeli, M Farhoud, M. Walsh, and Henry Smith, *J. Appl. Phys,* **91**, 6848 (2002).

[40] Y. Zheng, J. -G. Zhu, *J. Appl. Phys,* **81** (8), 5471 (1997).

[41] T. Schrefl, J. Fidler, K. J. Kirk, J. N. Chapman, *J. Appl. Phys,* **85** (8), 6169 (1999).

[42] J. Gadbois, J. -G. Zhu, *IEEE Trans. Magn*., **31**, 3802 (1995).

[43] J. Shi, S. Tehrani, *Appl. Phys. Lett*. **77** (11), 1692 (2000).

[44] J. Shi, S. Tehrani, T. Zhu, Y. F. Zheng, J. -G. Zhu, *Appl. Phys. Lett*. **74** (17), 2525 (1999).

[45] M. Prutton, *Thin Ferromagnetic Films*, pg 269, Butterworths, London (1964).

[46] E.E. Huber, D.O. Smith, J.B. Goodenough, *J. Appl. Phys*., **29**, 294 (1958).

[47] B. D. Cullity, *Introduction to Magnetic Materials*, pg 436, Addison-Wesley Publishing Company (1972).

[48] C. Kittel, J.K. Galt, W.E. Campbell, *Phys. Rev.*, **77**, 725 (1950).

[49] F.E. Luborsky, *J. Appl. Phys*., **32**, 171S-183S (1961).

[50] I.S. Jacobs, C.P. Bean, *Phys. Rev.*, **100**, 1060 (1955).

[51] F.E. Luborsky, C.R. Morelock, *J. Appl. Phys*., **35**, 2055 (1964).

Learn from yesterday, live for today, hope for tomorrow. The important thing is to not stop questioning. *Albert Einstein*

Chapter 3

Spin Valves: Theory and Devices.

3.1 Interlayer Exchange Coupling.

GMR was first discovered in 1988 when Baibich *et al.* reported 50% resistance change at low temperatures with an applied field in $(Fe/Cr)_n$ multilayer thin films. The Fe/Cr superlattices were antiferromagnetically coupled in zero field and grown by molecular beam epitaxy [1]. With the application of a sufficiently high field, the exchange interaction could be overcome and the magnetisation of all the layers aligned parallel. The resistance of the structure depends upon the magnetic arrangement of the layers, and was observed to be higher when the moments were antiparallel to one another. When the GMR effect was first discovered in the $(Fe/Cr)_n$ system, there was an assumption for some time that the Cr spacer layer, with its unusual antiferromagnetic properties, was necessary for the interlayer antiferromagnetic exchange to exist. Work published by Parkin *et al*. in 1990 [2] showed that similar results could be obtained in polycrystalline Fe/Cr structures grown by the much simpler technique of magnetron sputtering. These experiments also revealed that GMR could be observed in a wide variety of transition-metal magnetic multilayers. One of these systems, namely ferromagnetic cobalt layers separated by thin copper layers, was found to exhibit very large GMR effects in excess of 110% at room temperature [3]. While the largest GMR values require magnetic fields exceeding ~20kOe, magnetoresistance values of 50-60% are obtained in fields of several hundred oersteds and values of ~20% or more in fields of a few tens of oersteds. These lower values are obtained by using thicker Cu layers, for which the interlayer exchange coupling is weaker. In addition, the experiments revealed that the magnitude of the GMR oscillated as the thickness of the non-ferromagnetic spacer layers between the ferromagnetic layers was increased [4,5]. This oscillation was shown to be caused by an oscillation in the sign of the interlayer exchange coupling between the ferromagnetic layers. The coupling oscillated between antiferromagnetic and ferromagnetic coupling such that the magnetic moments of successive ferromagnetic layers were either parallel (ferromagnetic) or antiparallel (antiferromagnetic) in small magnetic fields. Fig. 3.1 shows the room temperature saturation magnetoresistance versus Cu spacer thickness for a series of polycrystalline sputter-deposited Co/Cu multilayers. The magnetic state of the multilayer is shown schematically for various Cu layer thicknesses (only two magnetic layers are shown). Oscillations of the GMR as a function of Cu thickness occur because the magnetoresistance effect is measurable only for those thicknesses of Cu for which the interlayer exchange coupling aligns the magnetic moments of the Co layers antiparallel. According to the reviews, it is the induced spin density wave in the spacer layer material that mediates the magnetic coupling of the magnetic layers in magnetic multilayers and sandwiches [6]. Oscillatory coupling has been shown to be a general property of almost all transition-metal magnetic multilayered systems in which the non-ferromagnetic layer comprises one of the *3d*, *4d*, or *5d*

transition metals or one of the noble metals. The oscillation period was found to be just a few atomic layers, typically about 10Å, but varying up to ~20Å**.** Only those multilayers for which the interlayer coupling is antiferromagnetic display significant giant magnetoresistance effects. Various models have been proposed to account for the long range of this oscillatory exchange coupling. Theoretical approaches based on quantum confinement [7,8] and on the Ruderman-Kittel-Kasuya-Yosida (RKKY) interaction [9,10] have been able to describe the origin of the coupling.

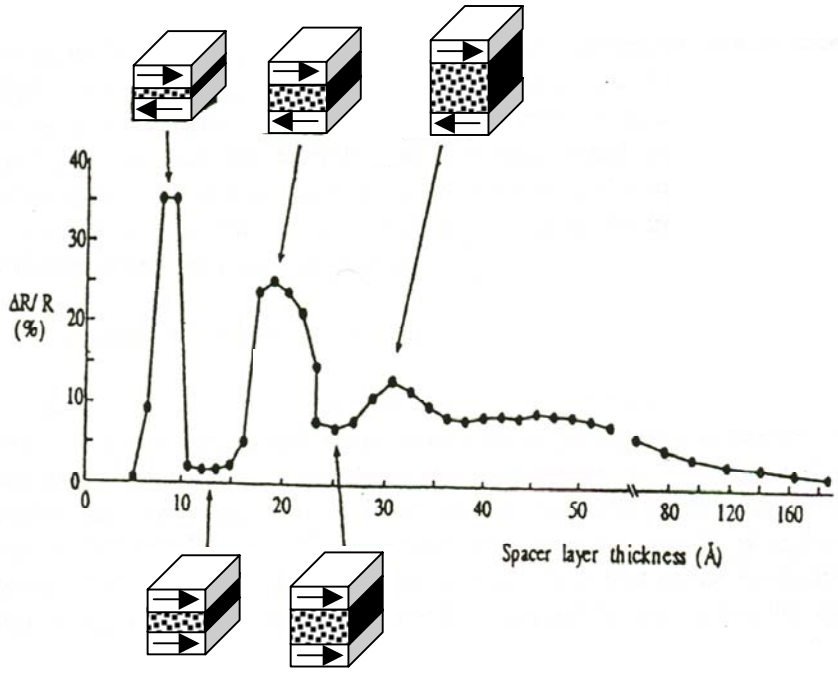

Fig. 3.1 *Room temperature saturation magnetoresistance versus Cu spacer layer thickness for a series of polycrystalline sputter-deposited Co/Cu (After Ref. [5]). The magnetic state of the multilayer is shown schematically for various Cu layer thicknesses (only two magnetic layers are shown).*

The decay in GMR with increasing Cu thickness can be described approximately by Eqn. (3.1), where t_{Cu} is the Cu thickness and λ_{Cu} describes the scattering within the Cu layer interior [6].

$$\frac{\Delta R}{R} \approx \frac{1}{t_{Cu}} \exp\left(-\frac{t_{Cu}}{\lambda_{Cu}}\right) \tag{3.1}$$

This functional dependence can be understood by considering two effects. Firstly increasing the Cu layer thickness dilutes the interfacial scattering regions because the measuring current,

which is parallel to the layers, is shunted through the bulk of the Cu layers away from these regions. Secondly, scattering within the interior of the Cu layers will diminish the flow of electrons between the Co layers. This scattering can be described by the scattering length, λ_{Cu}.

3.2 The Physical Origin of GMR.

The detailed origin of GMR has provoked considerable interest. Many theoretical models have been developed but most of them are based on a model of the electrical conduction in ferromagnetic metals due to Mott [11]. According to Mott, the electrical current in ferromagnetic metals is carried independently in two conduction channels corresponding predominantly to the spin-up and spin-down *s-p* electrons. These electrons are in broad energy bands with low effective masses. This assumption is believed to be good at temperatures significantly below the magnetic ordering temperature of the magnetic material so that there is little spin-mixing between the two conduction channels. Mott theorised that the conductivity can be significantly different in the two spin channels because the conduction electron scattering rates in these two channels will be related to the corresponding spin-up or spin-down density of empty states at the Fermi level.

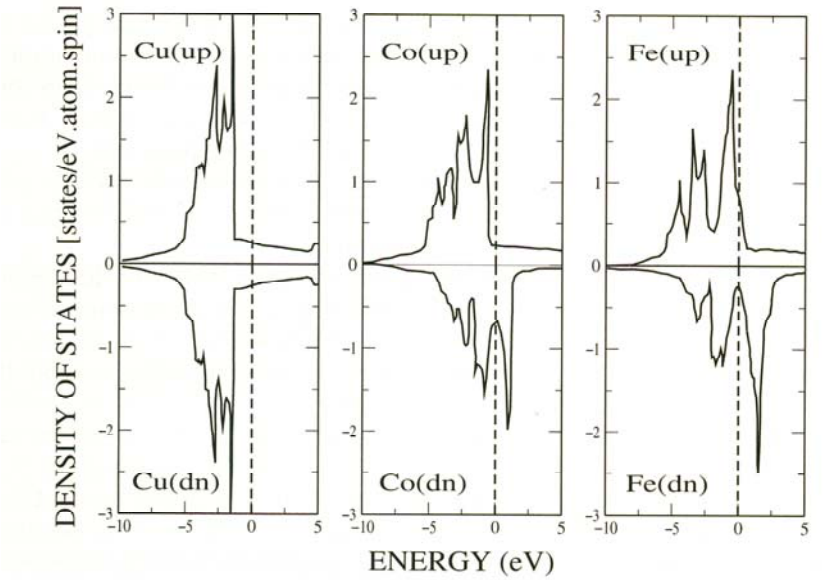

Fig. 3.2 *Density of states of copper, cobalt and iron. Broken line denotes the position of the Fermi level. (After Ref. [12]).*

These states will largely be of *d* character and as a result of the exchange split *d* bands the ratio of spin-up to spin-down density of empty states at the Fermi level can be significantly different in the ferromagnetically ordered states of Ni, Fe and Co and their alloys. The scattering probability and therefore the resistivity of the electron spin is proportional to the

number of states available for scattering at E_F, i.e. to the density of states $D(E_F)$. The density of states for copper, cobalt and iron for ↑ (upper panel) and ↓ (lower panel) spin orientations are shown in Fig. 3.2. The Fermi level in copper (and other noble metals) intersects only the conduction band whose density of states $D(E_F)$ is low. It follows that the scattering probability in copper is also low, which explains why copper is a good conductor. In the case of the magnetic transition metals, *d* bands for ↑ and ↓ spin electrons are split by the exchange interaction. This results in the relative shift of the ↑ and ↓ spin *d* bands which is clearly seen of Co and Fe in Fig. 3.2. The ↑ spin *d* band in cobalt is full which means that $D^{\uparrow}(E_F)$ is as low as in copper, but the Fermi level in the ↓ spin band lies in the *d* band and therefore, $D^{\downarrow}(E_F)$ is much higher than $D^{\uparrow}(E_F)$. The situation for iron is different in that the density of states at E_F is higher for ↑ spin electrons than for ↓ spin electrons.

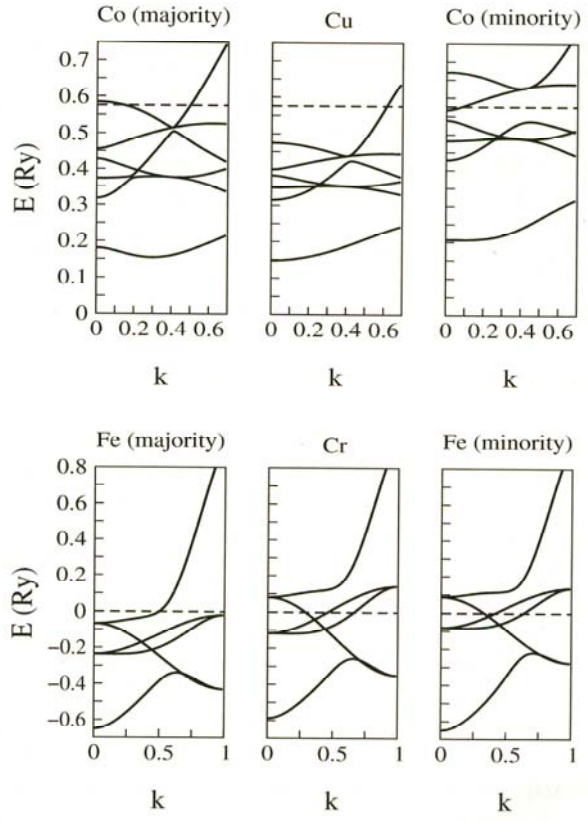

Fig. 3.3 *(Top) Band structures of cobalt and copper along the [001] direction in the vicinity of one of the Cu Fermi surface necks. (Bottom) Band structures of iron and chromium along the [001] direction. Broken line denotes the position of the Fermi level. (After Ref. [12]).*

Also the spin asymmetry in the density of states is not as large for iron as for cobalt. Metals in which the majority *d* band is entirely full are known as *strong ferromagnets* and those which have both *d* bands partially filled as known as *weak*. Thus Co is a strong ferromagnet and Fe

is a weak ferromagnet. Figs. 3.3 (a) and 3.3 (b) show the band structures of the most common combinations of magnetic and non-magnetic metals used in GMR multilayers, Co/Cu and Fe/Cr. Fig. 3.3 (a) shows that there is a good match between the bands of Cu and the ↑ (majority) spin band of Co, and therefore, the spin ↑ electrons crossing the Cu/Co interface experience only weak scattering. There is a large mismatch between the Cu and Co for the ↓ (minority) spin electrons, it follows that the ↓ spin electrons are strongly scattered at the Co/Co interfaces. On the other hand, matching of the Fe and Cr bands is almost perfect for ↓ spin electrons but poor for the ↑ spin electrons. The spin dependent scattering based on the mismatch of bands of the magnetic and non-magnetic components of the magnetic multilayers allows us to understand which combinations of magnetic and non-magnetic metals should lead to optimum GMR. It is important to look for as good a match as possible between the bands of the magnetic layers and those of the spacer layer in one spin channel and as large as possible mismatch in the other spin channel.

The GMR effect relies on the experimentally established fact that electron spin is conserved over distances of up to several tens of nanometers, which is greater than the thickness of a typical multilayer. Therefore, the electric current in the trilayer flows in two channels, one corresponding to electrons with spin projection ↑ and the other to electrons with spin projection ↓. Since the ↑ and ↓ spin channels are independent (spin is conserved) they can be regarded as two wires connected in parallel and the GMR can be explained using a simple resistor model, as shown in Fig. 3.4. The essential ingredient is that electrons with spin projections parallel and antiparallel to the magnetisation of the ferromagnetic layer are scattered at different rates when they enter the ferromagnet. Let us assume that electrons with spin antiparallel to the magnetisation are scattered more strongly. In the ferromagnetic configuration Fig. 3.4 (a) of the trilayer, electrons with spin ↑ are weakly scattered both in the first and second ferromagnet, whereas the ↓ spin electrons are strongly scattered in both ferromagnetic layers. This is modelled by two small resistors in the spin ↑ spin channel and by two large resistors in the spin ↓ channel in the equivalent resistor network. Since the ↓ and ↑ spin channels are connected in parallel (CIP geometry), the total resistance of the trilayer is determined by the low resistance ↑ spin channel which shorts the high-resistance ↓ spin channel. Therefore the total resistance of the trilayer in the ferromagnetic configuration is low. On the other hand, ↓ spin electrons in the antiferromagnetic configuration are strongly scattered in the first ferromagnetic layer but weakly scattered in the second ferromagnetic layer. The ↑ spin electrons are weakly scattered in the first ferromagnetic layer and strongly scattered in the second. This is modelled in Fig. 3.4 (b) by one large and one small resistor in

each spin channel. There is no shorting and the total resistance in the antiferromagnetic configuration is therefore, much higher than in the ferromagnetic configuration.

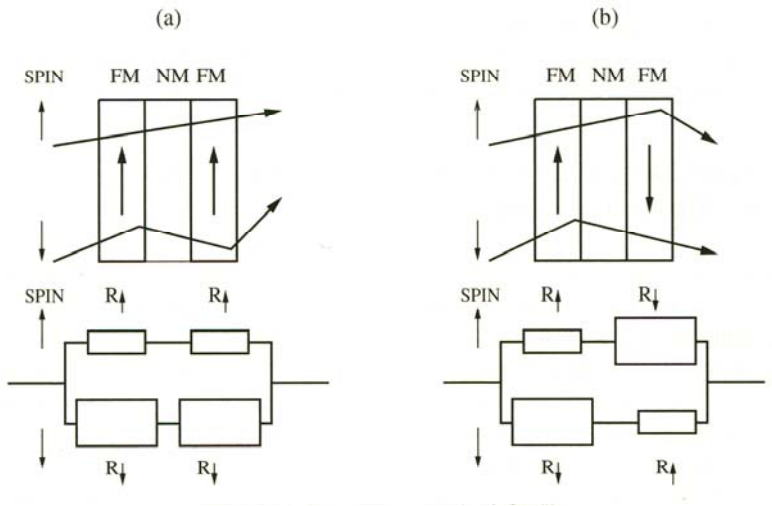

Fig. 3.4 *Resistor model of GMR. (After Ref. [12])*

In summary, for GMR to occur two conditions must be met:

(1) There must be a way to change the relative orientations of the magnetisation in adjacent magnetic metal layers.

(2) The thickness of the films involved must be less, preferably a fraction, of the mean free path of an electron in the multilayer array.

3.3 Exchange Biased Spin Valve Structures.

Exchange biased spin valve layered structures were first described by Dieny *et al*. [13-15]. In the original structure (Fig. 3.5 (a)) two ferromagnetic layers are separated by a non-ferromagnetic spacer layer. A third magnetic layer of a properly chosen composition and structure is antiferromagnetic, and is in contact with one of the ferromagnetic layers. Suitable preparation conditions, for example growth in a magnetic field, lead to the pinning of the ferromagnetic layer in contact with the antiferromagnetic due to an exchange interaction across the interface. The unpinned ("free") ferromagnetic layer is usually magnetically soft, and the non-magnetic interlayer is sufficiently thick to minimise magnetic coupling between the ferromagnetic layers. Typical layer thicknesses are 3 to 10nm for the magnetic layers, and 2 to 3nm for the spacer layer. Depending on the position of the AFM layer, the spin valves can be classified into top SV, bottom SV or symmetric SV, as shown in Fig. 3.5. 'Symmetric' spin valves have been studied by several groups [17-20]. These structures contain one free magnetic layer between two pinned magnetic layers, separated by nonmagnetic spacer layers, and allow higher GMR ratios than simple spin valves. Recent publications by Egelhoff *et al*.

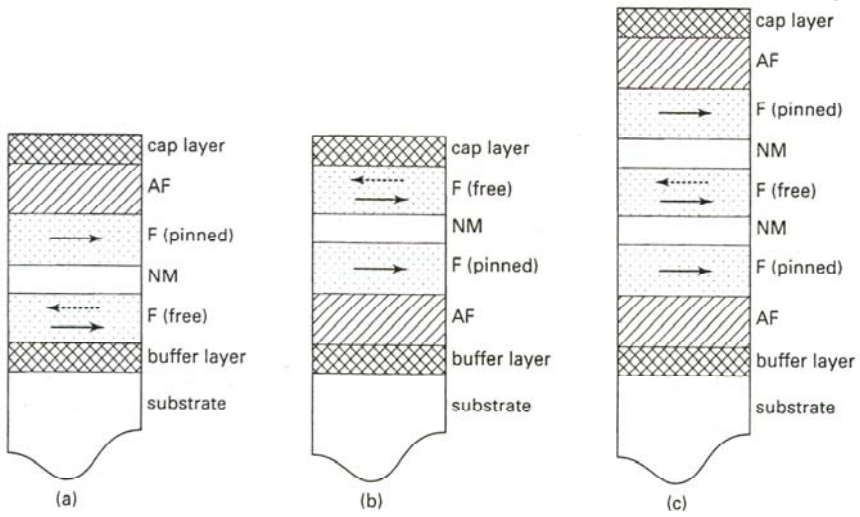

Fig. 3.5 *Schematic cross-sections of a top (a), bottom (b) and a symmetric (c) exchange-biased spin valve structure. (After Ref. [16]).*

on symmetric spin valves with two NiO pinning layers, showing an MR ratio above 20%, are [21] and [22]. Sugita *et al*. have obtained the highest MR ratio for a symmetric spin valve reported so far, ≈27.8% for an α-Fe_2O_3/Co/Cu/Co/Cu/Co/α-Fe_2O_3 system [23].

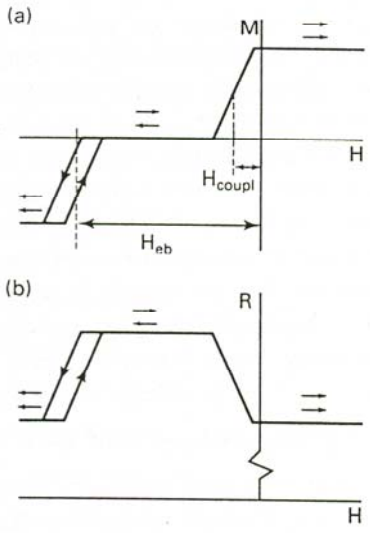

Fig. 3.6 *Schematic curves of magnetic moment (a) and resistance (b) of a simple exchange biased spin valve layered structure. Ferromagnetic layers with equal magnetic moments per unit of area have been assumed. (After Ref. [16])*

For suitable layer compositions and nanometer-scale layer thicknesses these spin valve structures combine a fair Giant Magnetoresistance (GMR) effect with a small field interval close to zero field in which the resistance change takes place. The resulting high sensitivity

and low coercivity makes these structures attractive for sensor applications and other magnetoelectronic devices. The functioning of the spin valve structure is illustrated schematically by the magnetisation and resistance curves shown in Fig. 3.6. Defining the positive field direction as the direction of magnetisation of the pinned layer, the layers have parallel magnetisation for $H>0$. In a small field interval close to $H=0$ the magnetisation of the free layer reverses, whereas the magnetisation of the pinned F layer remains fixed. Only upon the application of a large negative field (equal to the exchange biasing field H_{eb}), the exchange biasing interaction is overcome, and the pinned ferromagnetic layer reverses direction. The GMR effect is the increase of the resistance upon the change of the angle between neighbouring magnetic layers from a parallel to an antiparallel alignment. For combinations of F- and NM-layer compositions for which the GMR effect is high, the resistance curve shows a steep increase close to zero field, where the free layer magnetisation direction switches. The resistance stays high until the pinned layer reverses at the exchange bias field. There is usually a small magnetic coupling between the free layer and pinned layer, which leads to an offset, (H_{coupl} in Fig. 3.6) of the field around which the free layer switches. The magnitude of the free layer coupling is important for the functioning of a spin valve, because a low offset for the free layer enables the GMR effect to take place at a lower field, which is desirable for device application. It was found that this coupling has a strong dependence on the copper interlayer thickness [24,25]. This copper dependence has been explained [26-31] as a superposition of three different mechanisms: ferromagnetic pinhole coupling, oscillating RKKY coupling and magnetostatic (Néel or orange-peel coupling). It is important that the Cu thickness is thin enough to give a good signal response, but thick enough to minimise coupling between the ferromagnetic layers. As already explained in section 3.1, the coupling between the ferromagnetic layers oscillates with increasing thickness, and it was found that the second antiferromagnetic peak (≈2nm Cu) gives a good compromise between high signal response and minimum coupling.

The main advantages of exchange-biased spin-valve structures over GMR multilayers is the high sensitivity combined with the low coercivity. The sensitivity of an MR material is defined as the slope $s \equiv (\partial R/R)/\partial H$ of the relative resistance versus field curve, obtained at a suitable working point. Sensitivities up to 18%/(kA/m) at room temperature have been reported for spin valves using permalloy ($Ni_{80}Fe_{20}$) for the free and pinned layers, and Cu for the spacer layer [32]. The AMR effect for these films gives a sensitivity of about 5%/(kA/m). A recent design for an integrated magnetic sensor is based on a Wheatstone bridge of micropatterned spin valve resistors with the addition of a soft adjacent layer structure that controls the principle characteristics by channelling the magnetic field. The design differs

from earlier devices in that the local field direction rather than the local anisotropy of the spin valve is varied around the bridge. The design offers high sensitivity, small size, a relatively easy manufacturing process and potentially low price [77].

3.3.1 Dependence on magnetic anisotropy.

For most sensor applications, switching of the free layer should preferably be free of hysteresis. Rijks *et al*. [32], showed that this can be accomplished for spin valves within which the free layers have an in-plane, uniaxial anisotropy, with the easy axis perpendicular to the unidirectional anisotropy axis of the pinned layer. In such systems with crossed anisotropies, with the external field parallel to the biasing direction, the magnetisation of the free layer switches by a coherent rotation. In the parallel case, magnetisation reversal is the result of domain wall movement, leading to hysteresis [32]. As a result, strong Barkhausen noise will be superimposed on the sensor output signal due to pinning and depinning of domain walls.

3.3.2 Dependence on non-magnetic layer thickness and composition.

Rijks *et al*. studied the dependence of the MR ratio on the Cu-layer thickness in spin valves with the composition (8nm $Ni_{80}Fe_{20}$/t_{Cu} nm Cu/6nm $Ni_{80}Fe_{20}$/8nm $Fe_{50}Mn_{50}$), grown on a 3nm Ta underlayer on Si (100) and covered with a 3nm Ta cap layer [24].

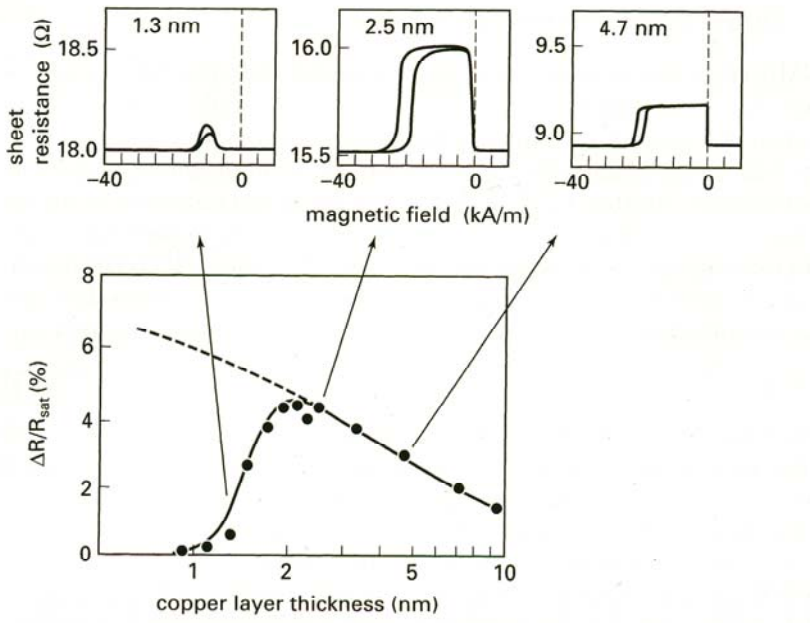

Fig. 3.7 *Dependence of the MR curves and the MR ratio at room temperature on the Cu-layer thickness, for ($Ni_{80}Fe_{20}$/Cu/$Ni_{80}Fe_{20}$/$Fe_{50}Mn_{50}$) spin valves [24]. Layer thicknesses are given in the text. The dashed line gives a fit to the data, using Eqn. (4.2), for the Cu thicknesses for which full antiparallel alignment is obtained.*

Fig. 3.7 shows the results obtained. The MR ratio reaches a maximum of almost 5% at a critical thickness ≈2nm. Below this value the Cu spacer is not sufficiently thick to allow a perfectly antiparallel alignment of the magnetisation in the two layers, which leads to a decreased GMR ratio. A detailed analysis of the resistance and magnetisation curves, in terms of competing interlayer coupling and exchange biasing, has been carried out by Rijks *et al*. [24].

Speriosu *et al*. [33] have proposed the following expression for the dependence of the MR ratio of spin valves on spacer layer thickness:

$$\frac{\Delta R}{R} = \left(\frac{\Delta R}{R}\right)_0 \frac{\exp\left(-t_{NM}/\ell_{NM}\right)}{1 + t_{NM}/t_0}. \qquad (4.2)$$

The factor $\exp\left(-t_{NM}/\ell_{NM}\right)$ represents the probability that an electron which potentially contributes to the GMR effect by crossing through the NM layer, is *not* diffusely scattered in the NM layer. The denominator represents the shunting effect due to the NM layer. The parameter ℓ_{NM} is related to the conduction electron mean free path λ_{NM} in the NM layer. The parameter t_0 represents the conductance in the absence of the NM layer. Speriosu's equation can be fitted to Rijk's data as shown by the dotted line in Fig. 3.7. Dieny proposed that for systems of interest, ℓ_{NM} is approximately equal to 1/2 λ_{NM} [34], leading to a $\lambda_{Cu} \approx 32$nm.

Dieny *et al.* [15] have investigated the dependence of the MR ratio on the composition of the NM spacer material. They measured the variation in the MR ratio with NM layer thickness for structures of the type Co/NM/$Ni_{80}Fe_{20}$/$Fe_{50}Mn_{50}$, (NM=Cu, Ag and Au).

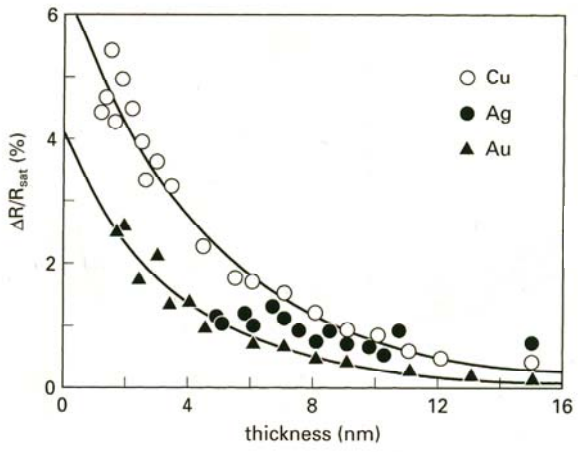

Fig. 3.8 *Dependence on the noble metal spacer layer thickness of the MR ratio at room temperature for spin valves with the structure Si/7nm Co/ t_{NM} nm NM/ 4.7nm $Ni_{80}Fe_{20}$/ 7.8nm $Fe_{50}Mn_{50}$/ 1.5nm NM. (After Ref. [15]).*

Fig. 3.8 shows that the MR ratio decreased exponentially for all the materials as the NM layer thickness was increased. The critical thickness above which fully antiparallel alignment is achieved is about 2nm for Cu and Au, and 4-5nm for Ag. Dieny *et al.* suggested that coupling through pinholes might be of importance up to much higher spacer thicknesses for Ag. The extrapolated MR ratio for t_{NM}=0 is about 50% larger for Cu than for Au. This is thought to be due to a lower transmission of electrons for F/Au than for F/Cu interfaces. Dieny *et al*. also concluded that the higher resistance of Au explained the smaller decay length for Au than for Cu, 3.6nm and 4.5nm respectively. In [14], Dieny *et al.* have reported that for F/NM/F/$Fe_{50}Mn_{50}$ spin valve structures, with F=$Ni_{80}Fe_{20}$, the spin valve effect is also observed for NM=Pt, but is not seen for NM=Ta, Al, Cr and Pd.

3.3.3 Dependence on the ferromagnetic layer thickness and composition.

Fig. 3.9 shows the results obtained by Dieny *et al.* [35] on the dependence of the GMR ratio on the free layer thickness for F=Co, NiFe and Ni.

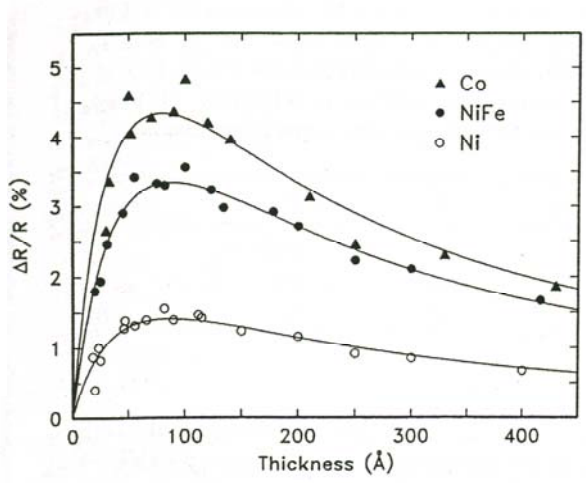

Fig. 3.9 *Variation of the magnetoresistance versus the thickness of the "free" ferromagnetic layer M(1), with M(1)=Co, NiFe, or Ni at room temperature. The lines are two-parameter fits according to Eq. (4.3) given in text. (After Ref. [35]).*

The spin valve structure investigated was F/Cu/$Ni_{80}Fe_{20}$/$Fe_{50}Mn_{50}$. Dieny *et al.* proposed the following expression for the variation of the MR ratio with the F layer thickness:

$$\frac{\Delta R}{R} = \left(\frac{\Delta R}{R}\right)_0 \frac{1-\exp\left(-t_F/\ell_F\right)}{1+t_F/t_0}. \qquad (4.3)$$

The factor $(\Delta R/R)_0$ is a function of the NM-layer thickness. The factor $\left[1-\exp\left(-t_F/\ell_F\right)\right]$ is the angle-averaged probability for an electron with a large mean free path to be scattered within the ferromagnetic layer before being diffusely scattered at the outer boundary. This

shows that if the ferromagnetic layers are too thin, the contrast between the mean free paths for both spin directions will be reduced, because the electron spin with longer mean free path will be scattered at the outer boundary, thus reducing the MR ratio. Again, the parameter t_0 depends on the conductance of the remainder of the structure (in the absence of the F layer).

3.3.4 Dependence on the exchange bias material and thickness.

The antiferromagnetic pinning layer plays an important part in the function of spin valve structures. For example for read head applications the blocking temperature (temperature where the exchange field vanishes) should exceed 300°C, to prevent accidental de-pinning of the pinned layer during head fabrication or head life [36]. Exchange biasing decreases approximately linearly with increasing temperature, down to zero at the blocking temperature. The exchange energy should be large (>0.2mJ/m^2), to withstand demagnetising fields at head level. Also the corrosion resistance of the exchange layer should not be worse than that of $Ni_{80}Fe_{20}$ used as reference [37]. Fig. 3.10 is a table comparing some exchange bias materials.

materials	T_b (°C)	exchange energy (mJ/m^2)	corrosion resisitance	requires anneal?
$Fe_{50}Mn_{50}$	150	0.13	bad	no
NiO	190	<0.1	good	no
$Mn_{76}Ir_{24}$	300	0.2-0.4*	fair	yes

* Bottom spin valve after anneal.

Fig. 3.10 *Comparison of exchange bias materials. (After Ref. [36]).*

The variation of the exchange bias with the thickness of the antiferromagnetic layer changes depending on the specific system, the microstructure and the measurement temperature [38]. The general trend is that for thick AFM layers, e.g. over 20nm, the exchange field is independent of the thickness of the AFM layer. As the AFM thickness is reduced, the exchange field decreases abruptly and becomes zero when the AFM layer is a few nanometers thick. The dependence of the exchange bias for varying thickness of the antiferromagnetic layer in the system $Fe_{80}Ni_{20}$/FeMn is shown in Fig. 3.11.

3.3.5 Interfacial roughness and structural quality.

The influence of interfacial roughness on the spin valve characteristics has been heavily debated, a good review is given in [39]. In Fe/Cr multilayers, some studies conclude that the MR amplitude is higher for rougher interfaces [40] up to an optimal roughness [41]. However, these results seem to depend on the growth conditions. Interfacial roughness plays various

roles in influencing the spin valve MR amplitude depending on the combination of ferromagnetic and nonmagnetic transition metals under consideration.

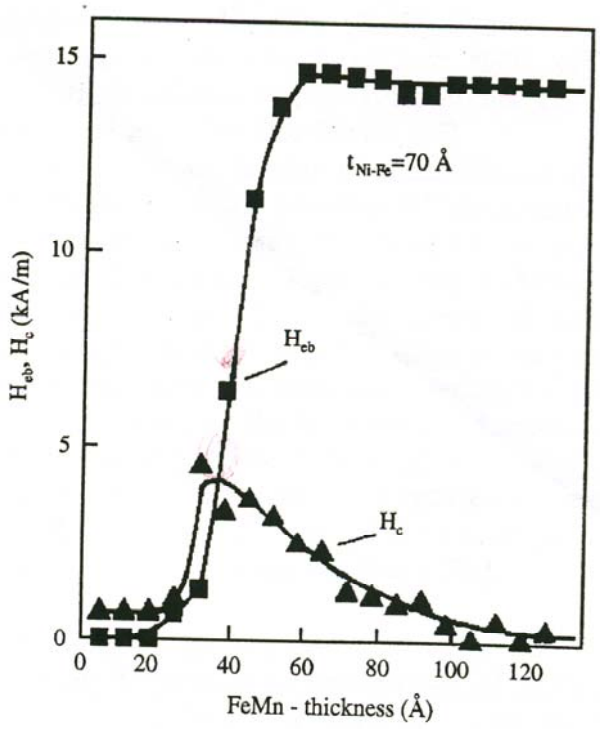

Fig. 3.11 *Dependence of exchange bias (square symbols) and coercivity H_c (triangular symbols) with the AFM layer thickness for $Fe_{80}Ni_{20}$/FeMn at a fixed t_{FM}=7nm [38].*

In (Fe/Cr) or (Co/Cu) multilayers for which the interfacial spin dependent scattering is very important, some interfacial roughness may increase the density of scattering centres at the interfaces and therefore lead to a larger MR. In contrast in (NiFe/Cu) multilayers or spin valve sandwiches for which the interfacial spin dependent scattering is not as important as the bulk scattering, an increase in the interfacial roughness leads to a systematic decrease in the MR amplitude [42,43]. One reason for this decrease is the formation of some paramagnetic NiFeCu alloy layers at the NiFe/Cu interfaces. These paramagnetic layers provoke significant spin-flip scattering of the incoming or outgoing conduction electrons. This spin-flip scattering leads to a loss of the 'spin memory' of the electrons crossing the Cu spacer layer, and therefore reduces the MR amplitude. This effect is even more pronounced at Ni/Cu interfaces [35]. If the interfaces are too rough, the mean-free path of the conduction electrons become too small compared to the period of the multilayer, and a coherent interplay of spin dependent scattering between the successive magnetic layers cannot occur efficiently. In the opposite case when the interfaces are too flat, the specular reflection of the conduction electrons on the interfaces can lead to channelling of the electrons within each layer.

The structural quality of the multilayer certainly influences the proportion of antiparallel alignment between the magnetisations in the successive magnetic layers. In particular, the

existence of pin-holes through the nonmagnetic spacer may significantly reduce the MR amplitude by inducing a local ferromagnetic coupling between the magnetic layers [3, 44-46].

3.3.6 Temperature dependence.

The variation of the MR spin valve amplitude with temperature has been investigated by various groups [47-49, 35]. Generally the MR amplitude decreases monotonically with temperature by a factor of the order of 1.5-3, depending on the system under consideration, between 4K and room temperature. The decrease in spin valve amplitude as the temperature is increased is due to two main factors:

(i) the intermixing of the spin ↓ and spin ↑ currents caused by scattering in the bulk of the ferromagnetic layers, or by paramagnetic fluctuations at the FM/NM interfaces. A clear correlation has been established between the Curie temperature of a ferromagnet and the slope of the decrease in the spin valve MR versus temperature [37, 51]. The higher the Curie temperature, the less the thermal variation of the spin valve MR. Structures based on Co- (T_c=1130°C) or Fe- (T_c=770°C) rich ferromagnetic materials should therefore give less thermal variation of the spin valve MR than Ni-rich alloys (T_c=358°C).

(ii) The phonon scattering (especially in the non-magnetic layer), dilutes the spin dependent scattering which gives rise to the spin valve MR and prevents the exchange of conduction electrons between the successive ferromagnetic layers through the spacer.

3.3.7 Other exchange biased spin valve structures.

Several modifications to the simple, Fe-Mn-biased spin valve structures have been reported to yield higher GMR ratios. Parkin demonstrated that a very thin Co layer at the $Ni_{80}Fe_{20}$/Cu interfaces in ($Ni_{80}Fe_{20}$/Cu/$Ni_{80}Fe_{20}$/$Fe_{50}Mn_{50}$) spin valves (interface "dusting") may lead to a drastic increase in the MR ratio [50]. As shown in Fig. 3.12, the MR ratio for the structure (5.3nm $Ni_{81}Fe_{19}$/3.2nm Cu/2.2nm $Ni_{81}Fe_{19}$/9nm $Fe_{50}Mn_{50}$/1nm Cu) was found to increase (at room temperature) from 2.9% in the absence of Co, up to 6.4% for Co thicknesses above approximately 0.6nm. Conversely, adding permalloy layers of a thickness of only 0.4nm to the Co/Cu interfaces of Co/Cu/Co/FeMn spin valves was found to decrease the MR ratio from 6.8% to 3.9%. The effect of the Co layers was strongly localised to the interfaces, by varying the distance *d* to the interface of 0.5nm Co layers that were buried in the permalloy layers: no significant increase of the MR ratio was found for d>0.6nm. Parkin's experiment demonstrated the crucial role player by the interfaces in a spin valve structure.

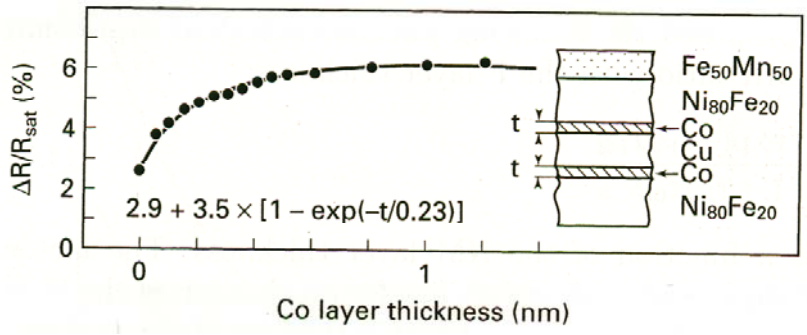

Fig. 3.12 *Dependence on the Co interface layer thickness t_{Co} of the MR ratio for spin valves with the structure (Si/[5.3-t_{Co}]nm $Ni_{80}Fe_{20}$/t_{Co}nm Co/3.2nm Cu/[2.2-t_{Co}]nm $Ni_{80}Fe_{20}$/9nm $Fe_{50}Mn_{50}$/1nm Cu) [50].*

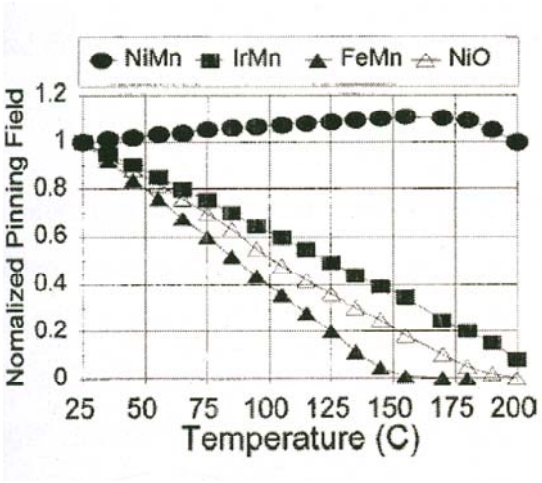

Fig. 3.13 *Normalised pinning field versus temperature for spin valves pinned by four different antiferromagnetic materials. [51].*

Although much effort has gone into improving spin valve design, there are intrinsic problems which are difficult to address. One of the problems is the blocking temperature, Fig. 3.13 shows the normalised pinning field versus temperature for spin valves pinned by four different antiferromagnetic materials [51]. The NiMn antiferromagnetic layer shows an improved normalised pinning field over a wider temperature range compared to NiO, IrMn and FeMn.

Synthetic spin valves, which were first suggested by Berg *et al.* [52] offer increased exchange fields and blocking temperatures. They consist of an antiferromagnetically coupled (FM/NM) bilayer structure instead of a single AFM layer. The choice of the spacer layer thickness in the

(FM/NM) stack enables antiferromagnetic coupling between the ferromagnetic layers. Fig. 3.14 shows a schematic diagram of a synthetic SV structure.

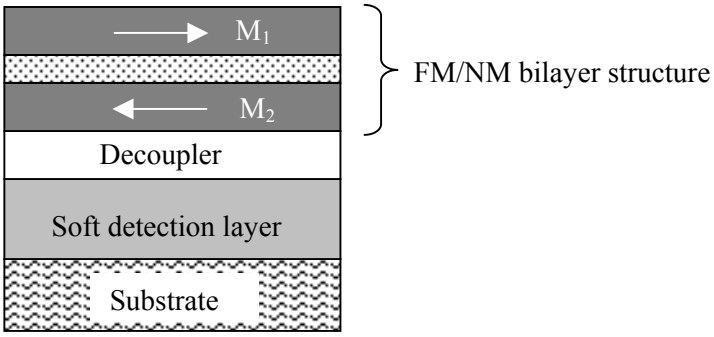

Fig. 3.14 *Schematic diagram of a synthetic spin valve structure.*

The GMR bilayer structure stack at the bottom shows strong interlayer exchange coupling and defines the magnetisation direction of the pinned ferromagnetic layer. The free layer is decoupled from the pinned layer by the relatively thick spacer in the sandwich, enabling a spin valve response. An optimum GMR response is observed when the angle between the magnetisation in the ferromagnetic layers changes from completely parallel to antiparallel in an applied field. Hence the formation of domain walls or magnetisation ripple will reduce the GMR response. Synthetic spin valves show a higher thermal stability, because the antiparallel magnetisation alignment will only be destroyed when the temperature is above the Curie temperature of the FM layers, which is generally higher than the blocking temperature in AFM materials. Another advantage is that the effective moment of the pinned layer is low, and therefore the contribution to the demagnetising and coupling fields acting on the free layer is much weaker than in conventional spin valves. Synthetic spin valves have also been incorporated in dual (symmetric) spin valve structures [53]. An optimum GMR response is observed when the angle between the magnetisation in the ferromagnetic layers changes from completely parallel to antiparallel in an applied field. Hence the formation of domain walls or magnetisation ripple will reduce the GMR response.

3.4 Pseudo Spin Valve Structures and MRAM.

A pseudo spin valve (PSV), unlike an exchange-biased spin valve, does not contain an AFM layer. The different switching fields for the two magnetic layers arise from dissimilar properties. The dissimilar properties can be induced by a difference in geometrical, materials, or structural factors, such as thickness, material type, or deposition conditions. A variety of PSV designs have been studied and this section will give an overview of some of the designs investigated.

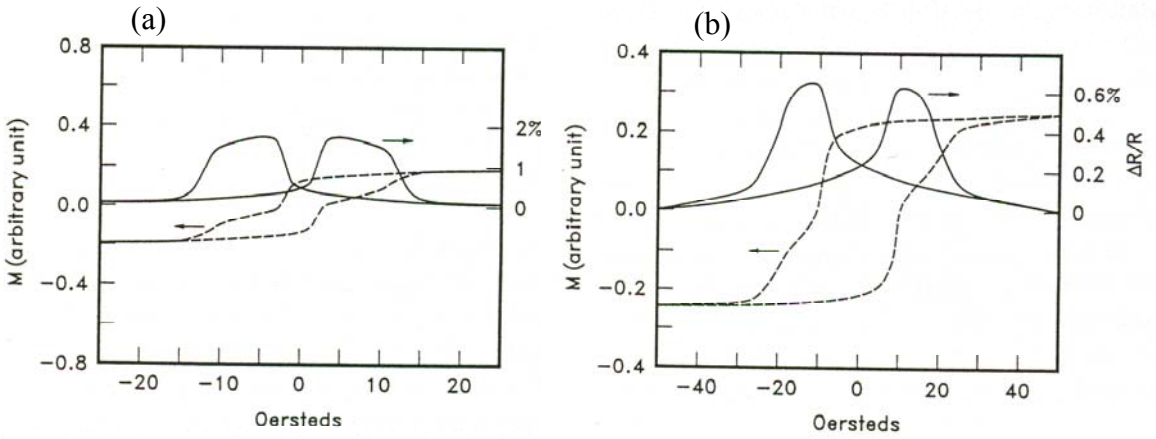

Fig. 3.15 *(a) Hysteresis loop and magnetoresistance at room temperature of a sample with structure Si/100Å Ta/40Å NiFe/60Å Cu/40Å NiCo/50Å Ta. (b) Hysteresis loop and magnetoresistance at room temperature of a sample with structure Si/30Å Fe/62Å Ag/30Å Co/62Å Ag. [14]* .

Dieny *et al.* showed that a spin valve response could be obtained from samples consisting of ferromagnetic layers with different coercivities [14]. Fig. 3.15 (a) shows the magnetisation curves and resistivity variations for samples with the structures: Si/100Å Ta/40Å NiFe/60Å Cu/40Å NiCo/50Å Ta and Si/30Å Fe/62Å Ag/30Å Co/62Å Ag. In Fig. 3.15 (a), NiFe has a lower coercivity than NiCo, while in Fig. 3.15 (b) Fe has a lower coercivity than Co. When the field is swept from the positive to the negative saturations of the structure, the magnetic configuration changes from parallel to antiparallel magnetic alignment between the two coercive fields associated with the two types of magnetic layers. The shape of the MR is intimately related to the magnetic hysteresis loops. The MR curve can exhibit a well defined plateau if the hysteresis loops associated with the two types of ferromagnet are well separated (Fig. 3.15 (a)), or a well rounded maximum if they tend to overlap (Fig. 3.15 (b)). In this type of structure, the fields required to obtain the full spin valve MR amplitude are usually much lower than in antiferromagnetically coupled multilayers. These fields are of the order of the saturation field of the softer of the two ferromagnetic materials (typically a few Oe or tens of Oe). However, in comparison to antiferromagnetically biased spin valves, the GMR ratio tends to be much smaller (≈2%).

Recent work by Schmidt et al [54] exploited the idea of designing a pseudo spin valve structure using ferromagnetic layers with very different coercivities, by investigating the use of CoTi as an ultra-soft material. The full structure was: $(Ti2Å/Co8Å)_2$/Co 25Å/Cu-d_{Cu}/Co20Å), ($8Å \leq d_{Cu} \leq 38Å$). This structure exploits the difference in coercive fields of pure

Co and the Co/Ti multilayer, and an additional Co 25Å layer was added to avoid problems with poor interface quality caused by Ti impurity. A magnetoresistance response was observed when d_{Cu}>24Å, with MR values reaching 5% with a sensitivity of 2%/Oe.

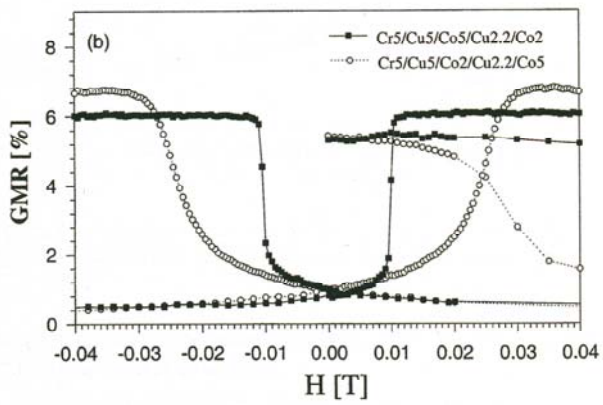

Fig. 3.16 *Low field magnetoresistance of Co-Cu-Co-Cu-Cr spin valves of different layering orders. [61].*

Some interesting work has been carried out by Ross *et al*. on nano-sized pseudo spin valve dots and wire arrays [55-61]. Interference lithography was used to fabricate the pseudo spin valves with the structures: Co/Cu/Co, and NiFe/Cu/Co. It is well known that the coercive field of a thin film is inversely proportional to the thickness [62] and the first structure relies on the different coercivities due to the different thicknesses of the ferromagnetic layers to produce a spin valve effect. The latter structure relies on the different coercivities of the ferromagnetic materials. Fig. 3.16 shows the low field electrical response for Co/Cu/Co pseudo spin valve nano-dots patterned with 100nm diameter and 200nm period. As shown, the system has a very rapid low field response in MR at the switching field of 100Oe. In particular, the MR for the PSV switches from the high field to the almost full maximum MR within a narrow field range <10Oe. The maximum MR value is about 6.5%.

Fig. 3.16 also shows the MR response of a similar PSV but with reverse ordering of the two Co layers. Comparing with the first PSV the only difference is that the thinner Co layer is deposited first. However, the MR response is dramatically different; the low field switching field is increased by almost a factor of three and the MR switching is more gradual. The magnetic properties of the more sensitive structure was analysed, and the results showed that the rapid low field response was due to the magnetisation reversal of the thicker ferromagnetic layer.

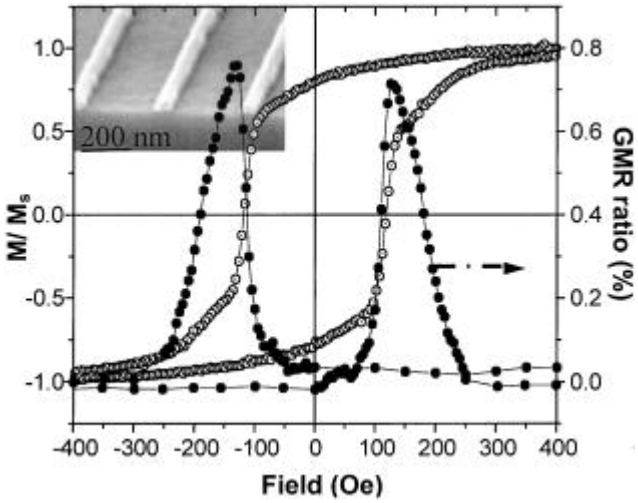

Fig. 3.17 *Magnetoresistance (solid) and hysteresis (open circles) measured on an array of 250μm long, 60nm wide wires patterned from a 6nm NiFe/3.7nm Cu/3nm Co/3nm Cu film. The field was applied parallel to the wires. [55].*

Fig. 3.17 shows an array of wires patterned from a NiFe/Cu/Co/Cu multilayer with widths of 60nm and 250μm length. The wires were patterned using interference lithography and argon ion milling and 940 wires were patterned. When a field is applied parallel to the wires, the resistance follows the magnetic hysteresis loop, having a higher value when the magnetisation directions of the NiFe and Co layers are antiparallel.

Further work by Castaño *et al*. [56] investigated how the spin valve response changes as the width of the nanopatterned pseudo spin valve wires varied from 60-150nm. The starting PSV thin film consisted of sputtered NiFe (6nm)/Cu (3.7nm)/Co (3nm)/Cu (3nm), exhibiting a room temperature giant magnetoresistance ratio of 2.5%. The effects of reducing the width of the wires are a monotonic decrease in the GMR ratio (from 2.55% to 0.74%) and the saturation magnetisation, and an increase of both the resistivity of the wires and the average switching fields of the magnetic layers. On cooling the samples to 77K, the resistivity decreased slightly and the GMR amplitude increased independently of the width of the wires. The authors suggested the presence of a disordered region at the edges of the wires as a result of processing, which increased the resistivity and decreased the saturation magnetisation as the wire width decreased.

McMichael *et al*. used an obliquely sputtered Ta underlayer to produce a high anisotropy in one of the ferromagnetic layers in a PSV design. Anisotropy fields in excess of 1500Oe were produced in 3-5nm thick polycrystalline films of Co, many times larger than the typical

anisotropy of polycrystalline Co films in this thickness range, and large enough for application as a robust "pinned" film in a spin valve. It has been known for many years that the oblique deposition of magnetic materials can produce uniaxial anisotropy in magnetic films [64-70].

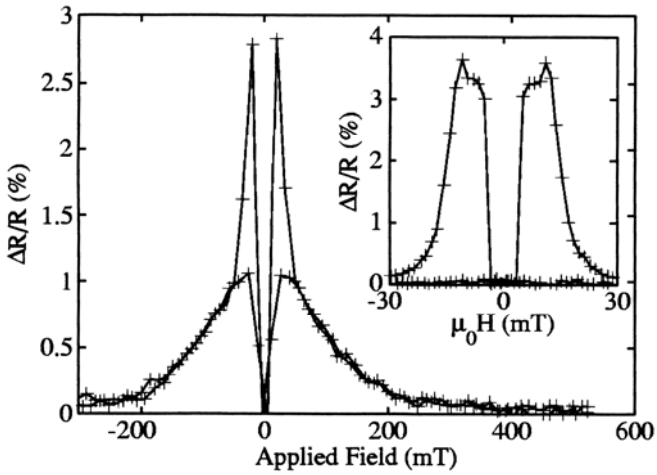

Fig. 3.18 *Magnetoresistance of a spin valve measured for fields applied at $\phi \approx 90°$, near the hard axis. The inset shows the magnetoresistance curve for $\phi \approx 0°$. [63].*

The source of the anisotropy is an anisotropic roughness that develops perpendicular to the incidence direction during oblique deposition of the Ta underlayers. Co films deposited normally on this underlayer experience large magnetostatic fields when magnetised perpendicular to the corrugations. Fig. 3.18 shows the magnetoresistance of the 7.5nmTa/3nmCo/4nmCu/3nmCo pseudo spin valve for fields applied at $\phi \approx 90°$, where ϕ is the angle between the applied field and the anisotropy axis. The inset shows the magnetoresistance curve for $\phi \approx 0°$, and the results show a maximum MR ratio of 3.5%.

3.4.1 Magnetic Random Access Memories (MRAMs).

There is a strong interest in non-volatile memory devices based on magnetic materials, Magnetic Random Access Memories (MRAMs), due to their non-volatile characteristic, radiation hardness, non-destructive read-out, low-voltage, and very large ($>10^{15}$) read-write cycle capability [71]. MRAMs can be as fast as Dynamic Random Access Memories (DRAMs), and almost as small as Static Random Access Memories (SRAM) in cell size. To compete with CMOS embedded memories, they must be fabricated with <125nm features, bringing several technological issues regarding micromagnetics and fabrication issues for deep submicron elements. MRAMs also compete with Ferroelectric Random Access

Memories (FERAMs) for non-volatile memories. In this case power consumption is a major issue. They compete directly with Flash memories used where speed is not a major concern (i.e. in some storage applications). Write speed for Flash technology is in the μs range in comparison to a few ns for MRAMs.

In the mid 1980s an MRAM concept was developed at Honeywell which has some common features with most modern version [72]:

- Writing data using magnetic hysteresis.
- Reading data using magnetoresistance of the same body where data is stored.
- Memory cells integrated on an integrated circuit chip.

The structure relied on sensing the AMR signal of a cobalt-permalloy alloy with normal AMR ratio of about 2%. The maximum differential resistance of the cell between '1' and '0' when it was read was about ¼ of the 2% magnetoresistance, or about 0.5%. In real arrays with practical sense current, this gave differential sense signals of 0.5 to 1.0mV. These sense signals allowed 16K bit integrated MRAM chips to operate with read access time of about 250ns [73]. Write times for the MRAM was 100ns and could have been faster if needed. The discovery of GMR multilayer materials gave hope for higher signals and faster read access rime. Magnetic films sandwiching a copper layer and etched into stripes showed a magnetoresistance ratio of about 6% and read access times of under 50ns [73]. However, GMR multilayer MRAM cells had serious limitations; the MRAM read access time was slower than for semiconductor memory because of the low MRAM sense signal, and the cell size was limited to 1μm due to magnetisation curling along the edges of the stripe.

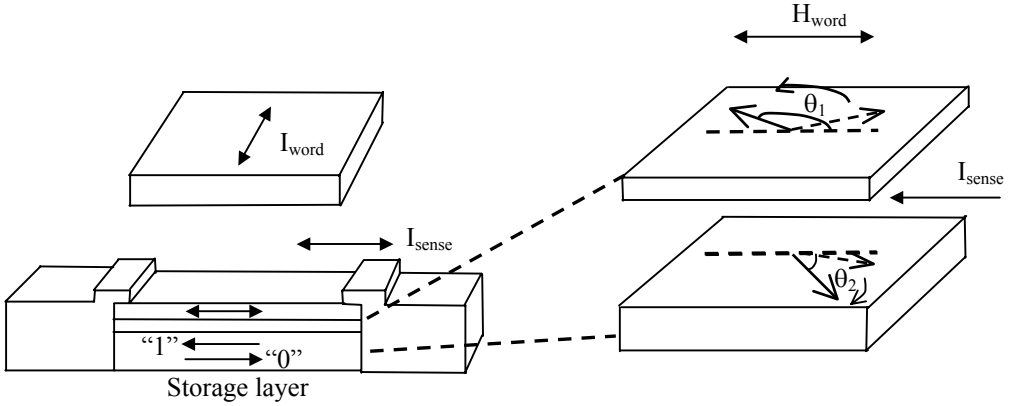

Fig. 3.19 *Pseudo spin valve cell. (Adapted from Ref [73].)*

The invention of the pseudo-spin valve (PSV) cell [74] significantly improved signal levels, thus improving the read access time of MRAM while maintaining densities competitive with other solid state memory technologies. Not only was nearly all of the ≈6% GMR available,

but also the signal swing was plus or minus 6% making the difference between a '0' and '1' about 12% of the cell resistance. This gave eight times improvement over the original mode of operation and put MRAM on a much more even footing with semiconductor memory or read access time. Fig. 3.19 illustrates the construction of a PSV cell, where the two magnetic layers have mismatched properties. In this case, the thinner film switches at lower fields, or is the 'soft' film and the thicker film switches at a higher field and is the 'hard' film. Without switching the hard film, the soft film can be manipulated to be parallel or antiparallel to the hard film. With a sequence of word fields, which starts with a negative field and ends with a positive field, the resistance either rises or falls, depending on whether a '1' or a '0' is stored. With simple electronics, the difference between the initial and final resistances can be sensed and the polarity of this difference indicates whether a '1' or '0' is stored. PSV memory cells can be at least as narrow as 0.2μm using a 2D memory organisation, and may find initial applications as a replacement for EEPROM or flash memory where high density or fast writing is important.

Spin Dependent Tunnelling (SDT) devices provide a higher percentage magnetoresistance than PSV structures and therefore have the potential for higher signals and higher speed. Recent results indicate SDT tunnelling giving over 40% magnetoresistance [75, 76], compared to 6-9% magnetoresistance in good PSV cells. One of the major disadvantages of SDT devices is the resistance of the small tunnelling cells tends to be at least several 1000s of ohms and they are subject to dielectric breakdown at the 1V to 2V level. Therefore currents of more than 1mA through the devices is not practical and the currents used to sense the state of the SDT cell probably cannot be used to aid in the switching of the cell, unlike for the PSV cell. Measurements have indicated that low time constants (<1ns) can be attained for PSV cells [75]. The intrinsic speed of SDT elements configured into a DRAM type architecture or a flip-flop like cell should provide signals of 30-40mV, which is comparable to semiconductor memory cells signal levels and should thus run at comparable speeds. SDT memory devices show promise for high performance non-volatile applications.

In summary, MRAM has the potential to be as fast and dense as DRAM with the additional advantage of non-volatility. Compared with flash and EEPROMs, MRAM writes much faster and does not deteriorate with millions of write cycles. Ferroelectric RAM (FRAM) is like MRAM in that it is non-volatile and fast write and there have been some limited FRAM applications. While FRAM is a competitor to MRAM, it is likely that MRAM can be denser.

References

[1] M.N. Baibich, J.M. Broto, A. Fert, F. Nguyen-Van-Dau, F. Petroff, P. Etienne, G. Creuzet, A. Friedrich, J. Chazelas: *Phys. Rev. Lett.,***61**, 2472 (1988).

[2] S. S.P. Parkin, N. More, K.P. Roche: *Phys. Rev. Lett.,* **64**, 2304 (1990).

[3] S.S.P. Parkin, Z. G. Li, and D. J. Smith, *Appl. Phys. Lett.*, **58**, 2710 (1991).

[4] S.S.P. Parkin, *Phys. Rev. Lett.*, **67**, 3598 (1991).

[5] S.S.P. Parkin, R. Bhadra, and K. P. Roche, *Phys. Rev. Lett.*, **66**, 2152 (1991).

[6] S.S.P. Parkin, *Ultrathin Magnetic Structures II*, Springer-Verlag Berlin Heidelberg, **Chapter 2.4**, 148-194 (1994).

[7] D.M.Edwards, J. Mathon, R.B. Muniz, and M.S. Phan, *Phys. Rev. Lett.*, **67**, 493-496 (1991).

[8] P. Lang, L. Nordström, R. Zeller, and P.H. Dederichs, *Phys. Rev. Lett.*, **71**, 1927-1930 (1993); L. Nordström, P. Lang, R. Zeller, and P.H. Dederichs, *Phys. Rev. B***, 50**, 13058-13061 (1994).

[9] R. Coehoorn, *Phys. Rev. B***, 44**, 9331-9337 (1991).

[10] P. Bruno and C. Chappert, *Phys. Rev. Lett.*, **67**, 1602-1605, 2592 (1991); P. Bruno and C. Chappert, *Phys. Rev. B***, 46**, 261-270 (1992).

[11] N. Mott, *Proc. Roy. Soc*. **156**, 368 (1936).

[12] J. Mathon, Spin Electronics, Springer-Verlag Berlin Heidelberg, Chapter 4, 71-88, (2001).

[13] B. Dieny, V.S. Speriosu, S.S.P. Parkin, B.A. Gurney, D.R. Wilhoit, and D. Mauri, *Phys. Rev. B* **43**, 1297 (1991).

[14] B. Dieny, V.S. Speriosu, B.A. Gurney, S.S.P. Parkin, D.R. Wilhoit, K.P. Roche, S. Metin, D.T. Peterson, and S. Nadimi, *J. Magn. Magn. Mater*. **93**, 101 (1991).

[15] B. Dieny, V.S. Speriosu, S. Metin, S.S.P. Parkin, B.A. Gurney, P. Baumgart, and D.R. Wilhoit, *J. Appl. Phys*. **69**, 4774 (1991).

[16] R. Coehoorn, J.C.S. Kools, Th.G.S.M. Rijks and K.–M.H. Lenssen, *Philips J. Res*. **51**, 93-124, (1998).

[17] T.C. Anthony, J.A. Brug and S. Zhang, *IEEE Trans. Magn*. **30**, 3819 (1994).

[18] W.F. Egelhoff, Jr. et al. *J. Appl. Phys*. **78**, 273 (1995).

[19] P.M. Baumgart, B. Dieny, B.A. Gurney, J.P. Nozières, V.S. Speriosu and D.R. Wilhoit, *U.S. Patent* **5287238** (1994).

[20] S. Noguchi, R. Nakatani, K. Hoshino and Y. Sugita, *Jpn. J. Appl. Phys*. **33**, 5734 (1994).

[21] W.F. Egelhoff, Jr. et al. *J. Appl. Phys*. **79**, 5277 (1996).

[22] W.F. Egelhoff, Jr. et al. *J. Appl. Phys*. **82**, 6142 (1997).

[23] Y. Sugita, Y. Kawawake, M. Satomi, H. Sakakima, *Jpn. J. Appl. Phys*. **37**, 5984 (1998).

[24] Th. G.S.M. Rijks, R. Coehoorn, J.T.F. Daemen, and W.J.M. de Jonge, *J. Appl. Phys*. **76**, 1092 (1994).

[25] K. Hoshino, S. Noguchi, R. Nakatani, H. Hoshiya, and Y. Sugita, *Jpn. J. Appl. Phys*. Part 1 **33**, 1327 (1994).

[26] J.C.S. Kools, *J. Appl. Phys*. **77**, 2993 (1995).

[27] J.C.S. Kools, Th. G.S.M. Rijks, A.E.M. De Veirman and R. Coehoorn, *J. Appl. Phys*. **31**, 3918 (1995).

[28] J.L. Leal and M.H. Kryder, *J. Appl. Phys*. **79**, 2801 (1996).

[29] J.L. Leal and M.H. Kryder, *IEEE Trans. Magn*. **32**, 4642 (1996).

[30] D. Wei and H.N. Bertram, *IEEE Trans. Magn*. **32**, 3434 (1996).

[31] C.M. Park, K.I. Min, and K.H. Shin, *IEEE Trans. Magn*. **32**, 3422 (1996).

[32] Th. G.S.M. Rijks, W.J.M. de Jonge, W. Folkerts, J.C.S. Kools, R. Coehoorn, *Appl. Phys. Lett.* **65**, 916 (1994).

[33] V. Speriosu, J.P. Nozières, B.A. Gurney, B. Dieny, T.C. Huang, H. Lefakis, *Phys. Rev. B* **47**, 11579 (1993).

[34] B. Dieny, *J. Magn. Magn. Mater*. **136**, 335 (1994).

[35] B. Dieny, P. Humbert, V.S. Speriosu, S. Metin, B.A. Gurney, P. Baumgart and H. Lefakis, *Phys. Rev. B* **45**, 806 (1992).

[36] P.P. Freitas, *Spin Electronics*, Springer-Verlag Berlin Heidelberg, **Chapter 19**, (2001).

[37] A. Veloso, N.J. Oliveira, and P.P. Freitas, *IEEE Trans. Magn*.,**34**, 2343 (1998).

[38] J. Nogués, I.K. Schuller, *J. Magn. Magn. Mater*. **192**, 203 (1999).

[39] A. Fert and P. Bruno, *Ultrathin Magnetic Structures II,* Springer-Verlag Berlin Heidelberg, **Chapter 2.2**, 110 (1994).

[40] E.E. Fullerton, D.M. Kelly, J. Guimpel, I.K. Schuller, Y. Bruynseraed, *Phys. Rev. Lett*., **68**, 859 (1992).

[41] F. Petroff, A. Barthelemy, D.H. Mosca, D.K. Lottis, A. Fert, P.A. Schroeder, W.P. Pratt, R. Loloee, S. Lequien, *Phys. Rev. B.,***44**, 5355 (1991).

[42] T.C. Huang, J.P. Nozières, V.S. Speriosu, B.A. Gurney, H. Lefakis, *Appl. Phys. Lett.* **62**, 1478 (1993).

[43] V.S. Speriosu, J.P. Nozières, B.A. Gurney, B. Dieny, T.C. Huang, H. Lefakis, *Phys. Rev. B.,***47**, 11579 (1993).

[44] R.J. Highmore, W.C. Shih, R.E. Somekh, J.E. Evetts, *J. Magn. Magn. Mater*. **116**, 249 (1992).

[45] Y. Saito, S. Hashimoto, K. Inomata, *Appl. Phys. Lett.* **60**, 2436 (1992).

[46] J. Kohlepp, S. Cordes, H.J. Elmers, U. Gradmann, *J. Magn. Magn. Mater*. **111**, 231 (1992).

[47] D.H. Mosca, F. Petroff, A. Fert, P.A. Schroeder, W.P Pratt, R. Loloe, *J. Magn. Magn. Mater*. **94**, L1 (1991).

[48] B. Dieny, V.S. Speriosu, S. Metin, *Europhys. Lett*., **15**, 227 (1991).

[49] A. Vedyayev, B. Dieny, N. Ryzhanova, J.B. Genin, C. Cowache, *Europhys. Lett*., **25**, 465 (1994).

[50] S.S.P. Parkin, *Phys. Rev. Lett.*, **71**, 1641 (1993); S.S.P. Parkin, *Appl. Phys. Lett.* **61**, 1358 (1993).

[51] S.N. Mao, N. Amin, E. Murdock, *J. Appl. Phys*. **83** (11Pt2), 6807 (1998).

[52] H.A.M. van der Berg et al., *IEEE Trans. Magn*.,**32** (5Pt2), 4624 (1996).

[53] A. Tanaka, Y. Shimizu, H. Kishi, K. Nagasaka, H. Kanai, M. Oshiki, *IEEE Trans. Magn*.,**35**, 700 (1999).

[54] M. Schmidt, F. Stobiecki, B. Szymański, *Phys. Stat. Sol. (a)* **196** (1), 56 (2003).

[55] C. A. Ross, S. Haratani, F.J. Castaño, Y. Hao, M. Hwang, M. Shima, J.Y. Cheng, B. Vögeli, M. Farhoud, M. Walsh, H.I. Smith, *J. Appl. Phys* **91** (10), 6848 (2002).

[56] F.J. Castaño, S. Haratani, Y. Hao, C. A. Ross, H.I. Smith, *Appl. Phys. Lett.* **81** (15), 2809 (2002).

[57] X. Zhu, P. Grütter, Y. Hao, F.J. Castaño, S. Haratani, C. A. Ross, B. Vögeli, H.I. Smith, *J. Appl. Phys* **93** (2), 1132 (2003).

[58] N. Dao, S.L. Whittenburg, Y. Hao, C. A. Ross, L.M. Malkinski, J.Q. Wang, *J. Appl. Phys* **91** (10), 8293 (2002).

[59] F.J. Castaño, Y. Hao, S. Haratani, C. A. Ross, B. Vögeli, M. Walsh, H.I. Smith, *IEEE Trans. Magn*., (2000).

[60] F.J. Castaño, Y. Hao, C. A. Ross, B. Vögeli, H.I. Smith, S. Haratani, *J. Appl. Phys* **91** (10), 7317 (2002).

[61] J.Q. Wang, L.M. Malkinski, Y. Hao, C. A. Ross, J.A. Wiemann, C.J. O'Connor, *Mater. Sci. and Eng.*, **B76**, 1 (2000).

[62] J. H. Fluitman, *Thin Solid Films*, **16**, 269 (1973).

[63] R.D. McMichael, C.G. Lee, J.E. Bonevich, P.J. Chen, W. Miller, W.F. Egelhoff, Jr., *J. Appl. Phys* **88** (9), 5296 (2000).

[64] D.O. Smith, *J. Appl. Phys* **30**, 264S (1959).

[65] T.G. Knorr, R.W. Hoffman, *Phys. Rev.,* **113**, 1039 (1959).

[66] Y. Hoshi, E. Suzuki, M. Naoe, *J. Appl. Phys* **79**, 4945 (1996).

[67] K. Itoh, K. Hara, M. Kamiya, K. Okamoto, T. Hashimoto, H. Fujiwara, *J. Magn. Magn. Mater*. **148**, 132 (1995).

[68] J.M. Alameda, F. Carmona, F.H. Salas, L.M. Alvarez-Prado, R. Morales, G.T. Pérez, *J. Magn. Magn. Mater*. **154**, 249 (1996).

[69] K. Tanaka, S. Yamauchi, E. Makino, T. Fujii, M. Inoue, M. Izaki, *IEEE Trans. Magn*.,**35**, 2916 (1999).

[70] M. Michijima, H. Hayashi, M. Kyoho, T. Nakabayashi, T. Komoda, T. Kira, *IEEE Trans. Magn*.,**35**, 3442 (1999).

[71] G.B. Granley, T. Hurst, *Sixth Biennial IEEE International Non-Volatile Memory Technology Conference Proceddings*, pg 138 (1996).

[72] J. Daughton, *Thin Solid Films*, **216**, 162 (1992).

[73] J.M. Daughton, A.V. Pohm, R.T. Fayfield, C.H. Smith, *J. Phys. D: Appl. Phys*., **32**, R169 (1999).

[74] A. Pohm, B. Everitt, R. Beech, J. Daughton, *IEEE Trans. Magn*.,**33**, 3280 (1997).

[75] S. Parkin, *Intermag Conf. (Kyongiu, Korea, 18-21 May 1999)* paper GA-01.

[76] S. Carsoso, V. Gehanno, R. Fereira, P. Freitas, *(Kyongiu, Korea, 18-21 May 1999)* paper FC-03.

[77] J.L.Prieto, N.Rouse, N.K. Todd, D. Morecroft, J. Wolfman, J.E.Evetts, M.G. Blamire. *Sensors & Actuators A,* **94**, 64 (2001).

Any intelligent fool can make things bigger and more complex….It takes a touch of genius---and a lot of courage to move in the opposite direction. *Albert Einstein.*

Chapter 4

Experimental Techniques

CHAPTER 4

This chapter will describe the experimental techniques used in this thesis. The first part will describe the device microfabrication including optical lithography, argon ion milling and d.c. sputter deposition. The second part will describe the device nanofabrication including r.f. sputter deposition and Focused Ion Beam (FIB) lithography. The final part will describe the various characterisation techniques used including electrical characterisation using four-point resistance measurements, magnetic characterisation using the Vibrating Sample Magnetometer (VSM) and structural characterisation using Atomic Force Microscopy (AFM). Magnetic domain imaging using the Bitter technique is also described at the end of the chapter.

4.1 Device microfabrication.

Microfabrication of the ferromagnetic thin films and pseudo spin valves was carried out using optical lithography in the group clean room, and the masks were designed using AutoCAD™. High resolution optical exposure was done in a Karl Suss contact mask aligner (Karl Suss MJB 3), using a UV light-source. An argon ion miller was used to transfer the structure into the sample, and sputter deposition was used to deposit copper for electrical contact. Fig. 4.1 shows the typical processing steps involved in the fabrication of an array of microwires across the surface of the chip, including electrical contacts. The left part of the diagram shows the mask design (a), and the cross-section across the width is shown on the right, (b). Step 1 involves ion milling away the edges of the chip. This enables better contact between the mask and the chip for the following lithography steps. Step 2 is another milling step to fit the size of the spin valve to the size of the wire array. In step 3 copper contact pads are deposited by sputter deposition and liftoff. Holes are patterned in the photoresist where the contact pads are required. After exposure and before developing the sample is submersed in chlorobenzene for two minutes and then dried using an air gun. The chlorobenzene hardens the surface of the photoresist and creates a ledge profile, which aids the lift-off procedure [1]. The chamber was pumped to below $5x10^{-5}$mbar, and before sputtering the copper target was pre-sputtered to clean the surface. The copper was then deposited over the entire surface of the film using D.C. sputter deposition. The copper was sputtered at a pure argon pressure of $2x10^{-3}$mbar and 40W power, the copper deposition rate at this power is ≈1.56nm/s. After deposition, the resist was stripped with acetone leaving the copper contact pads. The sample holder was water cooled throughout the deposition.

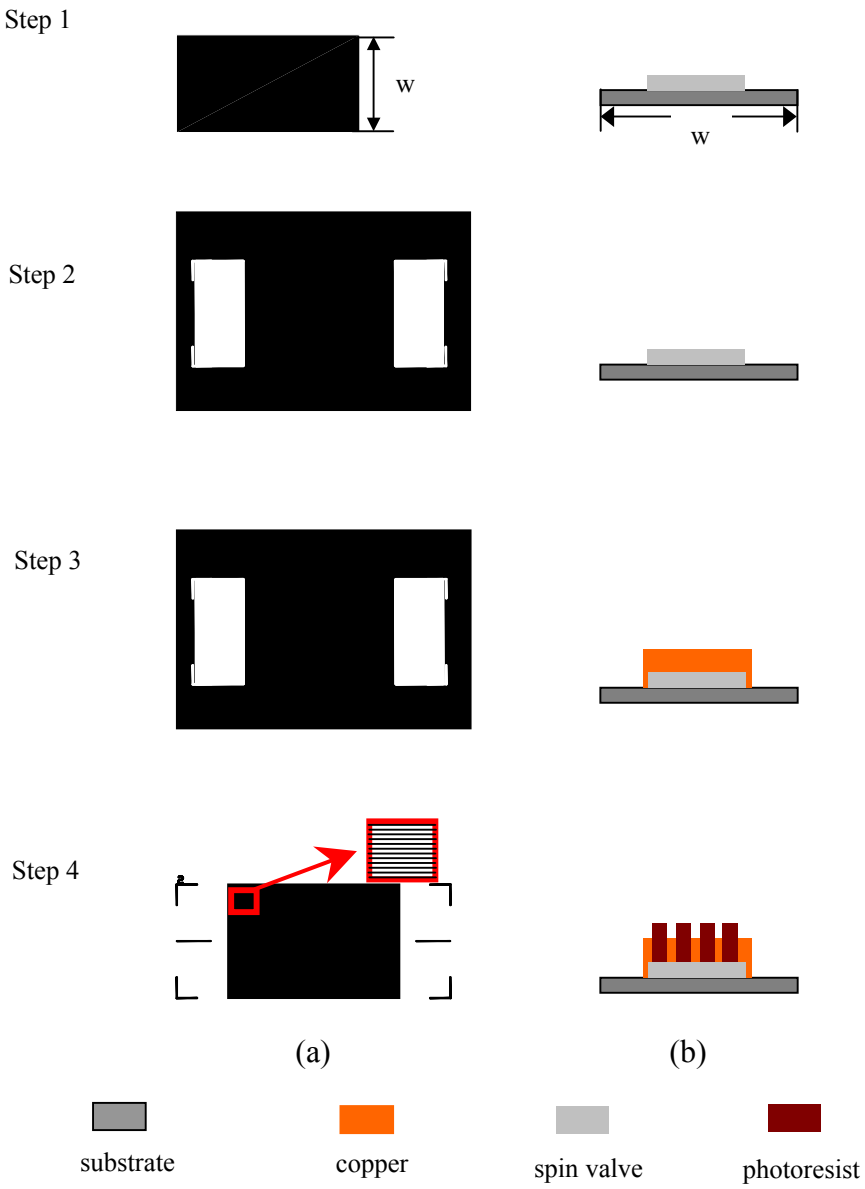

Fig. 4.1 *The four steps involved in the fabrication of an array of micro-wires across the surface of the sample with electrical contacts. Steps 1, 2 and 4 involve lithography and milling. Step 3 involves lithography and lift off of the sputter deposited of copper contact pads.*

Argon Ion Milling.

After the resist was patterned, ion milling was used to physically etch away the unwanted areas of the film. Ion milling is strictly a mechanical process, it involves no chemical reactions with the sample because it uses a noble gas. It relies on striking a plasma to produce the etch species, and the plasma is initiated by applying a voltage across a gap containing the low-pressure argon gas. The Kaufman ion gun was powered with a Princeton Applied

Research power supply, and the chamber was pumped down to less than $4x10^{-6}$mbar using a diffusion pump prior to milling. Argon gas with a 2% oxygen mixture was used to mill the samples at a pressure of $2x10^{-4}$mbar. The oxygen enhances the etch rate by oxidising the debris from the areas of film being removed. The beam current of the Ar^+ ions was 10mA with a 500V accelerating voltage. The sample holder was water cooled and rotated during milling to improve the uniformity across the surface. The milling rate was calibrated using Atomic Force Microscopy (AFM), and was found to be approximately 10nm/min for NiFe.

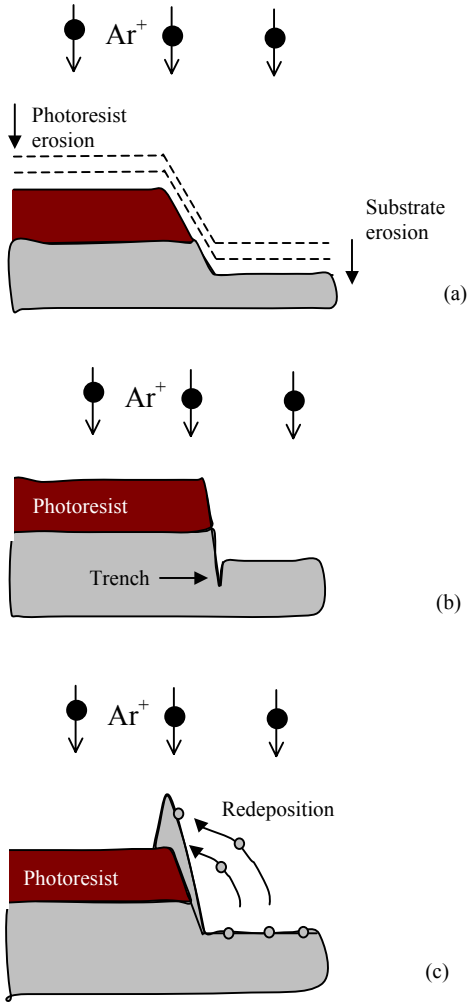

Fig. 4.2 *Problems that may occur during ion milling: (a) mask taper transfer, (b) trenching, (c) re-deposition of the etched material.*

Fig. 4.2 shows some of the problems that occurred during milling of the highly anisotropic wire arrays. Since the process erodes the mask, any taper in the masking layer will be transferred to the pattern. After etching is finished and the photoresist mask is removed, the resultant pattern is broadened, Fig. 4.2 (a). This problem can be minimised by optimising the contact during lithography and rotating during milling. An enhanced erosion rate at the edge

of the pattern is called trenching, and occurs when mask erosion causes the sidewalls of the pattern to be tapered at a steep angle. Some of the low angle ions will reflect off at the tapered surface towards the pattern edge, where they cause trenches, Fig. 4.2 (b). The etched materials are not volatile and tend to be re-deposited on any surface where they come into contact, e.g. the side-wall of the patterned wire, even after the photoresist has been removed, Fig. 4.2 (c). This problem can also be minimised by rotating during milling. When the film is rigid enough the side-wall can be removed by gently scrubbing with a cotton bud. Also, although the re-deposited material is evident in the AFM images, it contributes a small fraction of the total signal from the wire array.

D.C Sputter deposition.

Fig. 4.3 shows a schematic diagram of the sputtering system. The sputtering flange is positioned directly above the sample holder, and a rotary pump is used to rough the system and back the diffusion pump. Sputtering relies on striking a plasma between the anode (sample holder) and cathode (target) to produce the reactive species. Once the plasma is formed, ions in the plasma are accelerated toward the target and strike the surface. When an energetic ion strikes the surface of the target, four things can happen as shown in Fig. 4.4.

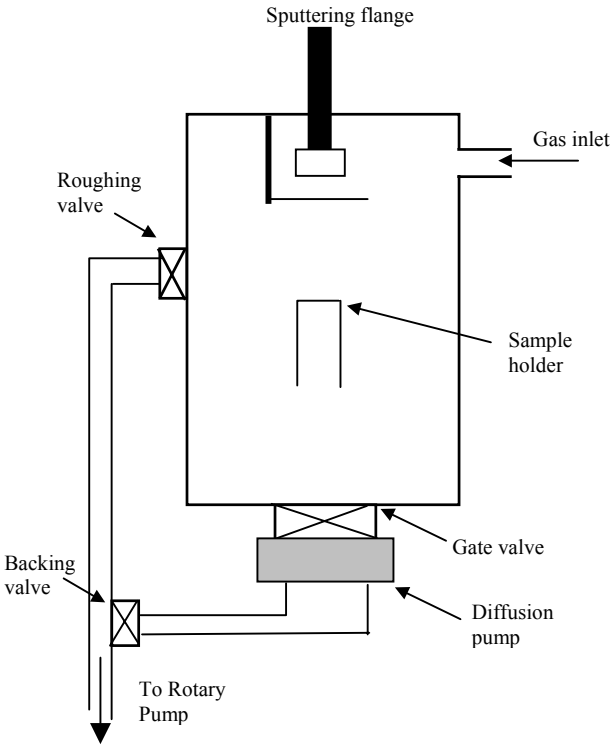

Fig. 4.3 *A schematic picture of D.C. sputtering system.*

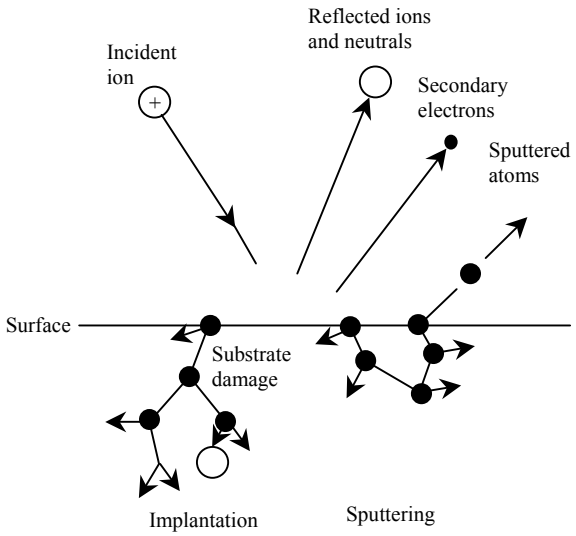

Fig. 4.4 *Possible outcomes for an ion incident on the surface of a wafer. (After Ref. [2]).*

Ions with very low energy will simply bounce off the surface. At energies less than about 10eV, the ion may adsorb to the surface, giving up its energy to phonons (heat). At energies above about 10eV, the ion penetrates into the material, transferring most of its energy deep into the target, where it changes the physical structure. These energies are typical for ion implantation. Between these two extremes, both energy transfer mechanisms occur; part of the ion energy is deposited in the form of heat, and the remainder goes into the physical rearrangement of the target material. Most of the energy transfer occurs within several atomic layers, and the atoms and clusters of atoms are ejected from the surface of the material. The atoms and clusters of atoms ejected escape with energies of 10 to 50eV. This energy provides sputtered atoms with additional surface mobility for good step coverage. Planar magnetron sputtering was used, which causes the electrons to spiral around the direction of the magnetic field lines. The orbital motion of the electrons increases the probability that they will collide with neutral species and create ions. The increased ion density increases the rate of ion bombardment of the target. A resolution of ≈1μm could be achieved by optical lithography. Although the UV light produces a wavelength of ≈400nm, the resolution is limited by the minimum mask feature size, the contact between the mask and the sample and the thickness of the photoresist.

4.2 Device nanofabrication.

The samples were initially prepared for Focused Ion Beam (FIB) nanofabrication using optical lithography, ion milling, D.C. sputter deposition and R.F. sputter deposition. Fig. 4.5

shows the sample preparation, which involves 4 steps: (1) optical lithography and milling to pattern the mesostructures, (2) optical lithography and D.C. sputter deposition to deposit contact pads, (3) optical lithography, R.F. sputter deposition and lift off to deposit the silica hard mask, and finally (4) D.C. sputter deposition of a gold over-layer, which enabled imaging in the FIB.

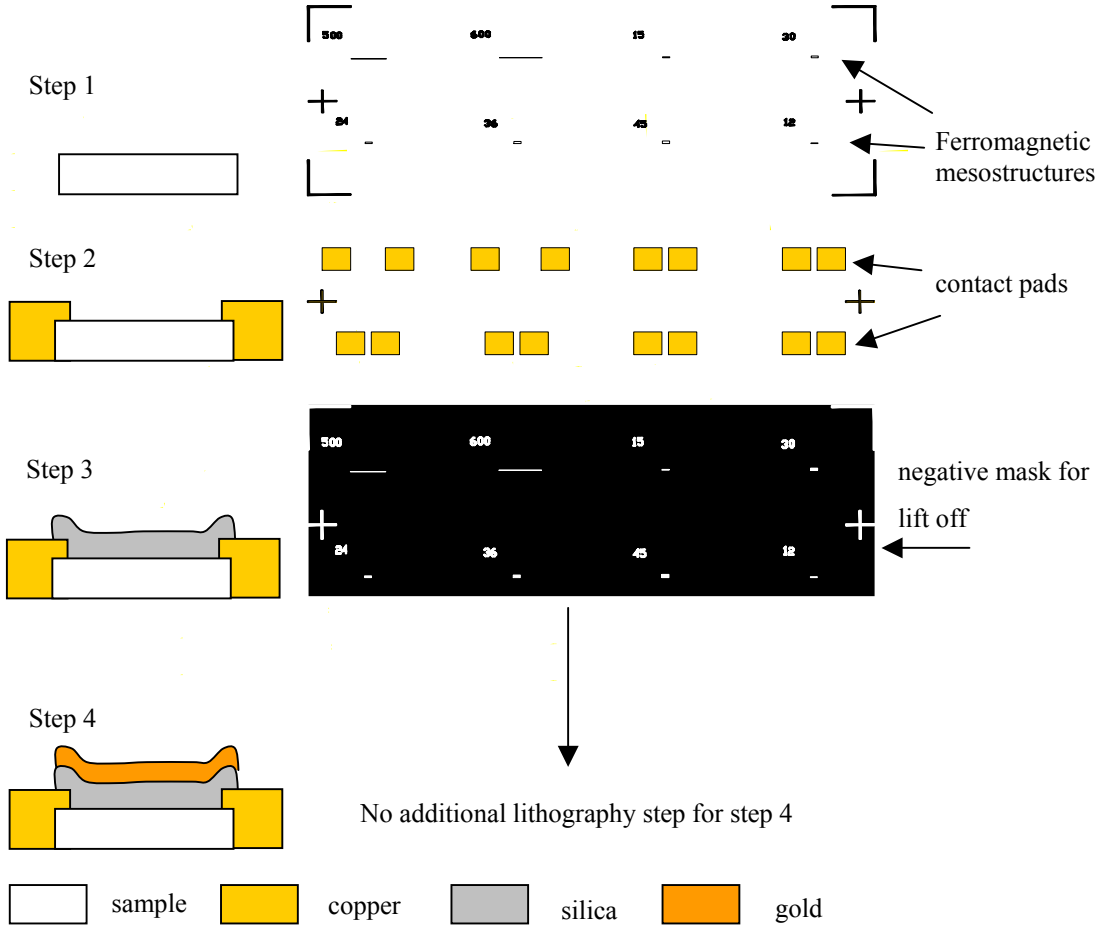

Fig. 4.5 *The four steps involved in preparation of the ferromagnetic mesostructures for FIB nanofabrication. The schematic diagram shows the cross-section of the sample for each step, the mask design is shown on the right. Each step involves optical lithography, step 1 involves ion milling, step 2 D.C. sputter deposition, step 3 R.F. sputter deposition, and step 4 D.C. sputter deposition.*

The left part of the diagram shows the cross-section for each step, and the right shows the mask design. After depositing the copper contact pads and before depositing silica, the samples were characterised using transport measurements as described in section 4.4. After depositing silica and before carrying out the lift off, a gold layer was deposited on top of the silica. The chamber was pumped down to 4×10^{-6}mbar using a diffusion pump, and the target was pre-sputtered for 3mins. Deposition was carried out at 2×10^{-3}mbar and 40W power, the

gold deposition rate at this power is 25nm/min. Approximately 30nm of gold was deposited on top of the silica. Afterwards, lift of was carried out to remove the unwanted silica and gold.

Radio Frequency (R.F.) Sputter deposition.

R.F. sputter deposition was used to deposit approximately 50nm of insulating silica on top of the ferromagnetic mesostructures. R.F. sputter deposition is used to deposit insulating materials because it prevents the material from becoming charged during deposition, and extinguishing the plasma. Optical lithography, lift off and R.F. sputter deposition was used to deposit the silica directly above the ferromagnetic mesostructures. Fig. 4.6 shows a schematic of a typical R.F. plasma system. A tuning network is used to match the impedance between the plasma and the power source. A blocking capacitor is used to dc isolate the supply from the chamber. Sources are in the radio frequency (R.F.) range, commonly 13.56MHz. The chamber was pumped down to $\times 10^{-7}$ mbar before deposition using a diffusion pump. The silica was deposited in argon gas at a power of 50W, a pressure of 3Pa and a deposition rate of 300nm every 25mins. Approximately 50nm of silica was deposited, and the magnetron was water cooled throughout the deposition.

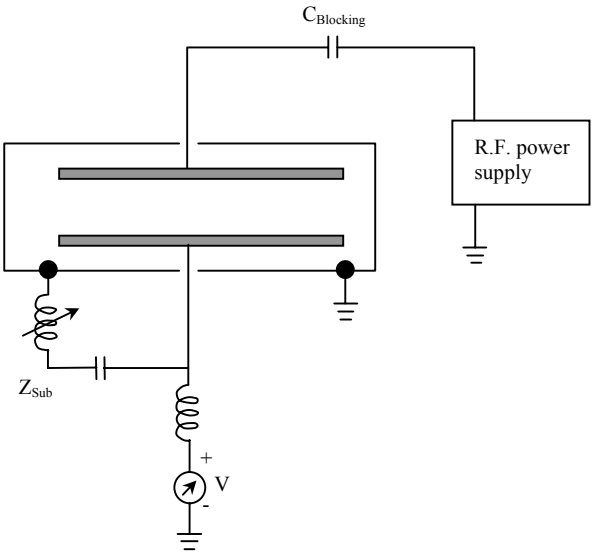

Fig. 4.6 *A schematic diagram of an R.F. plasma system. (After Ref. [3]).*

Focused Ion Beam (FIB) lithography.

This section will serve as a brief introduction to the operation of the FIB, a more detailed account of the operation of the FIB and possible uses can be found elsewhere [4]. The Focused Ion Beam technique (FIB) was mainly developed during the late 1970s and early 1980s, and the first commercial instruments were introduced more than a decade ago [5]. Modern FIB systems are becoming widely available in semiconductor research and processing environments, as well as in failure analysis and chip-design centres. The

technology enables localised milling and deposition of conductors and insulators with high precision, hence its success in device modification, mask repair, process control and failure analysis [6-10]. Focused ion beam systems effectively combine together a scanning ion microscope and a precision milling system. By scanning the ion beam over a specimen and collecting the ion beam-induced secondary-electron or -ion signal an image of the surface is formed. The position for a milled pattern can be selected from the image taken, and then the structure can be produced using Ga^+ ions without the use of a patterned resist mask. One of the advantages over conventional etch methods is that the etch depth can be varied across the structure, by varying the dwell time from point to point within the pattern.

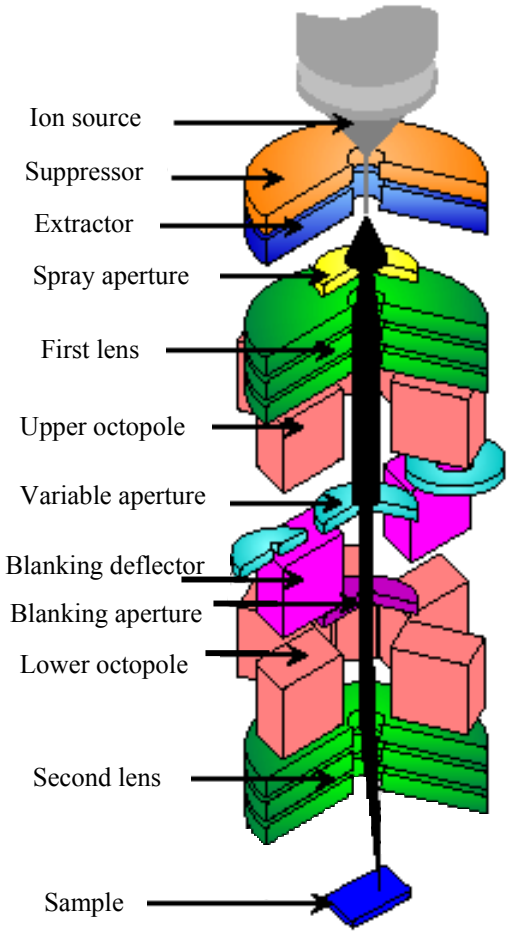

Fig. 4.7 *A schematic diagram of a FIB ion column. (After Ref. [5]).*

Fig. 4.7 is a schematic diagram of a FIB ion column. The structure of the column is similar to that of a scanning electron microscope, the major difference being the use of a gallium ion (Ga+) beam instead of an electron beam. The ion beam is generated from a liquid metal ion source (LMIS) by the application of a strong electric field. This electric field causes the emission of positively charged ions from a liquid gallium cone, which is formed on the tip of a tungsten needle. The Ga LMIS is used because of its stability, simplicity of operation and

the fact that Ga ions give good sputtering yields. A vacuum of about 1×10^{-7} mbar is maintained inside the column. After a first refinement through the spray aperture, the ion beam is condensed in the first electrostatic lens. The upper octopole then adjusts the beam stigmatism. For patterning the samples in this thesis, the beam voltage was 30keV and the beam current was approximately 80pA. Using the variable aperture mechanism, the beam current can be varied over four decades, allowing for both a fine beam for high-resolution imaging and a heavy beam for fast and rough milling. The blanking deflector and aperture enable blanking of the beam away from the sample into a Faraday cup. This system not only protects the sample from constant milling, but can also measure the current. The lower octopole is used for scanning the beam over the sample in a user-defined pattern. In the second electrostatic lens, the beam is focused to a fine spot, enabling a best resolution in the sub 10nm range. A secondary electron detector is used to collect the secondary particles for imaging.

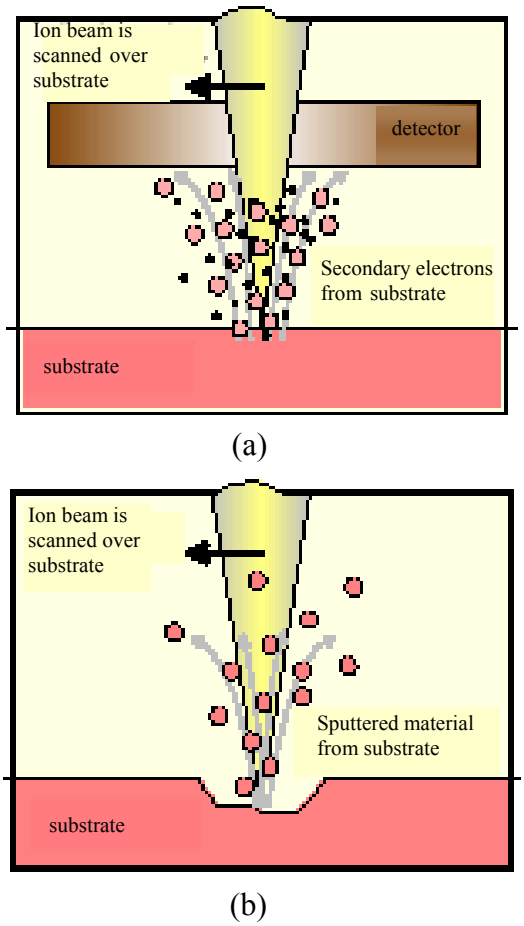

Fig. 4.8 *Schematic diagrams showing the principle of FIB (a) imaging and (b) milling. (After Ref. [5]).*

Fig. 4.8 is a schematic showing the principle of FIB imaging (a) and milling (b). During FIB imaging the finely focused ion beam is raster scanned over a substrate, and secondary particles (neutral atoms, ions and electrons) are generated in the sample. As they leave the sample, the electrons or ions are collected by the secondary electron detector. To prevent positive surface charges from building up, the samples were wire bonded to the sample holder, which was grounded. FIB imaging inevitably induces some damage to the sample. Most of the Ga^+ ions that arrive at the sample surface enter the sample, leading to ion implantation. The depth of the implanted region is related to the ion energy and the angle of incidence. When the Ga^+ ion energy is 30keV, the implantation depth in SiO_2 is 25± 8nm [5]. Also, some milling always occurs when the ion beam is scanned across the sample surface, although the milling effect can be reduced by using a fine ion beam (fine spot and low ion current).

The removal of sample material is achieved using a high ion current beam, as shown in Fig. 4.8 (b). The result is a physical sputtering of the sample material. The milling process was calibrated using 'end-point detection'; this is a real-time graph of the average brightness in the milling area. An insulator will appear darker than a conductor since the secondary electron yield of the latter is much higher. This effect results in a typical end-point detection curve as shown in Fig. 4.9.

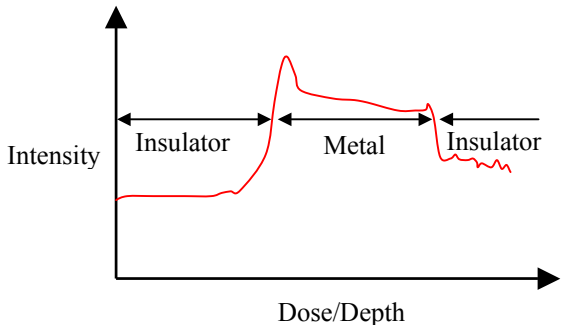

Fig. 4.9 *End-point detection. The graph shows the average brightness in the milling area as a function of the delivered dose. This is used to monitor the milling operation in real time. The insulator-metal-insulator transition is clear.*

The first part (low brightness) corresponds to the insulating dielectric layer over the metal conductor. The metal itself is the central high-intensity part. Finally, after milling through the metal, the intensity diminishes again when the underlying insulating layer is reached. This technique was used to detect the amount of time to mill through the gold and silica layers, and therefore enable milling to the correct depth to design the hard mask. The resistance of the samples was measured before and after patterning the silica hard mask in the FIB. This

indicated the amount of Ga^+ implantation of the spin valve; the higher the resistance above the initial value, the greater the amount of Ga^+ implantation.

4.3 Device characterisation.

A number of different characterisation techniques were used for evaluating the samples in this thesis work, including electrical, magnetic and structural characterisation. This section will briefly go through the different techniques used throughout this thesis work.

4.3.1 Electrical characterisation.

Resistivity values of thin film materials tend to be larger than the bulk due to increased surface scattering. The problem of electron scattering from thin film metal surfaces has been of interest for more than a century, and the subject is still not completely free from controversy. In 1901 Thomson used classical physics to provide a simple way to visualise the increase in resistivity as the film thickness decreases compared to the bulk value [11]. He derived the expression given in Eqn. (4.1), which shows that as the thickness is decreased, the mean free path of the thin film is reduced and the resistivity rises; a size effect is exhibited.

$$\frac{\sigma_f}{\sigma_0} = \frac{\rho_0}{\rho_f} = \frac{\kappa}{2}\left(\ln\frac{1}{\kappa} + \frac{3}{2}\right). \qquad (4.1)$$

Where σ_f and λ_f are the resistivity and mean free path of the thin film, σ_0 and λ_0 are the resistivity and mean free path of the bulk material, and $\kappa = d/\lambda_0$, where d is the thickness of the film. A more accurate quantum theory of thin-film conductivity was developed by Fuchs in 1938 [12] and elaborated upon in the ensuing half-century by other investigators, most notably Sondheimer [13]. The Fuchs-Sondheimer (F-S) theory is in close agreement with the Thomson equation.

A standard four-point measurement technique was used to measure the resistance of the thin films and trilayers. A constant current is applied across the film and the resistance is measured by detecting the voltage drop through separate connections. Copper contact pads were used to make electrical contact and distribute the current flow evenly across the ends of the thin film. The effect of the increased current density on the resistance of the nanopatterned samples was investigated by applying a constant current and studying the change in resistance with time in zero applied field. It was found that the resistance of the sample remained constant, which was a direct indication that the increased current density was not detrimental to the GMR response.

Magnetoresistance measurements provide an effective method for analysing the magnetisation reversal processes of ferromagnetic thin films and trilayers. The change in resistance with applied field can give a direct indication of the orientation of the magnetisation in a thin film with respect to the current, and an indication of the relative orientation of two ferromagnetic layers with respect to each other. Coercivity, switching fields and magnetic saturation values can be extracted from the measurements. Two types of magnetoresistance measurements were carried out: *in-situ* during milling and *ex-situ* for a range of temperatures from liquid nitrogen to 493K. The set-up for *in-situ* magnetoresistance measurements was purpose built and is described in detail in Chapter 6. For the *ex-situ* measurements, the sample was wire bonded to the sample holder using an ultrasonic wire bonder. The sample holder was placed in a probe, which was positioned between the pole pieces of an electromagnet. Typically 0.5mA constant current was supplied to the sample, and the field was swept between ±100Oe. The magnetoresistance of the sample was extracted from the change in voltage as the field was swept, and the current remained constant. The percentage MR of the sample is determined by Eqn. (4.2),

$$\left(\frac{R(H) - R(H_s)}{R(H_s)} \times 100 \right) \tag{4.2}$$

where $R(H)$ is the resistance in an applied field H and $R(H_s)$ is the resistance at the saturation field.

For low temperature measurements the probe was placed in liquid nitrogen and left for a couple of hours before measuring to allow the temperature to stabilise. High temperature measurements were carried out by placing the probe in the centre of a quartz tube, which was sealed at one end to contain the heat. The quartz tube was resistively heated using a steel coil, which was wrapped in both directions to avoid any unwanted magnetic fields. The temperature was carefully monitored using a thermo-couple attached to the sample holder in close proximity to the sample. The furnace was placed between the pole pieces of the magnet.

4.3.2 Magnetic characterisation.

Magnetic characterisation was carried out using a Vibrating Sample Magnetometer (VSM), which was first described by Foner [14], and is basically a comparator, which measures the difference in induction between a region of space with and without the specimen. It therefore gives a direct measure of the magnetisation *M*. Fig. 4.10 is a schematic of the mechanism of a VSM. The sample is oscillated vertically in a region of uniform field, and if the sample if driven by a loudspeaker mechanism, the frequency is usually near 80Hz and the amplitude is 0.1-0.2mm. The AC signal induced in the pick-up coils (according to the Faraday law of electromagnetic induction) by the magnetic field of the sample is compared with the signal

from a reference specimen, and is converted to a number proportional to the magnetic moment. The advantages of this technique are that it is non-destructive, has a high sensitivity, and is easy to operate.

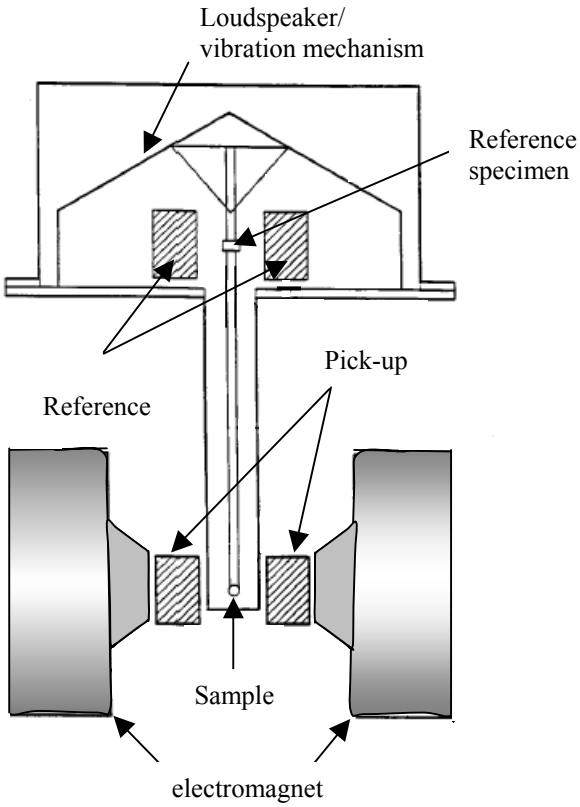

Fig. 4.10 *Schematic diagram of a Vibrating Sample Magnetometer (VSM). (After Ref [15]).*

The system is designed to measure small samples with high accuracy (less than 4 by 4mm). For larger samples a calibrated correction is required in order to determine the magnetisation values. However, a comparative analysis of other magnetic properties including coercivity and the magnetisation reversal process is always possible.

4.3.3 Structural characterisation.

Scanning probe microscopy (SPMs) consists of microscopy forms that are used to measure the properties of surfaces. There are many different types of SPMs including atomic force microscopes (AFM), scanning tunnelling microscopes (STMs), and magnetic force microscopes (MFMs). A review of SPMs can be found in [16]. This section will describe AFM used in tapping mode and contact mode, both of which were used for this thesis work. The first commercially available AFM, the NanoScope® AFM (Digital Instruments) was introduced in 1989.

AFM was used throughout this thesis work to probe and map the topolography of the patterned samples using a cantilever with a sharp tip on the end. The two different modes of AFM are shown in Fig. 4.11. Contact mode uses silicon nitride tips probes, which are soft enough to be deflected by very small forces and have a high enough resonant frequency not to be susceptible to vibrational instabilities. The tip is scanned across the sample surface while monitoring the change in the cantilever deflection with a split photodiode detector. A feedback loop maintains a constant deflection between the cantilever and the sample by vertically moving the scanner at each (*x,y*) data point to maintain a "setpoint" deflection. By maintaining a constant cantilever deflection, the force between the tip and the sample remains constant. The distance the scanner moves vertically at each (*x,y*) data point is stored by the computer to form the topographic image of the sample surface.

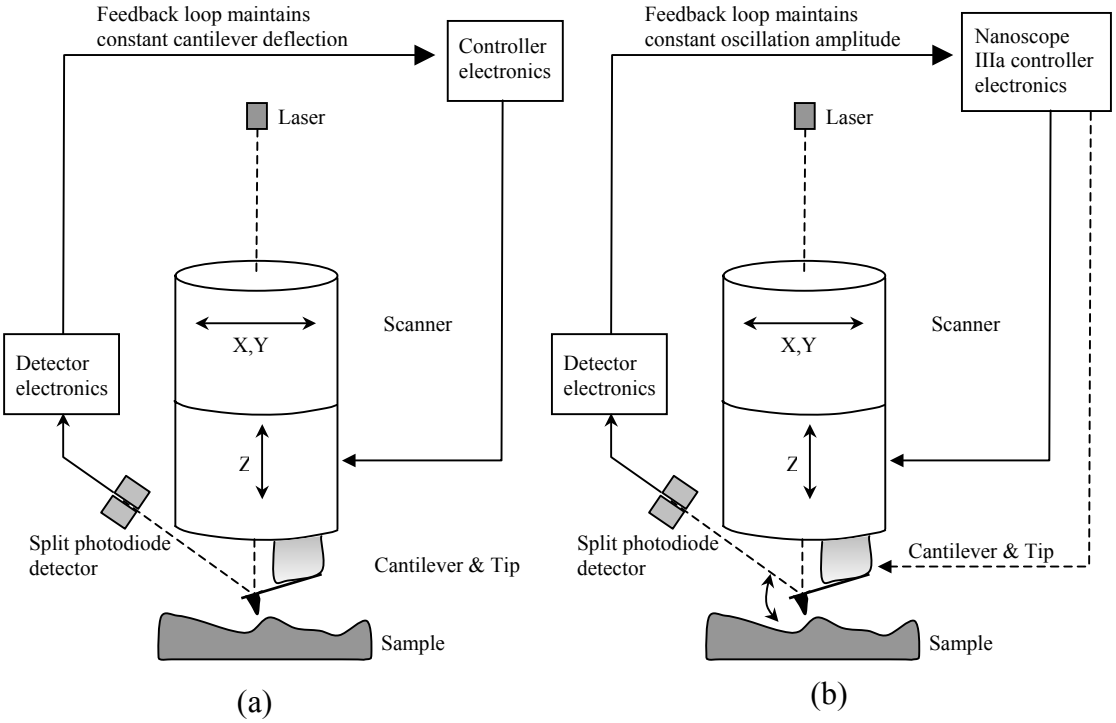

Fig. 4.11 *Schematic diagram showing (a) AFM contact mode, and (b) AFM tapping mode. (After Ref. [16]).*

In tapping mode silicon probes are used, which are much stiffer than the silicon nitride probes, resulting in larger force constants and resonant frequencies. Tapping mode operates by scanning a tip attached to the end of an oscillating cantilever across the sample surface. The cantilever is oscillated at or near its resonant frequency with amplitude ranging typically from 20nm to 100nm. The frequency of oscillation can be at or on either side of the resonant frequency. The tip lightly "taps" on the sample surface during scanning, contacting the surface at the bottom of its swing. The feedback loop maintains constant oscillation amplitude

by maintaining a constant RMS of the oscillation signal acquired by the split photodiode detector. The vertical position of the scanner at each (*x,y*) data point in order to maintain a constant "setpoint" amplitude is stored by the computer to form the topographic image of the sample surface. By maintaining constant oscillation amplitude, a constant tip-sample interaction is maintained during imaging. The *x*- and *y*-axis topographic resolution for most SPM scanning techniques, including AFM, is typically 2 to 10nm. The z-axis resolution is better than 0.1nm.

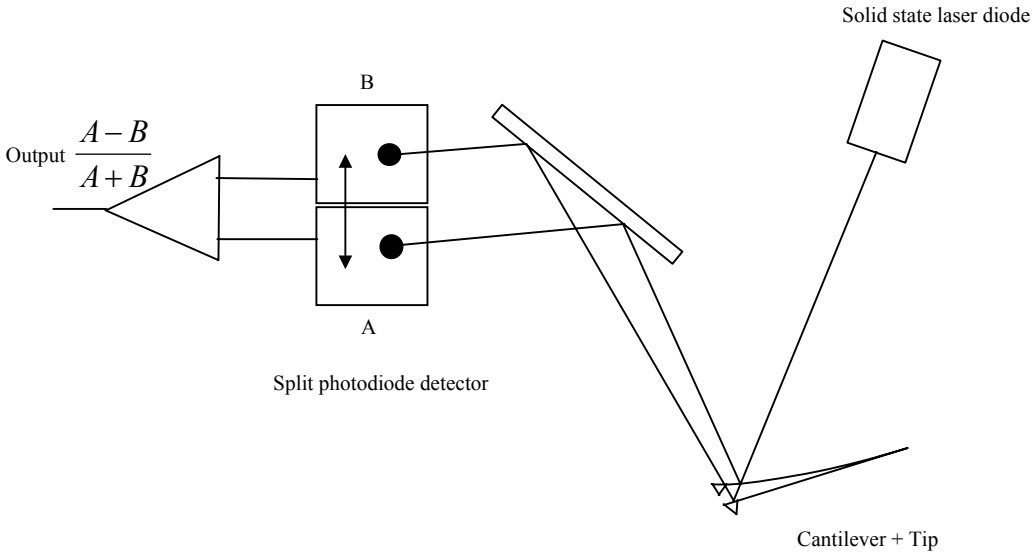

Fig. 4.12 *The mechanism of "beam deflection" detection for both contact and tapping mode. (After Ref. [16]).*

Fig. 4.12 shows the mechanism of "beam deflection" detection for both contact and tapping mode. Laser light from a solid state diode is reflected off the back of the cantilever and collected by a position sensitive detector (PSD) consisting of two closely spaced photodiodes whose output signal is collected by a differential amplifier. The angular displacement of the cantilever results in one photodiode collecting more light than the other photodiode, producing an output signal (the difference between the photodiode signals normalized by their sum), which is proportional to the deflection of the cantilever. This system can detect cantilever deflection < 1Å, and the long beam path (several cm) amplifies changes in the beam angle.

The advantages of contact mode include the high scan speeds, it is the only AFM technique which can obtain "atomic resolution" images, and it is particularly good for samples with extreme changes in vertical topography. The mode was used for scanning the nanopatterned samples, which required accurate vertical profile analysis over small lateral distances.

Tapping mode was used for the larger micropatterned samples, due to the better lateral resolution.

A wide variety of analysis functions are available in the off-line menu for measuring captured SPM images. The two techniques most commonly used in this thesis were:

- Section analysis

Depth, height, width and angular measurements can be easily made using this analysis technique.

- Depth analysis

The depth feature may be used to make automated depth histogram measurements over many images.

4.3.4 Magnetic Domain Imaging.

The Bitter technique makes use of 'magnetic liquids', which are colloidal suspensions of very small magnetic particles, usually of a ferrite such as Fe_3O_4, in a carrier liquid, which may be water or an organic solvent. Stray fields are present near the surface of the ferromagnet, which are strongest along the lines where domain walls meet the surface. When a drop of magnetic liquid is placed on the surface, the particles tend to delineate the domain walls, making the domain pattern observable under a microscope. Bitter pattern imaging has been reviewed by Kittel and Galt [17] and Craik [18]. For the purpose of this thesis work, commercially available water-based Ferrofluids® was used, which consists of roughly isometric magnetite particles of about 10nm diameter, covered with various surfactants. The sensitivity of Bitter colloids can be enhanced by an external field perpendicular to the surface of the sample. The resolution of the Bitter technique reaches easily 100nm and is limited by the particle size of non-agglomerating colloids (~10nm).

References

[1] S.A. Campbell, *The Science and Engineering of Microelectronic Fabrication*, **Chapter 11**, 274, Oxford University Press, Inc. (1996).

[2] S.A. Campbell, *The Science and Engineering of Microelectronic Fabrication*, **Chapter 12**, 294, Oxford University Press, Inc. (1996).

[3] S.A. Campbell, *The Science and Engineering of Microelectronic Fabrication*, **Chapter 10**, 246, Oxford University Press, Inc. (1996).

[4] J. Melngailis, *J. Vac. Sci. Technol. B*, **Vol. 5**, No. 2, 469, Mar/ April (1987)

[5] S. Reyntjens, R. Puers, *J. Micromech. Microeng*. **11**, 287 (2001)

[6] D.K. Stewart, A.F. Doyle, *J.D. Casey Jr, Proc. SPIE*, **2437**, 276 (1995)

[7] S. Reyntjens, D. De Bruyker, R. Puers, *Proc. 1998 Microsystem Symp.*, 125 (1998)

[8] B.W. Ward, N.P. Economou, D.C. Shaver, J.E. Ivory, M.L. Ward, L.A. Stern, *Proc. SPIE*, **923**, 92 (1988)

[9] J. Glanville, *Solid State Technol*. **32**, 270 (1989)

[10] D.K. Stewart, L.A. Stern, G. Foss, G. Hughes, P. Govil, *Proc. SPIE*, **1263**, 21 (1990)

[11] J.J. Thomson, Proc. *Cambridge Phil. Soc*., **11**, 120 (1901).

[12] K. Fuchs, Proc. *Cambridge Phil. Soc*., **34**, 100 (1938).

[13] E.H. Sondheimer, *Advan. Phys*., **1**, 1 (1951).

[14] S. Foner, *Rev. Sci. Inst.*, **30**, 548 (1959).

[15] S. Foner, *J. Appl. Phys.*, **79**, 4740 (1996).

[16] Digital Instruments Veeco Metrology Group, Training Notebook (1999), http://www.veeco.com/html/library.asp

[17] C. Kittel, J.K. Galt, *Ferromagnetic Domain Theory, in Solid State Physics* **Vol. 3**, (F. Seitz and D. Turnbull Eds.), 437-564, Academic Press, New York (1956).

[18] D.J. Craik, *The Observation of Magnetic Domains, in Methods of Experimental Physics*, **Vol. 11**, (R.V. Coleman ed.) 675-743, Academic Press, New York (1974).

New ideas pass through three periods: *It can't be done. *It probably can be done, but it's not worth doing *I knew it was a good idea all along ! *Arthur C. Clarke*

Chapter 5

Control of the Switching Properties of Magnetic Thin Films and Spin Valve Devices by Patterning.

The effects of patterning highly anisotropic repeating structures in soft magnetic thin films have been examined. Arrays of wires with equal mark/space ratios were patterned in resist using optical lithography. Broad beam ion milling was used to etch narrow (3μm) and wide (4mm) regions in $Ni_{80}Fe_{15}Mo_5$ thin films. The results show that the wider regions dominate the magnetisation reversal, and the coercivity increases by a factor of ten along the wire axis when the wider regions are removed. The results suggest the possibility of designing structures which can be engineered to reverse domains in narrow wires within a controlled field range. Measurements were also carried out for partial milling through the thickness of the wire array structures to assess the dependence of the magnetic properties on the degree of interconnection between the wires. These structures show a progressive increase in coercivity and a transition between single and two-stage switching with increasing milling depth. A similar micropatterning technique has been applied to unpinned ($Ni_{80}Fe_{20}$/Cu/$Ni_{80}Fe_{20}$) pseudo spin valve (PSV) structures in order to enhance the coercivity of one of the ferromagnetic layers; the increased coercivity induced by patterning changes the natural similarity of the magnetic layers and the completed structure exhibits a small spin valve response.

5.1 Motivations

There has been a great deal of interest in artificially "engineering" the magnetic properties of thin film magnetic microstructures by altering the lateral size [1-12]. Induced anisotropy is an important parameter for controlling the magnetisation of thin films. Although anisotropy can be induced by a variety of different techniques, the present generation of devices based on the giant magnetoresistive (GMR) effect makes use of the exchange anisotropy induced in ferromagnetic layers by contact with antiferromagnetic (AF) materials such as IrMn. A practical disadvantage of this technique is the reduction in the pinning strength as the temperature is increased as discussed in recent reviews of exchange anisotropy [13] and synthetic AF pinning in spin valves [14].

The initial experiments in this chapter have been designed to investigate how the magnetisation processes of materials can be controlled by patterning. In order to simplify the experiments, $Ni_{75}Fe_{20}Mo_5$ was chosen as the material to pattern because it has a low value of crystalline anisotropy. By minimising this energy term it is possible to investigate how domain wall motion and domain rotation can be influenced by patterning. Obtaining a thorough understanding of these two mechanisms will help to design tailored magnetic devices for specific applications. The pattern chosen for these experiments consists of long thin ferromagnetic wires, which represent the extreme case of shape anisotropy. The initial experiments in this chapter investigate the magnetisation reversal of structures containing both high and low shape anisotropy regions. This allows an investigation of the gradual change from two- to one- dimensional magnetism. The second part of this chapter investigates the change in the hysteresis by partially patterning through the thickness of the pseudo spin valve (PSV), which creates shape anisotropy. The milled depth between the wires affects the magnetisation reversal by varying the degree of interconnection. The final part of the chapter investigates patterning one of the ferromagnetic layers in an unpinned PSV with the aim of introducing a difference in the coercivities of the two ferromagnetic layers in the structure. Transport and magnetisation measurements were performed in order to characterise the PSVs. These preliminary investigations were carried out using optical lithography to enable direct comparison between magnetic and transport measurements.

5.2 Laterally patterned thin films.

Three 10mm by 5mm silica substrates were prepared with approximately 250nm thick $Ni_{75}Fe_{20}Mo_5$ film sputter deposited on top. (The samples were sputtered under the same conditions; the sample to target distance was 90mm, the deposition power was 30W, the pressure was 0.3Pa and the deposition time was 40 minutes). The VSM was calibrated using a Ni sample of known saturation. The first sample was then placed in the VSM and hysteresis

measurements were carried out for different orientations of the chip with respect to the applied field. At 0° the magnetic field was along the 10mm length of the chip, and at 90° it was along the 5mm width.

The second sample was put in a beaker of acetone and cleaned for 5 minutes in the ultrasonic cleaner. It was then washed with propanol using a spray gun, and dried using an air gun. A few drops of photoresist (5214) were deposited onto the surface of the sample. The sample was spun at 5000rpm for 30 seconds to spread the photoresist across the sample, and baked at 100°C for one minute to remove any moisture. Contact photolithography was used to remove the edge bead, and then the sample was baked again to remove any moisture. The chip was patterned into an array of 5mm long by 3μm wide wires, and the spacing between the wires was 3μm. Unpatterned rectangular regions of approximately 2mm by 4mm remained at either end of the wires. Fig. 5.1 (a) shows a schematic of the patterned wire array with unpatterned regions at either end of the wires. Below the schematic diagram there is a table summarising the lithographic technique.

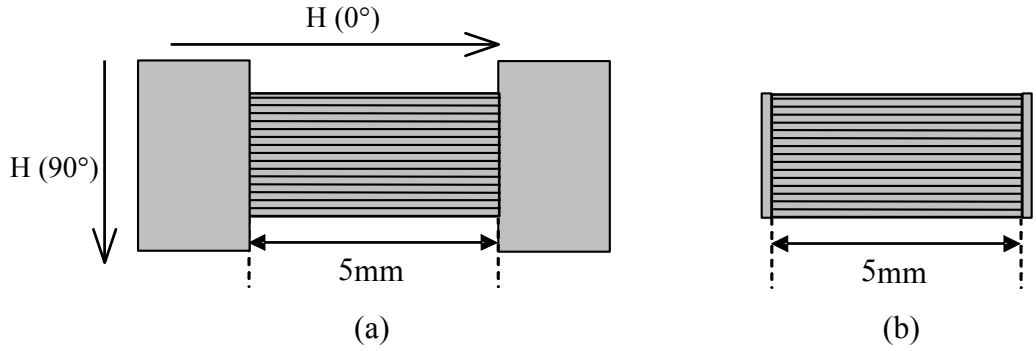

Process step	Exposure	Developing	Developing
	Time(s)	Type*	Time(s)
Edge bead removal	20	4:1	20
Patterning wires	8	3:2	13

* The type of developer is in terms of parts developer to parts water.

Fig 5.1 *(a) is a schematic diagram showing the patterned $Ni_{75}Fe_{20}Mo_5$ film with a wire array structure at the centre and with unpatterned rectangular regions at the ends of the wires. The direction of the applied field at 0° and 90° is shown. (b) is a schematic diagram showing the patterned $Ni_{75}Fe_{20}Mo_5$ film with the unpatterned regions at the end of the wires removed. The table summarises the lithographic technique.*

After lithographic patterning, the sample was loaded into the argon ion miller and the chamber was pumped down to 4×10^{-6}mbar. The sample was positioned directly in front of the source and rotated during milling to obtain a uniform etch. Milling was carried out for 60mins to ensure that the sample was milled through the $Ni_{75}Fe_{20}Mo_5$ layer to the silica substrate. The

beam current was maintained at 10mA, and the accelerator voltage and discharge voltage were 70V and 41V respectively. The pressure in the chamber was 2.1×10^{-4}mbar during milling. After milling the sample was cleaned to wash away the remaining photoresist, and examined under the microscope. Magnetic hysteresis measurements were then carried out as the orientation of the sample was changed with respect to the applied field.

For the third chip, the same lithography process was carried out as shown above. After milling, a second photoresist layer was spun on using the same speed and time as above. After baking, contact photolithography was used to remove the resist from the rectangular regions on the chip. The same exposure and developing times were used as for edge bead removal. The sample was loaded again into the OAR, and milled for another 60mins to remove the unpatterned regions. A schematic diagram of the third chip is shown in Fig. 5.1 (c) with the rectangular regions at either end of the wires removed. (A small overlap of approximately 20μm remains at the end of the wires). Topography scans were carried out using the AFM, and hysteresis measurements were taken at different orientations of the sample with respect to the applied field. The AFM showed that the thickness of the magnetic film was ≈265nm. Fig. 5.2 (a) shows the magnetisation versus field for the wire array with the field applied at 30°, 70°, and 80° to the length of the wires. Only half of the hysteresis loops are shown for clarity.

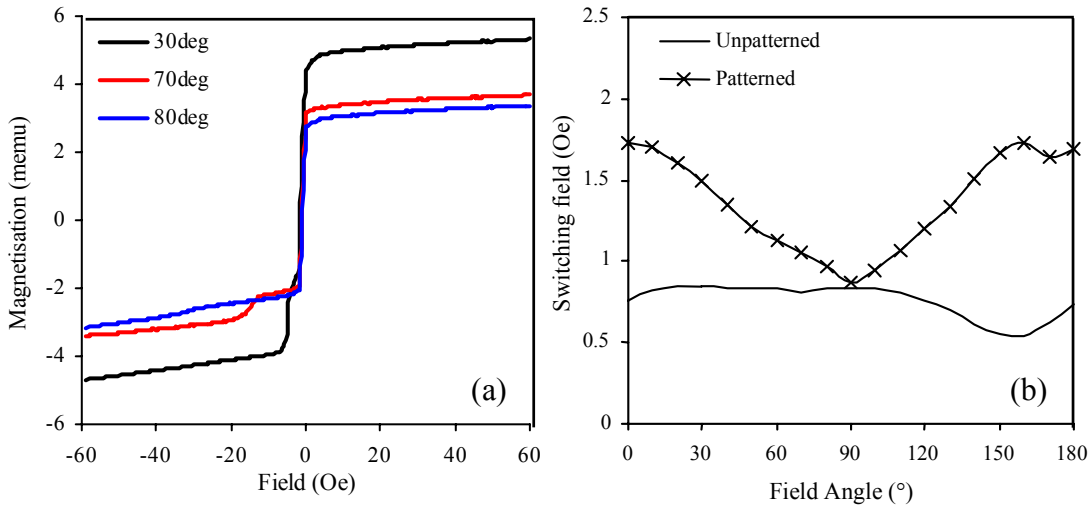

Fig 5.2 *(a) Magnetisation reversal graphs for the $Ni_{75}Fe_{20}Mo_5$ film with a 5mm by 3μm wire array patterned through the thickness. Only half of the hysteresis is shown for clarity. The three graphs represent three angles of applied field relative to the length of the wire array. (b) Shows the initial switching field versus applied field angle for the unpatterned and patterned $Ni_{75}Fe_{20}Mo_5$ thin film. The patterned structure consisted of an array of 5mm long by 3μm wide wires.*

There appears to be two M/H loops superimposed upon one another, for example for the 30° hysteresis there is an initial magnetisation reversal at ≈2Oe and another change in susceptibility at ≈5Oe. The sample behaves this way because the pattern consists of two parts; a highly anisotropic array of wires and a low anisotropy unpatterned region. The lower coercivity corresponds to the magnetisation reversal of the unpatterned part, and the higher coercivity is the reversal of the ferromagnetic wires. Similar work by Lee et al. [16] studied the domain nucleation processes in mesoscopic $Ni_{80}Fe_{20}$ wire junctions. Each wire consisted of a wide region (w_1=5μm) and a narrow width (w_1=1,2μm), both of equal length 200μm. Magnetic force microscopy and micromagnetic calculations showed that several domain walls nucleate at the wider part and are trapped in the junction area. This implies that domain nucleation at the junction of the wire initiates magnetisation reversal in the narrow half. The hysteresis graphs in Fig. 5.2 (a) show that the susceptibility of the wires decreases with increasing angle, and the switching field of the wires increases significantly with increasing angle. Fig. 5.2 (b) shows how the initial switching field changes with the angle of the applied field for the unpatterned and the partially patterned samples. The switching field of the unpatterned film remains approximately the same ±0.15Oe as the field angle is varied between 0° and 180°. However, the partially patterned film shows a maximum switching field at 0° and 180°, and a minimum at 90°. The difference between the maximum and minimum is ≈1Oe, which indicates a small change in the switching field of the unpatterned region. The switching field (H_s) of a multidomain structure is the sum of the fields required for nucleation and propagation of the domains through the sample, given by $H_s=H_n+H_p$, where H_n is the nucleation field and H_p is the propagation field. In this case, H_s is changing with angle due to a change in the propagation field H_p, and the difference can be explained by considering that the domain wall movement is perpendicular to the direction of the applied field. In other words, when the field is applied along the wire axis the domain walls are pinned by the ends of the wires during the magnetisation reversal. When the field is applied perpendicular to the wire length, there is no interaction with the end of the wires and the switching field is similar to the unpatterned film.

Fig. 5.3 (a) shows the hysteresis at 70° for the partially patterned and fully patterned thin films. It is possible to see that when the sample is fully patterned the coercivity increases and the hysteresis shows a single loop. The switching field of the wire array part of the partially patterned film corresponds to the coercivity of the fully patterned sample. Fig. 5.3 (b) shows the switching field versus orientation for the unpatterned, partially patterned and fully patterned samples. The coercivity of the fully patterned wire array is much larger, and also the shape of the graph with applied field angle is different. The coercivity is a minimum at 0 and 180°, a maximum and 80° and decreases sharply at 90°. The change in the coercivity can be

better understood by looking at Fig. 5.4, which shows the hysteresis graphs at 0°, 80° and 90° applied field orientations.

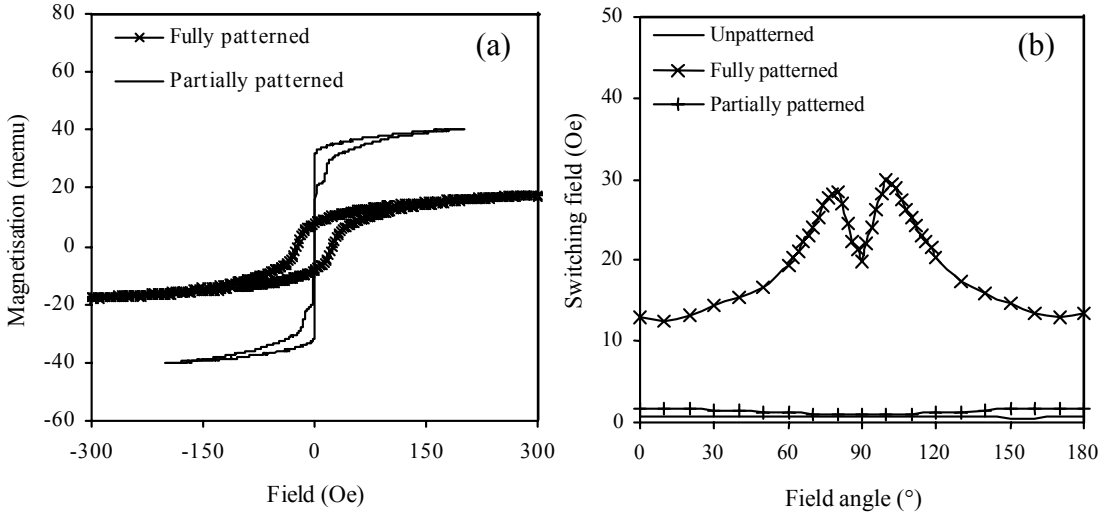

Fig 5.3 *(a) Magnetisation hysteresis curves at 70° for the partially patterned and fully patterned $Ni_{75}Fe_{20}Mo_5$ thin films. (b) Switching field versus angle for the unpatterned, partially patterned and fully patterned $Ni_{75}Fe_{20}Mo_5$ thin films.*

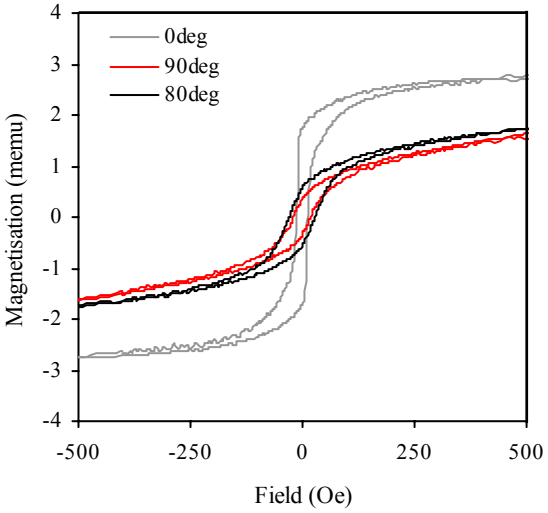

Fig 5.4 *(a) Magnetisation reversal graphs at 0°, 80° and 90° for the 3μm wire array patterned in the $Ni_{75}Fe_{20}Mo_5$ thin film.*

At 0° it is possible to see the sharp change in magnetisation, which is normally observed when the magnetisation reversal occurs by domain wall motion. At 80° the magnetisation reversal occurs by a combination of both domain wall motion and rotation, and the overall coercivity is larger. At 90° there is a much less sharp transition, and the magnetisation reversal is dominated by rotation with increasing field until it reaches saturation. However, the reversal process is not pure rotation because there is still some area under the M/H loop.

The saturation field at 90° is increased due to the larger demagnetising factor across the width. For simplicity, we can consider the cross section of the strip to be elliptic so that the demagnetising factors N_α can be assigned to the three principal axes [17]. These demagnetising factors are [18] $N_w=t/(t+w)\approx t/w$ across the width w; $N_t=w/(t+w) \approx 1$ through the thickness; and zero along the axis of the wire. The applied field was in the plane of the film so N_t has no relevance, and N_w=0.08. The demagnetising field is the magnitude of the magnetic saturation multiplied by the demagnetising factor, since the gap between the wires is large enough for the magnetostatic interactions to be negligible [3]. The magnetic saturation of $Ni_{80}Fe_{15}Mo_5$ is $0.63\times10^6 Am^{-1}$ [19], this produces a demagnetising field of 630Oe when the film is saturated along the width.

5.3 Patterning through the thickness of thin films.

Plain $Ni_{75}Fe_{20}Mo_5$ films of thickness 100nm were deposited on 10mm × 5mm Si substrates by ultra-high vacuum DC magnetron sputtering. The deposition chamber walls were cooled below -100°C, and the Ar pressure during deposition was kept constant at 0.5Pa. The substrate to target (S-T) distance was 80mm, and the system base pressure was better than 3×10^{-9} mbar. The thicknesses of the films were determined by the deposition of a calibration sample with the same S-T distance and Ar pressure, which was measured by AFM.

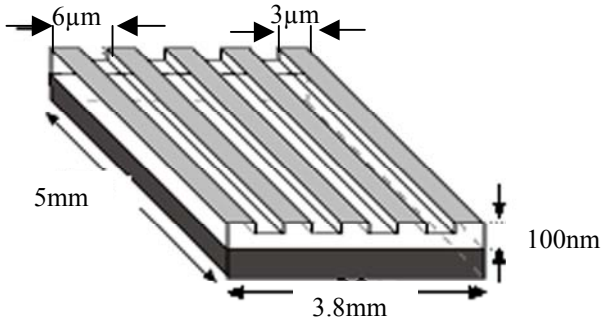

Fig. 5.5 *A schematic diagram of an array of 3μm wide wires with equal mark/space ratio.*

The samples were patterned into 3μm wide wires arrays with equal mark space ratios using contact optical lithography and ion beam milling, as shown in Fig. 5.5. The wires were 5mm long and the array extended over a distance 3.8mm. The same lithographic patterning technique was used as summarised in Fig. 5.1. Before milling the chamber pressure was pumped down to 4×10^{-6}mbar. Throughout the milling the chamber was kept at a constant 2.1×10^{-4}mbar, the beam current was maintained at 10mA, and the accelerator voltage and discharge voltage were 70V and 41V respectively. The aim of the experiments was to

investigate the effect of partially milling the gaps between the wires so that a continuous film remains (see Fig. 5.5). Successive magnetic measurement and milling sequences were performed on the samples. Magnetisation measurements were carried out using a Princeton Measurements Corporation vibrating sample magnetometer (VSM), with fields applied along the length of the wires (the easy axis).

The change in the magnetisation of the 100nm $Ni_{75}Fe_{20}Mo_5$ film was measured as the milling depth of the magnetic material between the wires increased. Fig. 5.6 (a) shows the change in the magnetisation versus applied field for the same sample as the amount of material between the wires was successively removed; only half of the hysteresis loop is shown for clarity. As the thickness of the residual material (t) between the wires is reduced compared to the original thickness (t_0), the magnetisation begins to show a double coercivity. This indicates that the patterned structure is becoming magnetised in two stages.

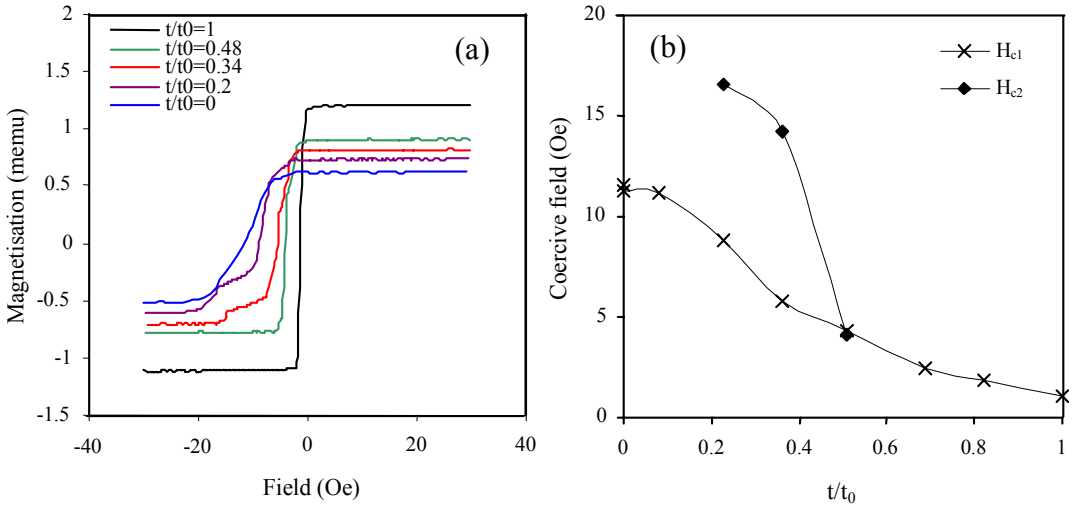

Fig. 5.6 *(a) Magnetisation versus applied field for a $Ni_{75}Fe_{20}Mo_5$ sample with decreasing interconnection between the patterned wires: t/t_0 = 1 (largest saturation moment), 0.48, 0.34, 0.2 and 0 (highest coercivity). (b) Coercive field versus residual thickness between the wires for a $Ni_{75}Fe_{20}Mo_5$ sample with decreasing interconnection between the patterned wires: crosses indicate the zero moment coercive field, closed symbols the field at which a second magnetic transition occurs.*

At very low values of t the hysteresis loop returns to a single transition, as show in Fig. 5.6 (b). The initial reversal field H_{c1} increases with increasing milling depth and shows a maximum enhancement of a factor of 10. The second switching field H_{c2} also increases with increasing milling depth and shows a maximum enhancement of a factor of 4. Fig. 5.6 (a) and (b) show that it is possible to greatly increase the coercivity of a permalloy thin film by patterning a highly anisotropic structure through the thickness.

A simple mathematical model was used to investigate the double switching field response of the sample at large milling depths with respect to the volume magnetisation of each part of the hysteresis. The aim of the model was to determine whether the patterned and unpatterned regions of the sample were reversing independently in an applied field. Two different configurations were investigated as shown in Fig. 5.7. In Fig. 5.7 (a) the cross section of the sample is divided into β representing the patterned wire array, and α the unpatterned area. In (b) the cross section is divided into β representing the patterned wire array plus the material beneath the wires, and α the material between the patterned wires. A single switching behaviour is observed until the milling approaches half the depth, although a larger field is required to complete the reversal as the milling depth increases.

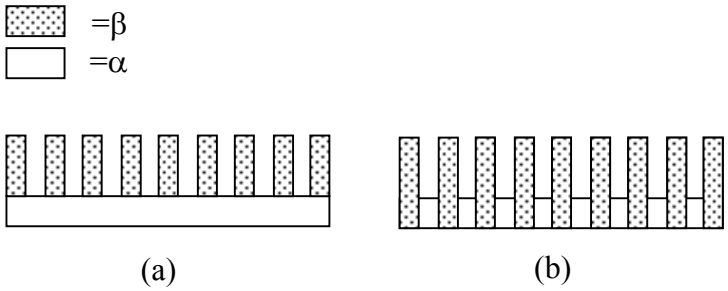

Fig. 5.7 *The two configurations of the model used to investigate the double switching response of the patterned film at large milling depths. (a) β represents the patterned wire array and α is the unpatterned region. (b) β is the patterned wire array plus the material directly below and α is the region between the wires.*

This could be due to the larger field required to move the domain walls past the partially patterned wires. Until half the depth is reached, the entire structure is coupled together during the magnetisation reversal. For the measurements showing a double coercivity, the relative proportion of magnetisation from the hysteresis was compared to the cross sectional areas in Fig. 5.7 (a) and (b). It was calculated that the volume magnetisation of α and β do not correspond directly with the hysteresis results for either configuration (a) or (b). In other words the model shows that the patterned and unpatterned regions of the sample do not reverse completely independently at any part of the hysteresis. However the results also show that for small milling depths the reversal is most similar to Fig. 5.7 (a) where the unpatterned regions behaves more like a continuous film. For large milling depths the magnetisation reversal is more similar to (b), where the thick wire array dominates the magnetisation reversal of the material directly beneath and α is restricted to the material between the wires, which shows an increased coercivity as the thickness is decreased. The model shows that the

high field switching observed at large milling depths is most likely to be due to the reversal of the thin film layer between the patterned wires.

It is also important to consider the domain structure within the $Ni_{80}Fe_{20}$ thin film as the thickness is milled away. The literature shows that at a film thickness of 100nm Bloch walls have a lower energy than cross-tie or Néel walls. As the thickness is reduced cross-tie walls become more stable until ≈50nm when Néel walls form to reduce the magnetostatic energy. The widths of Bloch and Néel walls also vary in different ways with film thickness: the thinner the film the narrower the Bloch wall and the wider the Néel wall. Materials with wider domain walls tend to have a lower coercivity, although the results in Fig. 5.6 show that the increase in coercivity due to the shape anisotropy is larger than the effect of increasing the domain wall thickness.

5.4 NiFe Pseudo Spin Valve Measurements

Pseudo spin valve sandwiches were grown without a pinning layer using a production spin valve sputtering system (Nordiko 9606 Plasma Vapour Deposition (PVD) Sputter Deposition System) and with the structure: Ta(3nm)/$Ni_{80}Fe_{20}$(6nm)/Cu(2.2nm)/$Ni_{80}Fe_{20}$(15nm)/Ta(3nm). The anisotropy axes in the two ferromagnetic layers were perpendicular with respect to each other. The PSVs were diced into 10mm by 5mm samples, and then patterned into 4mm by 3.3mm rectangles using optical lithography and argon ion milling. The anisotropy axis of the thicker top ferromagnetic was along the length of the rectangular patterned structure.

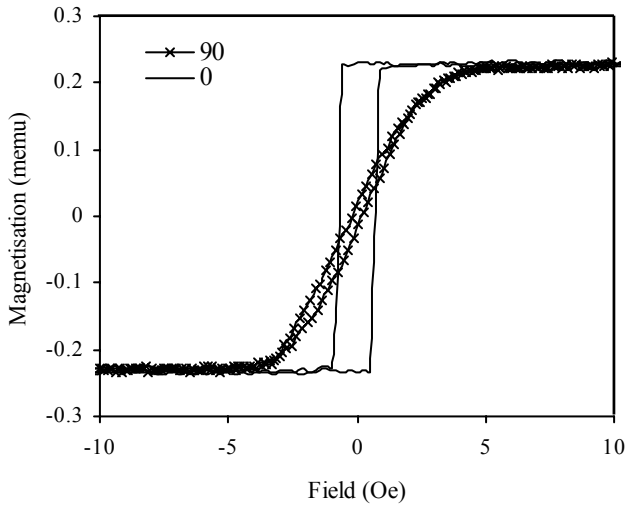

Fig. 5.8 *Magnetisation measurements of the rectangular 4mm by 3.3mm patterned pseudo spin valve along the length of the sample (0°) and along the width (90°).*

Magnetic hysteresis measurements were carried out on the patterned sample as shown in Fig. 5.8. Measurements were taken along the length (0°) and width (90°) of the PSV rectangle, and

the hysteresis loops show a single transition despite the presence of two ferromagnetic layers. The total coupling between the two ferromagnetic layers is the sum of the exchange interaction and the magnetostatic coupling across the nonmagnetic interlayer. Previous work has shown that magnetostatic coupling occurs in bilayers of the structure $Ni_{80}Fe_{20}/Cu/Ni_{80}Fe_{20}$, where the thickness of the copper interlayer is 10nm and the two ferromagnetic layers are 100nm thick [20]. The results showed the occurrence of quasi walls due to flux closure from the domain walls. The shape of the graphs in Fig. 5.8 is characteristic of the anisotropy in the thicker ferromagnetic layer, which is in the same direction as the applied field at 0° orientation. The hysteresis shows that the two ferromagnetic layers are coupled together and the magnetisation reversal is dominated by the anisotropy of the thicker (15nm) ferromagnetic layer. The $Ni_{80}Fe_{20}$(15nm) top layer of the spin valve sandwich was patterned with the same wire array pattern as in the previous section and milled to different depth to investigate the effect on the switching of the device. The spin valve structure chosen for these experiments had a deliberately thick top $Ni_{80}Fe_{20}$ layer to enable controlled milling trials. Fig. 5.9 shows a schematic of the 3μm wire array structure patterned into the top ferromagnetic layer of the pseudo spin valve, the anisotropy axes K_α and K_γ, of the layers were induced during sputter deposition.

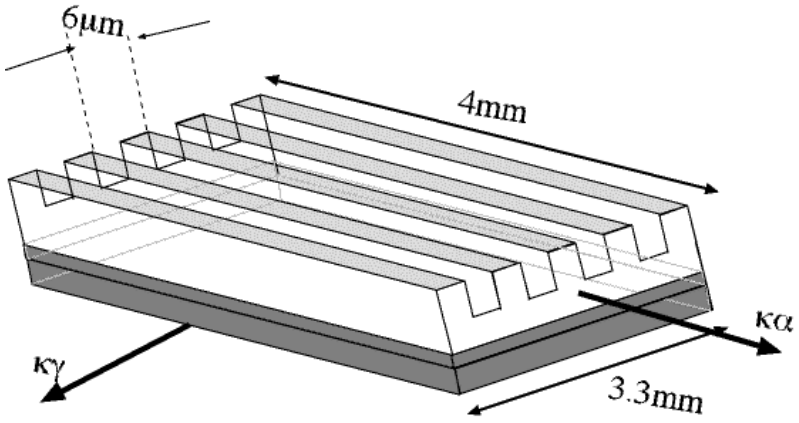

Fig. 5.9 *NiFe/Cu/NiFe pseudo spin valve with a 3μm wide wire array patterned into the top ferromagnetic layer. The diagram also shows the anisotropy axes, K_α and K_β of the two ferromagnetic layers, which were induced during sputter deposition.*

Magnetisation measurements were taken of the sample at different milling depths through the top ferromagnetic layer. The results for the spin valve device show a similar trend to the permalloy film, the coercivity of the patterned layer increases with increasing milling depths. For large milling depths the coercivity of the top layer becomes large enough to change the natural similarity of the ferromagnetic layers, and the magnetisation shows a double

coercivity. This can be seen in Fig. 5.10 for milling depths of 14.4 nm and 16.8 nm, where the field was applied along the length of the wires. The second coercivity increases by a factor of 8 with increasing milling depth through the top ferromagnetic layer.

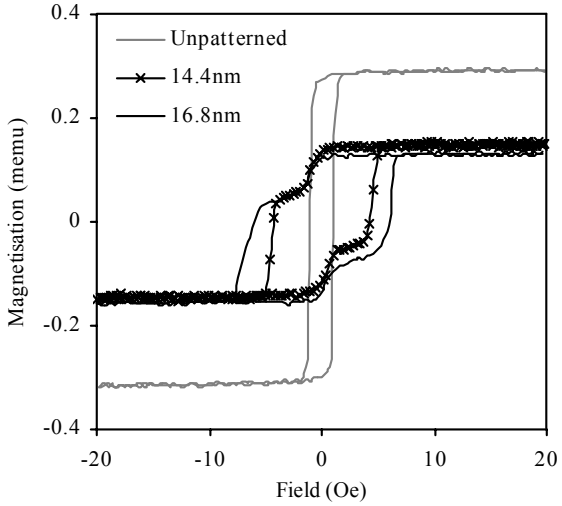

Fig 5.10 *Hysteresis measurements for pseudo spin valve samples with decreasing interconnection between the patterned wires in the upper ferromagnetic layer: milled depths are 14.4nm and 16.8 nm. At 16.8nm the structure is milled through to the Cu interlayer. The field was applied along the length of the wires.*

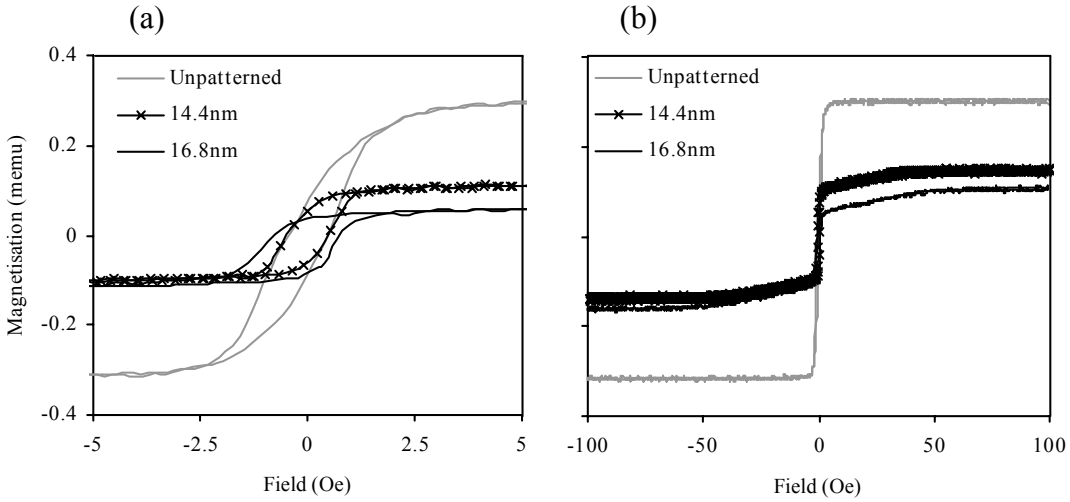

Fig 5.11 *Hysteresis measurements for pseudo spin valve samples with decreasing interconnection between the patterned wires with the field applied perpendicular to the length of the wires, and (a) at low fields and (b) high fields.*

Fig. 5.11 shows the hysteresis measurements for different milling depths with the field applied perpendicular to the length of the wires for low (a) and high (b) fields. In this case, the field is applied along the anisotropy axis of the bottom unpatterned ferromagnetic layer. At

low fields (a) the hysteresis loop shows a small increase in coercivity, at higher fields (b) there is a distinct change in susceptibility before saturation. At a depth of 16.8nm, the magnetisation reversal at low fields corresponds to the switching of the unpatterned layer, which has become decoupled from the thicker ferromagnetic layer due to the difference in coercivity. The high field change in susceptibility corresponds to the reversal of the patterned ferromagnetic layer by magnetisation rotation.

The magnetoresistance of the samples was also measured by passing a DC current through the wires and measuring the change in resistance using a four-point probe technique as the field was applied along the length of the patterned wires. Fig. 5.12 (a) shows the MR response of the 16.8nm milled spin valve with the field applied along the wire axis, the magnetic response is also superimposed. Fig. 5.12 (a) shows that the initial magnetisation reversal corresponds to an AMR≈0.3% which turns into a GMR≈0.45% as the field is increased. Although the relative proportions of γ and α indicate towards the magnetisation reversal of the thinner (6nm) and thicker (15nm) ferromagnetic layers respectively, it was found that the proportions do not correspond directly with the dimensions of the two layers.

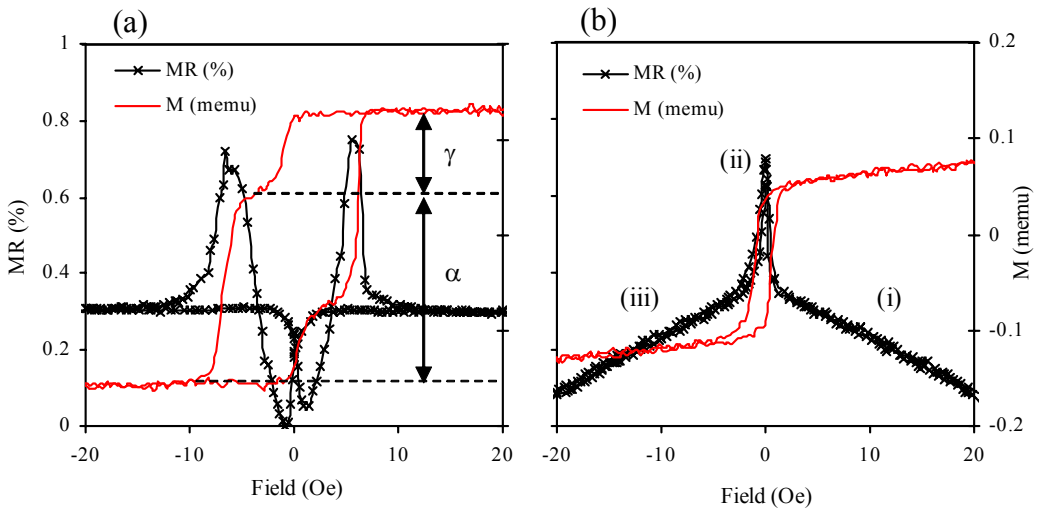

Fig. 5.12 *Magnetoresistance and magnetisation measurements of the pseudo spin valve sample milled to a depth of 16.8nm, the y-axis for the MR (%) is on the left and the y-axis for the Magnetisation (memu) is on the right. In (a) the field is applied along the wire axis. The insets γ and α indicate different regions in the magnetisation reversal. In (b) the field is applied perpendicular to the wire axis and the insets (i), (ii), and (iii) indicated different parts of the magnetoresistance measurement.*

Although the GMR signal indicates that the layers are decoupled, the hysteresis shows that the decoupling is only partial and antiparallel alignment between the two magnetic layers is not fully achieved. The decoupling is due to the increased coercivity of the patterned layer changing the natural similarity of the two ferromagnetic layers, and also due to the reduction in the moment of the top layer. The results show that the 6nm base layer switches at a considerably lower field than the patterned upper layer. The magnetoresistance changes sign once the unpatterned layer has reversed which is a clear manifestation of the desired GMR response. This positive resistance increase disappears once the patterned layer has reversed.

Fig. 5.12 (b) shows the magnetoresistance and magnetisation when the field is applied perpendicular to the wire axis. As the field is decreased from positive saturation field (i), the magnetisation rotation of the patterned layer is shown by an AMR in the magnetoresistance measurement. The GMR peak close to zero field (ii) is the switching of the unpatterned layer. As the field is increased to negative saturation field (iii) AMR is again seen which corresponds to the rotation of the patterned layer until the structure is saturated in the opposite direction. A larger field is required to saturate the patterned layer due to the large demagnetising field.

Minor loop magnetoresistance analysis was carried out on the spin valve as shown in Fig. 5.13. Transport measurements were taken up to reversal fields of -5Oe, -6Oe and -7Oe, the measurements are offset for clarity. The results show that the magnetisation reversal is completely reversible up to –5Oe. Using some simple mathematical analysis it was possible to calculate the maximum GMR and AMR of the PSV sample. The analysis makes the following assumptions:

(1) Up to -5Oe the only reversal process is the magnetisation rotation of the bottom layer.

(2) The MR response consists of an AMR and GMR component and can be described by the Eqn. (5.1)

$$MR = G\left[1-\cos^2\frac{\theta}{2}\right] - A\left[1-\cos^2\theta\right] \tag{5.1}$$

where G=maximum GMR and A=maximum AMR.

The relative magnetic volumes of the top (V_t) and bottom (V_b) layers were calculated from the dimensions of the sample, where $V_b+V_t=1$. The normalised magnetisation of the spin valve is given by Eqn. (5.2).

$$\frac{M(H)}{M_s} = \frac{M_s(V_b\cos\theta + V_t)}{M_s} = V_b\cos\theta(H) + V_t \tag{5.2}$$

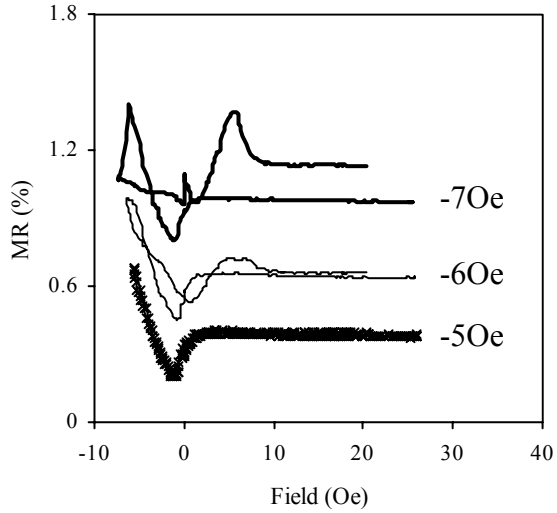

Fig. 5.13 *Minor loop magnetoresistance analysis carried out on the pseudo spin valve patterned through the top ferromagnetic layer. Analysis was carried out with reversal fields up to -5Oe, -6Oe and -7Oe, the graphs are vertically displaced for clarity.*

Where *M(H)* is the magnetisation for an applied field *H*, and M_s is the saturated magnetisation. By rearranging the equation it is possible to calculate cosθ, where θ represents the angle between the ferromagnetic layers.

$$\cos\theta(H) = \frac{\dfrac{M(H)}{M_s} - V_t}{V_b} \tag{5.3}$$

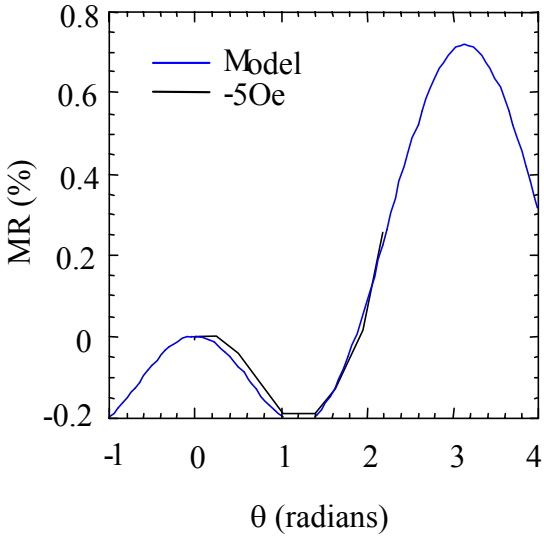

Fig. 5.14 *The magnetoresistance versus the angle between the magnetisation in the two ferromagnetic layers.*

The *M(H)* values were extracted from the hysteresis loop. These values give *θ(H)* through

Eqn. (5.3), and therefore the MR versus H plot from the -5Oe plot in Fig. 5.13, could be converted to MR versus θ as shown by the black curve in Fig. 5.14. In Fig. 5.14 the curve generated from Eqn. (5.1) and the converted MR versus θ data were superimposed, and the values of G and A were adjusted to fit the experimental results. It can be seen that the model fits well to the measured data, and the result predicts a maximum value of GMR=0.72% and AMR=0.51%.

5.5 Conclusions.

The initial experiments on plain permalloy films were performed in order to assess the extent to which lateral partial patterning could enhance the coercivity of the film. The results show that when the structure consists of a patterned wire array and an unpatterned region, the magnetisation reversal is predominantly determined by the wider region for fields applied parallel to the wire axis. The results imply that domain nucleation at the junction of the wire initiates magnetisation reversal in narrow part. These results are in agreement with previous work [16], which suggests the possibility of designing structures which can be used to "launch" reverse domains in narrow wires within a controlled field range.

The second set of measurements investigated partially patterning through the thickness of the ferromagnetic film. The results show that a maximum coercivity is achieved when the structure is fully milled through, which corresponds to a factor of ten enhancement in coercivity. These results show that it is possible to tailor the magnetisation reversal by patterning through the thickness as well as laterally.

The final measurements in this chapter investigated applying the patterning technique to create a pseudo spin valve. The results shown here demonstrate that even relatively course micron-scale patterning of one layer in an otherwise unpinned spin valve can create a small GMR effect. When a field is applied along the wire axis, a small AMR is seen due to the magnetisation reversal of the unpatterned layer. As the field is increased a GMR response is observed because the ferromagnetic layers have become decoupled due to the increased shape anisotropy in the top layer. When the field is applied along the wire width a small GMR response is seen at low fields due to the reversal of the unpatterned layer. A large field is required to saturate the sample because of the high demagnetising field across the width of the wires.

The work of McMichael et al. [15] has shown that nanoscale patterning induced by deposition onto a morphologically textured surface has a much more pronounced effect on the magnetic response and leads to a substantial GMR effect. The results indicate that it may be possible to extend this work to the nano-scale, which is more in line with the current demand for miniaturisation. Since the anisotropy generated by these processes is expected to have low

temperature dependence, this approach to spin valve design has considerable potential for high temperature device operation.

References

[1] C. Mathieu *et al.*, Appl. Phys. Lett. **70**, 2912 (1997)

[2] A. O. Adeyeye, J. A. C. Bland, C. Daboo, D. G. Hasko, and H. Ahmed, J. Appl. Phys. **79**, 6120 (1996)

[3] A. O. Adeyeye, G. Lauhoff, J. A. C. Bland, C. Daboo, D. G. Hasko, and H. Ahmed, Appl. Phys. Lett. **70**, 1046 (1997)

[4] C. Shearwood, S. J. Blundell, M. J. Baird, J. A. C. Bland, M. Gester, H. Ahmed, and H. P. Hughes, J. Appl. Phys. **75**, 5249 (1994)

[5] S. J. Blundell, C. Shearwood, M. Gester, M. J. Baird, J. A. C. Bland, and H. Ahmed, J. Magn. Magn. Mater. **135**, L17 (1994)

[6] K. Hong and N. Giordano, Phys. Rev. B **51**, 9855 (1995)

[7] K. Hong and N. Giordano, J. Magn. Magn. Mater. **151**, 396 (1995)

[8] A. Maeda, M. Kume, T. Ogura, K. Kuroki, T. Yamada, M. Nishikawa, and Y. Harada, J. Appl. Phys. **76**, 6667 (1994)

[9] M. S. Wei and S. Chau, J. Appl. Phys. **76**, 6679 (1994)

[10] J. F. Smyth, S. Schultz and D. R. Fredkin, D. P. Kern, S. A. Rishton, M. Cali, and T. R. Koehler, J. Appl. Phys. **69**, 5262 (1991)

[11] A. D. Kent, S. von Molnar, S. Gider, and D. D. Awschalom, J. Appl. Phys. **76**, 6656 (1994)

[12] J. I. Martin, J. Nogues, Ivan K. Schuller, M. J. Van Bael, K. Temst, C. Van Haesendonck, V. V. Moshchalkov, and Y. Bruynseraede, Appl. Phys. Lett. **72**, 255 (1998)

[13] A. E. Berkowitz, K. Takano, J. Magn. Magn. Mater. **200,** 552-570, (1999)

[14] Y. Sugita, Y. Kawawake, M. Satomi and H. Sakakima, J. Appl. Phys. **89**, 6919 (2001)

[15] R. D. McMichael, C. G. Lee, J. E. Bonevich, P.J. Chen, W. Miller, and W. F. Egelhoff, Jr, J. Appl. Phys. **88** (9), 5296 (2000)

[16] W. Y. Lee, C. C. Yao, A. Hirohata, Y. B. Xu, H. T. Leung, S. M. Gardiner, S. McPhail, B. C. Choi, D. G. Hasko, and J. A. C. Bland, J. Appl. Phys. **87** (6), 3032 (1996)

[17] J. H. Fluitman, Thin Solid Films, **16**, 269 (1973)

[18] J. A. Osborn, Phys. Rev., 67, 351 (1945)

[19] D. Jiles, Introduction to Magnetism and Magnetic Materials, pg 94, Chapman and Hall (1998)

[20] J. L. Prieto, P. Sánchez, C. Aroca, M. Maicas, E. López, M. C. Sánchez, J. Magn. Magn. Mater. **177-181**, 215 (1998)

La Buena suerte la buscas, la mala suerte te encuentra. (We have to chase good luck, but bad luck finds us). *José Luis Prieto*

Chapter 6

The Design, Building and Testing of an *In-situ* Magnetoresistance Measurement Rig in an Argon Ion Miller.

An in situ magnetoresistance test rig has been designed and built into an argon ion milling rig. The measurements from the rig allow direct analysis of the evolution of magnetic and electrical properties of ferromagnetic structures during patterning. This chapter describes the design, building and testing of the rig including; the fully rotating sample holder, the various coils for applying a field, the four-point resistance measurement set-up, the voltage offset amplifier and the signal transmission through the measurement.

6.1 Motivations

The previous measurements have shown that it is possible to change the natural similarity of two ferromagnetic layers in a PSV structure by patterning one of the layers to produce a small GMR response. The milling and electrical characterisation were done in separate steps, which proved to be an inefficient method for a number of reasons. It meant that either a series of samples needed to be prepared, milled to different depths and characterised individually, or the same sample was removed after milling, characterised and then put back into the argon ion miller. The disadvantage of the first technique is that there is always some variation between the different samples, for example a variation in the material properties from deposition or some variation in the lithography. The disadvantages of the second technique include that that it is very time consuming (≈2hrs to pump down to a good vacuum before milling), degradation of the PSV by oxidation, contamination or mechanical damage from the wire bonding to make electrical contact. It was decided that it would be ideal to design a technique to do *in-situ* measurements during milling. This meant that the same sample could be tested in a much cleaner and more efficient process. Many more milling steps could be carried out enabling trend graphs to be obtained on the variation of the resistance R during milling and also the change in resistance ΔR in the presence of an applied field. As previously described ΔR is a direct indication of the relative orientation of the magnetisation in the two ferromagnetic layers. As the dimensions are reduced the magnetic configuration will change from multi-domain to single domain and *in-situ* measurements will allow direct analysis of this change.

This chapter describes the design, testing and calibration of the *in-situ* magnetoresistance set-up which was used throughout this thesis.

6.2 The Electrical Set-up.

The aim of this *novel* experimental set-up is to enable *in-situ* magnetoresistance measurements during patterning by argon ion milling. In order to achieve this, a system for applying a magnetic field and measuring the change in resistance under vacuum ($\approx 4\times10^{-6}$ mbar base pressure) was designed. Fig. 6.1 is a schematic diagram showing the electrical set-up.

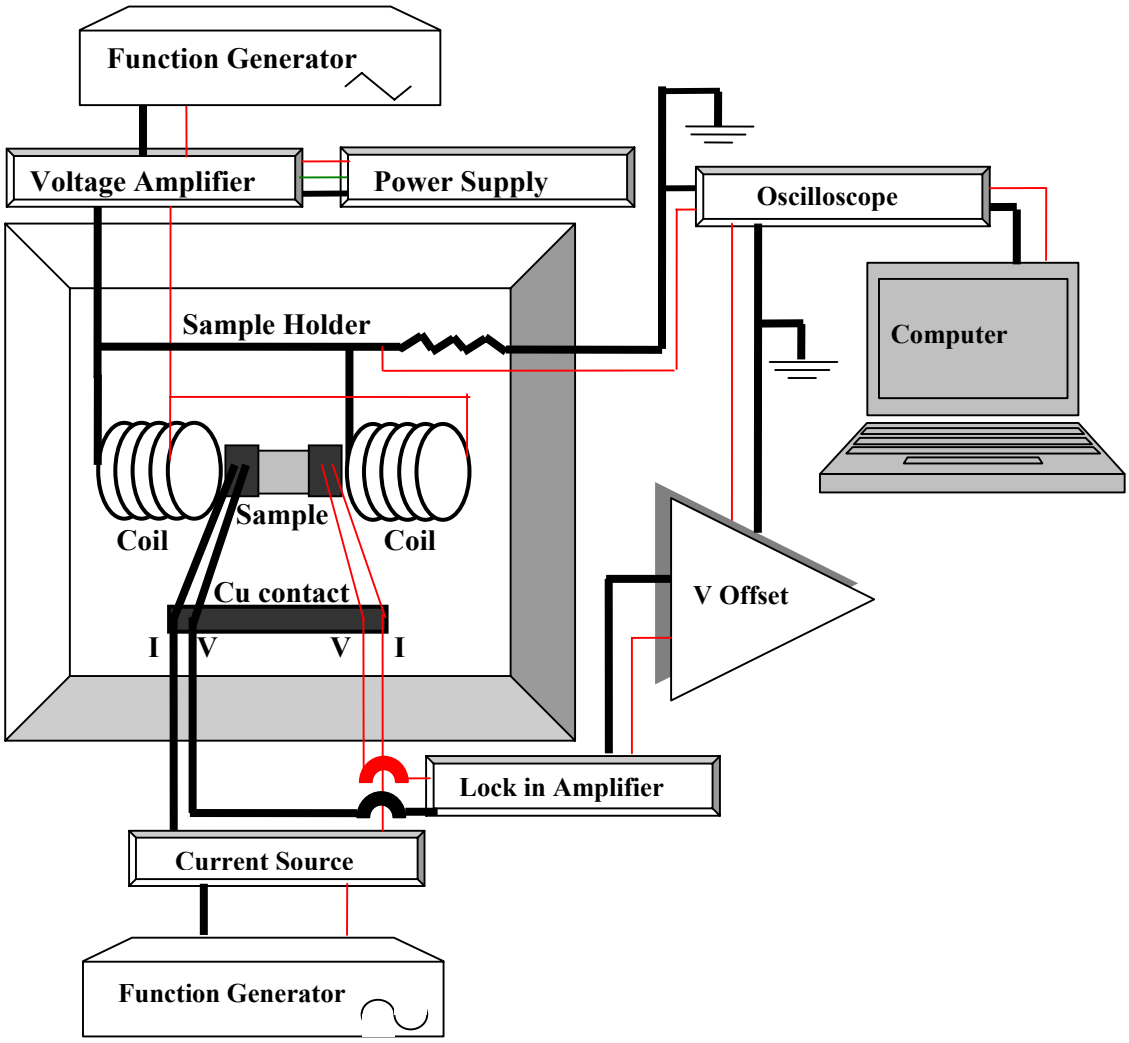

Fig. 6.1 *A schematic of the electrical set up for the in-situ magnetoresistance measurement rig.*

The sample is placed on the sample holder which can be fully rotated in the argon ion milling chamber and is water cooled to avoid any unwanted heating effects. A triangular wave is swept at a low frequency (0.05Hz) by the function generator through a current amplifier to the field coils on either side of the chip. The power operational amplifier LM675 was used for the

current amplifier set to a gain of 22. The LM675 was chosen because it is capable of delivering output currents in excess of 3 amps, operating at supply voltages of up to 60V. The circuit diagram for the voltage amplifier is shown in Fig. 6.2.

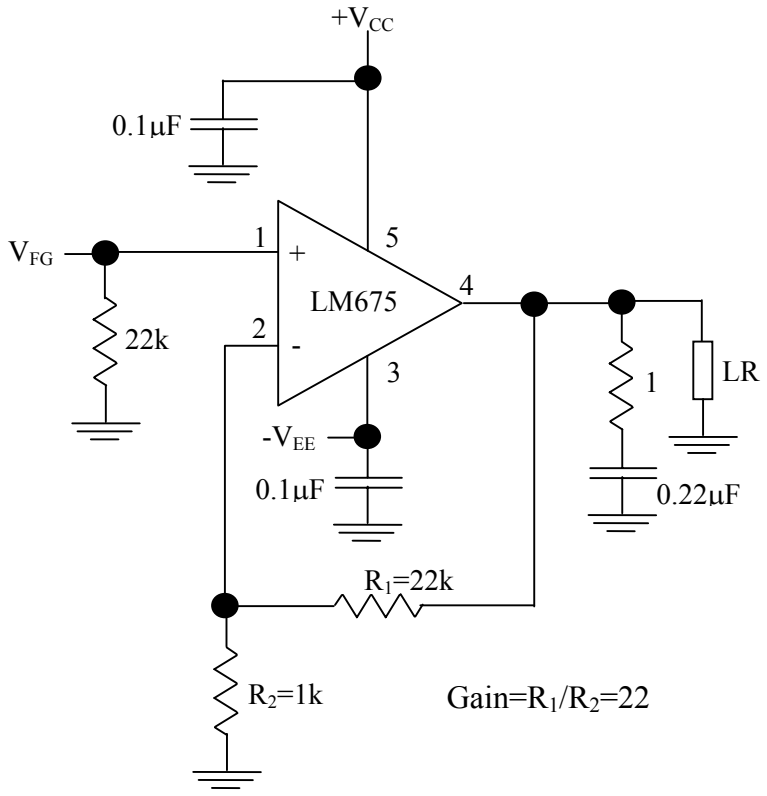

Fig. 6.2. *Circuit diagram for the voltage amplifier supplying current to the field coils [1].*

In the circuit diagram V_{FG} is the voltage from the function generator, and LR is the load resistance equal to the resistance of the field coils plus a resistor in series with the coils. The Tektronix digital oscilloscope measures the voltage across the series resistor to calculate the current through the coils; this gives a more accurate current measurement than measuring directly across the coils due to heating effects. Pre-calibration measurements were carried out in order to convert the current to field for the different field coils. The resistance of the chip is measured by depositing copper contact pads and using a four-point resistance measurement. A higher frequency function generator (1kHz) drives a sine wave current across the chip, and a EG&G model number 5210 lock in amplifier locks into the 1kHz signal to read the voltage data. The voltage is offset to remove the initial resistance of the chip from the measurement and ΔR is amplified and then sent to the oscilloscope, which displays the field and resistance as voltage versus voltage graphs. The data is recorded by 'Wavestar Software for Oscilloscopes' on the computer and later converted into field versus resistance or magnetoresistance using Microsoft Excel. During milling the beam voltage was 500V and the

beam current was 10mA. The pressure in the chamber was kept at a constant 2.1×10^{-4}mbar, and the milling process was cut-off during the measurement time (≈1min).

6.3 The Sample Holders.

The sample holder was designed to incorporate the chip, the field coils and the necessary electrical connections. It was designed to fit on top of the fully rotating stage in the argon ion milling chamber. Fig. 6.3 shows the initial design for the sample holder.

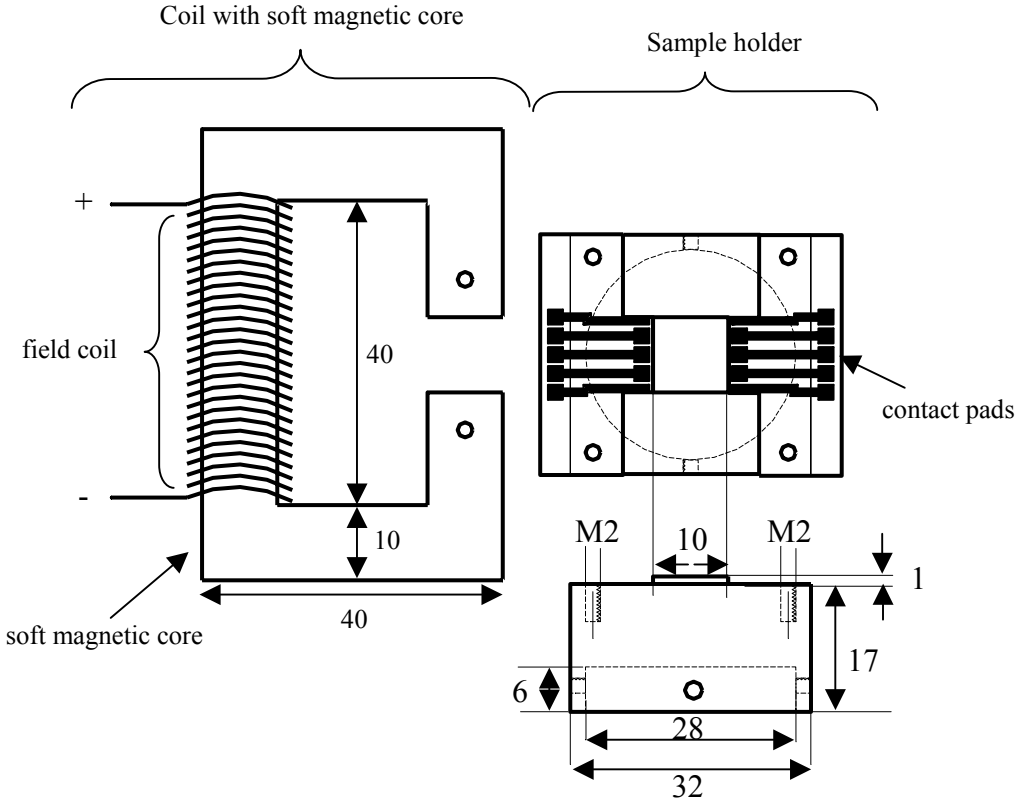

Fig. 6.3. *The initial sample holder incorporating a sample stage, electrical contact pads, and the field coil which consisted of a coil wrapped around a soft magnetic core.*

The sample holder is machined from copper and the stage is 10mm by 10mm in size, enabling the 10mm by 5mm samples to be measured with the field and current parallel or perpendicular to each other respectively. The underside of the sample holder has a circular hollow with side screws to allow it to be mounted onto the rotating stage in the chamber. The contact pads were made using single-sided copper circuit board, which was patterned using optical lithography and etched using Ferric Chloride ($FeCl_3$). The circuit board was cut and sanded to the correct shape. The field coil consists of a coil wound around a soft magnetic core, and is described in detail in section 6.4.

Fig. 6.4 shows the second design for the sample holder, the main differences being the sample holder was machined from aluminium, two field coils on either side of the sample, no soft magnetic core, and the size of the sample stage.

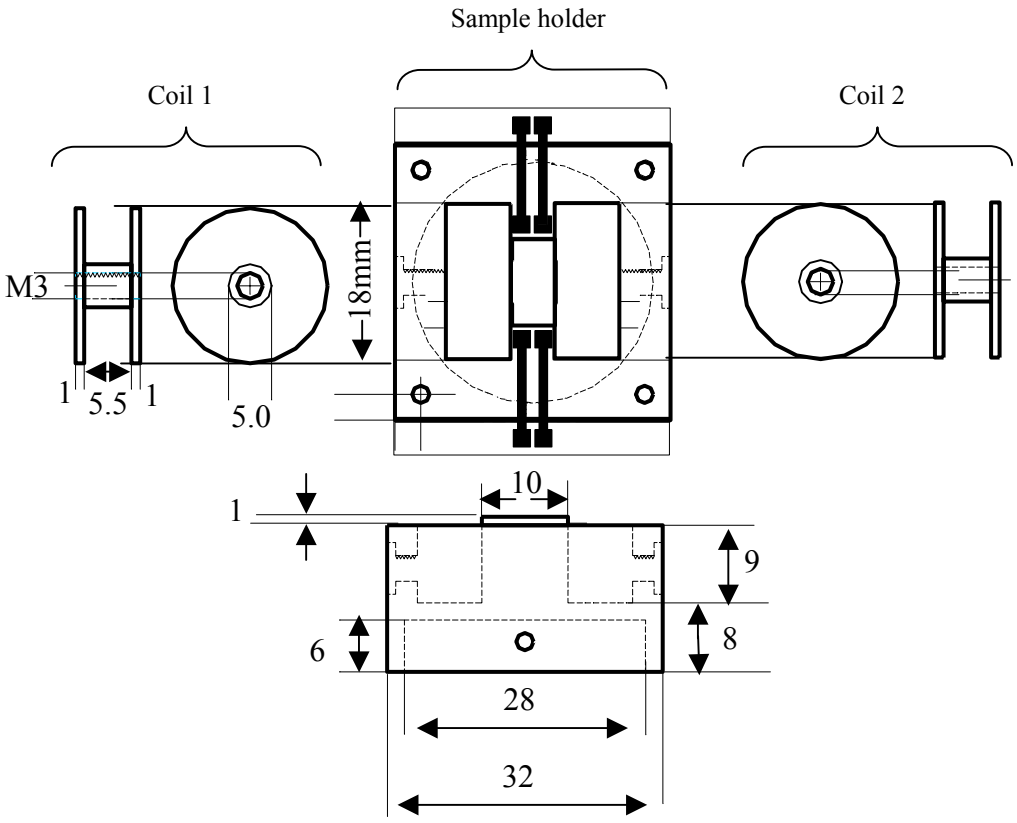

Fig. 6.4. *The second design for the sample holder incorporating a sample stage, electrical contact pads, and two field coils on either side of the stage.*

The sample holder was made from aluminium to reduce the load on the rotating stage. The stage was made narrower to achieve a larger, more uniform field across the chip in the absence of the soft magnetic core. The two field coils holders were made of aluminium and were light and compact. The coil configuration is not Helmholtz, but provides a uniform field on the micron scale which is sufficient for the devices. The slow rate of change of field also influenced the material choice.

6.4 The Field Coils.

6.4.1 The field coil with a soft magnetic core.

The field coil designed for sample holder 1 incorporates a coil wound around a soft magnetic core. The soft magnetic core is used to concentrate the flux and distribute the magnetic field uniformly across the chip. The field between the pole pieces of the soft magnetic core is uniform over the millimetre range. This design of field coil was used to magnetise millimetre-

sized samples patterned by optical lithography. Two different materials were tested for the soft magnetic core: mild steel and permalloy. The mild steel core was constructed as shown in Fig. 6.3 and was wound with 3000 turns of 150μm diameter copper wire. The resistance of the coil was 58.3Ω. A current source was used to drive a current through the coil and the field between the poles of the core was measured using a Hall probe. In this design the magnetic field produced by the coils magnetises the magnetic core, and the polarisation of the core produces a field across the chip. At a high enough applied current the magnetic field from the coils is large enough to saturate the core, this is the limit of the applied magnetic field across the chip.

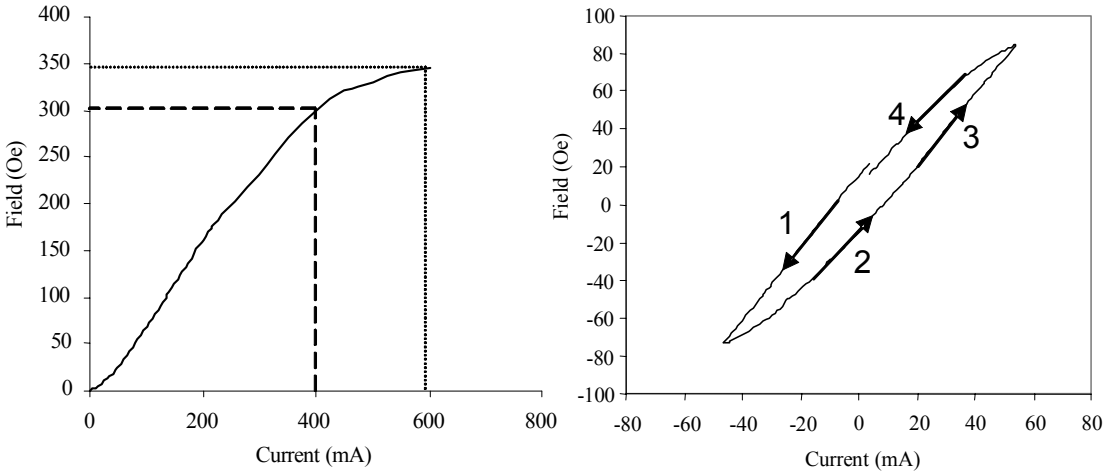

Fig. 6.5 (a) *A graph showing the current versus field for the field coil with 3000 copper turns and a mild steel core. The graph shows the applied current for which the magnetic core saturates. The dotted lines are guides for the eye.(b) A graph to show the amount of field produced for a given applied current by the field coil with 3000 copper wire turns and a mild steel core. The numbers indicate the direction of the applied current.*

Fig. 6.5 (a) shows that the mild steel core saturates at ≈ 600mA, achieving a maximum field of 350Oe. However the graph loses linearity at ≈ 400mA, showing a field of 300Oe. It is also important to study the magnetic field produced from the field coil when the current is cycled in the negative and positive direction, as shown in Fig. 6.5 (b). Before the measurement was taken the core was saturated by a permanent magnet. The current versus field graph shows hysteresis with $H_c \approx 8$Oe, due to the remanence of the mild steel core. In order for this field coil to be used in magnetoresistance measurements the hysteresis of the core needs to be pre-calibrated. This was done by dividing the field measurement into four parts as shown in Fig. 6.5 (b), and curve fitting to each part. Using this technique it was possible to mathematically predict the field from the current input. Two different methods of saturating the core were

investigated: applying a large current (a) and applying a large magnetic field (b) from a permanent magnet, as shown in Fig. 6.6.

The application of a large current (1A) to saturate the core showed poor reproducibility due to heating effects. When the core was saturated using a large magnetic field, the reproducibility was much better. When using this design of field coil for the *in-situ* experiment, the core was saturated before the measurement using a permanent magnet.

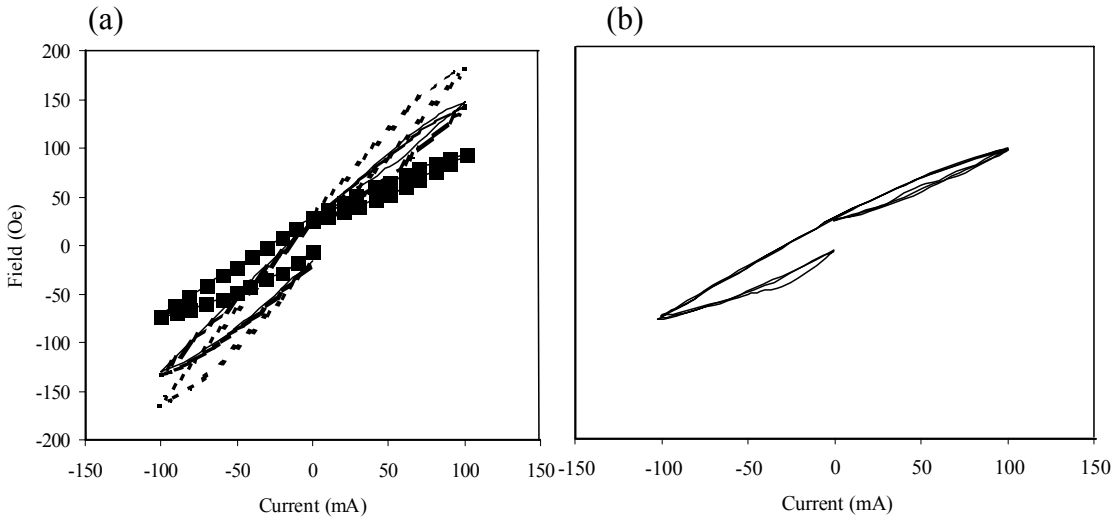

Fig. 6.6 *Graphs to show the reproducibility of the hysteresis of the field coil with a mild steel core by saturating with (a) a 1A current through the coils, (b) a permanent magnet.*

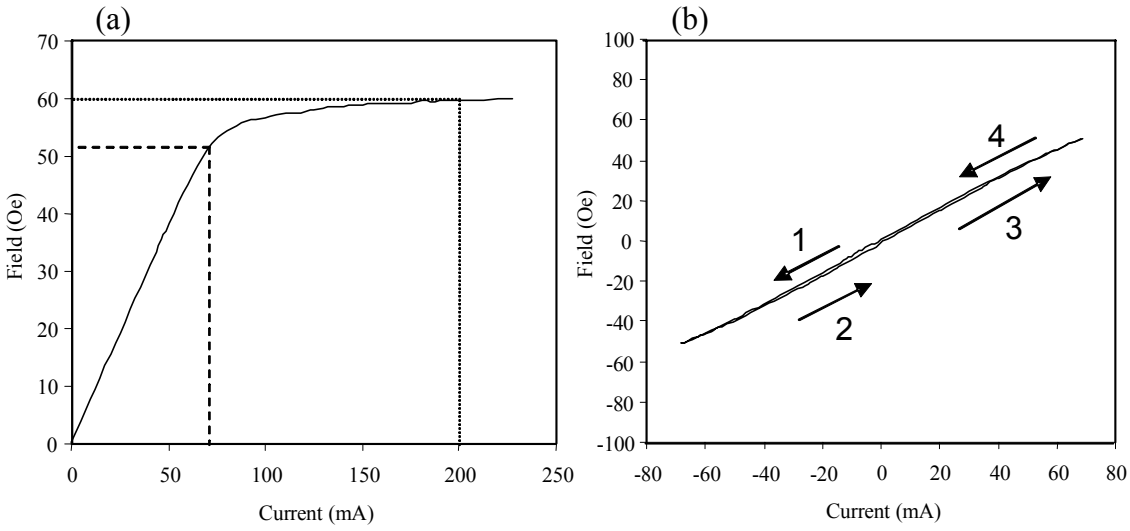

Fig. 6.7 (a) *A graph showing the current versus field for the field coil with 2100 copper turns and a permalloy core. The graph shows the applied current for which the magnetic core saturates. The dotted lines are guides for the eye. (b) A graph to show the amount of field produced for a given applied current by the field coil with 2100 copper wire turns and a permalloy core. The numbers indicate the direction of the applied current.*

A field coil with a permalloy core was constructed using the same design, 2100 copper turning were wound and the initial resistance was 32.1Ω. The magnetic field from the core was tested as the applied current was increased to investigate the saturation of the core, as shown in Fig. 6.7 (a). The permalloy core is fully saturated at 200mA, producing a maximum field of 60Oe. However, the magnetic field loses linearity at ≈ 70mA producing a magnetic field of ≈52Oe. The core was saturated with a 250mA current, and the current was swept from negative to positive to investigate the hysteresis of the permalloy core. Fig. 6.7 (b) shows that the permalloy core has nearly zero hysteresis, a linear curve fit was used to predict the field from the applied current for the in-situ measurement rig. The results from the field coils with soft magnetic core are summarised in the table shown in Fig. 6.8.

	Mild Steel Core	Permalloy Core
Saturation current (mA)	600	200
Saturation field (Oe)	350	60
Maximum linear current (mA)	400	70
Maximum linear field (Oe)	300	52
Saturation method	Permanent magnet	250 mA current
Hysteresis	Yes, H_c≈8Oe	Small
Curve fit	Polynomial	Linear

Fig. 6.8 *A table summarising the properties of the mild steel and permalloy cores.*

The mild steel produces a larger field than the permalloy core, but it also requires a larger current which can lead to heating of the coil. It also has a larger hysteresis and requires a four part polynomial equation to convert the applied current to field. In order to optimise the reproducibility, the core is saturated by a permanent magnet before pumping down to achieve a good vacuum. The mild steel core was used when larger fields were required for the *in-situ* magnetoresistance measurement. The permalloy core is only capable of fields up to 60Oe, but it has close to zero hysteresis and can be saturated by applying a current at anytime during the measurement. The permalloy core was used when low fields were sufficient for the *in-situ* magnetoresistance measurement.

Transport measurements were carried out using spin valve material supplied by Nordiko with the construction: Ta(50)/NiFe(25)/CoFe(20)/Cu(26)/CoFe(20)/IrMn(100)/Ta(50), where the thicknesses are given in Å. The wafer was diced into 10mm by 5mm sized chips, with the direction of anisotropy of the ferromagnetic layers parallel to each other and also parallel to

the length of the chip. The experiment was carried out at room temperature and pressure, with the applied field perpendicular to the current and anisotropy in the layers. The results were used to compare the *in-situ* magnetoresistance measurement rig to a regularly used transport measurement rig to check that the set-up was working properly.

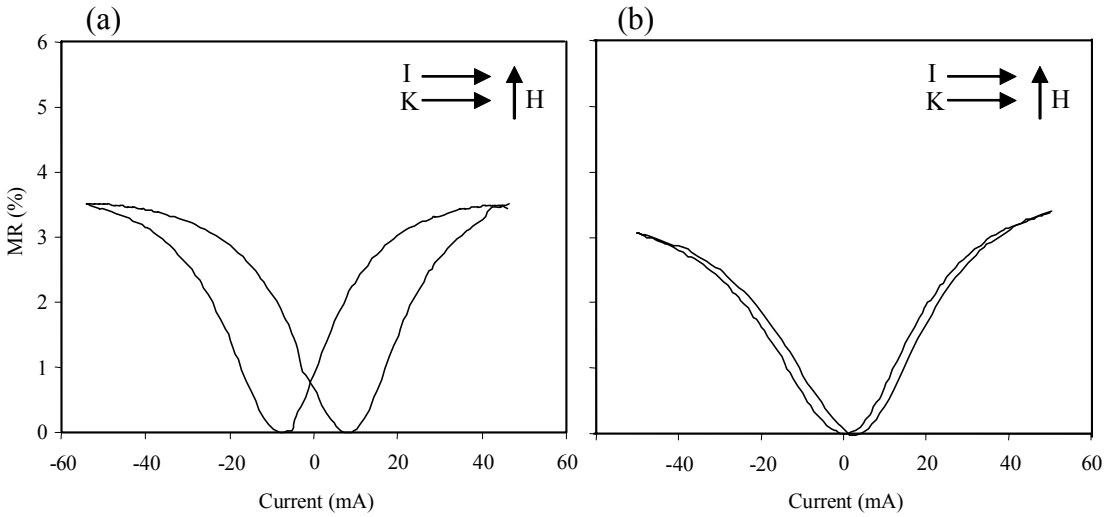

Fig. 6.9 *Measurements of applied current versus MR for the spin valve sample using mild steel (a) and permalloy (b) field coils. The inset shows the direction of the current I, anisotropy K and applied field H for clarity.*

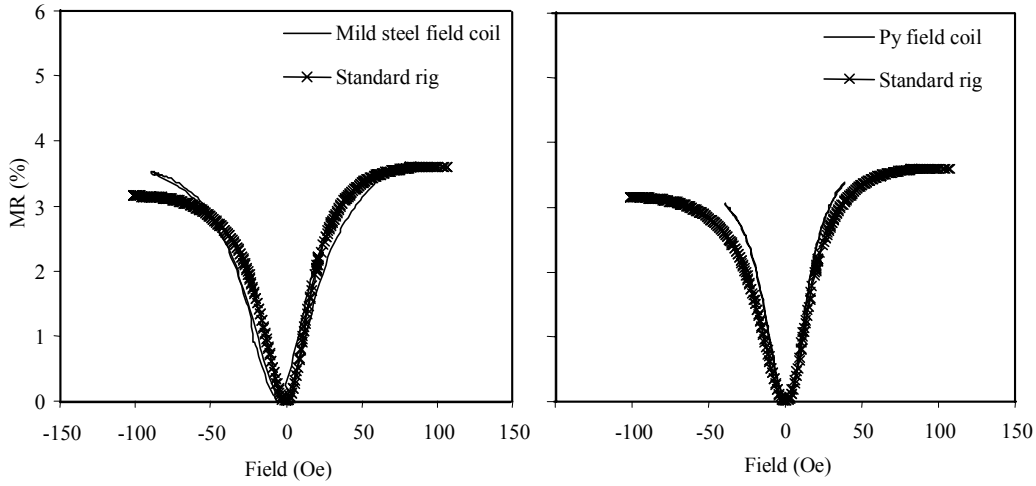

Fig. 6.10 *Measurements of applied current versus MR for the spin valve sample using mild steel (a) and permalloy (b) field coils.*

Fig. 6.9 shows the current versus MR measurement for the spin valve sample measurement using the mild steel (a) and permalloy (b) field coils. The inset shows the direction of the current *I*, anisotropy *K* and applied field *H* for clarity. The hysteresis from the mild steel core can be clearly seen compared to the permalloy core. The current axes were converted into

field using the calibration measurements shown in Figs. 6.5 (a) and 6.7 (a), and the *in-situ* transport measurement results were compared to those obtained from a standard transport measurement rig. Fig. 6.10 compares the results for the mild steel (a) and permalloy cores (b) respectively. The *in-situ* transport measurements for the mild steel and permalloy cores compare well to the standard measurement rig, the graphs show the characteristic bell shape seen when the field is applied perpendicular to the anisotropy axis. The permalloy core sample follows the measurement rig particularly well for low fields, and shows an increasing deviation as the field increases, which emphasises the fact that it should only be used for low field measurements. The mild steel field coil follows the standard rig measurement closely up to higher fields, some deviation is seen because the sample is not properly saturated. The *in-situ* magnetoresistance measurements carried out using these fields coils measured between ±50Oe in order to avoid any saturation problems.

6.4.2 Field coils without a soft magnetic core.

The field coils designed for sample holder 2 incorporate two coils on either side of the sample wound around a non-magnetic aluminium holder. Insulated 80μm diameter copper wire was used, and 3250 turns were wound on each holder. The coils were connected electrically in parallel in order to reduce the resistance seen by the current amplifier. The resistance of the coils was 200Ω. A hall probe was positioned in the centre between the coils, and the field was measured as a current was supplied to the coils.

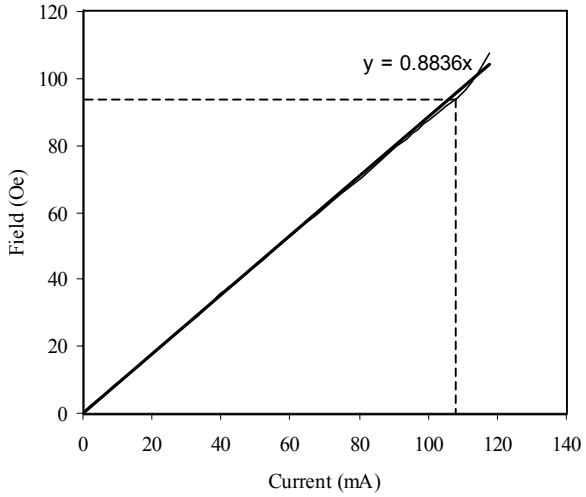

Fig. 6.11 *Current versus field graph for the field coils in sample holder 2.*

Fig. 6.11 shows the current versus field graph for the coils. The field increases linearly with current and can be fitted with the equation y=0.8836x. Above ≈110mA the coils start to heat up, they can produce a maximum field of ≈95Oe and have sufficient uniformity for the

micron and nano sized samples.

6.5 The Lock-in amplifier.

The EG&G model number 5210 lock-in amplifier is an important part of the apparatus because it enables the measurement of small signals. The lock-in provides a DC output proportional to the AC signal under investigation and it is capable of measuring very small AC signals.

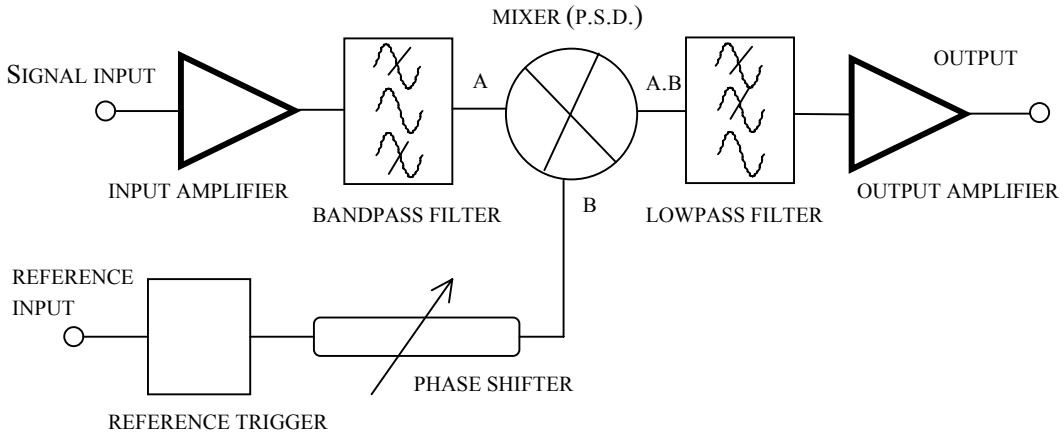

Fig. 6.12 *Block diagram of a typical lock-in amplifier [2].*

Fig. 6.12 shows a block diagram of a typical lock-in amplifier. The input signal to be measured is made to appear at a reference frequency. The signal is then amplified and applied to a phase sensitive detector (P.S.D.) operated at the reference frequency, which converts the AC input into the DC signal of interest. The output of the detector includes a value representing the amplitude of the signal of interest as well as components due to noise and interference, the AC noise can be reduced by selecting the appropriate filters. The lock-in amplifier has an internal oscillator, which is used to drive the current across the sample at the reference frequency. The voltage output from the sample is fed into a differential input of the lock-in, and the voltage information across the chip is derived from the amplifier at the reference frequency. A notch filter was set to limit the 50Hz noise and the lock-in gain typically varied between unity and 100 through the measurement.

The lock-in amplifier output was calibrated at different frequencies using a spin valve supplied by Nordiko with the construction:

Ta(50)/NiFe(25)/CoFe(20)/Cu(26)/CoFe(20)/Cu(10)/CoFe(20)/IrMn(100)/Ta(50). The MR, or $\Delta R/R$, was derived from $\Delta V/V$ from the lock-in at different frequencies and the results were compared to a standard transport measurement rig. At 1kHz the MR from the lock-in

was 9.34%, at 750Hz it was 9.32%, and at 500Hz it was 9.14%. According to the standard measurement rig the MR was 9.29%. The calibration shows that the lock-in is measuring correctly and that the response decreases with frequency. A standard reference frequency of 1kHz was chosen for the in situ measurement rig.

6.6 The Voltage-Offset Amplifier.

The output of the lock-in amplifier is connected to the input of the voltage-offset amplifier. The voltage-offset amplifier is an important piece of the apparatus because it extracts the small change in the resistance of the sample in an applied field. The output signal from the lock-in includes the initial voltage of the sample in zero field due to the initial resistance and the change in the voltage in the presence of the applied field. However, the initial resistance is much larger than the change in resistance, which makes it difficult to extract the ΔR information. The voltage-offset amplifier offsets the initial R and amplifies the ΔR to increase the sensitivity of the signal. This amplifier was designed and built specifically for the measurement system. Fig. 6.13 shows the circuit diagram for the offset-amplifier. It is powered by two 9V batteries, V_1 and V_2 represent the voltage input signals from the lock-in amplifier. NE5532 op-amps were used because they have low noise and low distortion [3]. The first two op-amps process the incoming voltage; V_1 passes through unchanged and V_2 is inverted. The third op-amp adds the incoming voltages from the first two op-amps and inverts the resulting voltage giving V_2-V_1, it also filters out the low frequency noise. Standard voltage regulator LM317 was used to regulate the voltage from the batteries and set the voltage range for the potentiometer, which was used to offset the initial resistance. The voltage range of the potentiometer is given by the V_{out} from the voltage regulator, where $V_{out}=1.25V[1+(R_2/R_1)]$ and R_2 and R_1 are the shown in Fig. 6.13. The potentiometer was set to offset between 8.38V and ground. The final op-amp combines the V_2-V_1 input and the offset voltage and amplifies ΔR using the gain settings. There are three gain settings; $\times 1$, $\times 10$, and $\times 50$, and the higher gains are filtered using capacitors to reduce the noise. The pattern for the circuit board was designed using Freehand, and optical lithography was used to expose the design onto the resist covered copper coated circuit board. The copper etching was carried out using ferric chloride $FeCl_3$.

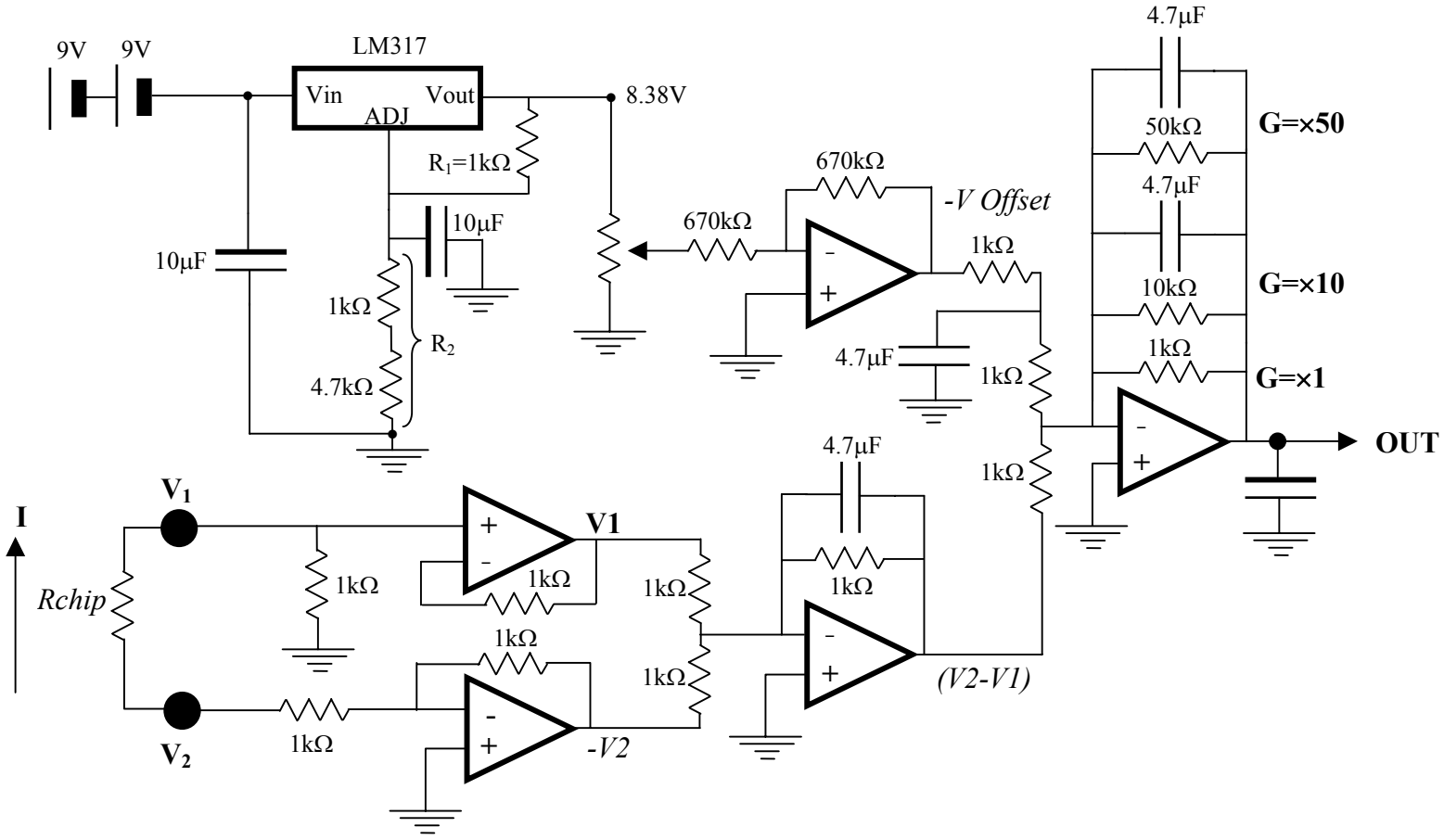

Fig. 6.13 *Circuit diagram for the Voltage-Offset amplifier used in the in-situ magnetoresistance measurement rig.*

6.7 Signal Transmission and Noise Reduction.

Fig. 6.14 shows the signal transmission through the in situ magnetoresistance measurement rig. Function generator 1 sends a low frequency triangular wave (0.05Hz) to the current amplifier, which amplifies the signal ×22 and sends the current to the field coils. The oscillator sends a high frequency (1kHz) sine wave to the current source, which drives the current across the chip.

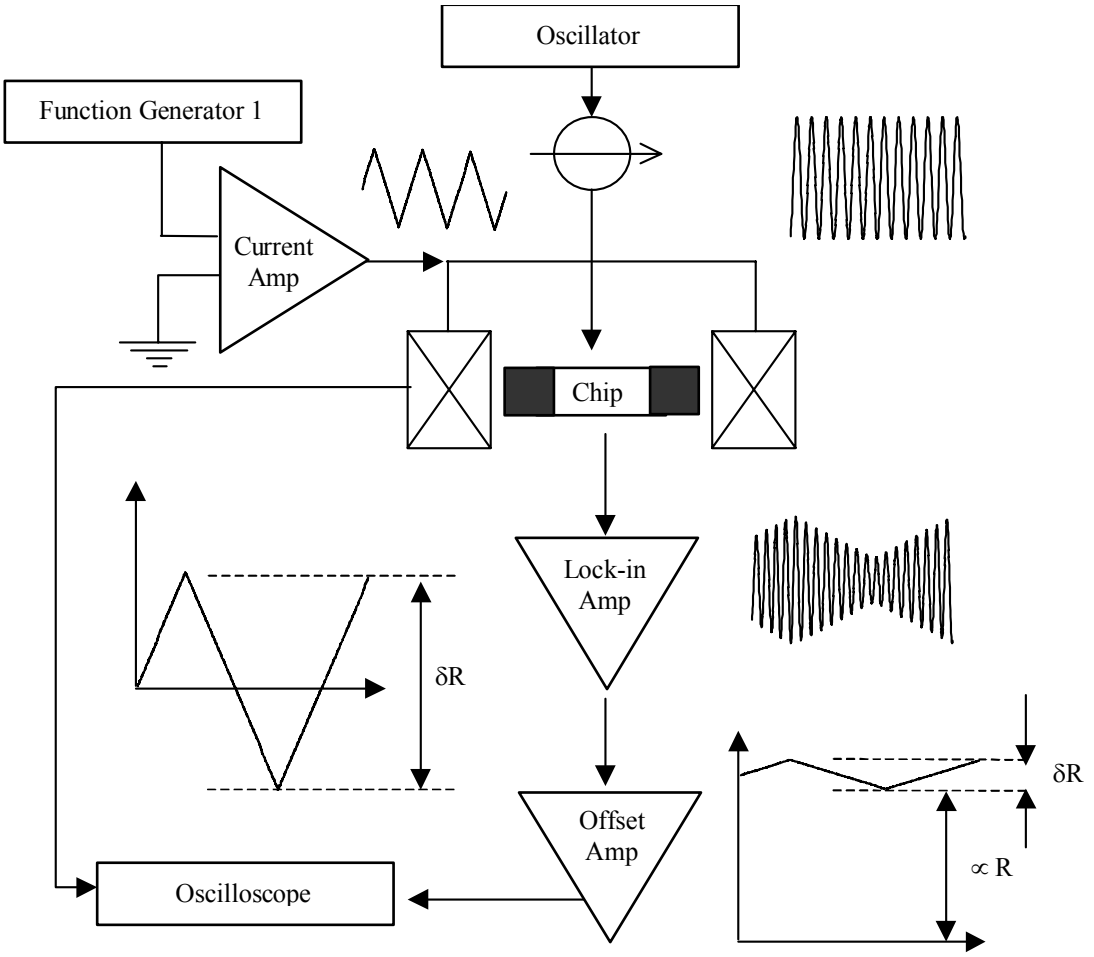

Fig. 6.14 *Schematic diagram showing the signal transmission through the in-situ magnetoresistance measurement rig.*

The voltage signal from the chip is fed into the differential input on the lock-in amplifier, which locks into the change in the 1kHz frequency voltage, filters the noise and amplifies the signal. The voltage offset amplifier offsets the initial signal which is proportional to *R*, and amplifies the voltage proportional to ΔR. Both the field voltage and the voltage from the offset amplifier are sent to the oscilloscope, which displays both signals on the screen. The voltage proportional to R is recorded from the lock-in display screen.

The MR is given in Eqn (6.1) and is calculated from:

$$\partial R = \frac{V_{oscill}}{G_{V-amp} \times G_{lock-in} \times I}$$

$$R = \frac{V_{lock-in}}{G_{lock-in} \times I}$$

$$\frac{\Delta R}{R} = \frac{V_{oscill}}{G_{V-amp} \times V_{lock-in}} \tag{6.1}$$

Where V_{oscill}= the chip voltage from the oscilloscope, $G_{V\text{-}amp}$= the gain from the voltage offset amplifier, $G_{lock\text{-}in}$= the gain from the lock-in, $V_{lock\text{-}in}$= the gain from the lock-in amplifier and I= the r.m.s. current from the current source.

Noise reduction was carried out by using shielded BNC and Lemo B-series connections, and by minimising the length of the cables. The effect of different grounding patterns was investigated by analysing the amount of noise in the transport measurement for different configurations. An unpatterned pseudo spin valve with the structure:
Ta(2nm)/$Ni_{80}Fe_{20}$(15nm)/Cu(2.2nm)/$Ni_{80}Fe_{20}$(6nm)/Ta(2nm) was used for the measurement, with the current and field applied perpendicular to each other respectively. A wide range of different configurations were tested, Fig. 6.15 is a table showing two of the configurations tested; A and B.

Apparatus	A	B
Function generator	×	×
Current source	×	×
Power supply for current amp	×	×
Lock-in amplifier	×	×
Voltage-offset amplifier	√	×
Oscilloscope	×	√
Argon ion milling chamber	√	√

Apparatus **grounded**=√ Apparatus **not grounded**=×

Fig. 6.15 *A table showing two different grounding pattern configurations; A and B tested to minimise the noise in the in-situ magnetoresistance measurement rig.*

The aim of the experiment was to determine which grounding pattern gave the least amount of noise. In configuration *A* the apparatus was grounded through a crows foot system; the voltage-offset amplifier was grounded by connecting to the main chamber, this created a single grounding path for all the apparatus at the output of the measuring system. In

configuration B there were two separate grounding paths through the oscilloscope and the main chamber. Fig. 6.16 shows the transport measurements taken for the two different configurations.

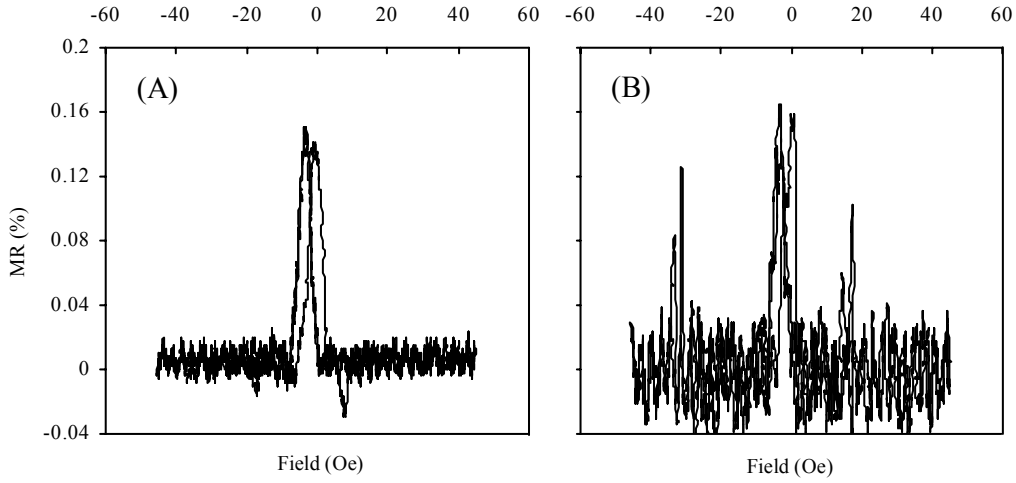

Fig. 6.16 *Transport measurements for two different grounding pattern configurations A and B in the in situ magnetoresistance measurement rig.*

The results show that configuration A gives the minimum noise with an average MR noise level of 0.02%. Configuration B gives an average noise level of 0.05% MR. These results show that the level of noise in the measurement can be minimised by connecting the apparatus grounds together, and connecting the single output ground to the main chamber at the final stage of the measurement system.

6.8 Rig calibration.

During the in situ measurement the shutter is used to control the bombardment of argon ions onto the sample surface. The shutter is opened to allow milling of the sample, and closed during the transport measurement to prevent any further milling or noise in the measurement. The shutter is re-opened once the data has been acquired to continue milling. It is important to close the shutter during the transport measurement, because it can take up to 4 minutes to acquire the data and the milling rate of the sample is approximately 5nm per minute. At this rate the sample would mill through in 6.5 minutes. The shutter is used to allow a series of measurements to be taken at different milling depths through the structure, typically 20 transport measurements are taken for a complete *in-situ* measurement. Between each milling step, the resistance in the absence of field is recorded versus the total time of milling, and this is later converted into resistance versus milling depth to give an indication of how deep the sample has been milled for each transport measurement. The effect of the movement of the

shutter was calibrated by carrying out resistance versus time measurements keeping the shutter continuously open, and also periodically opening and closing the shutter to investigate the difference. Pseudo spin valve samples with the construction: $Ta(3nm)/Ni_{80}Fe_{20}(15nm)/Cu(2.2nm)/Ni_{80}Fe_{20}(6nm)/Ta(3nm)$ were used for the experiment. The samples were patterned into 36μm wide and 100μm long rectangles using optical lithography and argon ion milling. Sputtering and lift off were used to deposit copper contact pads, and electrical contact was made by wire bonding in a four-point measurement configuration. For the experiment with the shutter continuously open, the four-point measurement was connected to a Keithley™ multimeter, and the resistance from the multimeter was sent to the computer. Labview™ software was used to record the resistance versus time, measuring and recording a resistance value every second.

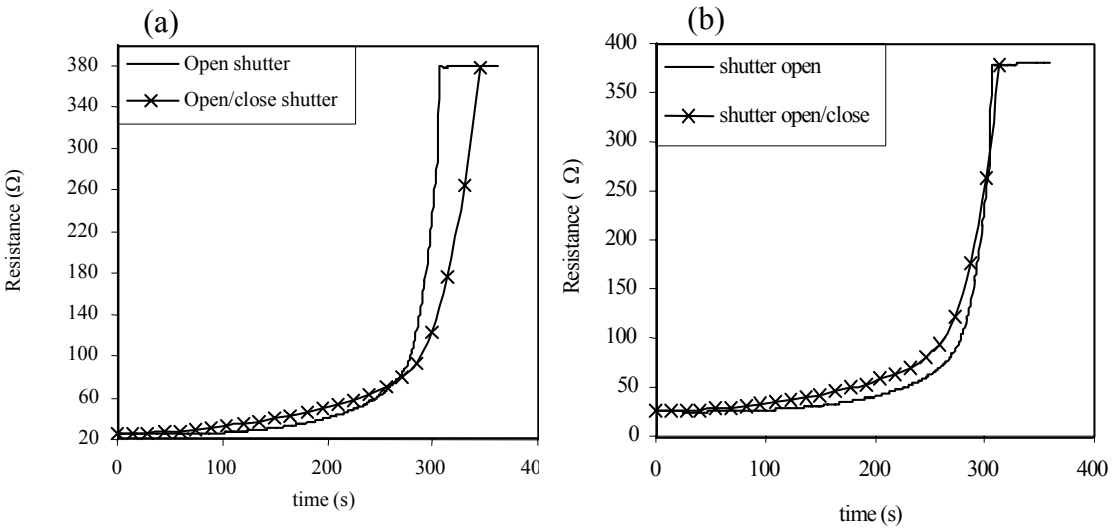

Fig. 6.17 *(a) Resistance versus time measurements in the argon ion miller with the shutter continuously open and with the shutter opening and closing. (b) The corrected resistance versus time graph for the measurement with the shutter opening and closing compared to the continuous milling measurement.*

The *in-situ* measurement rig was used to measure the resistance versus time with the shutter periodically open and closed. The resistance was calculated from the current supplied to the chip and the voltage display on the lock-in. Fig. 6.17 (a) shows the change in resistance versus time when the shutter is continuously open and when it is periodically open and closed. The results show that the samples are fully milled through after 313s and 345s, giving a final resistance of ≈378Ω. After this final measurement the resistances became infinite. Although the shape of the graphs is similar, there is a time delay for the increase in resistance when the shutter is opening and closing. This could be due to some plasma instability due to the plasma

being close to the gun [4] or a small oxidation of the surface during the measurement because the argon gas contains 3% oxygen. Assuming that the 'dead time' of the shutter is a constant every time it is opened, it can be calculated by dividing the difference in the fully milled through milling time of the two samples by the number of times the shutter is opened. This calculation gives a shutter 'dead time' of 1.3s, the resistance versus time data was adjusted to remove the shutter 'dead time' for each data point. Fig. 6.17 (b) shows the corrected resistance versus time graph for the measurement with the shutter opening and closing compared to the continuous milling measurement. The two graphs are very similar. In order to reliably predict the milling depth, a simple mathematical model was used to convert the resistance versus time data into resistance versus depth milled.

6.8.1 The Resistance Model.

Lee *et al*. used a series resistance model to predict the magnetoresistance of a multilayer structure when the current was applied perpendicular to the plane of the film [5]. In their model the total change in resistance ΔR was calculated by summing the contribution to ΔR from each of the layers. This model was adapted for current in plane and applied to these measurements in order to predict the milling depth through the spin valve structures from the resistance versus time data in the *in-situ* measurement. The model visualises each layer in the spin valve as a separate resistance, and the total resistance is the addition of all the resistors in parallel.

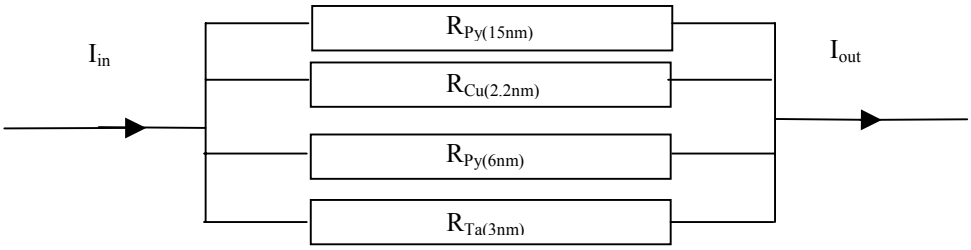

$$\frac{1}{R_{total}} = \frac{1}{R_{Py\,(15nm)}} + \frac{1}{R_{Cu}} + \frac{1}{R_{Py\,(6nm)}} + \frac{1}{R_{Ta}}$$

Fig. 6.18 *A schematic of the resistance model for the PSV structure with the current applied in the plane of the film. The equation for calculating the total resistance of the PSV is shown.*

Fig. 6.18 is a schematic diagram showing the resistance model for the pseudo spin valve structure. The Ta capping layer oxidised to TaO_2 which is highly resistive, and has therefore been neglected from the model. The sheet resistance of each layer is calculated using

$R = (\rho\ell)A$, where ρ=resistivity, ℓ=length and A=cross-sectional area. Assuming that the milling is even across the surface, each layer acts as a variable resistor during milling. Also shown in Fig. 6.18 is the equation used to calculate the total resistance of the PSV structure. If bulk values of resistivity are used in the model the calculated resistance is much lower than the measured resistance. It is known that thin film values of resistivity can be considerably larger than the bulk value [6]. Recent work carried out in our research group investigated the difference between the bulk and thin film resistivity values for NiFe, Cu and Nb, and the results are shown in Fig. 6.19.

Material	RT layer resistivity ($10^{-8}\Omega$m)	RT Bulk resistivity ($10^{-8}\Omega$m)
NiFe	23.6 (± 2.5)	~15
Cu	22.3 (± 2.6)	1.7
Nb	157 (± 16)	14.5

Fig. 6.19 *A table to show the difference in the resistivity values for thin film and bulk metals.[7]*

The increase in resistivity of the materials in thin film form is due to the increased surface scattering and the increased number of defects in sputtered films compared to the bulk. The defects are in the form of grain boundaries, impurities, dislocations, etc. When the values of the layer resistivity were substituted into the model, the calculated and measured values of resistance corresponded almost exactly. According to the reference books the thin film resistivity for Ta is 25-50μΩcm [8]. The calculated resistance value of a 36μm by 100μm area of spin valve without the Ta layer was 28.1Ω. By adding the Ta layer resistance to the spin valve resistance in parallel it is possible to calculate the total resistance of the structure.

$$\frac{1}{R_{sv}} + \frac{1}{R_{Ta}} = \frac{1}{R_{total}}$$

$$\frac{1}{R_{Ta}} = \frac{(36\times10^{-6})(3\times10^{-9})}{(50\times10^{-8})(100\times10^{-6})} = 2.16\times10^{-3}\Omega^{-1}$$

$$\frac{1}{R_{total}} = \frac{1}{28.1} + 2.16\times10^{-3}$$

$$R_{total} = 26.49\Omega$$

The experimental value of the full spin valve structure using a four-point measurement was 26.13Ω, which is in close agreement to the calculated resistance using the resistance model 26.49Ω.

6.8.2 In-situ milling depth calculation.

The resistance model described above was used to predict the resistance of the pseudo spin valve as the structure is gradually milled through the 23.2nm thickness. Fig. 6.20 (a) shows the change in resistance as the structure is milled through the 15nm NiFe layer, the Cu layer and the 6nm NiFe layer. The shaded regions on the graph indicate the different layers in the structure.

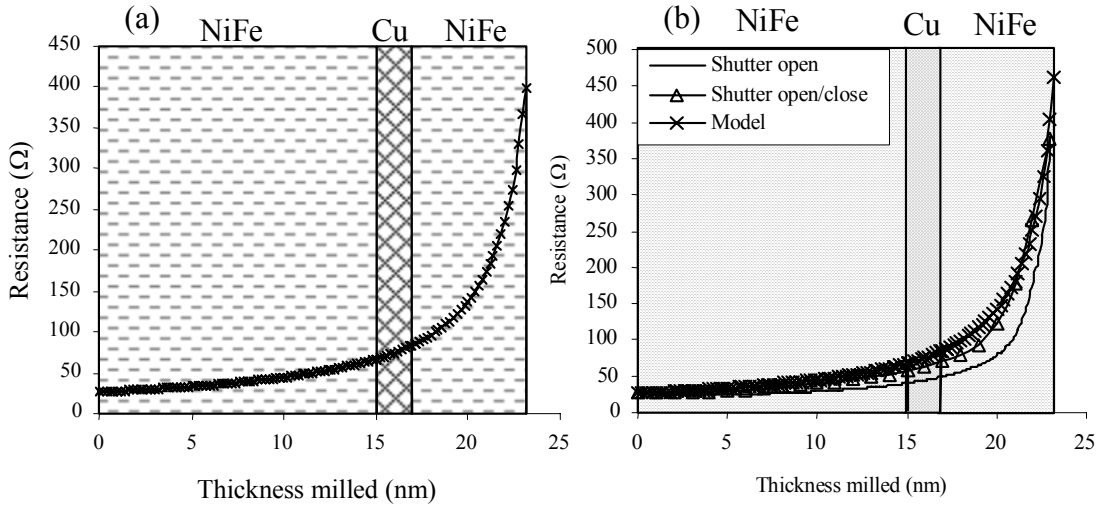

Fig. 6.20 *(a) A graph to show the change in resistance versus thickness milled for the pseudo spin valve calculated by the resistance model. The shaded regions indicate the different layers in the structure. (b) Resistance versus milling depth calculations for the sample with the shutter continuously open, for the shutter periodically open and closed, and the resistance model.*

According to the model the resistance of the pseudo spin valve is 397Ω when milled through to the end of the 6nm thick NiFe layer. According to the experimental data, the final resistance for both the sample measured by continuous milling and periodic milling is ≈378Ω. When the measured resistance is fitted to the predicted milling depth from the model, the shape of the graphs can be compared, as shown in Fig. 6.20 (b). The measurement when the shutter is periodically open and closed fits quite well to the model, the data for the continuous milling sample does not fit so well. One possible source of error in the measurement is a change in the average resistivity of the structure during milling. The model assumes that the resistivity of the layers remains constant throughout the milling. Fig. 6.21 shows a graph of the inverse resistance (*1/R),* versus the thickness (t) of the pseudo spin valve.

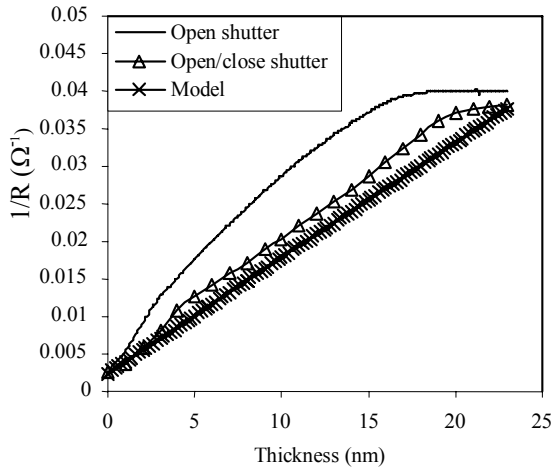

Fig. 6.21 *A graph of inverse resistance 1/R versus thickness t with the shutter continuously open, with the shutter periodically open and closed, and as calculated by the resistance model.*

The model assumes that the resistivity, length and width remain constant during milling, and the graph of $1/R$ versus t is linear, with the gradient equal to $w/\rho\ell$. When the shutter is opened and closed through the measurement the graph is also approximately linear, and the shape of the graph follows the resistance model quite closely. When the shutter is continuously open the 1/R versus t data shows an increased deviation from linearity.

The thicknesses of the layers in the pseudo spin valve are similar or smaller than the mean free path of the electrons, typical mean free paths in metals are of the order of tens or even hundreds of interatomic distances, and for NiFe≈15nm and Cu≈20nm. According to Mathon [9] when the mean free path is much longer than the thickness of the layers, the conduction electrons sample equally layers with low and high resistivity, and the resistivity of the layers can be given by an average resistivity calculated as shown in Eqn. (6.2).

$$\bar{\rho} = \frac{a\rho^a + b\rho^b + c\rho^c + d\rho^d}{a+b+c+d} \tag{6.2}$$

where a and ρ^a are the thickness and resistivity of the top NiFe layer, b and ρ^b are the thickness and resistivity of the Cu interlayer, c and ρ^c are the thickness and resistivity of the bottom NiFe layer and d and ρ^d are the thickness and resistivity of the Ta underlayer.

Using Eqn. (6.2), the average resistivity of the structure is $26.5\times10^{-8}\Omega$m. When the average resistivity is derived from the gradient of the graph of 1/R versus t for the resistance model,

the value obtained is $24\times10^{-8}\Omega$m, which is in close agreement with the equation shown above. The experimental value of the average resistivity when the shutter is open and closed equals $22.5\times10^{-8}\Omega$m, and when the shutter is continuously open the resistivity equals $21.18\times10^{-8}\Omega$m. The deviation in linearity of the measured resistivity when the shutter is continuously open is due to the effect of the argon ions bombarding the surface during the measurement.

6.9 Conclusions.

An in-situ magnetoresistance measurement rig was successfully built and calibrated to allow direct analysis of the change in electrical and magnetic properties of spin valve devices during patterning. Different designs for applying the field have been investigated and it was found that coils with a soft magnetic core were more suitable for samples on the millimetre scale. For smaller samples field coils without cores were sufficient and more convenient to use. Noise reduction was achieved with the use of a lock-in amplifier and carefully arranged grounding patterns. A voltage-offset amplifier was designed to amplify the signal response and offset the initial resistance of the sample. Various techniques were used to ensure that the rig was properly calibrated. A mathematical resistance model was developed to calculate the depth milled from the resistance of the sample.

References

[1] National Semiconductor (http://www.national.com/pf/LM/LM675.html)

[2] Perkin Elmer Instruments (http://www.cpm.uncc.edu/programs/tn1000.pdf)

[3] Texas Instruments Dual Low-Noise Operational Amplifiers (http://www.physics.brocku.ca/faculty/razavi/231/datasheets/slos075a.pdf)

[4] G.G. Lister, Low-pressure gas discharge modelling, *J. Phys. D: Appl. Phys*., **25**, 1649-1680 (1992).

[5] W.Y. Lee, S. Gardelis, B.-C. Choi, Y.B. Xu, C.G. Smith, C.H.W. Barnes, D.A. Ritchie, E.H. Linfield, J.A.C. Bland, *J. Appl. Phys*. **85**(9), 6682 (1999)

[6] M. Ohring, *The Materials Science of Thin Films*, **Chapter 10.2.2**, 457-463, Academic Press Ltd (1992)

[7] D. Leung, *Ph.D. thesis*, Cambridge University (2003)

[8] M. Ohring, *The Materials Science of Thin Films*, **Chapter 10.2.2**, 464, Academic Press Ltd (1992)

[9] J. Mathon, *Spin Electronics*, **Chapter 4**, 84, (Eds.) M. Ziese, M.J. Thornton, Springer-Verlag Berlin Heidelberg (2001)

The mathematical sciences particularly exhibit order, symmetry, and limitation; and these are the greatest forms of the beautiful. *Aristotle (384-322 BC) Metaphysica*.

Chapter 7

In-situ Micropatterning of Pseudo Spin Valves

The new test rig gives the opportunity to progressively measure the effect of changing selected parameters on the samples. Arrays of micro-wires with varying aspect ratio and equal mark/space ratio were patterned in ferromagnetic trilayers with the structure: Ta(3nm)/$Ni_{80}Fe_{20}$(6nm)/Cu(2.2nm)/$Ni_{80}Fe_{20}$(15nm)/Ta(3nm). The *in-situ* test rig was used to analyse the change in the magnetoresistance response as the shape anisotropy of the trilayer was increased during milling. The results confirm the measurement results from Chapter 5 by showing that it is possible to partially decouple the $Ni_{80}Fe_{20}$ ferromagnetic layers. The progressive measurements in this chapter show that a maximum spin valve response is observed when the structure is fully milled. The transport measurements show that magnetisation reversal occurs in two stages, with the lower switching field corresponding to the thinner ferromagnetic layer. It is also shown that as the shape anisotropy is further increased by decreasing the width of the micro-patterned wires, the spin valve response is magnified. Highly anisotropic structures were also patterned in PSVs with the construction Ta(3nm)/CoFe(6nm)/Cu(2.2nm)/CoFe(15nm)/Ta(3nm). The CoFe ferromagnetic layers do not become decoupled during patterning in the *in-situ* rig. This is thought to be due to larger magnetostatic and interlayer coupling energies. The $Ni_{80}Fe_{20}$ pseudo spin valve design shows a higher thermal stability than a conventional spin valve with an IrMn antiferromagnetic pinning layer.

7.1 Motivations.

The characteristics of magnetic stripes have been extensively studied because of their importance in both magnetoresistance devices [1-16] and, more recently magnetoelectronic devices [17,18]. There have been numerous efforts [1-16] to investigate the magnetisation reversal and MR behaviour in ferromagnetic wires so far. Very recent studies [9-13] have demonstrated that the switching field and magnetisation reversal process depend strongly on the end shape as well as the width of the ferromagnetic wires. The shape of a wire structure has a decisive influence on the magnetic properties in the micron size range. For example, the magnetisation reversal process and MR behaviour are found to change significantly in micron-sized $Ni_{80}Fe_{20}$ modulated width [15], "elbow"-shaped and cross-shaped wire structures [16] due to the modified shape-dependent demagnetising fields. The previous chapters have shown that it is possible to decouple two ferromagnetic layers in a spin valve sandwich by patterning a highly anisotropic structure in one of the layers using optical lithography and argon ion milling. An array of 3μm wide wires with equal mark-space ratio was patterned in the top layer of the structure, whilst the bottom layer remained unpatterned. The decoupling effect was shown to increase as the material between the wires was milled away to the Cu spacer, and a small spin valve response was observed. In this chapter we present results for the *in-situ* magnetoresistance response of micro-patterned wire arrays in spin valve structures. The results show the evolution in the transport measurements as the milling depth between the wires is increased, and also the effect of further increasing the shape anisotropy by changing the dimensions of the array. The change in MR was also investigated using different ferromagnetic materials in the trilayer. As mentioned previously, the practical disadvantage of using exchange anisotropy to pin one of the ferromagnetic layers in a spin valve is the reduction in pinning strength as the temperature is increased [19]. Temperature measurements were carried out to compare the pseudo spin valve devices with conventional spin valves with an IrMn antiferromagnetic pinning layer. The results of this study show how the spin valve response from the micro-patterned trilayers can be optimised in terms of the material properties and the structure of the ferromagnetic layers.

7.2 Sample preparation.

Pseudo spin valves with the configuration:
Ta(3nm)/$Ni_{80}Fe_{20}$(6nm)/Cu(2.2nm)/$Ni_{80}Fe_{20}$(15nm)/Ta(3nm) were diced into 10mm by 5mm samples. The samples were patterned into 4mm by 3.3mm rectangles using optical lithography and argon ion milling. Copper contact pads were deposited on either side of the 4mm long rectangles as shown in Fig. 7.1, using optical lithography and lift off. Fig. 7.1 also shows the direction of anisotropy in the two ferromagnetic layers, the electrical four-point

measurement set-up and the field measurement directions 0° and 90°. The anisotropy direction of the top 15nm ferromagnetic layer is along the 4mm length of the sample, which also corresponds to the 0° measurement direction. Magnetic hysteresis measurements taken at 0° and 90° showed a single hysteresis loop, which confirmed the ferromagnetic coupling between the layers, with the magnetisation reversal being dominated by the thicker top ferromagnetic layer as explained in Chapter 5. The same optical lithography technique was used as summarised in Fig. 5.1 (Chapter 5) to pattern a 3μm wide wire array with equal mark-space ratio along the 4mm length of the rectangle, (see Fig. 5.9). The samples were wire bonded in a 4-point transport measurement configuration and loaded into the argon ion miller for *in-situ* magnetoresistance measurements.

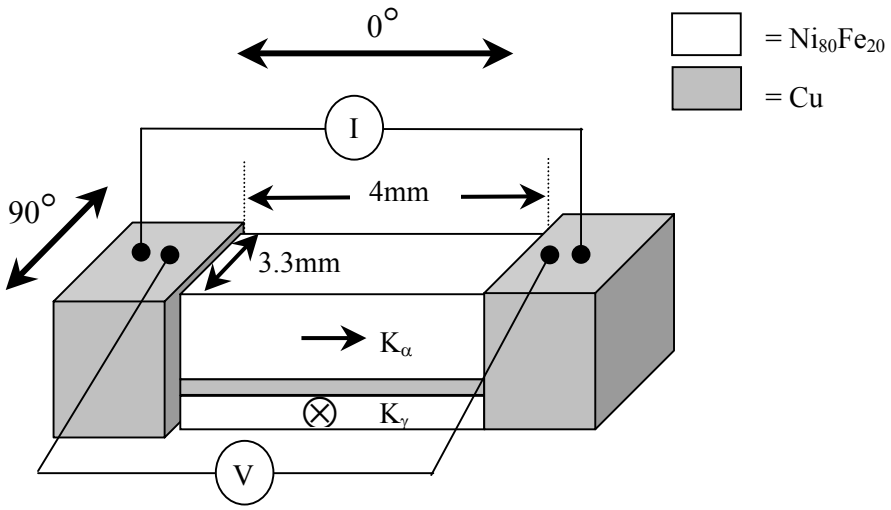

Fig. 7.1 *A schematic diagram showing the patterned pseudo spin valve including the anisotropy directions of the ferromagnetic layers, dimensions, the electrical four-point measurement, and the measurement directions 0° and 90°.*

7.3 *In-situ* magnetoresistance measurements.

Previous transport measurements in Chapter 5 showed an AMR and a GMR response when the wire array structure was milled through to the copper interlayer (Fig. 5.12). Using the magnetoresistance measurement rig, the results in this chapter study the change in the MR as the structure was fully milled through. Fig. 7.2 shows the evolution in the transport properties for the 3μm wide wire array from the *in-situ* measurement. Graph (a) shows the initial transport measurement before any milling. An AMR of ≈0.2% is seen, and the shape of the graph shows that the response is dominated by the anisotropy of the thicker top ferromagnetic layer, which is parallel to the applied field. The AMR response agrees with the magnetisation measurement along the 0° direction. Graph (b) shows that as the milling continues the AMR

decreases and a small GMR is seen, this result was observed in Chapter 5. However as the milling is continued, graphs (c) and (d) show that the AMR disappears and only GMR is seen. A maximum GMR of 0.8% is observed when the sample is fully milled through. As described in Chapter 5, the appearance of a GMR signal as the milling depth increases is due to the two ferromagnetic layers becoming decoupled. The total energy of the structure before patterning is the sum of the Zeeman energy, the ferromagnetic interlayer coupling energy, the magnetostatic energy, and the perpendicular induced anisotropy energies. Initially the interlayer coupling energy and the magnetostatic energy dominate the induced anisotropy energies in the layers and they remain coupled together in an applied field. The results in Chapter 5 showed that as the shape anisotropy was gradually increased by patterning through the top layer of the pseudo spin valve, the coercivity of the top layer increased and eventually the shape anisotropy energy became larger than the interlayer coupling. The patterning changed the natural similarity of the two ferromagnetic layers and they started to move separately in an applied field creating a small GMR signal. Originally it was expected that if one layer was patterned and the other layer remained unpatterned, a maximum GMR would be seen because the energies in the two layers would be very different.

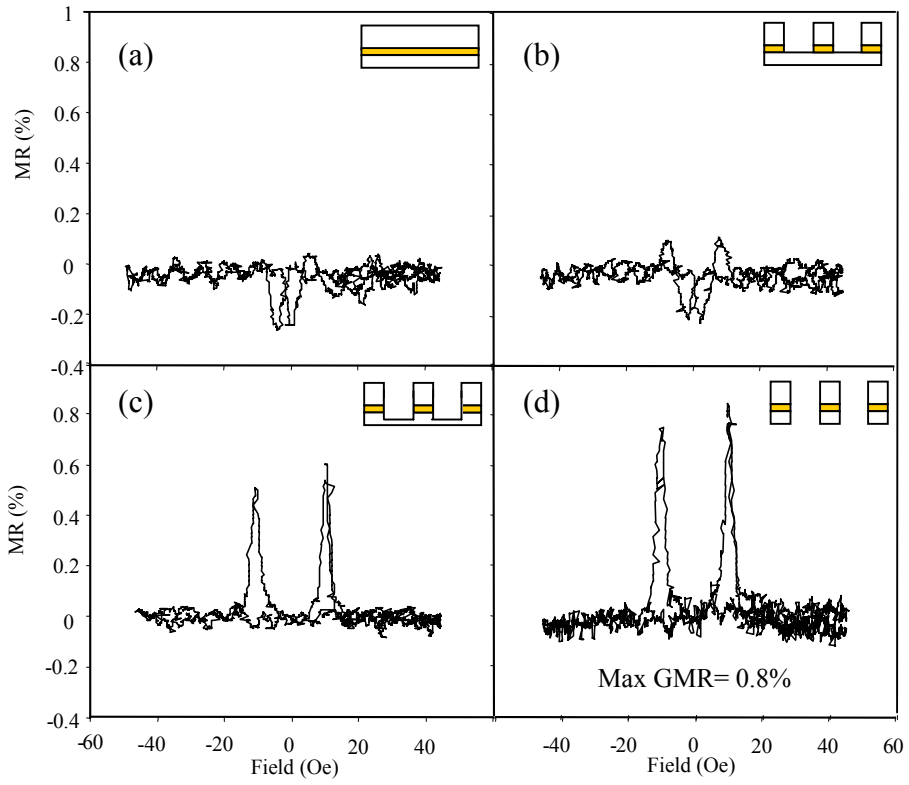

Fig. 7.2 *In-situ magnetoresistance measurements showing the evolution in transport properties when an array of 3μm wide wires is patterned in a $Ni_{80}Fe_{20}$/Cu pseudo spin valve sample.*

The results shown in Fig. 7.2 are surprising because they show that a maximum GMR is observed when the two ferromagnetic layers are patterned with the same high shape anisotropy structure. The effect of further increasing the induced shape anisotropy was investigated by decreasing the width of the patterned wires. The length of the patterned wires was kept at a constant 4mm, but the wire width was reduced from 3μm to 2μm and 1.5μm, creating aspect ratios of 1:1333, 1:2000 and 1:2666 respectively. Fig. 7.3 shows the change in the transport measurement as the structure was milled through according to the *in-situ* magnetoresistance measurements for the 2μm wide wire array. Fig. 7.3 shows that the 2μm wide wire array shows the same trend as the 3μm wide wire array; the transport measurements show an initial AMR and a final GMR when fully milled through. However the maximum GMR is 2.21%, this result indicates that increasing the shape anisotropy increases the GMR.

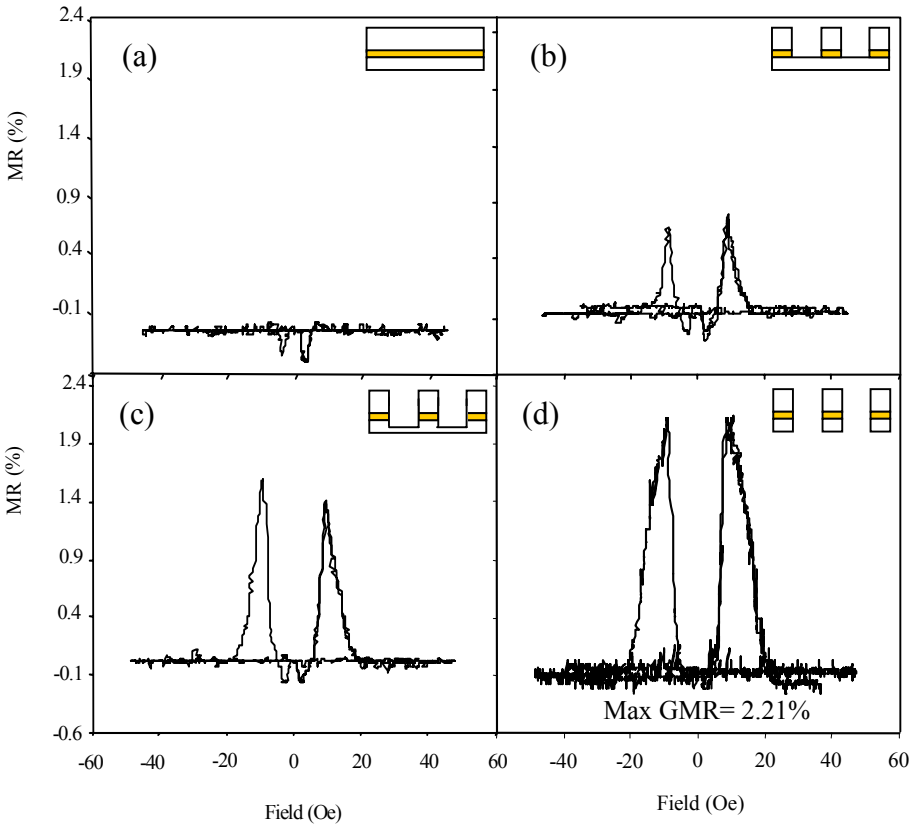

Fig. 7.3 *In-situ magnetoresistance measurements showing the evolution in transport properties when an array of 2μm wide wires is patterned in a $Ni_{80}Fe_{20}$/Cu pseudo spin valve sample.*

Fig. 7.4 shows the *in-situ* measurements for the 1.5μm wide wire array, they also show the same trend with a small increase in GMR of 2.36%.

7.4 Milling Depth Calculations.

Chapter 6 introduced a parallel resistance model, which can be used to estimate the milling depth of the sample in the *in-situ* magnetoresistance rig. The model assumes that each layer in the pseudo spin valve acts as a separate resistance, and the resistance of each layer is equal to $R=(\rho\ell)/A$, where ρ=resistivity, ℓ=length and A=cross-sectional area. The total resistance of the spin valve is the sum of the resistances of all the layers added in parallel. The resistance model can be adapted to allow for the wire array structure patterned through the spin valve multilayer. Assuming that the milling is even across the surface, each layer acts as a variable resistor during milling and can be sectioned into two parts; α and β, where α represents the unpatterned part and β represents the patterned part, as shown in Fig. 7.5.

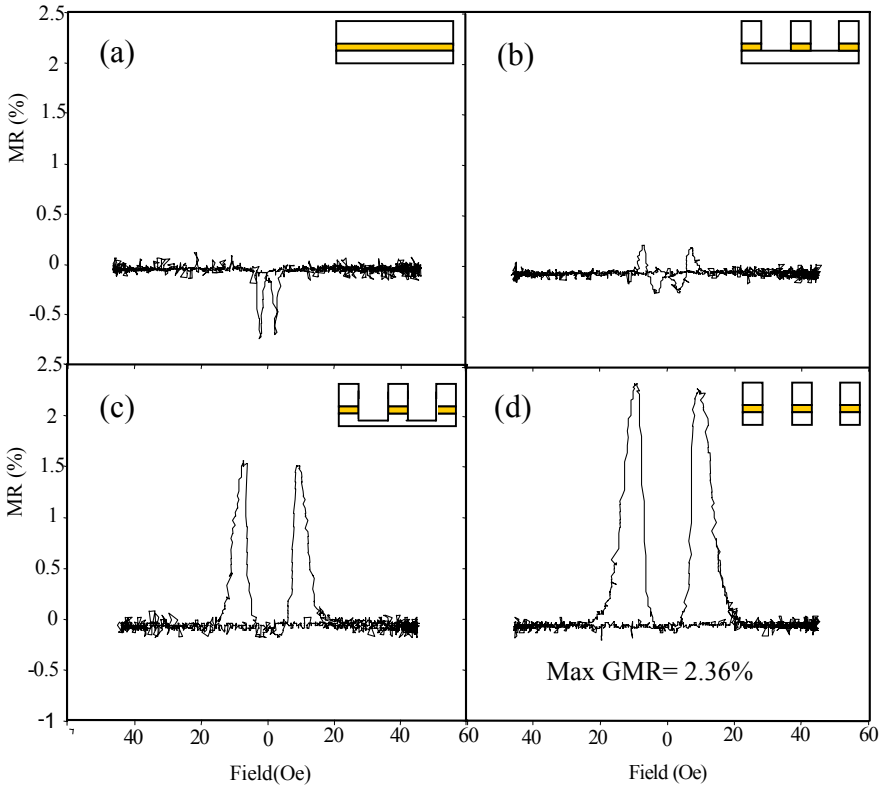

Fig. 7.4 *In-situ magnetoresistance measurements showing the evolution in transport properties when an array of 1.5μm wide wires is patterned in a $Ni_{80}Fe_{20}$/Cu pseudo spin valve sample.*

Figure 7.5 also shows the equation used to calculate the total resistance of the structure, which assumes the parts α and β as separate resistors in the model. According to the diagram, the total resistance of the top NiFe layer is the sum of the resistance of the α part plus the total resistance of each β-wire connected in parallel. When the layer is fully milled through the resistance is equal to the sum of the β-wires, because α is completely removed.

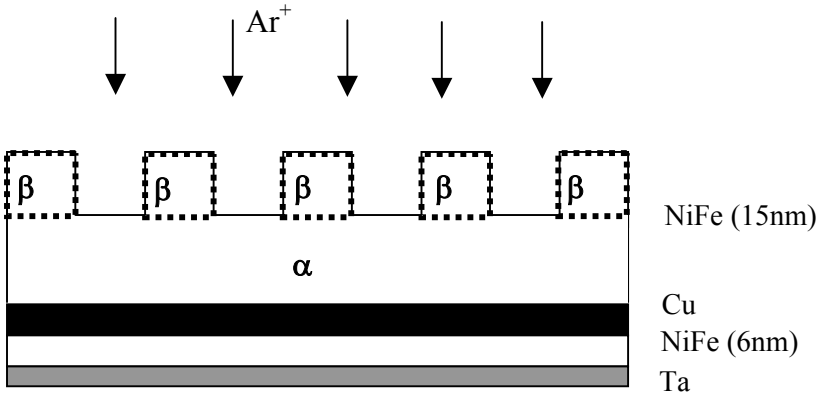

$$\frac{1}{R_{Total}} = \left(\left(\frac{1}{R_{\beta}} \times number \right) + \frac{1}{R_{\alpha}} \right)_{Py(15nm)} + \frac{1}{R_{Cu}} + \frac{1}{R_{Py(6nm)}} + \frac{1}{R_{Ta}}$$

Fig. 7.5 *A schematic diagram showing how the resistance model is used to calculate the total resistance of the pseudo spin valve as a micro-wire array is patterned through the top layer of the structure. During milling, each layer is divided into two parts: α and β, where α represents the unpatterned part and β represents the patterned part. The total resistance of the structure is calculated as shown by the equation.*

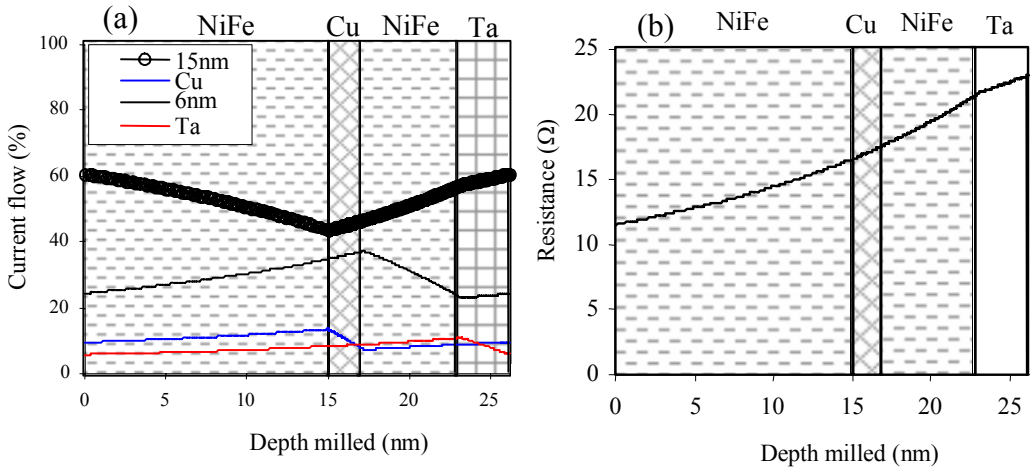

Fig. 7.6 *The percentage current flow through each layer in the NiFe/Cu/NiFe/Ta PSV as the 3μm wire array is milled through the structure according to the resistance model.(b) A graph to show the change in the resistance with milling depth calculated by the resistance model for the micro-patterned PSV structures.*

Figure 7.6 (a) shows the percentage current flow through each layer in the PSV as the 3μm wire array is milled through the structure according to the calculated resistance model.

Although a constant current is applied to the pseudo spin valve, the change in the shape of the layers during milling changes the current distribution throughout the structure. The graph shows that most of the current flow is through the two ferromagnetic layers with less than 15% traveling through the Cu interlayer and the Ta underlayer throughout the milling. In order to achieve accurate transport measurements it is important that the current is not shunted away from the ferromagnetic layers by lower resistance channels. Also, according to Chapter 6 the mean free path of the electrons in the $Ni_{80}Fe_{20}$ layer is approximately equal to the thickness of the layer before milling, i.e. ≈15nm. In Cu the mean free path is ≈20nm, which is much longer than the 2.2nm thickness. When the thickness is equal to or less than the mean free path, the electrons are forced to be distributed through the spin valve structure whatever the total resistance of the layers. In other words they travel through the structure without being scattered, apart from at the interfaces of the layers. Although the resistance of each layer and therefore the current distribution through the structure changes during milling, the MR information is not effected because the electrons are scattered through the entire structure. Fig. 7.6 (b) shows the resistance versus depth milled of the micro-patterned PSV as calculated by the resistance model. The graph represents the change in resistance with milling for the 3μm, 2μm and 1.5μm width wires, because although the wire width is decreased, the number of wires in a given area increases and therefore the total resistance of the spin valve structure remains the same. There are no obvious transitions regions between the $Ni_{80}Fe_{20}$ and Cu layers because the thin film resistivity values are similar, as shown in Fig. 6.19 in Chapter 6. A change in gradient can be seen when the milling continues through to the Ta underlayer because the resistivity is higher.

The resistance versus time data from the micro-patterning *in-situ* measurements was converted into resistance versus milling depth using the resistance model. The change in the shape of the magnetoresistance measurements could then be analysed with respect to the milling depth. Fig.7.7 shows how the AMR and GMR of the pseudo spin valve changed as the milling depth increased with patterning 2μm and 1.5μm wide wire arrays. The two graphs show the same trend; the AMR gradually decreases and the GMR rapidly increases with milling through the bottom ferromagnetic layer. The resistance of the sample at the peak GMR was input into the resistance model, which showed a milling depth of 23.4nm, i.e. when fully milled through.

Fig. 7.8 shows how the shape of the *in-situ* magnetoresistance measurements can be characterised in terms of the three reversal fields H_1, H_2 and H_3. H_1 is the switching field of the AMR signal, H_2 is the field representing the peak of the GMR signal and H_3 is the field required to saturate the GMR signal.

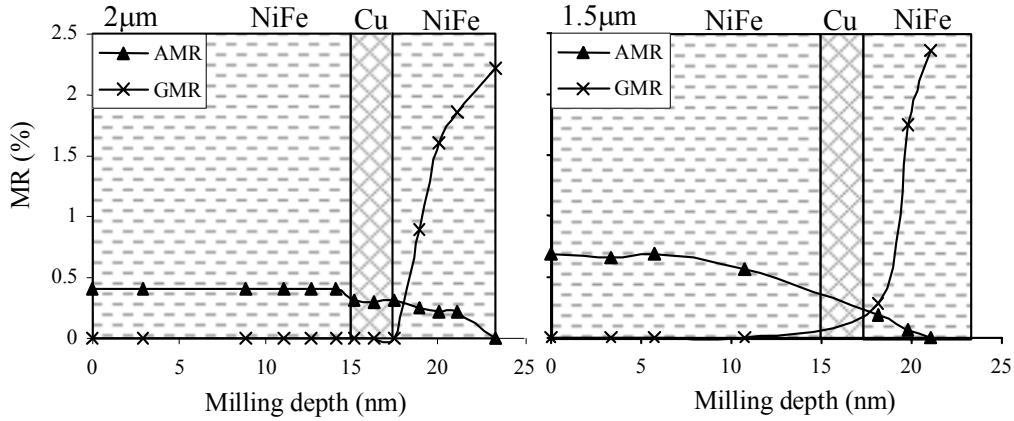

Fig. 7.7 *Graphs showing how the AMR and GMR of the pseudo spin valve structure changes as an array of 2µm (a) and 1.5µm (b) wide wires is patterned through the structure.*

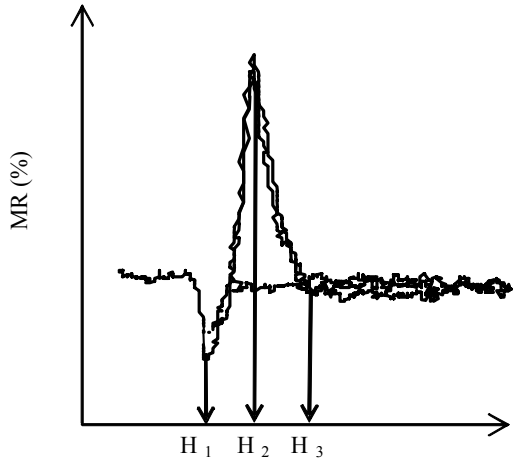

Fig. 7.8 *A graph of MR versus field demonstrating how the shape of the graphs can be characterised in terms of three reversal fields H_1, H_2 and H_3.*

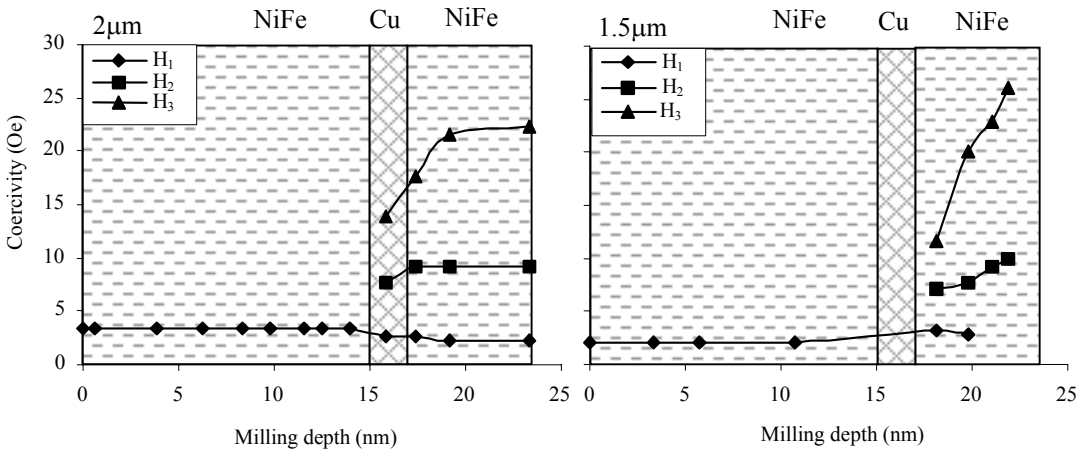

Fig. 7.9 *Graphs to show how the three reversal fields H_1, H_2 and H_3 change as an array of 2µm (a) and 1.5µm (b) wide wires is patterned through the PSV structure.*

Fig. 7.9 shows how the three reversal fields vary during milling of the wire arrays for (a) the 2μm wide wire array and (b) the 1.5μm wide wire array. Figures 7.7 and 7.9 show that although the AMR decreases as the milling depth increases, the reversal field H_1 remains approximately the same. The large increase in GMR as the structure is milled through the bottom ferromagnetic layer is accompanied by a small increase in reversal field H_2 of the peak GMR. The most significant change in reversal field with milling depth is shown by H_3, the field required to saturate the MR signal. Fig. 7.9 also shows how H_1, H_2 and H_3 change for the 1.5μm wide wire array. The change in shape is very similar to the 2μm wide wire array, except that H_2 and H_3 are larger with increasing milling depth.

Fig. 7.10 compares the final *in-situ* transport measurement of the 2μm wire array with the magnetic hysteresis after the sample was removed from the chamber.

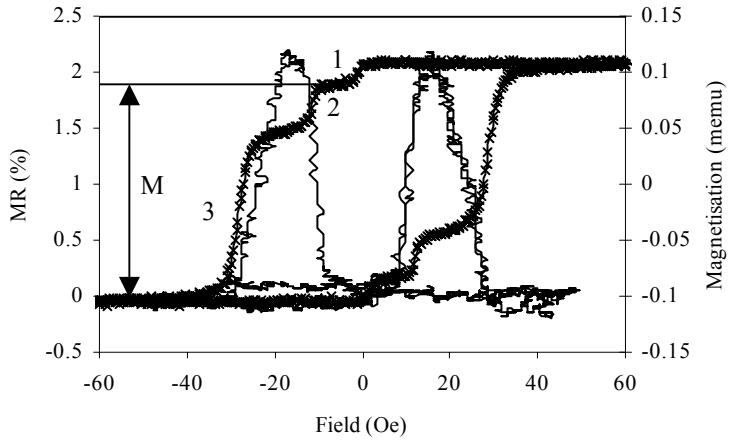

Fig. 7.10 *A graph comparing the transport and the magnetisation measurements for the fully milled through 2μm wide wire array in the pseudo spin valve structure. The numbers 1, 2 and 3 indicated three reversal steps in the magnetisation reversal, and the magnetisation M is equal to the total magnetisation of the wire array.*

The magnetisation measurement shows three reversal steps 1, 2 and 3. Step 1 corresponds to a small overlap between the spin valve material and the copper contact pads, which is not seen in the transport measurement. The magnetisation *M* represents the total magnetisation of the wire array, and steps 2 and 3 correspond to two parts in the magnetisation reversal. The value of step 1≈0.02memu and the initial magnetisation saturation before patterning of the pseudo spin valve ≈0.23memu. This shows that the overlap with the copper contact pad is ≈0.16mm on either side of the sample. The total magnetisation of the wire array ≈0.189memu, step 2 equals approximately 29% for the total magnetic material which corresponds to the 6nm thick NiFe layer. The magnetisation reversal of step three is proportional to the thickness of the 15nm thick ferromagnetic layer. Fig. 7.10 shows that the first part of the transport

measurement from zero field until the GMR peak corresponds to the reversal of the bottom 6nm NiFe layer. The change in the transport measurement from H_2 to H_3 is due to the reversal of the 15nm thick NiFe layer.

7.5 Induced anisotropy and shape anisotropy.

The effect of patterning the wires parallel and perpendicular to the induced anisotropy axis of the PSVs was also investigated. The initial measurements were carried out with the configuration shown in Fig. 5.9 (Chapter 5), where the shape anisotropy is in the same direction as the induced anisotropy in the thicker ferromagnetic layer. Fig. 7.11 shows the second configuration, where the shape anisotropy is perpendicular to the induced anisotropy during deposition. For both configurations, the field was applied along the length of the wires.

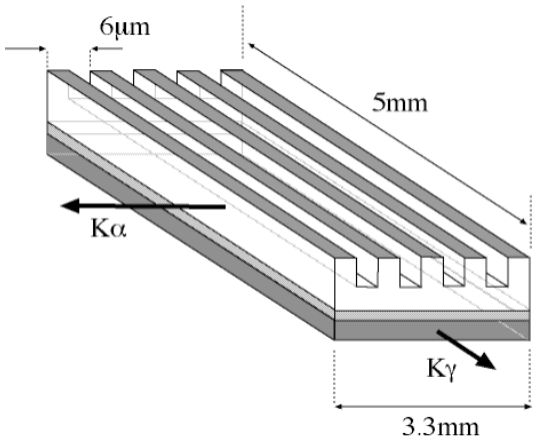

Fig. 7.11 *A schematic diagram showing the 3μm wide wire array with equal mark-space ratio being transferred into the pseudo spin valve during argon ion milling. The diagram also shows the anisotropy direction of the two ferromagnetic layers induced during deposition, K_α and K_γ. The induced anisotropy of the thicker ferromagnetic layer is perpendicular to the length of the patterned wires.*

Fig. 7.12 shows the evolution in the magnetic hysteresis as the 3μm wire array structure is patterned through the thickness of the $Ni_{80}Fe_{20}$ trilayer when the induced anisotropy in the thicker ferromagnetic layer and the shape anisotropy are (a) parallel, and (b) perpendicular. The insets in Fig. 7.12 show the relative orientation of the induced anisotropy (K_α and K_β) in the ferromagnetic layers with respect to the shape anisotropy (K_s). In (a) the applied field and induced anisotropy in the top layer (K_α) are parallel, and a square hysteresis loop is obtained for the plain film. In (b) the applied field and K_α are perpendicular, the plain film measurement shows less hysteresis and the shape is more characteristic of magnetisation rotation. This indicates that the magnetisation reversal is dominated by the induced anisotropy

in the thicker ferromagnetic layer. At a mill depth of ≈11nm, the results show that the magnetisation reversal still retains some of the characteristics of the plain film measurement, but there is a definite change in shape corresponding to the increased shape anisotropy energy, which changes the magnetisation reversal mechanism.

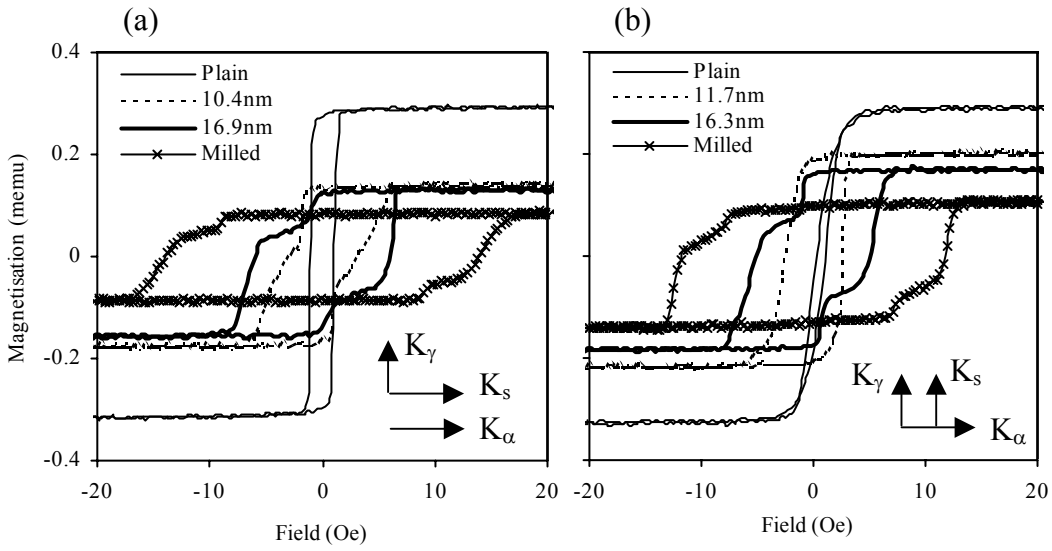

Fig. 7.12 *Hysteresis measurements for the $Ni_{80}Fe_{20}$ trilayer with a 3μm wide wire. The graphs show the evolution in the magnetic hysteresis as the anisotropic structure is patterned through the thickness when the shape anisotropy and the induced anisotropy in the thicker ferromagnetic layer are (a) parallel and (b) perpendicular. The insets show the relative orientations of the anisotropy in the thicker ferromagnetic layer K_α, the thinner ferromagnetic layer K_γ and the patterned shape anisotropy K_s.*

As the milling depth increases the shape anisotropy dominates and the fully milled through hysteresis measurements in (a) and (b) are similar. This result shows that the shape anisotropy energy is much larger than the anisotropy energy induced during deposition of the ferromagnetic layers. It also shows that the direction of the induced anisotropy energy doesn't need to be considered in the pseudo spin valve design when the shape anisotropy is large.

7.6 Thermal Stability Comparison.

Transport measurements were carried out at temperatures ranging between 291K and 493K to compare the thermal stability of the 2μm patterned PSV with an exchange biased spin valve of the construction:

Ta(5nm)/NiFe(2.5nm)/CoFe(2nm)/Cu(2.6nm)/CoFe(2nm)/IrMn(10nm)/Ta(5nm).

The conventional spin valve uses an IrMn antiferromagnetic pinning layer to create a uniaxial anisotropy in the adjacent CoFe ferromagnetic layer. The coupled NiFe and CoFe layers

underneath the copper reverse their magnetisation freely in an applied field. The samples were wire bonded and placed on a sample holder positioned in the centre of a quartz tube, which was sealed at one end to contain the heat. The quartz tube was resistively heated using a steel coil, which was wrapped in both directions to avoid any unwanted magnetic fields. The temperature was carefully monitored using a thermocouple attached to the sample holder in close proximity to the sample. The quartz tube was placed between the pole pieces of a magnet and four-point transport measurements were taken as the field was swept. Fig. 7.13 shows how the shape of the MR measurements changed as the temperature increased. Only half of the measurement (from positive to negative field sweep) is shown for clarity.

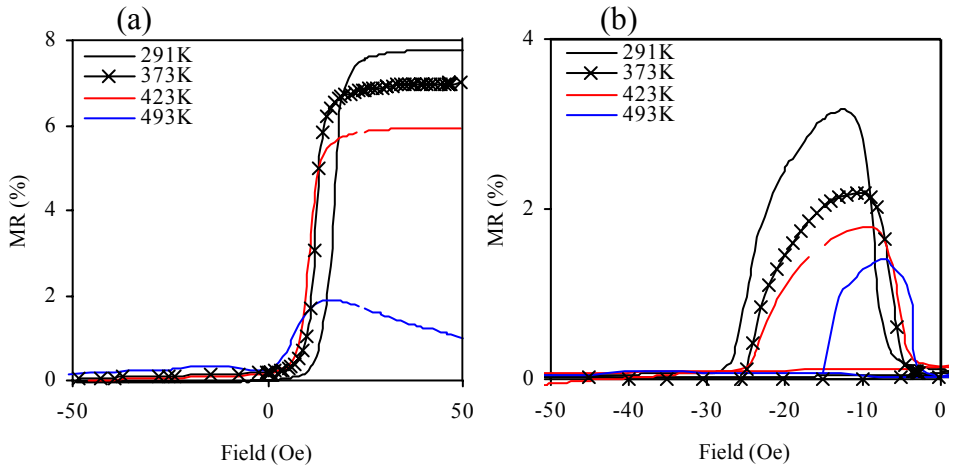

Fig. 7.13 *Graphs showing how the transport measurement changes with increasing temperature for (a) the conventional spin valve with an IrMn antiferromagnetic pinning layer, and (b) the 2μm wire array patterned pseudo spin valve.*

At room temperature the conventional spin valve shows the characteristic shape with a sharp change in MR close to zero field, which is caused by the free layer changing direction relative to the pinned ferromagnetic layer. As the temperature is increased the MR starts to decrease, partly due to a decrease in the spontaneous magnetisation of the NiFe layer, but also due to a decrease in the pinning properties of the IrMn antiferromagnetic pinning layer. As the pinning properties are decreased, the three ferromagnetic layers become more coupled together, and the relative orientations in an applied field become similar. The Curie temperature (T_c) of the NiFe layer is between 673 and 693K, and for CoFe the T_c is much higher ≈1253K [20]. The blocking temperature of IrMn is ≈523K [21]. As the measurement temperature approaches the IrMn blocking temperature, there is a large decrease in MR and the gradient of the graph also changes. The remaining MR≈1.77% is due to the difference in coercivities of the NiFe and CoFe layers. The PSV with the 2μm wire array also shows a decrease in MR due to the decrease in spontaneous magnetisation of the NiFe, however the relative change in MR over

the range of temperature is less than for the conventional spin valve. As the temperature increases the thermal energy seems to aid the magnetisation reversal and the graph becomes narrower and shifts closer to zero. Fig. 7.14 shows more clearly how the MR decreases with temperature for the conventional spin valve and the pseudo spin valve.

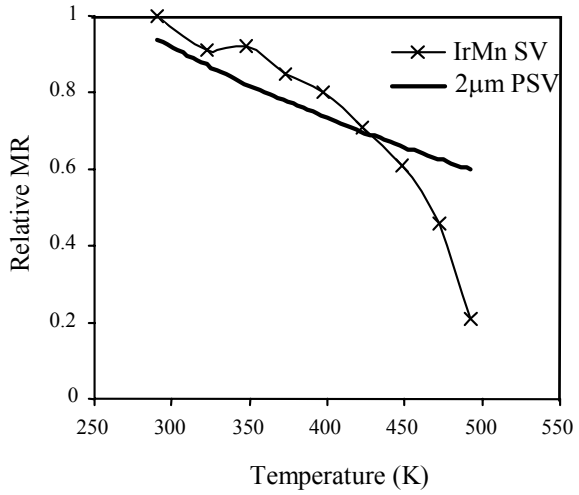

Fig. 7.14 *Graphs showing how the MR ratio decreases with increasing temperature for (a) the conventional spin valve with an IrMn antiferromagnetic pinning layer, and (b) the 2μm wire array patterned pseudo spin valve.*

Fig. 7.14 shows that the patterned pseudo spin valve has a higher thermal stability than the conventional spin valve above about 423K

7.7 Micro-patterning of CoFe Pseudo Spin Valves.

The previous results have shown that it is possible to create a PSV using NiFe and Cu, the next part of the experiment investigated whether the same effect could be observed using different materials. A pseudo spin valve with the construction:
Ta(3nm)/CoFe(6nm)/Cu(2.2nm)/CoFe(15nm)/Ta(3nm) was supplied by Nordiko. The spin valve was diced into 10mm by 5mm chips with the same anisotropy orientation as in the previous experiment; the anisotropy of the top 15nm thick ferromagnetic layer was parallel to the length of the chip and the anisotropy of the 6nm layer was perpendicular to the length. A VSM measurement was carried out to investigate the magnetisation reversal of the plain film. The same optical patterning and *in-situ* analysis was carried out to create a 1.5μm wide wire array in the CoFe/Cu/CoFe spin valve. After patterning the sample, another VSM measurement was taken in order to compare the before patterning and after patterning magnetisation reversal. Fig. 7.15 shows the fully milled through transport measurement and both VSM measurements.

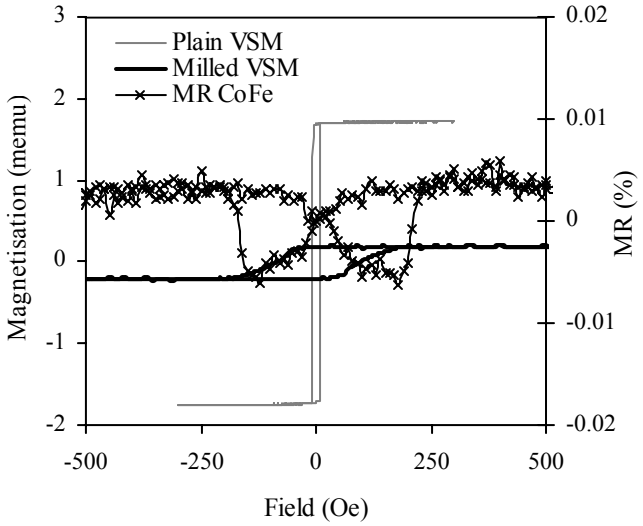

Fig. 7.15 *Graphs showing the magnetisation reversal of the unpatterned CoFe/Cu/CoFe spin valve along the 0° direction, the magnetisation reversal of the spin valve after patterning a 1.5μm wide wire array, and the transport measurement for the fully milled through structure along the length of the wires.*

The magnetisation reversal of the CoFe spin valve before patterning shows a single reversal loop, and the shape is characteristic of the anisotropy in the thicker ferromagnetic layer. This shows that the thicker ferromagnetic layer is dominating the reversal process, the same as for the unpatterned NiFe spin valve. However, the coercivity and magnetic saturation of the CoFe spin valve are larger than for the NiFe spin valve. For CoFe the M_s= 1.72Oe and H_c=7.5Oe, for NiFe M_s= 0.89Oe and H_c≈1Oe. When the 1.5μm wire array is patterned through the CoFe spin valve, the coercivity is considerably increased and the susceptibility decreases, but the hysteresis loop shows a single transition indicating that the two ferromagnetic layers are moving together. This is verified by the transport measurement, which shows a small AMR≈0.01% and the shape is characteristic of the anisotropy in the thicker ferromagnetic layer. This result shows that the induced shape anisotropy greatly increases the coercivity of the CoFe PSV, but it is not large enough to overcome the coupling between the ferromagnetic layers and allow them to move separately. As explained in Chapter 5, the coupling between the two ferromagnetic layers is due to magnetostatic energy and the interlayer coupling energy. The magnetostatic energy is directly related to the saturation induction B_s of the material, and B_s for CoFe≈2.45T and for $Ni_{80}Fe_{20}$≈0.7T. The saturation induction is 3.5× larger for CoFe than for NiFe, which is an indication that the magnetostatic energy is larger for CoFe than for NiFe. The interlayer coupling energy is related to the thickness of the non-magnetic interlayer and the exchange coupling constant A_{ex}. The thickness of the non-

magnetic interlayer is the same for both spin valves, so the interlayer coupling can be directly compared by the exchange coupling constant $A_{ex.}$ For CoFe $A_{ex}=3.0\times10^{-11}$J/m, almost five times larger than for NiFe where $A_{ex}=6.25\times10^{-12}$ J/m. This shows that the coupling between the CoFe PSV layers is stronger than for the NiFe layers due to larger magnetostatic and exchange coupling interactions.

7.8 Conclusions.

Previous work has shown that when an array of 3μm wide wires are patterned on the top layer of a ferromagnetic sandwich structure and milled through to the copper interlayer, a small spin valve response is shown. The results presented in this chapter show the progression of the change in the transport measurements as the milling depth is increased to the copper layer and then through the bottom layer to the substrate. The results in Chapter 5 suggest that the AMR can be attributed to the magnetisation rotation of the unpatterned layer, and the GMR corresponds with the switching of the patterned layer. These results support this theory and also show that increasing the milling depth through the bottom layer of the spin valve structure can decrease the AMR and increase the GMR of the samples. Finally it is shown that the maximum GMR is achieved when the material between the wires is completely removed. In this case the GMR is caused by the switching of the thinner layer at lower switching fields and the thicker layer at higher switching fields. The results show that there is an increase in GMR as the anisotropy of the structure is further increased by patterning with thinner wires. Magnetic hysteresis measurements have shown that the direction of the induced anisotropy during deposition does not have a significant effect on the device operation. At large milling depths the shape anisotropy dominates over the induced anisotropy. Temperature measurements have shown that the pseudo-spin valve has a better thermal stability than a conventional spin valve with an antiferromagnetic pinning layer. According to these results optimum device performance can be achieved using materials with low magnetostatic and interlayer coupling energies. However, the interlayer coupling energy is directly related to the Curie Temperature T_c, and a high Curie temperature is required for good thermal stability of the device. Therefore a compromise between high thermal stability and low interlayer coupling energy will need to be made for this device design. The results show that the optimum device design will have high shape anisotropy.

In-situ transport measurements on CoFe trilayers did not show a spin valve response with increasing shape anisotropy. This is believed to be due to larger magnetostatic and interlayer coupling energies. We anticipate that it will be possible to extend this work to the nanoscale for high density operation.

References

[1] J. H. J. Fluitman, *Thin Solid Films* **16**, 269 (1973)

[2] M. H. Kryder, K. Y. Ahn, N. J. Mazzeo, S. Schwarzi, and S. M. Kane, *IEEE Trans. Magn*. **16**, 99 (1980).

[3] C. Tsang and S. K. Decker, *J. Appl. Phys*. **53**, 2602 (1982)

[4] E. J. Ozimek and D. I. Paul, *J. Appl. Phys*. **55**, 2232 (1984)

[5] J. F. Smyth, S. Schultz, D. R. Fredkin, D. P. Kern, S. A. Rishton, M. Cali, and T. R. Koehler*, J. Appl. Phys.* **69**, 5262 (1991)

[6] C. Shearwood, S. J. Blundell, M. J. Baird, J. A. C. Bland, M. Gester, H. Ahmed, and H. P. Hughes, *J. Appl. Phys*. **75**, 5249 (1994)

[7] K. Hong and N. Giordano, *Phys. Rev. B* **51**, 9855 (1995)

[8] A. O. Adeyeye, J. A. C. Bland, C. Daboo, D. G. Hasko, and H. Ahmed, *J. Appl. Phys*. **82**, 469 (1997)

[9] K. J. Kirk, J. N. Chapman, and C. D. W. Wilkinson, Appl. Phys. Lett. **71**, 539 (1997); M. Rührig, B. Khamsehpour, K. J. Kirk, J. N. Chapman, P. Aitchison, S. McVite, and C. D. W. Wilkinson, *IEEE Trans. Magn.* **32**, 4452 (1996)

[10] T. Schrefl, J. Fidler, K. J. Kirk, and J. N. Chapman, *J. Magn. Magn. Mater*. **175**, 193 (1997)

[11] J. Shi, T. Zhu, M. Durlam, E. Chen, and S. Tehrani, *IEEE Trans. Magn*. **34**, 997 (1998); J. Shi, S. Tehrani, T. Zhu, Y. F. Zheng, and J. G. Zhu, *Appl. Phys. Lett*. **74**, 2525 (1999)

[12] J. McCord, A. Hurbert, G. Schröpfer, and U. Loreit, *IEEE Trans. Magn*. **32**, 4806 (1996)

[13] J. Gadbois, J. G. Zhu, W. Vavra, and A. Hurst, *IEEE Trans. Magn*. **34**, 1066 (1998)

[14] R. D. Gomez, T. V. Luu, A. O. Pak, K. J. Kirk, and J. N. Chapman, *J. Appl. Phys*. **85**, 2525 (1999).

[15] C. C. Yao, D. G. Hasko, Y. B. Xu, W. Y. Lee, and J. A. C. Bland, *J. Appl. Phys*. **85**, 1689 (1999)

[16] W. Y. Lee, Y. B. Xu, C. A. F. Vaz, A. Hirohata, H. T. Leung, C. C. Yao, B. C. Choi, J. A. C. Bland, F. Rousseaux, E. Cambril, and H. Launois, *IEEE Trans. Magn*. **35**, 3883 (1999)

[17] W. Y. Lee, S. Gardelis, B. C. Choi, Y. B. Xu, C. G. Smith, C. H. W. Barnes, D. A. Ritchie, E. H. Linfield, and J. A. C. Bland, *J. Appl. Phys*. **85**, 6682 (1999)

[18] F. G. Monzon, D. S. Patterson, and M. L. Roukes, *J. Magn. Magn. Mater*. **195**, 19 (1999)

[19] A. E. Berkowitz, K. Takano, *J. Magn. Magn. Mater*. **200,** 552-570, (1999)

[20] J. Evetts, *Concise Encyclopaedia of Magnetic and Superconducting Materials*, 216 and 352, Pergamon Press Ltd (1992)

[21] J. Nogués, I. Schuller, *J. Magn. Magn. Mater*. **192,** 203-232, (1999)

Our doubts are traitors, And make us lose the good that we oft may win, By fearing to attempt. *William Shakespeare.*

Chapter 8

In-Situ Nanopatterning of Pseudo Spin Valves.

The change in the electrical properties of nano-patterned Pseudo Spin Valve (PSV) structures of the form Ta(2nm)/$Ni_{80}Fe_{20}$(15nm)/Cu(2.2nm)/$Ni_{80}Fe_{20}$(6nm)/Ta(2nm) have been studied *in-situ* during patterning. Magnetoresistance measurements were taken as the shape of the nanowire array was milled through the PSV structure using a SiO_2 hard mask designed using Focused Ion Beam (FIB) lithography. The results show that as the shape anisotropy is increased by increasing the milling depth of the nanowires, the MR increases. Further increasing the shape anisotropy by decreasing the width of the wires also increases the MR, and the ferromagnetic materials are shown to be sensitive to the gallium ion dosage. Micromagnetic simulations confirm the experimental results and emphasise the importance of the closure domains at the end of the PSV wires in the magnetisation reversal process.

8.1 Motivations

Due to the recent advances in lithographic patterning techniques, it has been possible to study the magnetisation reversal and electrical properties of submicron mesostructures with a range of materials, geometries and dimensions [1-26]. From a fundamental point of view, as the particle dimensions become comparable to characteristic lengths such as the magnetic domain-wall size, interesting behaviour may be expected. The study of nanomagnetics is also important in applied physics, mainly due to the applications in data storage devices and sensors. High density data storage devices and magnetoelectronic devices are now being designed to take advantage of the properties of small magnetic structures. For example, arrays of small magnetic elements have been proposed as patterned media, in which each uniaxial element stores one bit of data [27-31]. Ferromagnetic wires can be engineered with high shape anisotropy so that the magnetisation is directed either parallel or antiparallel to the wire axis [32,33]. Magnetic logic gates have been suggested in which data can be manipulated through magnetostatic interactions between chains of magnetic elements [34].

Different mechanisms have been proposed for the magnetisation reversal of sub-micron mesostructures including coherent rotation [35], fanning [36], curling [37], or buckling [37]. More recently, experimental results have shown that other factors also need to be considered including edge roughness [38] and non-uniform magnetisation configurations [39].

There has been some discrepancy between the theory and experimental results obtained from nanopatterning PSV structures. The theory predicts that as the dimensions are reduced and the layers approach single domain, the amplitude of the GMR should increase due to the more perfect alignment of magnetisation within the layers [40]. However, the experimental results indicate that the GMR tends to decrease as the dimensions are reduced [41-43]. According to the authors, the electron scattering at the pattern edges plays a greater role in the electron transport when the pattern becomes narrow. Also, the ion-milling process can affect the transport behaviour at the edges of a pattern, which becomes significant in the narrow pattern. Both of these factors contribute towards the decrease in GMR. However, the experimental results tend to agree that as the dimensions are reduced, the coercivity of both the hard and soft layer is increased. The advantage of the *in-situ* magnetoresistance measurements carried out in this chapter is that they allow direct analysis of the change in the initial resistance R, and the change in the resistance in an applied field ΔR, during patterning. It is therefore possible to derive how much of the change in GMR is due to a change in the initial resistance of the structure and how much is due to the change in domain configuration.

Magnetotransport measurements have been shown to offer a sensitive probe of extremely small quantities of magnetic material, for example some work by Ono et al. studied the magnetic domain wall propagation in a single submicrometer wire [33]. Therefore, it is an ideal technique for characterising the change in electrical and magnetic properties of the nanopatterned PSVs. The FIB has been shown to produce high quality magnetic nanostructures in thin films of soft magnetic materials such as permalloy [44]. Other authors have demonstrated that Ga^+ ion irradiation can comprehensively modify the ferromagnetic properties of $Ni_{80}Fe_{20}$ thin films for high dosage densities [45].

This chapter starts by describing the sample preparation and analysis before nanopatterning, including transport measurements and Bitter technique imaging of the micro-patterned NiFe/Cu/NiFe mesostructures. Analysis was also carried out on CoFe/Cu/CoFe mesostructures. The next part describes the patterning in the FIB including the milling depth calibration using end-point detection, and the electrical and structural characterisation of the nanopatterned SiO_2 hard mask. Then *in-situ* measurement results are shown for three different wire widths nanopatterned in the PSVs. The final part of the chapter compares the experimental results with micromagnetic simulation.

8.2 FIB sample preparation and analysis.

Pseudo spin valves with the structure:
Ta(2nm)/$Ni_{80}Fe_{20}$(15nm)/Cu(2.2nm)/$Ni_{80}Fe_{20}$(6nm)/Ta(2nm) were micro-patterned using optical lithography and argon ion milling into a series of rectangles with lengths from 100 to 600μm and widths from 2μm to 45μm. The patterned rectangles showed aspect ratios from 1:2 to 1:300. The mask design shown in Fig. 4.5, chapter 4 was used for the lithography. This is an important step because it enables mapping of the chip during patterning in the FIB, and the position of each PSV rectangle is precisely known. Copper contact pads were deposited by sputtering. Each PSV rectangle was characterised using transport measurements to check the initial response of the structures before nanopatterning. Standard four-point measurements were carried out with current I=800μA applied along the length of the chip and the field applied along both the length (0°) and along the width (90°). The anisotropy direction of the 15nm $Ni_{80}Fe_{20}$ layer was along the length of the rectangle, and the anisotropy direction of the 6nm $Ni_{80}Fe_{20}$ layer was along the width of the rectangle. Fig. 8.1 shows the transport measurements with the field applied at 0° and 90° for the 36μm wide pseudo spin valve rectangle. The measurement is clearly dominated by the AMR of the top layer, which is in agreement with the results from the previous chapters. The longitudinal AMR is 0.16%, and the transverse AMR is 1.68%.

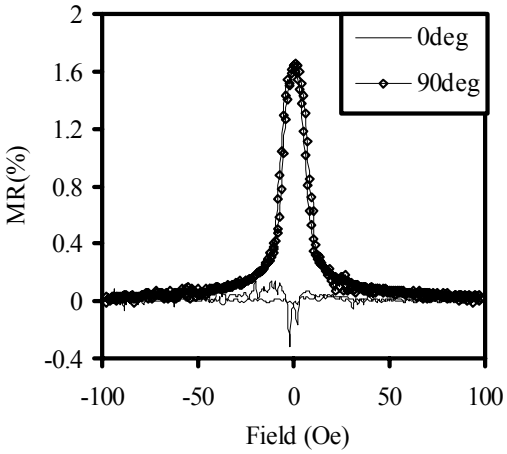

Fig. 8.1 *MR measurements with the field applied at 0° and 90° to the direction of the current for a 100μm by 36μm NiFe/Cu/NiFe PSV rectangle.*

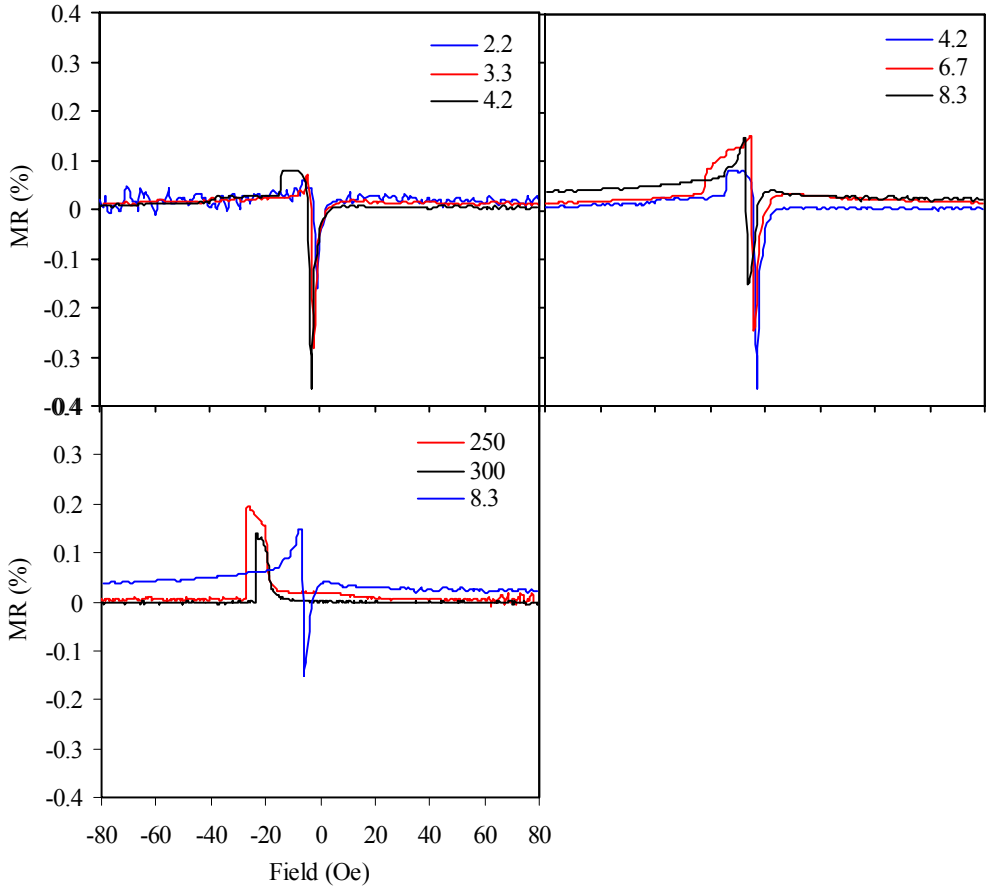

Fig. 8.2 *Consecutive transport measurements for the Ni/Cu/Ni PSVs showing the gradual change from AMR to GMR as the shape anisotropy is increased by patterning higher aspect ratios from 1:2.2 to 1:300. The decreasing field sweep from positive to negative field is shown for clarity.*

Fig. 8.2 shows the results from the transport measurements as the shape anisotropy of the structures was increased by increasing the aspect ratio from 2.2 to 300. For clarity, only half the graph is displayed. Initially as the aspect ratio increases the AMR increases because the shape anisotropy forces a more parallel alignment between the magnetisation and the current. However, as the aspect ratio continues to increase the AMR starts to decrease and a small GMR is shown. According to previous authors an increase in the shape anisotropy can lead to a decrease in the magnetostatic coupling between the two ferromagnetic layers [46]. A decrease in the magnetostatic coupling allows the ferromagnetic layers to move individually, and at an aspect ratio of 6.7 the transport measurement clearly shows a combined AMR and GMR. For large aspect ratios there is no AMR and the GMR reaches a peak value of 0.2%. The coercivity also increases as the shape anisotropy increases. If the coercivity is taken as the peak of the GMR, it increases from -8Oe to -27Oe. The results from the previous chapters have shown that the thinner layer reverses at a lower field than the thicker NiFe layer, and the high anisotropy structures show a distinct two-step reversal corresponding to the two ferromagnetic layers.

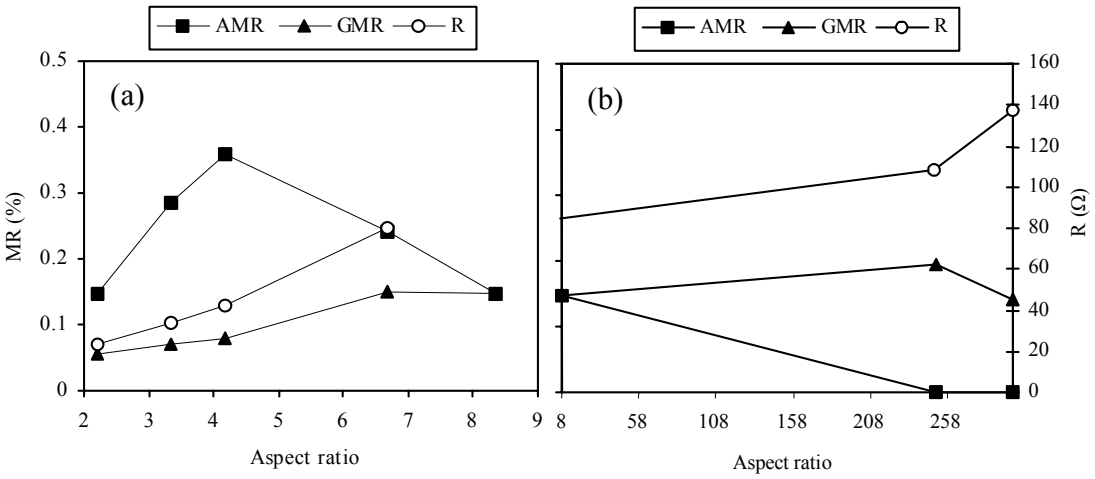

Fig. 8.3 *Graphs showing how the AMR, GMR and R change for low aspect ratios (a) and for high aspect ratios (b).*

Fig. 8.3 shows how the AMR, GMR and R change for low aspect ratios (a) and for high aspect ratios (b). For low aspect ratios the AMR increases, peaking at about 4, and then decreases. The R and the GMR follow the same trend and increase as the aspect ratio increases. For high aspect ratios the AMR drops to zero, and the GMR and R continue to rise gradually until the R rises steeply and the GMR drops off. This data indicates that the decrease in GMR at high ratios is related to the increase in the initial resistance. The AMR decreases when the shape anisotropy is high, due to the difficulty in forming a multi-domain

structure. When the shape anisotropy is high the magnetisation will tend to align along the length of the sample in zero field instead of forming a multi-domain configuration. The initial increase in GMR is because the ferromagnetic layers become decoupled due to a decrease in magnetostatic coupling through domain walls in the layers. These results are in agreement with the previous chapters, but it is interesting to note that the shape anisotropy starts to change the magnetisation reversal process at much smaller ratios than previously thought necessary. However, it is also worth noting that the GMR is much smaller (0.2%) with the lower aspect ratio. In the previous chapter a maximum MR of 2.36% was observed for 1.5μm wide wires with an aspect ratio of 2666.

A bitter technique image was taken of a patterned NiFe/Cu/NiFe PSV sample with 50μm wide tracks in the absence of an applied field as shown in Fig. 8.4. The anisotropy of the top ferromagnetic layer, K_u, is along the width of the tracks as shown in the diagram. The anisotropy of the bottom layer is along the length. The previous results have shown that the magnetisation is dominated by the top ferromagnetic layer, and the Bitter technique image shows a multi-domain structure. Since the layers are coupled, we can assume the same domain configuration in both layers. It is possible to estimate the total anisotropy energy of the PSV bilayer from the bitter technique image by summing the energy contributions of the domains and the domain walls and then minimising the total energy as shown in the calculation below.

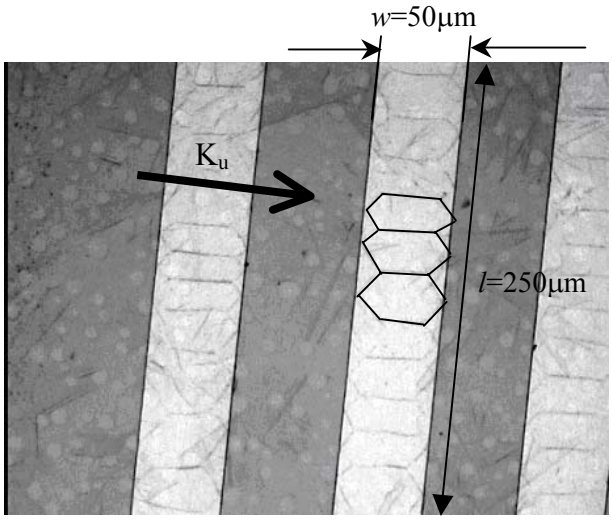

Fig. 8.4 *A Bitter Technique image of the NiFe/Cu/NiFe pseudo spin valve patterned into 50μm wide tracks. The anisotropy direction of the top ferromagnetic layer, K_u, is along the width of the tracks, and the image clearly shows the domain configuration.*

The total energy of the domain configuration is given by Eqn. (8.1).

$$E_{tot} = K_u A\left(t_{top}\sin^2\theta_{top} + t_{bottom}\sin^2\theta_{bottom}\right) + K_u A_1\left(t_{top}\sin^2\theta_{top} + t_{bottom}\sin^2\theta_{bottom}\right) + \\ + \gamma_{180}A_2 + \gamma_{90}A_3 \qquad (8.1)$$

The total energy E_{tot} includes terms from both the top and bottom ferromagnetic layers, where K_u is the anisotropy energy in (J/m^3), θ is the angle between the domain orientation and the anisotropy direction in the layer, A is the area of the domains perpendicular to the wire axis, A_1 is the area of domains parallel to the wire axis, A_2 is the area of the 180° domain walls, A_3 is the area of the 90° domain walls. Note that A and A_1 are areas in the x-y plane, while A_2 and A_3 area areas in the x-z plane. γ_{180} is the energy of the 180° domain walls (J/m^2), and γ_{90} is the energy of the 90° domain walls (J/m^2).

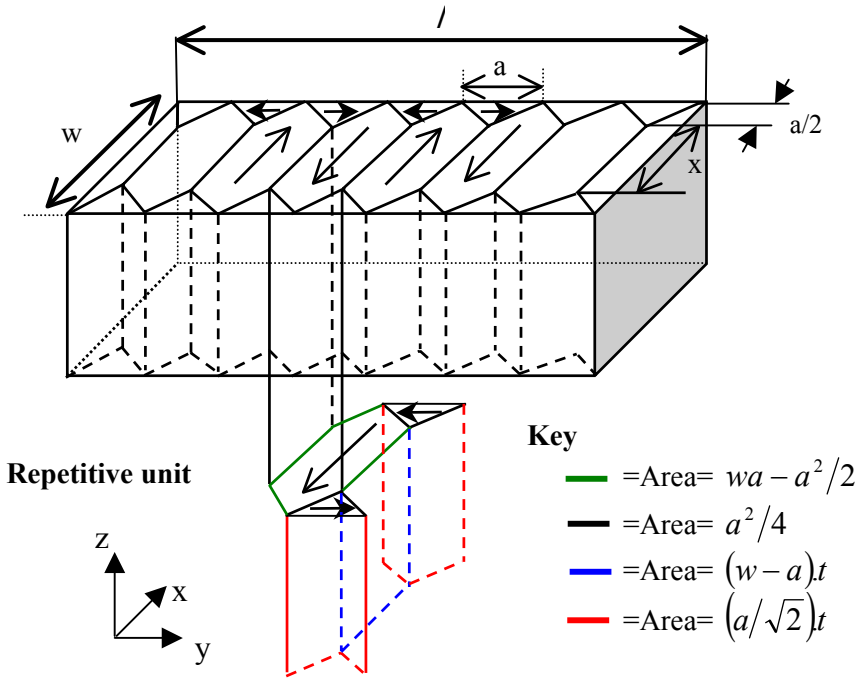

Fig. 8.5 *Schematic diagram of the domain configuration showing how the total energy of the PSV was calculated by taking into account the energy of different parts of the domain structure including the domain aligned with the induced anisotropy axis, the closure domains, the 180° domain walls an the 90° domain walls.*

The energy of a 180° domain wall is given by Eqn. (8.2).

$$\gamma_{180} = 4\sqrt{A_{ex}K_u} \qquad (8.2)$$

The energy of a 90° domain wall is given by Eqn. (8.3).

$$\gamma_{90} = 2\sqrt{A_{ex}K_u} \tag{8.3}$$

Where A_{ex} is the exchange coupling constant for NiFe, which is equal to 6.25×10^{-12} J/m

Fig. 8.5 is a schematic diagram of the domain configuration showing how the total energy of the PSV structure was calculated by taking into account the different parts of the domain structure. The total energy of the domain configuration given in Eqn. (8.1) can be simplified because the energy contribution from the domains aligned in the anisotropy direction is zero. Therefore the total energy of the domain configuration is simplified to Eqn. (8.4).

$$E_{tot} = K_u(At_{bottom} + A_1t_{top}) + 4\sqrt{A_{ex}K_u}A_2 + 2\sqrt{A_{ex}K_u}A_3 \tag{8.4}$$

The areas A, A_1, A_2 and A_3 can be calculated by multiplying the area of each part in the repetitive unit by the number of units (l/a), as shown below.
A corresponds to the area of the domains (shown in green in Fig. 8.5)

$$A = \left(wa - \frac{a^2}{2}\right)\frac{l}{a} = wl - \frac{la}{2} \tag{8.5}$$

A_1 corresponds to the area of the closure domains (black in Fig. 8.5):

$$A_1 = \frac{2l}{a}\times\left(\frac{a}{2}\times\frac{a}{2}\right) = \frac{la}{2} \tag{8.6}$$

The area of the 180° domain walls (shown in blue):

$$A_2 = \left(\frac{l}{a}\right)\times(w-a)t = lt\left(\frac{w}{a}-1\right) \tag{8.7}$$

The area of the 90° domain walls (shown in red):

$$A_3 = \left(\frac{4l}{a}\right)\times\left[\sqrt{\left(\frac{a}{2}\right)^2+\left(\frac{a}{2}\right)^2}\right]\times t = \frac{4\ell t}{\sqrt{2}} \tag{8.8}$$

Substituting these values back into Eqn. (8.4) gives the total energy according to the dimensions from the Bitter Technique image.

$$E_{TOT} = K_u\left(wl-\frac{la}{2}\right)t_{bottom} + K_u\left(\frac{la}{2}\right)t_{top} + 4\sqrt{A_{ex}K_u}\left[lt\left(\frac{w}{a}-1\right)\right] + 2\sqrt{A_{ex}K_u}\left(\frac{4lt}{\sqrt{2}}\right) \tag{8.9}$$

To find the total anisotropy energy of the PSV, the total energy is differentiated with respect to *a,* and then minimised by setting equal to zero. This gives K_u as shown in Eqn. (8.10)

$$K_u = 64\frac{A_{ex}w^2}{a^4}\left(\frac{t}{t_{top}-t_{bottom}}\right)^2 \tag{8.10}$$

According to the Bitter technique image and the PSV construction, w=50μm, a=22.1μm, A_{ex}=6.25×10^{-12}J/m, t=21nm, t_{top}=15nm, t_{bottom}=6nm giving K_u=22.8J/m^3.

A NiFe film was deposited in an applied field and the anisotropy was measured as ≈400J/m^3, which is much larger than the calculated value for the PSV structure. The low anisotropy constant could be due to interlayer coupling between the two ferromagnetic layers. This coupling can be added as an extra term, J (J/m^2), to the total energy of the structure E_{TOT} given in Eqn. (8.9), as shown in Eqn (8.11), where A_{TOT} is the total area over which the layers are coupled together and θ is the angle between the two NiFe layers.

$$E_{TOT} = K_u\left(wl-\frac{la}{2}\right)t_{bottom} + K_u\left(\frac{la}{2}\right)t_{top} + 4\sqrt{A_{ex}K_u}\left[lt\left(\frac{w}{a}-1\right)\right] + 2\sqrt{A_{ex}K_u}\left(\frac{4lt}{\sqrt{2}}\right) - J(\cos\theta)A_{TOT} \tag{8.11}$$

The surface coupling J is a minimum when the layers are parallel and maximum when they are antiparallel. We know from the magnetic hysteresis measurements in the previous chapters that the layers are parallel (cosθ=1), and according to Fig. 8.5, A_{TOT} can be replaced by lw. The surface coupling can be calculated from Eqn. (8.11): E_{TOT} with K_u=22.85J/m^3 has to be the same energy as E_{TOT} with K_u=400J/m^3 plus the term for the interlayer coupling:

$$E_{TOT}\left(K_u = 22.8\,J/m^3\right) = E_{TOT}\left(K_u = 400\,J/m^3\right) - Jlw \tag{8.12}$$

When l=250μm, and w=50μm, **J=3.19×10^{-6}J/m^2**.

If we multiply the PSV surface coupling constant J by the Cu interlayer thickness (Cu=2.2nm) to get the coupling energy per unit distance, we can compare this value with the exchange coupling constant A_{ex} for NiFe.

J×(2.2×10^{-9})=**7.01×10^{-15}J/m**

A_{ex}=6.25×10^{-12} J/m and the coupling energy per unit distance between the ferromagnetic layers in the PSV≈7.01×10^{-15} J/m. From this calculation we can see that the exchange

coupling between the atomic magnetic moments is ≈900× larger than the coupling between the ferromagnetic layers in the NiFe/Cu/NiFe PSV.

8.3 FIB Nanopatterning the Pseudo Spin Valves.

RF sputter deposition was used to deposit ≈50nm of SiO_2 on top of the micropatterned NiFe/Cu/NiFe spin valve structures. DC Sputter deposition was then used to deposit ≈20nm of Au to enable imaging in the FIB. Before the nanowires were patterned into the hard mask, the milling time was calibrated using end-point detection (EPD) as described in chapter 4. This technique measures the absorbed current from the specimen stage. The absorbed current changes when the ion beam interacts with different materials, and shows a striking difference between dielectric and metallic materials. For metals the absorbed current increases, whilst for dielectric materials the absorbed current decreases. This technique was used to measure the amount of time it takes to mill half way through the silica layer, which was the milling depth required for the hard mask.

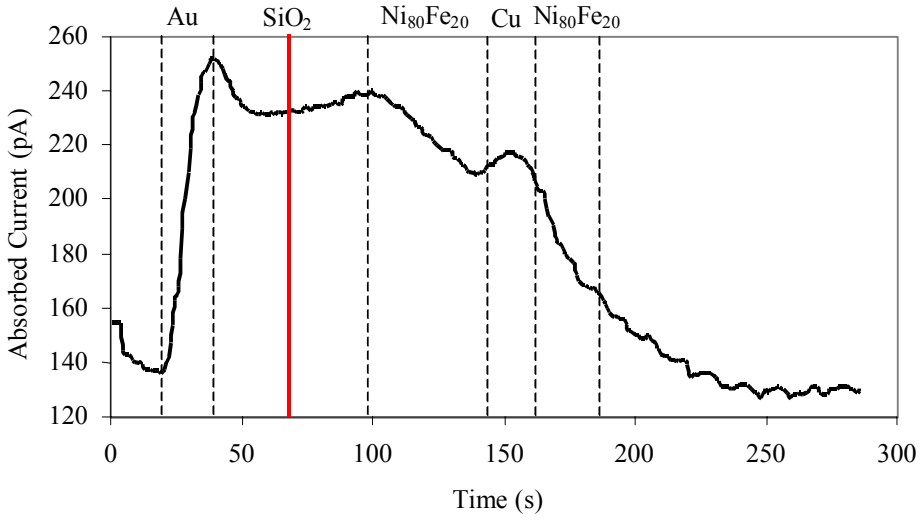

Fig. 8.6 *End-point detection calibration from the FIB for a current of 80pA and a voltage of 30keV. The dotted lines indicate milling through the different layers in the structure and the red line is the stopping distance for the silica hard mask.*

Fig. 8.6 shows the calibration EPD from the FIB. The dotted lines indicate milling through the different layers in the structure, the Au is milled away after the first 30s, and after 100s the milling has gone through the silica layer. The structure is fully milled through after 180s, and then the Ga ions are milling the Si substrate. The red line of the graph is the stopping time, which is the amount of time it takes to mill approximately half way through the silica layer ≈60s. This stopping time was chosen because the step height was enough carry out the *in-situ*

milling through the spin valve before milling away the SiO_2 hard mask. The structure and milling depth were verified using FIB imaging and AFM analysis as shown in Fig. 8.7.

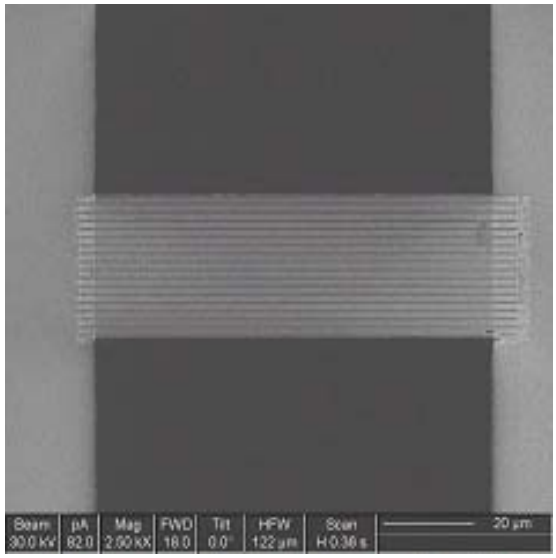

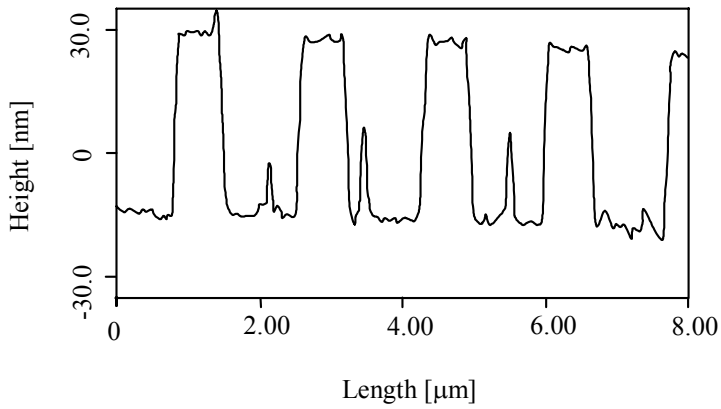

	Wire Width (nm)	Wire Gap (nm)	Wire Height (nm)	Aspect Ratio
Sample 1	734	984	41	136
Sample 2	468	957	42	213
Sample 3	265	1000	41	377

Fig. 8.7 *FIB image (above) showing the silica nanowire array on top of the NiFe/Cu/NiFe micropatterned mesostructure. AFM cross-section analysis (middle) was used to characterise the wire width, gap and height. A table is shown (bottom) with the dimensions of the nanopatterned wire array according to the AFM analysis.*

The table in Fig. 8.7 shows the width of the patterned wires, the gap between the wires and the height for three different samples taken from the AFM analysis. The values for wire width, gap and height are the average values taken from 30 measurements across the wire

arrays. Three samples were prepared to study the effect of increasing the anisotropy and decreasing the wire width of the PSVs on the nanoscale. The length of the wire arrays was 100μm and the width of the wires varied from ≈260nm to ≈730nm, creating aspect ratios from 136 to 377. The gap between the wires in the arrays was deliberately made large to avoid magnetostatic coupling effects.

Fig. 8.8 shows transport measurements taken directly before and after patterning the silica hard layer directly above the PSV with aspect ratio 136 in the FIB. Despite the use of the SiO_2 barrier layer, the Ga ions implanted the spin valve structure and changed the natural similarity of the two ferromagnetic layers. The initial AMR of the spin valve changed to a small GMR ≈0.13% and the coercivity increased from 4.93 to 17.67Oe. Previous authors have investigated the effect of the Ga ion implantation on the magnetic properties of ferromagnetic materials [44,45]. It was found that ion doses as low as 3.0×10^{14} ions/cm^2 at 30keV could change the magnetic properties of 15.5nm thick $Ni_{80}Fe_{20}$ ferromagnetic thin films. A dose of 1.0×10^{16} ions/cm^2 was enough to render the material non-ferromagnetic at room temperature. The results also showed that the coercivity decreased with increasing dosage, which was due to compositional changes from ion implantation. The ion dosage for the sample shown in Fig. 8.8 below is 3.3×10^{16} ions/cm^2, which is normally high enough to render the material non-ferromagnetic, but the PSV is protected by the silica barrier layer.

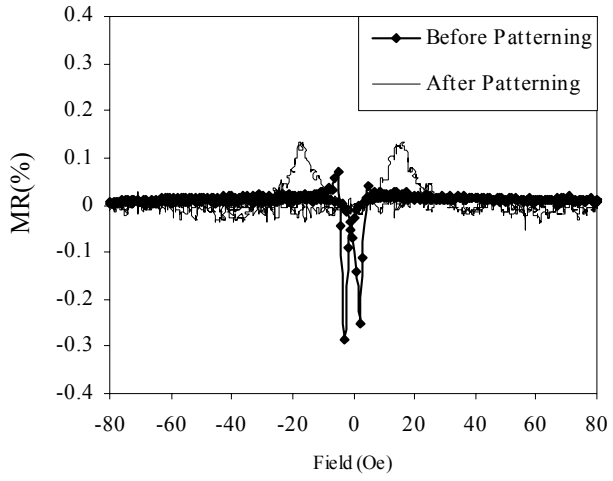

Fig. 8.8 *Transport measurements of the NiFe/Cu/NiFe PSV directly before and after patterning the silica hard mask in the FIB.*

Initially the Ga^+ implantation is not a problem because the silica layer is 50nm thick, and according to previous authors the implantation depth in silica at 30keV is 25± 8nm [49]. However, when the nanowire array is patterned in the silica, the layer is milled to half the depth. It is therefore likely that there is some ion implantation in the top (15nm) thick NiFe

layer of the PSV. The shape change in the transport measurement does not agree with previous authors reports of a decrease in coercivity with increasing dosage density. However, it can be explained by the ions inducing a local anisotropy in the structure. In other words even before any milling is carried out through the spin valve, the Ga implantation through the SiO_2 hard has locally changed the magnetic properties of the top ferromagnetic layer in the form of a highly anisotropic wire array.

8.4 *In-situ* Nanopatterning MR Measurements.

The three PSV samples with nanopatterned silica hard masks were loaded into the *in-situ* magnetoresistance measurement rig. A current of 1.5mA was supplied to the sample, the gain of the voltage amplifier was set to ×50 and a lock-in amplifier was used to minimise the noise and maximise the sensitivity of the measurement. Fig. 8.9 shows the evolution in the transport measurements for the 265nm wide wire array with aspect ratio 377 as the structure is gradually milled through. The graphs show that as the sample is milled, the MR gradually increases reaching a peak value of approximately 1.47%. As the milling continues the MR decreases, the insets indicate the milling depth as calculated by the Resistance Model described in Chapter 6.8 and Chapter 7.4. The MR measurements reach a rounded maximum rather than plateaux, which shows that the two ferromagnetic layers are not completely decoupled. The value of the MR is comparable with results from previous authors, for example Ross *et al.* patterned 250μm long and 60nm wide wires from NiFe/Cu/Co/Cu film and achieved an MR of ≈0.8% [47].

Fig. 8.10 shows a comparison between the initial measurement and the maximum MR from the fully milled through structure. By overlaying the graphs it is possible to study the change in the coercivity of the soft (H_{c1}) and hard (H_{c2}) ferromagnetic layers. The coercivity of the soft layer remains almost the same, but the coercivity of the hard layer shows an obvious increase. As explained in the introduction, previous work has shown that the coercivity of ferromagnetic thin films tends to increase as the thickness is decreased [48]. However, in these measurements the initial reversal field H_{c1} corresponds to the reversal of the thinner ferromagnetic layer and H_{c2} to the reversal of the thicker layer. This will be explained by the micromagnetic simulations in section 7.7. These results show that the MR increases as the nanowire array is patterned through the thickness of the PSV, reaching a maximum when fully milled through.

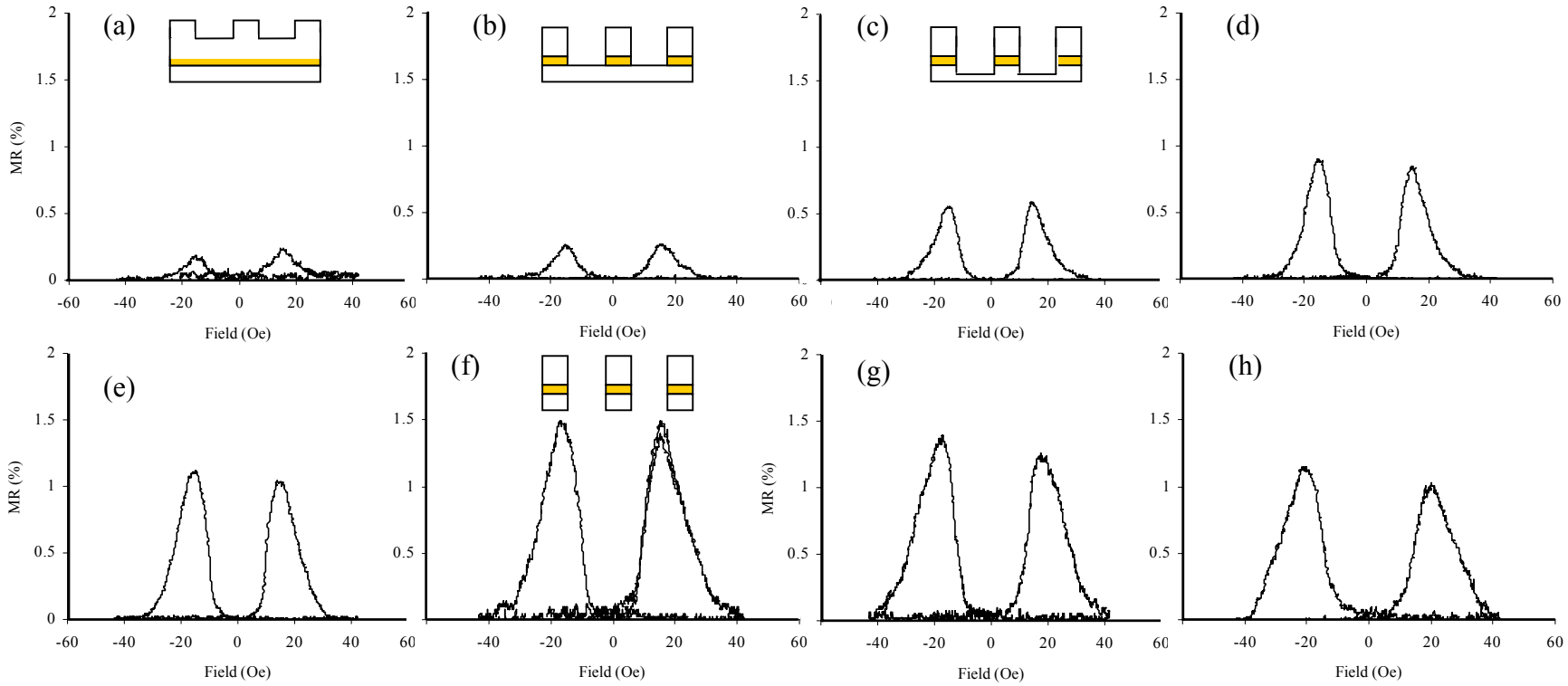

Fig. 8.9 *In-situ nanopatterning magnetoresistance measurements for a NiFe/Cu/NiFe PSV wire array with w≈265nm and aspect ratio 377. Graphs (a) to (h) show the evolution in the transport properties as the nanowire array structure is milled through the PSV.*

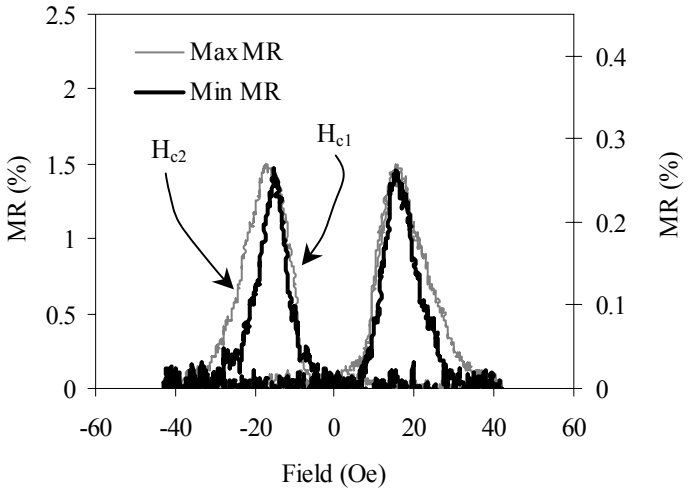

Fig. 8.10 *Graphs showing the initial and maximum MR measurements from the in-situ analysis of NiFe/Cu/NiFe PSV with wire width w=265nm and aspect ratio 377. The y-axis on the left is for the maximum MR measurement and the y-axis on the right is for the initial MR measurement before argon ion milling. H_{c1} indicates the magnetisation reversal field for the soft (thinner) ferromagnetic layer, and H_{c2} is the magnetisation reversal field for the hard (thicker) ferromagnetic layer.*

Fig. 8.11 shows the evolution in the transport measurements for the 730nm wide wire array with aspect ratio 137. The results show the same trend as for the PSV with 265nm wide wires. The MR gradually increases with increasing milling depth until it reaches a maximum of 1.1% when the nanowire array is fully milled through the PSV. The MR then decreases as the milling continues because the argon ions have milled through the silica mask and are milling the entire structure. The switching fields H_{c1} and H_{c2} also show the same trend. The final measurement on the 468nm wide wire array with aspect ratio 213 also showed the same trend, with a maximum MR of 2.35%. It is interesting to note that most of the increase in MR occurs when milling through the bottom (6nm) ferromagnetic layer, as shown in Fig. 8.12 for the 265nm wide wire array. Fig. 8.12 shows the change in MR, the resistance in zero field *R* and the change in resistance in an applied field *dR* as the milling depth increases through the spin valve. The resistance increases with milling depth as expected, but *dR* and MR increase more sharply as the milling continues past the copper interlayer (17.2nm) through the bottom ferromagnetic layer.

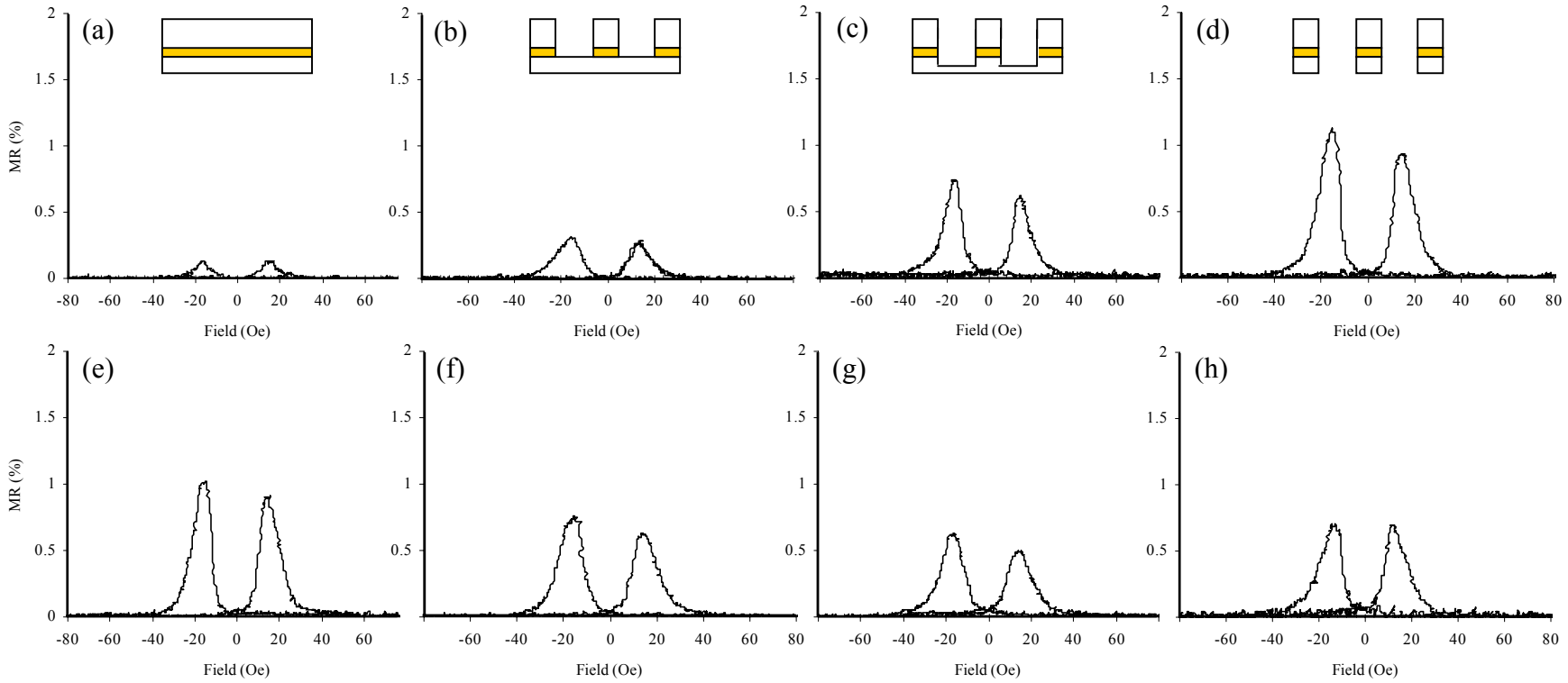

Fig. 8.11 *In-situ nanopatterning magnetoresistance measurements for a NiFe/Cu/NiFe PSV wire array with wire width w≈730nm and aspect ratio 137. Graphs (a) to (h) show the evolution in the transport properties as the nanowire array structure is milled through the PSV.*

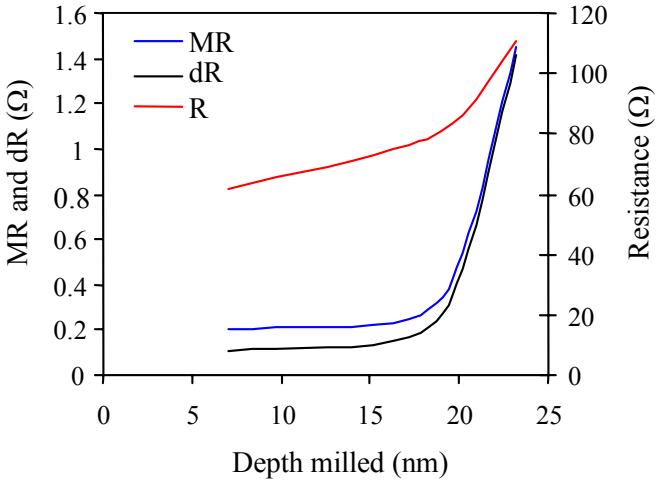

Fig. 8.12 *A graph showing how in MR, resistance in zero applied field R and the change in resistance in an applied field dR increase as the milling depth increases for a nanowire array with wire width ≈265nm.*

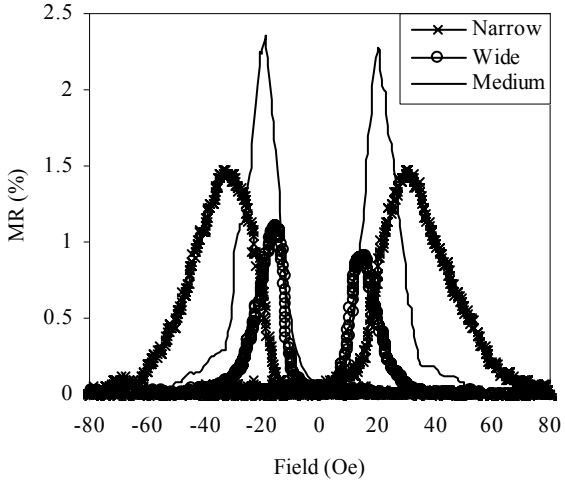

Wire width (nm)	Aspect ratio	H_{c1} (Oe)	H_{c2} (Oe)	Peak MR (%)
734	137	12	22	1.1
468	213	15	29	2.35
265	377	20	48	1.47

Fig. 8.13 *Graphs of the fully milled through in-situ magnetoresistance measurements from three different nanopatterned PSV samples with narrow (265nm), medium (468nm) and wide (734nm) wires. The table below the graphs summarises the differences between the measurements.*

Fig. 8.13 shows the fully milled through MR measurements for the three different patterned nanowire arrays; narrow (260nm), medium (460nm) and wide (730nm), and the table below

the graphs summaries the differences between the measurements. The switching fields of the soft and hard layers are H_{c1} and H_{c2} respectively, and are taken as the midpoint of the line. The results show that as the wire width is decreased (from 734nm to 468nm), the peak MR increased, but decreased for wire width 265nm. Also H_{c1} for the medium and wide wires are very similar, whilst H_{c1} for the narrow wires is larger. Generally H_{c2} increases as the wire width decreases. The change in H_{c1} and peak MR can be explained by looking at the Ga ion dosage density of the PSVs. For the 734nm wide array 62% of the total area was patterned, for the 468nm wide array 68% of the total area was patterned and for the 234nm array 87% of the total area was patterned. A much higher percentage of the total area for the 234nm wide array was implanted with Ga ions. Fig. 8.8 showed that the implanted Ga ions modified the transport measurement from AMR to GMR by inducing a high anisotropy structure by locally changing the magnetic properties of the top layer of the spin valve. The increased anisotropy of the top layer (hard) changed the natural similarity of the two ferromagnetic layers and the thinner (soft) layer was able to reverse more independently. The situation is similar for the 234nm wide wire array, except that the Ga ions have produced a higher anisotropy structure and therefore H_{c1} and H_{c2} are increased to higher values. Edge roughness can also increase the switching fields, and this becomes more significant as the wire width is decreased.

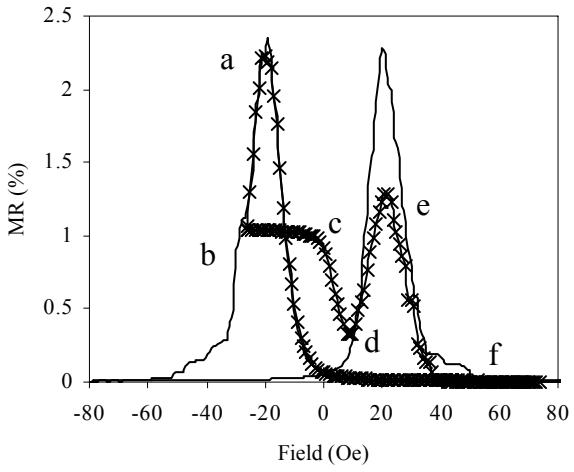

Fig. 8.14 *A graph showing the fully milled through MR measurement and minor loop analysis of the 468nm nanopatterned wide wire array.*

Fig. 8.14 shows the fully milled through MR measurement and minor loop analysis for the 468nm nanopatterned wire array. The different parts of the minor loop analysis are identified with letters from from *a-f* to guide the discussion. At a high positive field the MR is a minimum because the ferromagnetic layers are parallel with respect to one another. When the field is applied in the negative direction the resistance rises and the letter *a* indicates the

reversal of the thinner (soft) ferromagnetic layer. The layers do not achieve complete antiparallel alignment because a plateaux is not seen in the MR. The change from *a* to *b* is due to the reversal of the thicker (hard) layer, at point *b* the thicker layer has not completely reversed. At a field of -25Oe, the direction of the applied field is changed and initially no change in MR is observed, this indicates that the magnetisation of the hard layer is irreversible. When the field goes past zero, at *c* the soft layer starts to rotate towards the hard layer and at point *d* it moves past the hard layer and completes its reversal at *e*. The change in MR from *e* to *f* is the hard layer aligning with the field direction. At point *d* the two layers move past each other, but the MR doesn't reach the same minimum seen at saturation. This shows a spread in the magnetisation, perhaps due to closure domain like structures close to the edges.

8.5 Micromagnetic Simulations.

Micromagnetic simulations were carried out to investigate the magnetisation reversal of PSV nanowires at different milling depths and wire widths, using the micromagnetic software package LLG Micromagnetics Simulator™. LLG Micromagnetics Simulator™ is a full 3-dimensional simulation tool with integrated graphics that solves the Landau-Liftshitz-Gilbert-Langevin equations by relaxation and/or integration. With LLG, you can characterise micromagnetic structure and dynamics in films, on surfaces and in devices and materials. For further details of the theory behind the LLG Micromagnetics Simulator™, please refer to Appendix A. In order to compare the simulations with the experimental results a PSV construction was input into the simulation with similar parameters as the experiments (NiFe (15nm)/Cu (2.5nm)/NiFe (5nm)). The standard magnetic parameters for NiFe were input into the model, including A_{ex}= 6.25×10^{-12} J/m and M_s=6.37×10^{5} A/m. A NiFe film was deposited in an applied field and the induced anisotropy was measured as K_u= 400J/m^3. The anisotropy axis of the top (15nm) NiFe layer was along the wire axis and the anisotropy axis of the bottom (6nm) layer was perpendicular to the top layer. The cell size was input as 10×10×2.5nm, and the magnetisation in each cell has contributions from the anisotropy, exchange, magnetostatic and applied fields. The final dimensions of the fully milled structure according to the simulation was 100nm wide by 2μm long, and Fig. 8.15 (i), (ii), (iii) and (iv) show the change in the magnetisation reversal of the two ferromagnetic layers as the milling depth is increased to depths of 2.5nm, 10.3nm, 18.0nm and fully milled through respectively. Within each milling depth simulation, the top four bars show the magnetisation direction in the top (15nm) thick NiFe layer, and the bottom 4 bars show the same for the bottom (6nm) thick NiFe layer. The colour of the layers gives a direct indication of the magnetisation direction according to the colour indicator at the middle of each depth simulation, and the

arrows are a guide for the eye. Parts (a) to (d) indicate the reversal of the magnetic field from saturation in one direction to the other. Part (a) corresponds to magnetic saturation in the positive field direction (+H) and part (d) shows the magnetic saturation in the negative (-H) direction. Parts (b) and (c) show intermediate states. For the 2.5nm milling depth simulation (i), at saturation the middle of the wires are aligned parallel, but the ends show closure domains which are at 90° to the wire axis and are magnetostatically coupled antiparallel to each other. The closure domains form near the ends of the wires to minimise the magnetostatic energy, but in the bottom layer the closure domains extend further from the wire ends due to flux closure from the top (thicker) layer. The initial magnetisation reversal occurs by rotation from the closure domains, which enables the thinner layer to reverse for a smaller applied field. The anisotropy of the bottom NiFe layer is across the width of the wire, and this may also aid the magnetisation reversal. Fig. 8.15 (ii) shows the change in the magnetisation reversal process as the milling depth is increased to 10nm, which is 2/3rd of the way through the top layer. The increased shape anisotropy in the top layer restricts the magnetisation rotation, and reversal occurs more abruptly at a larger applied field. The edges rotate to 90º to the wire axis before the centre aligns with the field, and the edges of the layers appear to become coupled when the thicknesses become similar. It is interesting to note that the closure domains become coupled parallel at saturation (d). In Fig. 8.15 (iii) the simulation results are shown for a milling depth of 17.5nm, which corresponds to the complete patterning of the top ferromagnetic layer while the bottom layer remains unpatterned. The black regions at the edges of the top layer indicate the area of material removed. The shape anisotropy gives a greater contrast between the magnetisation reversal in the top and bottom layers and this is reflected in the distinctly different reversal fields in the two layers. The bottom layer still shows some magnetisation rotation, whilst the top layer reverses by switching state between (c) and (d) applied field directions. Fig. 8.15 (iv) shows the fully milled simulation, with both layers patterned with the same highly anisotropic structure. The bottom layer reverses before the top layer by switching abruptly between applied field directions (a) and (b). The top layer switches between applied field directions (c) and (d), and no magnetisation rotation is observed.

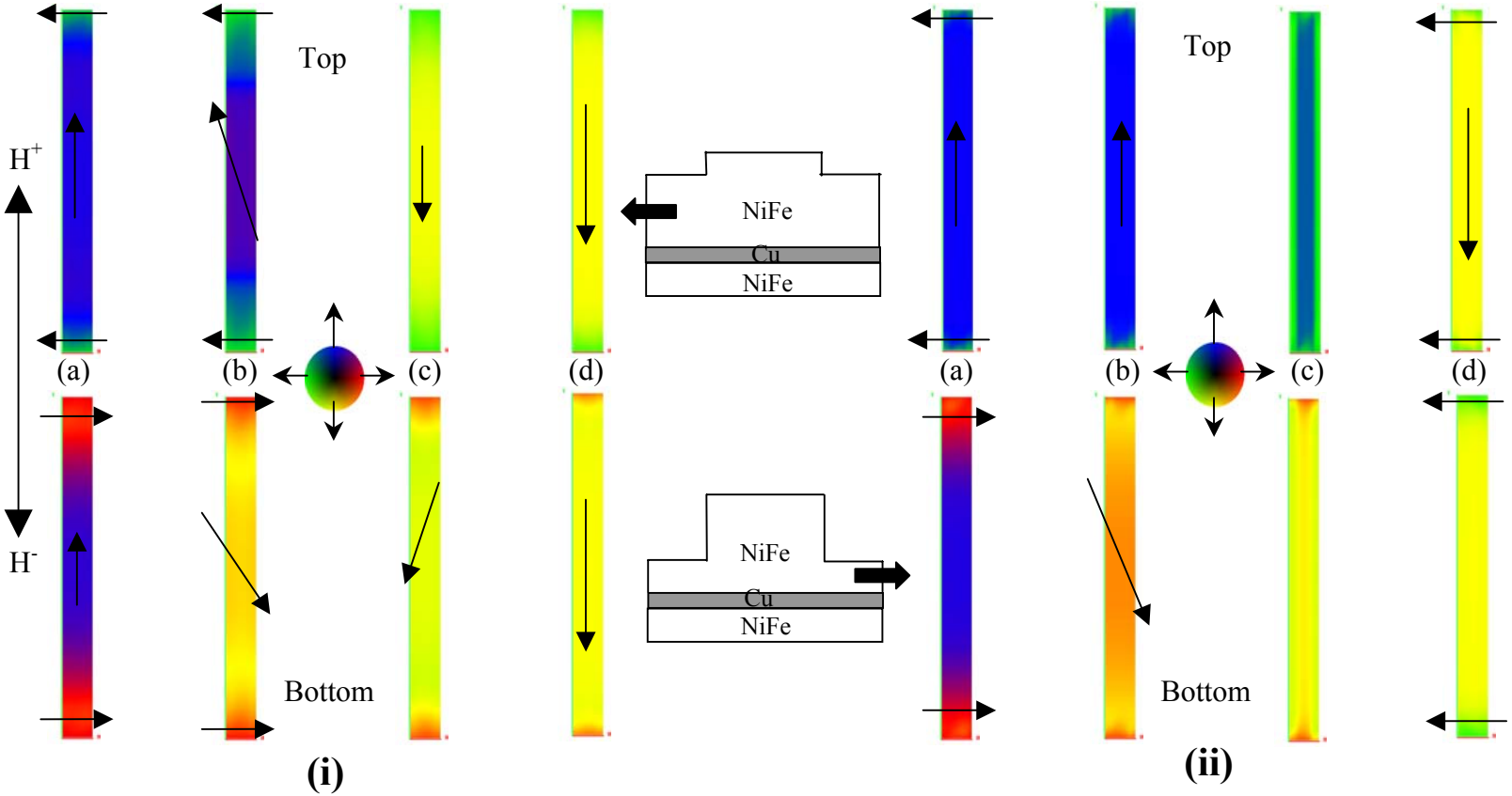

Fig. 8.15 *Micromagnetic simulations showing the magnetisation reversal in a PSV with the construction NiFe/Cu/NiFe at milling depths (i) 2.5nm, and (ii) 10nm. The top four bars in each simulation are the thicker (15nm) NiFe layer, and the bottom four are the thinner (6nm) NiFe layer. The direction of the applied magnetic field H is shown, and the colour code at the centre of each simulation indicates the direction of magnetisation within the layers. The arrows are to guide the eye, and the insets show the milling depth through the PSV structure.*

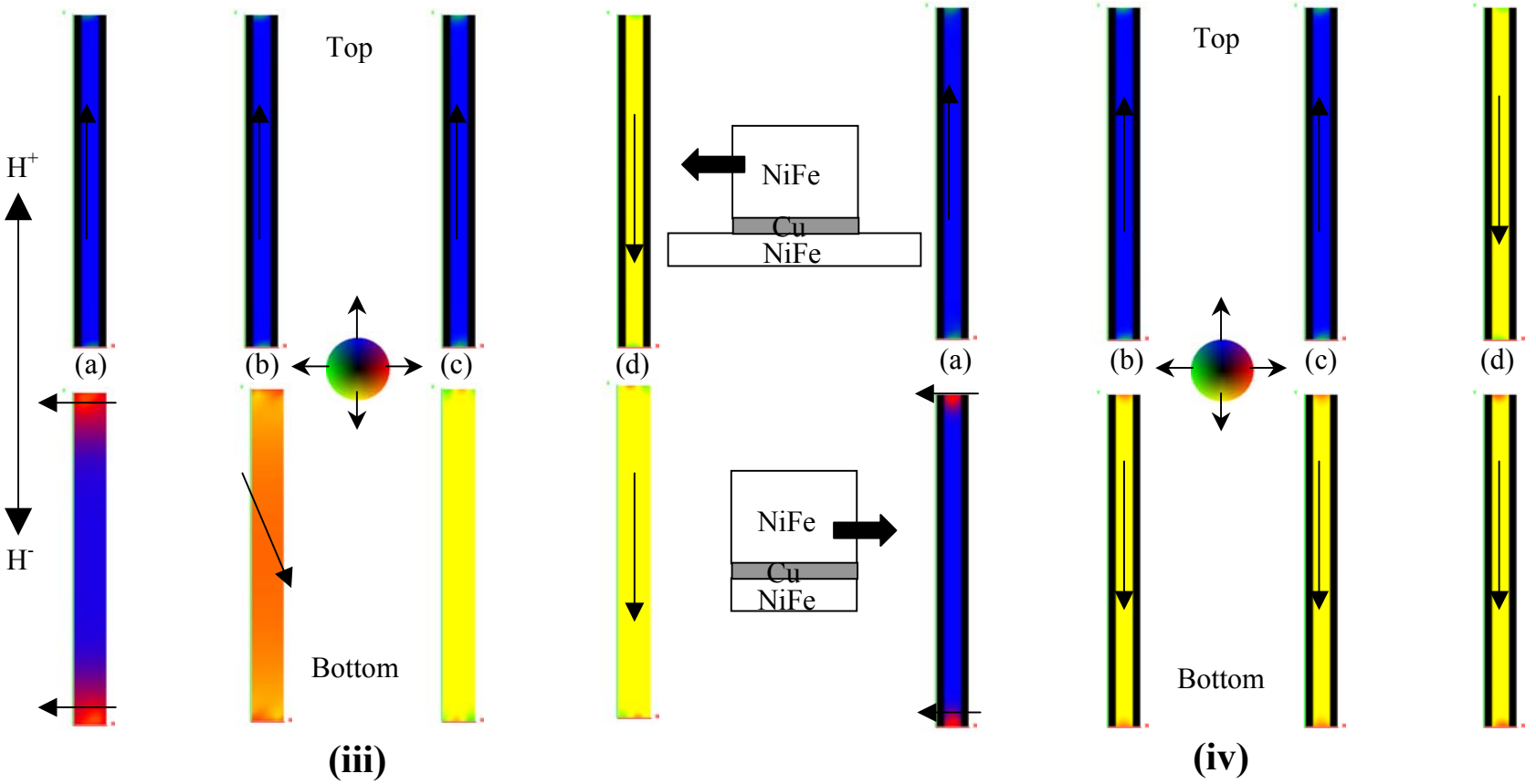

Fig. 8.15 *Micromagnetic simulations showing the magnetisation reversal in a PSV with the construction NiFe/Cu/NiFe at milling depths (iii) 17.5nm, and (iv) fully milled. The top four bars in each simulation are the thicker (15nm) NiFe layer, and the bottom four are the thinner (6nm) NiFe layer. The direction of the applied magnetic field H is shown, and the colour code at the centre of each simulation indicates the direction of magnetisation within the layers. The arrows are to guide the eye, and the insets show the milling depth through the PSV structure.*

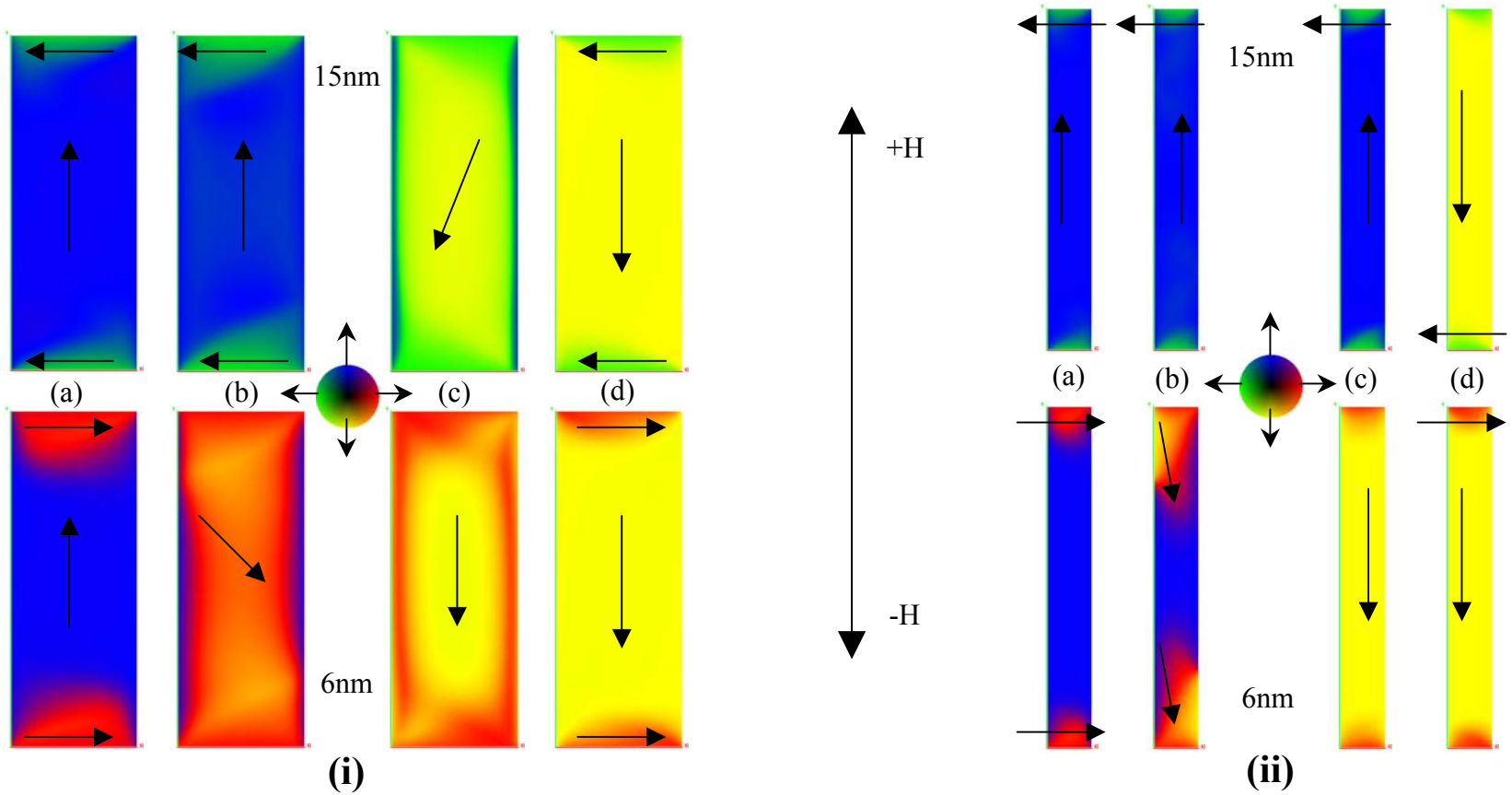

Fig. 8.16 *Micromagnetic simulations showing the magnetisation reversal in a PSV with the construction NiFe/Cu/NiFe with wire widths (i) 750nm, and (ii) 260nm. The top four bars in each simulation are the thicker (15nm) NiFe layer, and the bottom four are the thinner (6nm) NiFe layer. The direction of the applied magnetic field H is shown, and the colour code at the centre of each simulation indicates the direction of magnetisation within the layers. The arrows are to guide the eye.*

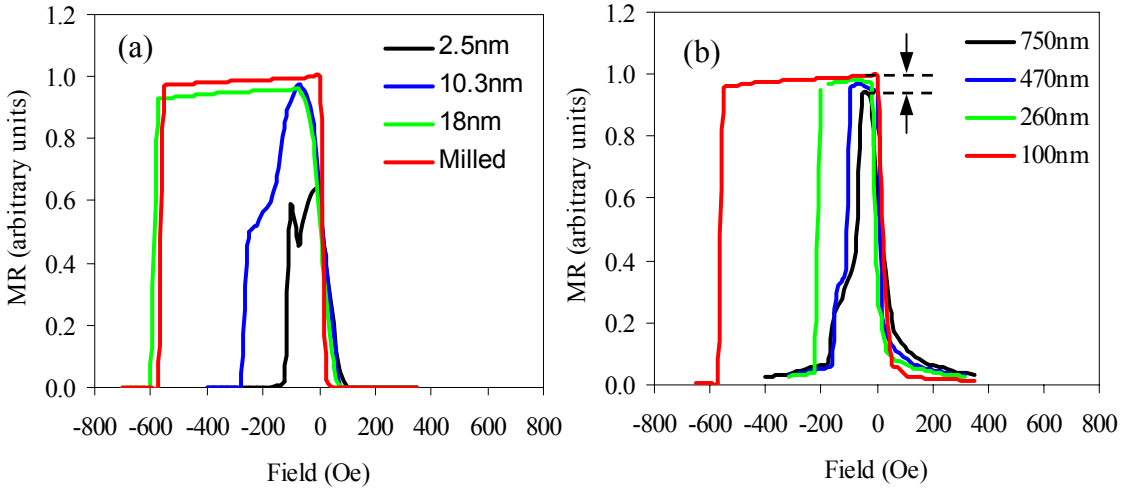

Fig. 8.17 *The change in MR according to the simulation results as (a) a PSV is patterned into a 100nm wide wire structure. Milling depth results are shown from 2.5nm milling to the fully milled through structure. (b) As the PSV wire width is decreased from 750nm to 100nm. The arrows in (b) indicate the change in the peak MR as the wire width is reduced. The MR is in arbitrary units and gives a maximum of 1 when the layers are antiparallel and a minimum 0 when they are parallel. Both graphs display the field sweep from positive to negative field for clarity.*

The simulations show how reducing the wire width changes the magnetisation reversal characteristic. Fig. 8.16 is divided into two sections; section (i) shows the magnetisation reversal for a 750nm wide PSV wire and section (ii) shows the same for a 260nm wide PSV wire. The wider wire exhibits more magnetisation rotation before finally reversing, but in contrast the narrow wire switches abruptly, which is consistent with the milling depth simulations shown in Fig. 8.15. Once again the bottom layer reverses before the top layer because of the larger closure domains.

Fig. 8.17 (a) shows the change in the MR of the 100nm wide wire as the structure is milled through as derived from the angles between the two layers in the micromagnetic simulations. The MR is given in arbitrary units, and gives a maximum value of 1 when the layers are antiparallel and a minimum value of 0 when they are parallel. The field sweep from positive to negative field is shown for clarity. The MR increases with milling depth reaching a maximum when fully milled, this is in agreement with the experimental data. The coercivity of the soft ferromagnetic layer H_{c1}, remains approximately the same with increasing milling depth, but the coercivity of the hard ferromagnetic layer H_{c2} shows an large increase. This result is confirmed experimentally in Fig. 8.10, which compares the initial MR and fully

milled through MR for the sample with wire width 265nm. Fig. 8.17 (b) shows the change in MR as the PSV wire width is decreased from 750nm to 100nm. As the wire width is decreased the simulations predict an increase in the MR (as shown by the arrows on the graph), due to an increase in the coercivity of the hard layer H_{c2} and a decrease in the magnetisation rotation of the bottom layer. Instead of magnetisation rotation at the ends of the wires as the field is increased, the bottom layer shows more of a switching behaviour. This increases the degree of antiparallel alignment between the layers and increases the MR. In the experimental data an increase in H_{c2} is observed as the wire width decreases, and there is also an initial increase in the MR as the wire width is decreased. However, the MR drops for wire width 265nm, this is thought to be due to the higher dosage of Ga ions.

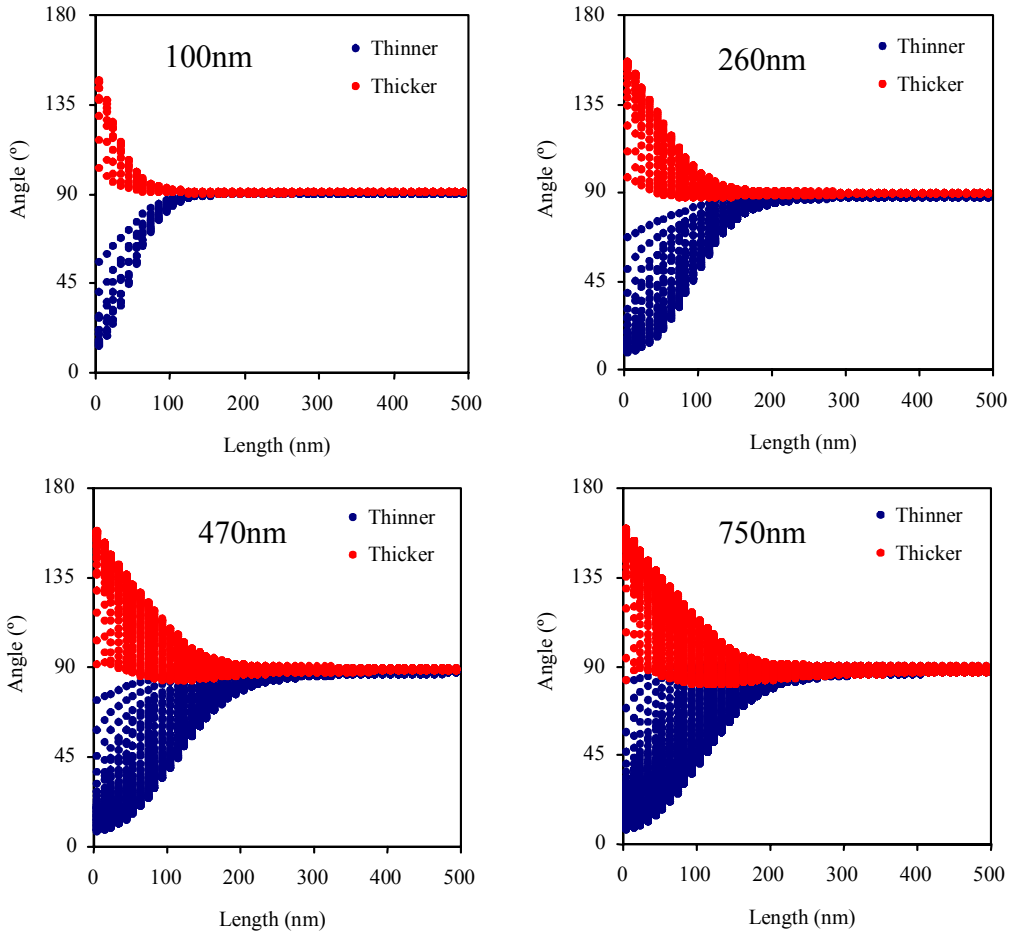

Fig. 8.18 *Graphs showing the spread of the angle of magnetisation at the end of the wires for 100, 260, 470, and 750nm wide PSV wires relative to the wire axis so that 90° is along the axis. Blue represents the bottom layer and red is the top layer.*

The micromagnetic simulations seem to indicate that the magnetisation reversal in the ferromagnetic wires is initiated by the closure domains at the end of the wires. Although in the experimental measurements the relative area of the closure domains is smaller than in the simulations (because the wires are much longer), the change in the size of the domains due to the change in the width of the wire is a real effect. Fig. 8.18 shows the spread in the angle of magnetisation at the end of the PSV wires for 100, 260, 470 and 750nm widths. Blue represents the bottom layer and red the top layer. The magnetic moments at 90° are aligned along the length of the wire. The graphs show that the spread of the magnetic moments in the thinner layer is larger than in the thicker layer. This is due to the flux closure from the thicker layer. As the wire width increases the spread of the magnetisation produces a greater number of angles with respect to the wire axis.

8.6 Conclusion

In-situ magnetoresistance measurements of nanopatterned PSVs have been carried out to investigate how the magnetic and electrical properties change with increasing shape anisotropy on the nano-scale. The measurements show that the MR increases as the milling depth between the patterned wires increases, mainly due to an increase in the coercivity of the hard ferromagnetic layer. The results also indicate that the MR increases as the wire width decreases, although the properties of the PSV are heavily dependent on the dosage of Ga ions during processing in the FIB. Minor loop analysis has shown that the magnetisation of the hard layer in the PSV nano-wires is irreversible. Micromagnetic simulations have confirmed the experimental results, and shown the increase in the coercivity of the hard layer to be due to a change in the magnetisation reversal from partial rotation at the centre of the wires to incoherent switching. The reversal of the soft layer also changes from partial rotation to switching as the dimensions are reduced. The simulations indicate that reversal initiates from closure domains at the end of the wires, which are larger in the bottom (thinner) ferromagnetic layer than in the top layer due to flux closure. The edges show a higher coercivity than the centre of the wires due to magnetostatic interactions.

References

[1] F.J. Himpsel, J.E. Ortega, G.J. Mankey, R.F. Willis, *Advances in Physics*, **47 (4)**, 511-597 (1998).

[2] C.A. Ross, H.I. Smith, T. Savas, M. Schattenburg, M. Farhoud, M. Hwang, M. Walsh, M.C. Abraham, R.J. Ram, *J. Vac. Sci. Technol. B*, **17(6)**, 3168 (1999).

[3] Y. Hao, F.J. Castaño, C.A. Ross, B. Vögeli, M.E. Walsh, H.I. Smith, *J. Appl. Phys.*, **91(10)**, 7989 (2002).

[4] C.A. Ross, M. Farhoud, M. Hwang, H.I. Smith, M. Redjdal, F.B. Humphrey, *J. Appl. Phys.* **91**, 6848 (2002).

[5] C.A. Ross, R. Chantrell, M. Hwang, M. Farhoud, T.A. Savas, Y. Hao, H.I. Smith, F.M. Ross, M. Redjdal, F.B. Humphrey, *Phys. Rev. B*, **62(18)**, 62 (2000).

[6] C. Shearwood, S.J. Blundell, M.J. Baird, J.A.C. Bland, M. Gester, H. Ahmed, H.P. Hughes, *J. Appl. Phys.,* **75(10)**, 5249 (1994).

[7] R.P. Cowburn, D.K. Koltsov, A.O. Adeyeye, M.E. Welland, D.M. Tricker, *Phys. Rev. Lett.*, **83(5)**, 1042 (1999).

[8] R.P. Cowburn, *J. Phys. D: Appl. Phys.*, **33**, R1-R16 (2000).

[9] R.P. Cowburn, D.K. Koltsov, A.O. Adeyeye, M.E. Welland, *Appl. Phys. Lett.*, **73(26)**, 3947 (1998).

[10] K.J. Kirk, J.N. Chapman, S. McVitie, P.R. Aitchison, C.D.W. Wilkinson, *J. Appl. Phys*. **87**, 5105 (2000)

[11] K.J. Kirk, J.N. Chapman, C.D.W. Wilkinson, *J. Appl. Phys.,* **85(8)**, 5237 (1999).

[12] K.J. Kirk, J.N. Chapman, C.D.W. Wilkinson, *Appl. Phys. Lett.*, **71(4)**, 539 (1997).

[13] S. Chou, P.R. Krauss, L. Kong, *J. Appl. Phys.,* **79(8)**, 6101 (1996).

[14] Y. Zheng, J.G. Zhu, *J. Appl. Phys.,* **81(8)**, 5471 (1997).

[15] J.F. Smyth, S. Schultz, D.R. Fredkin, D.P. Kern, S.A. Rishton, H. Schmid, M. Cali, T.R. Koehler, *J. Appl. Phys.,* **69(8)**, 5262 (1991).

[16] W. Wernsdorfer, B. Doudin, D. Mailly, K. Hasselbach, A. Benoit, J. Meier, J.-Ph. Ansermet, B. Barbara, *Phys. Rev. Lett.*, **77(9)**, 1873 (1996).

[17] J.-P. Jamet, S. Lemerle, P. Meyer, J. Ferré, B. Bartenlian, N. Bardou, C. Chappert, P. Veillet, F. Rousseaux, D. Decanini, H. Launois, *Phys. Rev. B*, **57(22)**, 14320 (1998).

[18] A.O. Adeyeye, J.A.C. Bland, C. Daboo, D.G. Hasko, H. Ahmed, *J. Appl. Phys.,* **82(1)**, 469 (1997).

[19] A.O. Adeyeye, J.A.C. Bland, C. Daboo, J. Lee, U. Ebels, H. Ahmed, *J. Appl. Phys.,* **79(8)**, 469 (1996).

[20] C. Mathieu, C. Hartmann, M. Bauer, O. Buettner, S. Riedling, B. Roos, S.O. Demokritov, B. Hillebrands, B. Bartenlian, C. Chappert, D. Decanini, F. Rousseaux, E. Cambril, A. Müller, B. Hoffman, U. Hartmann, *Appl. Phys. Lett.*, **70(21)**, 2912 (1997).

[21] J.I. Martín, J. Nogués, I. K. Schuller, M.J. Van Bael, K. Ternst, C. Van Haesendonck, V.V. Moshchalkov, Y. Bruynseraede, *Appl. Phys. Lett.*, **72(2)**, 255 (1998).

[22] J.I. Martín, Y. Jaccard, A. Hoffman, J. Nogués, J.M. George, J.L. Vicent, I.K. Schuller, *J. Appl. Phys.,* **84(1)**, 411 (1998).

[23] W. Wernsdorfer, K. Hasselbach, A. Benoit, B. Barbara, D. Mailly, J. Tuaillon, J.P. Perez, V. Dupuis, J.P. Dupin, G. Guiraud, A. Perex, *J. Appl. Phys.,* **78(12)**, 7192 (1995).

[24] M. Lederman, S. Schultz, M. Ozaki, *Phys. Rev. Lett.*, **73(14)**, 1986 (1994).

[25] D. Grundler, G. Meier, K.-B. Broocks, Ch. Heyn, D. Heitmann, *J. Appl. Phys.,* **85(8)**, 6175 (1999).

[26] O. Fruchart, J.-P. Nozières, W. Wernsdorfer, D. Givord, F. Rousseaux, D. Decanini, *Phys. Rev. Lett.*, **82 (6)**, 1305 (1999).

[27] R.L. White, R.M.H. New, R.F.W. Pease, *IEEE Trans. Magn.*, **33**, 990 (1997).

[28] S.Y. Chou, *Proc. IEEE*, **85**, 652 (1997).

[29] J.G. Zhu, X. Lin, L. Guan, W. Messner, *IEEE Trans. Magn.*, **36**, 23 (2000).

[30] C.A. Ross, *Ann. Rev. of Mater. Res.*, **31**, 203 (2001).

[31] S.Y. Yamamoto, R. O'Barr, S. Schultz, A. Scherer, *IEEE Trans. Magn.*, **33**, 3016 (1997).

[32] T. Ono, H. Miyajima, K. Shigeto, T. Shinjo, *Appl. Phys. Lett.*, **72(9)**, 1116 (1998).

[33] T. Ono, H. Miyajima, K. Shigeto, K. Mibu, N. Hosoito, T. Shinjo, Science, 468, 5413 (1999).

[34] R.P. Cowburn, M.E. Wellend, *Science*, **287**, 1466 (2000).

[35] E.C. Stoner, E.P. Wohlfarth, *Philos. Trans. R. Soc. London, Ser. A*, **240**, 599 (1948); reprinted in *IEEE Trans. Magn.*, **27**, 3475 (1991).

[36] I.S. Jacobs, C.P. Bean, *Phys. Rev.*, **100**, 1060 (1955).

[37] E.H. Frei, S. Shtrikman, D. Treves, *Phys. Rev.*, **106**, 446 (1957).

[38] J. Shi, S. Tehrani, *Appl. Phys. Lett.*, **77(11)**, 1692 (2000).

[39] J. Shi, S. Tehrani, T. Zhu, Y.F. Zheng, J.-G. Zhu, *Appl. Phys. Lett.*, **74(17)**, 2525 (1999); T. Schrefl, J. Fidler, K.J. Kirk, J.N. Chapman, *J. Appl. Phys.,* **85(8)**, 6169 (1999).

[40] M. Kume, A. Maeda, T. Tanuma, K. Kuroki, *J. Appl. Phys.,* **79(8)**, 6402 (1996).

[41] F.J. Castaño, S. Haratani, Y. Hao, C.A. Ross, H.I. Smith, *Appl. Phys. Lett.*, **81(15)**, 2809 (2002)

[42] L. Kong, Q. Pan, B. Cui, M. Li, S.Y. Chou, *J. Appl. Phys.,* **85(8)**, 5492 (1999).

[43] J.A. Katine, A. Palanisami, R.A. Buhrman, *Appl. Phys. Lett.*, **74(13)**, 1883 (1999)

[44] G. Xiong, D.A. Allwood, M.D. Cooke, R.P. Cowburn, *Appl. Phys. Lett.*, **79(21)**, 3461 (2001)

[45] W.M. Kaminsky, G.A.C. Jones, N.K. Patel, W.E. Booij, M.G. Blamire, S.M. Gardiner, Y.B. Xu, J.A.C. Bland, *Appl. Phys. Lett.*, **78(11)**, 1589 (2001)

[46] F.J. Castaño, Y. Hao, C.A. Ross, B. Vögeli, H.I. Smith, S. Haratani, *J. Appl. Phys.,* **91(10)**, 7317 (2002).

[47] C.A. Ross, S. Haratani, F.J. Castaño, Y. Hao, M. Hwang, M. Shima, J.Y. Cheng, B. Vögeli, M. Farhoud, M. Walsh, H.I. Smith, *J. Appl. Phys.,* **91(10)**, 6848 (2002).

[48] M. H. Kryder, K. Y. Ahn, N. J. Mazzeo, S. Schwarzl, and S. M. Kane, *IEEE Trans. Magn*., Vol. **Mag-16**, NO. 1, 99 (1980).

[49] S. Reyntjens, R. Puers, *J. Micromech. Microeng*. **11**, 287 (2001).

I may not have gone where I intended to go, but I think I have ended up where I intended to be. *Douglas Adams*

Chapter 9

Summary of dissertation

This dissertation describes an experimental study of the patterning of magnetic thin films and spin valve devices. The initial work was carried out on $Ni_{80}Fe_{15}Mo_5$ thin films and investigated the change in the magnetic properties as broad beam ion milling was used to etch narrow (3μm) and wide (4mm) regions. The results showed that the wider regions dominated the magnetisation reversal, and the coercivity increased by a factor of ten along the wire axis when the wider regions were removed. Measurements were also carried out for partial milling through the thickness of the wire arrays to assess the dependence of the magnetic properties on the degree of interconnection between the wires. The structures showed a progressive increase in coercivity, and a transition between single and two-stage reversal with increasing wire depth. Although the change in the magnetisation reversal with increasing shape anisotropy of ferromagnetic thin films has been well studied [1-4], this initial work was important because the aim was to apply the same patterning to the top layer of a NiFe/Cu/NiFe trilayer to achieve a spin valve response. The coercivity of the patterned ferromagnetic layer increased, which changed the natural similarity of the two layers, and a small spin valve response ≈0.45% was observed.

The *in-situ* magnetoresistance measurement rig, which was specifically designed for these experiments, enabled direct analysis of the evolution in the electrical properties as the structure was gradually milled. Graphs of the change in the resistance in zero applied field R, and the change in resistance in the presence of an applied field dR, could be plotted versus milling depth, which gave a direct indication of whether the MR was changing due to a change in the resistance or the magnetic configuration. Contrary to what was expected the micropatterned PSV structures showed a maximum MR when fully milled. Magnetic hysteresis measurements showed a two-step reversal and confirmed that the initial magnetisation reversal corresponded to the thinner ferromagnetic layer, which was surprising because previous work has shown that the coercivity tends to increase as the film thickness is decreased [5,6]. The effect of further increasing the anisotropy was investigated by decreasing

the wire width and the results showed that the GMR was enhanced by almost a factor of three as the wire width was decreased from 3μm to 1.5μm. These results showed that increasing the shape anisotropy increased the MR from the pseudo spin valve, and the optimum milling depth was when the structure was fully milled.

The effect of changing the material properties was investigated by using the same patterning technique for CoFe/Cu/CoFe pseudo spin valve structures. A spin valve response was not observed due to the larger interlayer and magnetostatic coupling effects. According to these results optimum device performance can be achieved using materials with low magnetostatic and interlayer coupling energies. However, the interlayer coupling energy is directly related to the Curie temperature T_c, and a high Curie temperature is required for good thermal stability of the device. Therefore, a compromise between high thermal stability and low interlayer coupling energy will need to be made for this device design. Temperature measurements were carried out to compare the thermal stability of the pseudo spin valve structures with exchange biased spin valves. As the temperature was increased from 291K to 493K the MR of the exchange biased spin valve decreased to ≈1/4 of the original value. The MR of the PSV also decreased, but to only 2/3 of the original value. These results show that the patterned PSV has a better thermal stability than the IrMn exchange biased spin valve.

Further experiments were carried out by reducing the dimensions to the nanoscale, which is more in keeping with the general trend towards miniaturisation of magnetic devices. Nanopatterning was carried out using a silica hard mask, which was deposited and then patterned on top of the PSV. The Focused Ion Beam (FIB) was used to nanopattern the silica hard mask, and then the pattern was transferred into the PSV by argon ion milling the entire structure. The results showed that the properties of the spin valve were strongly affected by gallium ion implantation during processing in the FIB, which created another form of anisotropy by locally changing the magnetic properties of the ferromagnetic material between the patterned wires, directly beneath the silica mask. The coercivity of the top ferromagnetic layer was increased and a small spin valve response was observed before milling in the argon ion miller. As the nanowire array was patterned through the PSV, the results showed the same trend as for the micropatterned samples; the MR increased with increasing milling depth showing a maximum when fully milled. An obvious increase in the coercivity of the hard layer was observed, whilst the coercivity of the soft ferromagnetic layer remained unchanged. The MR showed an initial increase from 1.1 to 2.35% as the wire width was decreased from 734 to 468nm, but decreased to 1.47% as the wire width was further decreased. This is thought to be due to the increased gallium dosage density, which changed the magnetic and

electrical properties of the structure. Despite the change in the magnetisation reversal as the wire width was decreased from the micron to the nanoscale, an increase in MR was not observed. This is thought to be due to in increase in the initial resistance of the structures. Minor loop analysis showed that the reversal of the hard ferromagnetic layer was irreversible for the fully milled 468nm wide wire array. The Bitter technique was used to study the domain configuration in a 50μm wide PSV structure, and simple mathematical analysis showed that the coupling energy per unit distance between the layers $J \approx 7.01 \times 10^{-15}$J/m. The calculation showed that the exchange coupling between the atomic magnetic moments A_{ex}, is ≈900× larger than the coupling between the ferromagnetic layers in the NiFe/Cu/NiFe PSV.

Micromagnetic modelling was used to simulate the change in the magnetisation reversal in the PSV as the milling depth was increased through the thickness in 100nm wide wires. The results showed that for small milling depths, the reversal was dictated by rotation from closure domains at the ends of the wires, with the bottom (thinner) layer reversing before the top (thicker) layer. These results emphasise the importance of magnetostatic interactions and flux closure at the ends of the wires. The anisotropy axis of the bottom ferromagnetic layer was along the width of the wire, which also helped the formation of the closure domains. As the milling depth increased the reversal occurred by switching; the thinner layer reversed direction first by nucleation and propagation initiating from the closure domains. The modelling also demonstrated the change in the magnetisation reversal from rotation to switching as the wire width was decreased from 750 to 260nm. The GMR was extracted from the modelling data, and graphs were plotted to show the change in MR with milling depth and decreasing wire width according to the simulations. The simulations agreed with the experimental results showing a large increase in MR as the structure was milled through, and a small increase as the wire width was decreased on the nanoscale. Both the simulations and the experimental results showed a large increase in the reversal field of the hard layer as the milling depth is increased and wire width decreased, whilst the reversal field of the soft layer remained almost the same.

References

[1] A.O. Adeyeye, J.A.C. Bland, C. Daboo, D.G. Hasko, H. Ahmed, *J. Appl. Phys.,* **82(1)**, 469 (1997).

[2] A.O. Adeyeye, J.A.C. Bland, C. Daboo, J. Lee, U. Ebels, H. Ahmed, *J. Appl. Phys.,* **79(8)**, 469 (1996).

[3] T. Ono, H. Miyajima, K. Shigeto, T. Shinjo, *Appl. Phys. Lett.*, **72(9)**, 1116 (1998).

[4] T. Ono, H. Miyajima, K. Shigeto, K. Mibu, N. Hosoito, T. Shinjo, Science, 468, 5413 (1999).

[5] J. H. Fluitman, Thin Solid Films, **16**, 269 (1973)

[6] M. H. Kryder, K. Y. Ahn, N. J. Mazzeo, S. Schwarzl, and S. M. Kane, *IEEE Trans. Magn*., Vol. **Mag-16**, NO. 1, 99 (1980).

Other Work

There has been considerable interest recently in the size dependence of exchange bias in antiferromagnetic/ferromagnetic bilayers (AFM/FM) [1-6]. This is partly due to the requirement for miniaturisation of spin valve read heads for the computer industry [7], but also due to some controversy over the fundamental understanding of how the magnetic configuration changes in the AFM/FM bilayer as the physical dimensions become comparable to characteristic length scales, such as the domain size in the FM and AFM materials. This work gives a novel insight into how the properties of spin valve devices change as the exchange bias is changed by milling through the AFM layer. The ferromagnetic layers remain unpatterned to investigate the effect of decreasing the AFM size on the pinning properties. Initially *in-situ* transport measurements were carried out on micropatterned spin valves to analyse the change in properties close to the AFM/FM interface. The work was then extended to patterning arrays of spin valve microwires and varying the spacing between the wires, to investigate whether it is possible to engineer localised spin valve regions. Finally the experiment was extended to the nanoscale to investigate the effect of miniaturisation. Mathematical modelling is used to help interpret the experimental results. *In-situ* transport measurements were carried out as the AFM layer was milled away in an exchange biased spin valve structure of the form Ta(9nm)/NiFe(6.5nm)/Cu(2.6nm)/NiFe(3nm)/IrMn(10nm)/Ta(3nm), where the AFM layer was at the top of the structure to allow direct milling. No change in MR was observed as the AFM layer was milled through the bulk. As the thickness of the AFM layer was reduced from 10nm to below 3nm a decrease in MR was observed and an applied field of 80Oe was large enough to overcome the exchange field from the AFM layer and align the ferromagnetic layers. When the AFM layer was completely milled away a small MR remained due to a combination of the AMR (the current and field were perpendicular) and a small GMR from the thickness difference of the ferromagnetic layers. The change in the MR and dR are shown in Fig. 10.1 for different thicknesses of IrMn. This result agrees with previous work [8], which indicates that the exchange anisotropy from the AFM layer is an interface effect.

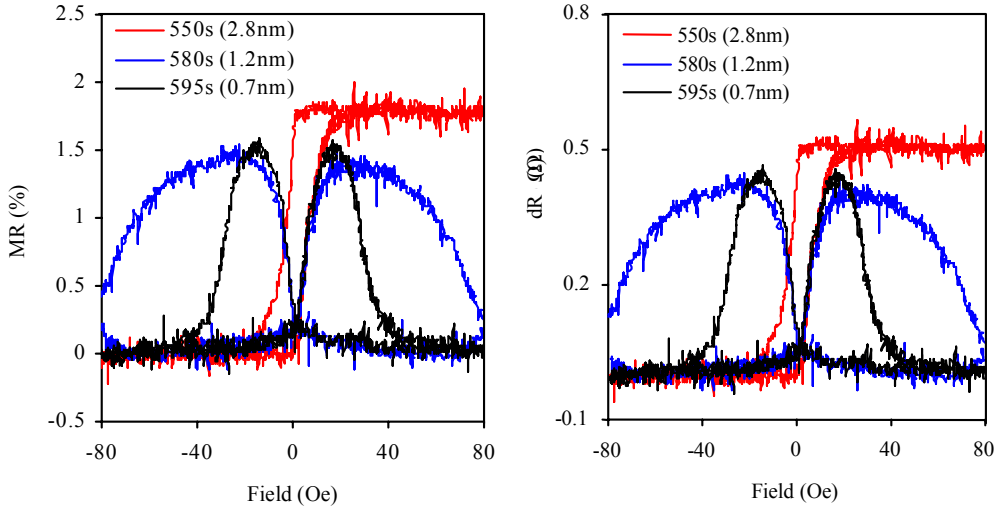

Fig. 10.1 (a) In-situ MR at milling times 550s, 580s and 595s. The number in brackets in the inset is an estimation of the thickness of IrMn remaining. (b) dR versus field for milling times 550s, 580s and 595s.

Optical lithography and argon ion milling were used to micropattern wire arrays in the AFM layer of exchange biased spin valves, as shown in Fig, 10.2.

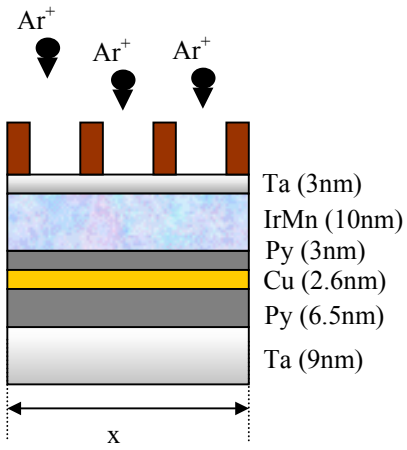

Fig. 10.2 *Schematic cross section of patterned sample showing wire array structure and lay-up of the spin valve. The width 'x' of the rectangular sample varies depending upon the spacing between the wires. (b) The direction of the current is perpendicular to the applied field and the wire axis. The wire width is 3μm, and the spacing varied from 8μm to 1.5μm. The length of the sample is 100μm.*

The width of the wires was kept constant at 3μm, and the experiments investigated the change in MR with milling as the spacing was varied between 8μm and 1.5μm. The results show a decrease in MR as the AFM regions between the wires are milled away. This is due to a

decrease in the antiparallel alignment of the ferromagnetic layers. The AFM wires produce a localised spin valve effect in the FM/NM trilayer directly beneath. The percentage decrease in MR corresponds to the area of AFM material milled away, showing a larger decrease when the spacing between the AFM wires was increased. This shows that the ferromagnetic regions between the wires are free to move in the applied field. Measurements were also taken with the wire width and spacing on the nanoscale. The results still show a localised spin valve effect, even over wire spacing as small as ≈200nm.

Mathematical modelling has been used to study the magnetisation dynamics of the ferromagnetic region between the pinned nanowires as the thickness of the AFM layer directly above is reduced. The results show that as the exchange field H_{ex} is reduced, the maximum angle of the magnetic moments is increased with respect to the pinning direction, as shown in Fig. 10.3 (a). As the field is increased the magnetic moments tend to align with the applied field, and the moments furthest away from the pinned regions reverse for smaller applied fields. As the spacing between the IrMn wires is reduced to 200nm the model shows that the moments don't completely align with the field direction even for low values of H_{ex}, this is because A_{ex} is strong and the spacing is small.

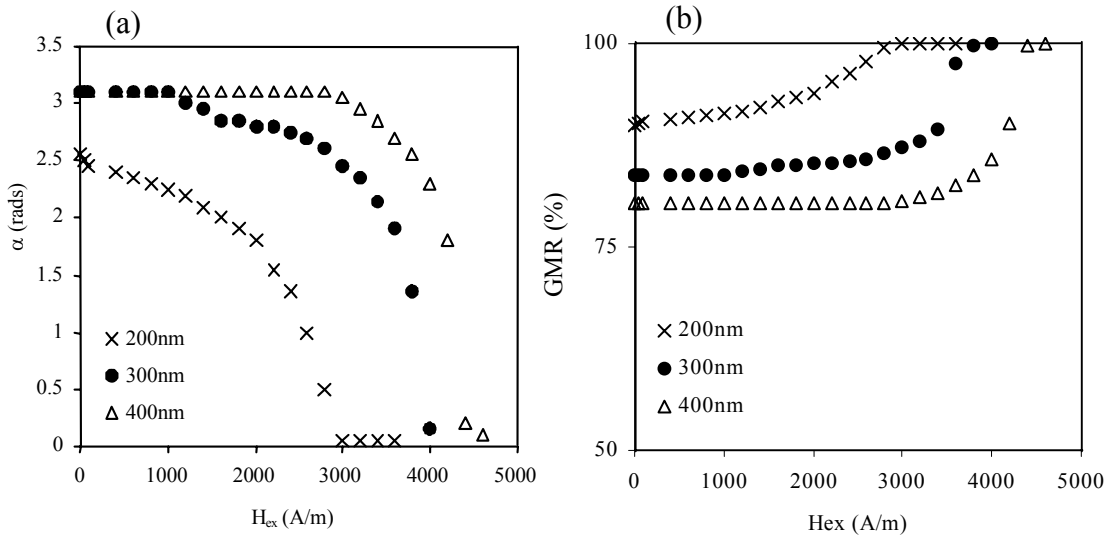

Fig. 10.3 *(a) Maximum angle α from the exchange bias direction for the magnetic moments in a region between two pinned wires called s, where s=200nm, 300nm and 400nm, as H_{ex} is reduced by milling away the IrMn. α=0rads indicates that the magnetic moments are aligned with the exchange bias direction. As α increases towards π rads, the moments become more aligned with H. (b) The change in GMR as the exchange field H_{ex} is reduced according to the energy minimisation model, where s=200nm, 300nm and 400nm. A constant applied field of 5000Am^{-1} was used.*

The relative angles of the magnetic moments in the ferromagnetic layers were converted into GMR as shown in Fig. 10.3 (b), by assuming that the zero field resistance of the spin valve remained constant. The model shows that as the spacing between the wires becomes smaller, a larger milling depth is required before a decrease in GMR is observed. When the AFM layer is milled to the FM interface, the decrease in GMR is proportional to the area of the AFM material removed.

References

[1] J. Yu, A. D. Kent, and S. S. P. Parkin, *J. Appl. Phys*. **87**, 5049 (2000)

[2] J. G. Zhu, Y. F. Zheng, and X. D. Lin, *J. Appl. Phys*. **81**, 4336 (1997)

[3] Y. Shen, Y. Wu, H. Xie, K. Li, J. Qui and Z. Guo, *J. Appl. Phys*. **91**, 8001 (2002)

[4] K. Lui, S. M. Baker, M. Tuominem, T. P. Russell, I. K. Schuller, *Phys. Rev. B* **63**, 63 (2001)

[5] M. Fraune, U. Rüdiger, G. Güntherodt, S. Cardoso, P. Freitas, *Appl. Phys. Lett*. **77**, 3815 (2000)

[6] S. Zhang, Z. Li, *Phys. Rev*. B **65**, 65 (2001)

[7] W. J. Gallagher, S. S. S. Parkin, W. Lu, X. P. Bian, A. Marley, K. P. Roche, R. A. Altmann, S. A. Rishton, C. Jahnes, T. M. Shaw, and G. Xiao, *J. Appl. Phys*. **81**, 3741 (1997)

[8] J. Nogués, I.K. Schuller, *J. Magn. Magn. Mater*. **192**, 203 (1999).

APPENDIX A

This appendix gives an overview of the theory behind the LLG Micromagnetic Simulator. The information was taken directly from the LLG Micormagnetics Simulator User Manual.

LLG Micromagnetics Simulator™ was founded in 1997 as a sole proprietorship by Michael R. Scheinfein, who was then a professor of physics at Arizona State University in Tempe, Arizona.

In 1997, the first users of LLG were a handful of scientists working on MRAM in corporate research labs. Now, there are over 100 corporate and academic users worldwide, including Europe, Asia and North America.

CHAPTER 3

INTRODUCTION TO USING LLG

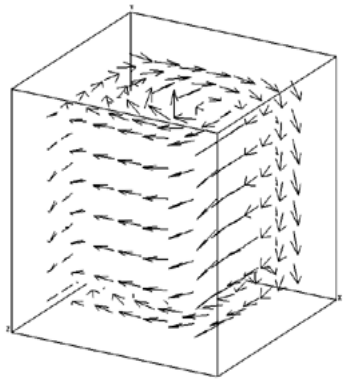

This section provides you with an overview of LLG's design, of how to use LLG and of LLG's functionality. For complete details and instructions, refer to the appropriate sections found later in the Manual.

THREE MODULES OF FUNCTIONALITY

LLG Micromagnetics Simulator has three functional modules. These modules are specified in terms of the serial process of defining the solutions to most problems, while maintaining consistency with the Windows event-driven programming interface. These modules are listed below with their corresponding menus.

- Input phase: data specification (LLG Input Sheet)
- Simulation phase: solution of the differential equations (LLG Simulation Sheet)
- Review phase: playback of results through graphical animation (movies) (LLG Movie Viewer)

INPUT PHASE: DATA SPECIFICATION

The **LLG Input Sheet** is the central interface for coordinating input parameters, error checking and setting critical global parameters. In general, inputting data specifications is the most tedious aspect of numerical simulations. The program has been designed to allow you flexibility in customizing simulations; however, this makes the data specification phase time-consuming and increases the risk of input error. Although, as a counter measure, LLG performs exhaustive error checking to prevent floating-point exceptions, defining a structure and how well it models an actual material or device is ultimately the user's responsibility.

Since the program solves the Landau-Lifshitz-Gilbert equations using finite differences for exchange energies and fields, as well as boundary elements for magnetostatic self-energies and fields, the structure of interest must be defined as a grid. The program uses rectangular pixels on a Cartesian grid. Although you can change the material parameters, including eliminating magnetic material altogether, this must be done on a Cartesian grid.

Once you have specified the structure and clicked the **Begin Simulation** button, LLG initializes all of the arrays, computes the demagnetization field coupling tensors and calculates the fields for any boundary conditions. Once these large arrays have been specified, the simulation phase can begin. Also, you are prompted to store the simulation parameters in several files.

SIMULATION PHASE: SOLUTION OF THE DIFFERENTIAL EQUATIONS

Once LLG has verified that you have input the data correctly, you have your first chance to set the graphical representation of the data. Many features can be viewed interactively.

REVIEW PHASE: PLAYBACK OF RESULTS THROUGH A GRAPHICALLY ANIMATED MOVIE

Once a simulation is complete, you can review the results by replaying them through a graphically animated movie or you can view a domain or field file in the viewer control. Graphical representation of the data is essential to comprehending the results of a simulation. The program provides complete two- and three-dimensional views in the form of bitmap images, contour maps and vector fields.

THEORY OF OPERATION

Micromagnetic structure, such as that present in surface domain walls, can be extracted with standard methods for the solution to the Landau-Lifshitz-Gilbert equation. Such methods have been given in the literature by Brown [1], LaBonte [1,2], Aharoni [3-9], Hubert [10,11], and Schabes [9,12]. The equilibrium magnetization configuration results from the minimization of the system's free energy. The energy of a ferromagnetic system is composed of 1) the mean field exchange energy E_{ex} between nearest neighbors characterized by the exchange coupling constant A (erg/cm); 2) the magnetocrystalline anisotropy energy E_K, which describes the interaction of the magnetic moments with the crystal field characterized by the constant K_v (erg/cm^3); 3) the surface magnetocrystalline anisotropy energy E_{ks}, which corrects for broken symmetry near surfaces in the interaction of the magnetic moments with the crystal field, and is characterized by the constant K_s (erg/cm^2); 4) the magnetostatic self-energy E_s, which arises from the interaction of the magnetic moments with the magnetic fields created by discontinuous magnetization distributions both in the bulk and at the surface; 5) the external magnetostatic field energy E_h, which arises from the interaction of the magnetic moments with any externally applied magnetic fields; and 6) the magnetostrictive energy E_r, which arises when mechanical stress (strains) are applied to a ferromagnetic material thereby introducing effective anisotropy into the system characterized by K_m (erg/cm^3).

The solution for the equilibrium magnetization distribution is a constrained boundary value problem in two or three spatial dimensions with the constraint of constant magnetization M_s. The continuous magnetization distribution of a ferromagnet is approximated by a discrete magnetization distribution consisting of equal volume cubes (3-D) or rods (2-D). Each individual discretized magnetization cell, interior to the array, will be addressed by the (X, Y, Z) coordinates of its centroid. There are N_x cells along X, N_y cells along Y, and N_z cells along Z interior to the structure to be modeled.

There is one plane (3-D) or column (2-D) of boundary cells bounding the discretized region. These boundary cells (conditions) can reflect the continuous uniform magnetization distribution present within the domains themselves on either side of the structure. If no boundary conditions are specified, the cells at the edges are free. In the absence of surface anisotropy, the normal derivative of the magnetization distribution at the surface is zero [2,13]. In the presence of surface anisotropy, the Rado-Weertman boundary conditions is used [13,14].

Fundamental to the solution of the micromagnetic equations is the assumption that the bulk saturation magnetization M_s (emu/cm^3) is constant microscopically throughout the ferromagnet. The parameter M_s represents saturation magnetization at room temperature. For most practical systems being considered (Fe, Co or Permalloy), there is little deviation in M_s at room temperature from the 0 K value. The value of the magnetization vector $\mathbf{M}(\mathbf{r})$ at each point within the ferromagnet is the saturation magnetization multiplied by the direction cosines, that is $\mathbf{M}(\mathbf{r}) = (M_x(\mathbf{r}), M_y(\mathbf{r}), M_z(\mathbf{r})) = M_s\alpha(\mathbf{r}) = M_s\,(\alpha(\mathbf{r}), \beta(\mathbf{r}), \gamma(\mathbf{r}))$. The constraint equation implied by the constant magnetization assumption is $|\alpha(\mathbf{r})| = 1$. The individual contributions to the energies in this continuum model are calculated by integrating the energy expressions over the structure in question. The energy integrals below are integrated over the appropriate dimension, dV. The exchange energy E_{ex} in the continuum approximation is given by.

$$E_{ex} = \int dV[|\nabla\alpha|^2 + |\nabla\beta|^2 + |\nabla\gamma|^2]$$

The exchange parameter A can be extracted from spin-wave theory [15-17], which shows that $A = A'M_s^2 = DS/2V$, where D is the spin-wave dispersion parameter, S is the spin per atom and V is the volume per atom. The spin-wave dispersion parameter, D, is related to the exchange constant, J, in the Heisenberg hamiltonian by D = 2JSa2, where 'a'

is the lattice spacing. This relationship is true for spin-wave modes along bcc [100], bcc [110], fcc [110] and fcc [100] directions.

The volume magnetocrystalline anisotropy for uniaxial (e.g. easy-axis in y) E_{Ku}, and cubic crystals E_{Kc}, is given by the following expressions, respectively,

$$E_{Ku} = \int dV\left[K_{u1}(1-\beta^2) + K_{u2}(1-\beta^2)^2\right]$$

$$E_{Kc} = \int dV\left[K_{c1}\left(\alpha^2\beta^2 + \beta^2\gamma^2 + \alpha^2\gamma^2\right) + K_{c2}\alpha^2\beta^2\gamma^2\right]$$

where the bulk anisotropy constants for cubic, Kc, and uniaxial, Ku, symmetry can be determined from torque magnetometry measurements. The energy due to magnetostriction can be included in the expression for the uniaxial anisotropy by appropriately adjusting the value of the anisotropy constant [20]. The surface magnetocrystalline anisotropy energy E_{Ks} is given by,

$$E_{Ks} = \int dS\frac{1}{2}(\hat{\alpha} \bullet \hat{n})^2$$

where the integration is along the (line increment dS in 2-D or a surface increment in 3-D) boundary at the film surfaces. The symmetry of the surface anisotropy energy was determined by Rado [21,22].The self-magnetostatic field energy E_s can be represented in a number of equivalent forms, but for these purposes the most convenient representation is

$$E_s = -\int dV\frac{1}{2}\vec{H}_s \bullet \hat{\alpha} M_s$$

where the self-field $\mathbf{H}_s$ is determined from the negative gradient of the scalar magnetic potential,

$$\vec{H} = -\nabla\phi$$

The magnetic scaler potential ϕ satisfies

$$\nabla^2\phi = 4\pi M_s \nabla \bullet \hat{\alpha}$$

inside the ferromagnet, and LaPlace's equation outside of the ferromagnet,

$$\nabla^2\phi' = 0$$

and at the surface $\varphi = \varphi'$ and

$$-\frac{d\phi}{dz} + 4\pi M_s\gamma = -\frac{d\phi}{dz}$$

in the two-dimensional case for example. The regularity of ϕ' at infinity is also required. This can be guaranteed by solving for the potential using Green's function methods. The calculation of this self- field energy is the most computationally intensive aspect of solving the micromagnetic equations. The external field energy E_h for an applied field of $\mathbf{H}_o$ is simply given as

$$E_h = -\int dV\vec{H}_o \bullet \hat{\alpha} M_s$$

To calculate the magnetic microstructure in ferromagnets, the time evolution of a magnetization configuration inside a ferromagnet, which is described by the Landau-Lifshitz-Gilbert equation, must be solved. The Landau-Lifshitz-Gilbert equation has been examined experimentally and theoretically [28,29,32,81,82], and found to yield an accurate description of the time evolution of a magnetic moment of fixed magnitude in a magnetic field. This equation has the following form.

$$\vec{dM}/dt = -\frac{\gamma}{1+\alpha^2}\vec{M}\times\vec{H}_{eff} - \frac{\gamma\alpha}{(1+\alpha^2)M_s}\vec{M}\times(\vec{M}\times\vec{H}_{eff})$$

Here, the gyromagnetic frequency $\gamma = g\omega_e/2$ is determined from the free electron value of ω_e and the spectroscopic splitting factor, g = 2. The gyromagnetic frequency γ, the damping parameter α and the magnitude of the effective fields determine the time scales of interest. For time domain simulations, the free electron gyromagnetic frequency of $\gamma = 1.78 \times 10^7$ (Oe sec-1) is used. The damping parameter α is not well known. Values of α between 0.005 and 2.0 have been used to solve LLG. The damping parameter was not found to change the equilibrium magnetization configurations in domain walls in uniform ferromagnetic systems [23]. The effective magnetic field on each magnetic moment is determined from the total system energy E_{tot} as

$$\vec{H}_{eff} = -\partial E_{tot}/\partial(M_s\hat{\alpha})$$

The effective magnetic field incorporates all the effects of exchange, anisotropy, external fields and demagnetizing fields. For the analysis of the equilibrium micromagnetic structure, the differential equation need not be integrated directly. Instead, notice that, for an equilibrium magnetization distribution, dM/dt = 0, which implies that the effective field, $\mathbf{H}_{eff}$, must be parallel to the magnetization **M**. The magnetization configuration can be relaxed iteratively by positioning each magnetization vector (almost) along the effective field vector direction throughout the mesh. The initial condition can be selected to provide a head start for the iteration procedure. When the largest residual of a single value of $(\mathbf{M}\times\mathbf{H}_{eff})/|\mathbf{M}||\mathbf{H}_{eff}|$ decreases below a convergence minimum, the iteration process is stopped. The convergence minimum for terminating the calculation is the value of the largest relative change in the largest component of the direction cosines. This value will depend upon the size of the mesh and on the closeness to a magnetization change, such as the reorientation close to the coercive field in a hysteresis loop calculation. Equilibrium domain wall configurations determined from this energy minimization scheme agree extremely well with configurations determined by solving the Landau-Lifshitz-Gilbert equation directly [23]. For equilibrium configurations for uniform systems, the more economical energy minimization scheme can be used to determine equilibrium configurations. For more complex systems, or in the presence on grain boundaries, which may serve as nucleation sites, the solution of the Landau-Lifshitz-Gilbert equation is necessary for accurate results [18,19].

The content of this section has been extracted and slightly altered from the original version published in a section of Micromagnetics of 180 Degree Domain Walls at Surfaces, M.R. Scheinfein, J. Unguris, J.L. Blue, K.J. Coakley, D.T. Pierce, R.J. Celotta, P.J. Ryan, Phys. Rev. B43(4), 3395 (1991).

1. W.F. Brown, A.E. LaBonte, J. Appl. Phys. **36**(4), 1380 (1965).
2. A.E. LaBonte, J. Appl. Phys. **40**(6), 2450 (1969).
3. A. Aharoni, J. Appl. Phys. **37**(8), 3271 (1966).
4. A. Aharoni, J. Appl. Phys. **38**(8), 3196 (1967).
5. A. Aharoni, Phil. Mag. **26**, 1473 (1972).
6. A. Aharoni, phys. stat. sol. (a) **18**, 661 (1973).
7. A. Aharoni, J. Appl. Phys. **46**(2), 908 (1975).
8. A. Aharoni, J. Appl. Phys. **46**(2), 914 (1975).
9. M.E. Schabes, A. Aharoni, IEEE Trans. Mag. MAG-**23**(6), 3882 (1987).
10. A. Hubert, phys. stat. sol. **32**, 519 (1969).

11. A. Hubert, phys. stat. sol. **38**, 699 (1970).
12. M.E. Schabes, H.N. Bertram, J. Appl. Phys. **64**(3), 1347 (1988).
13. G.T. Rado, J.R. Weertman, J. Phys. Chem. Solids, **11**, 315 (1959).
14. G.T. Rado, Phys. Rev. **B40**(1), 407 (1989).
15. R. Victora, J. Appl. Phys. **62**(10), 4220 (1987).
16. C. Herring, C. Kittel, Phys. Rev. **81**(5), 869 (1951).
17. G. Shirane, V.J. Minkiewicz, R. Nathans, J. Appl. Phys. **39**(2), 383 (1968).
18. C.C. Shir, J. Appl. Phys. **49**(6), 3413 (1978).
19. R. Victora, Phys. Rev. Lett. **58**(17), 1788 (1987).
20. B.D. Cullity, Introduction To Magnetic Materials (Addison Wesley Publishing Co, Reading, 1972).
21. G.T. Rado, Phys. Rev. **B26**, 295 (1982).
22. G.A. Prinz, G.T. Rado, J.J. Krebs, J. Appl. Phys. **53**(3), 2087 (1982).
23. M.R. Scheinfein and J.L. Blue, J. Appl. Phys. **69**(11), 7740 (1991).